

Experimental and Modeling Investigation of Radionuclide Interaction and Transport in Representative Geologic Media

Fuel Cycle Research & Development

Prepared for
U.S. Department of Energy
Used Fuel Disposition
Yifeng Wang, Andy Miller, Edward Matteo
Sandia National Laboratories
Paul Reimus, Mei Ding, Timothy Dittrich
Los Alamos National Laboratory
Liange Zheng, James Houseworth
Lawrence Berkeley National Laboratory
Pihong Zhao, Annie Kersting, Zurong Dai, Mavrik
Zavarin
Lawrence Livermore National Laboratory

September 15, 2013

FCRD-UFD-2013-000314



DISCLAIMER

This information was prepared as an account of work sponsored by an agency of the U.S. Government. Neither the U.S. Government nor any agency thereof, nor any of their employees, makes any warranty, expressed or implied, or assumes any legal liability or responsibility for the accuracy, completeness, or usefulness, of any information, apparatus, product, or process disclosed, or represents that its use would not infringe privately owned rights. References herein to any specific commercial product, process, or service by trade name, trade mark, manufacturer, or otherwise, does not necessarily constitute or imply its endorsement, recommendation, or favoring by the U.S. Government or any agency thereof. The views and opinions of authors expressed herein do not necessarily state or reflect those of the U.S. Government or any agency thereof.

Experimental and Modeling Investigation of Radionuclide Interaction and Transport in Representative Geologic Media

Executive Summary

This report summarizes work accomplished in FY13 to support the natural system evaluation and tool development within the Used Fuel Disposition Campaign (UFDC) in the area of radionuclide interaction and transport in representative geologic media. The natural system evaluation and tool development work directly supports the following UFDC objectives:

- Develop a fundamental understanding of disposal system performance in a range of environments for potential wastes that could arise from future nuclear fuel cycle alternatives through theory, simulation, testing, and experimentation.
- Develop a computational modeling capability for the performance of storage and disposal options for a range of fuel cycle alternatives, evolving from generic models to more robust models of performance assessment.

The natural system is an integral part of a geologic nuclear waste repository. Spatially, it extends from the disturbed rock zone (DRZ) around a disposal room, created by mechanical, thermal and chemical perturbations due to underground excavation or waste emplacement, to the surrounding geologic media, and continues all the way to a specified repository boundary. The natural system evaluation and tool development work package supports all four stages of geologic repository development: site screening, site selection, site characterization, and site suitability study. The information collected in this work package will play a pivotal role in site screening and site selection. From the well accepted multiple barrier concept for waste repository safety, each barrier is supposed to be utilized for its safety function independently to the optimal extent. In this sense the natural barrier needs to be evaluated and necessary research conducted to ensure its optimal safety function. From a repository design point of view, an appropriate balance must be maintained between the natural system and the engineered barrier system (EBS) in the contribution to the total system performance. In practice, there is a risk to place too much reliance on the engineered barrier while not fully taking credits for the natural system. Such practice often results in an overly conservative, very expensive EBS design. Thus, as one of its main objectives, the natural system evaluation and tool development work package will ensure that sufficient research will be conducted to fully exploit the credits that can be taken for the natural system barrier.

This reports documents the work that has been conducted in fiscal year 2013 on three topics that were identified based on the UFDC R&D roadmap (Wang, 2013).

- Topic #P10: Better understanding of radionuclide interaction with geomeia
- Topic #P11: New perspective of colloid-facilitated radionuclide transport
- Topic #P14: Technical basis for thermal loading limits.

The major accomplishments for FY13 are summarized as follows:

- *Iodide interactions with clays:* Understanding iodide interactions with clay minerals is critical to quantifying risk associated with nuclear waste disposal. A suite of clay minerals was used with

varying degrees of isomorphic substitution, chemical composition, and mineral structure. Iodide uptake experiments were completed with each of these minerals in a range of swamping electrolytes and concentrations. It has found that iodide uptake behaviors form distinct trends with cation exchange capacity and mineral structure. These trends change substantially with electrolyte composition and concentration, but do not appear to be affected by solution pH. The experimental results suggest that iodide may directly interact with clays by forming ion-pairs (e.g., $\text{NaI}_{(\text{aq})}$) which may concentrate within the interlayer space as well as the thin areas surrounding the clay particle where water behavior is more structured relative to bulk water. Ion pairing and iodide concentration in these zones is probably driven by the reduced dielectric constant of water in confined space and by the relatively high polarizability of the iodide species. This new conceptual model has far-reaching implications to the capability of clay materials as a geo-membrane for anion exclusion and isolation. To understand radionuclide interaction with compacted clay materials under relevant geologic conditions, a high pressure and high stress experimental setup has been developed, and it has been successfully tested for iodide sorption and diffusion.

- *In-situ characterization of pore structures of clay/shale samples:* Nano- to micro-scale structural characterization is crucial in providing insights into pore-scale transport processes, which are pertinent to upscale continuum model development. The Small-Angle Neutron Scattering (SANS) was used to characterize the pore features of various clay and shale samples. The results revealed the multi-scale nature of pore size distribution of clay/shale materials – a critical piece of information for understanding water migration and radionuclide transport in low-permeability clay materials and shale formations. The study suggests that the SANS be a useful technique to experimentally investigate flow and transport in low permeability and heterogeneous geologic media.
- *Column experiments of uranium interaction with granitic materials:* Small-scale columns appear to be useful for conducting relatively rapid and inexpensive dynamic transport experiments, which complement very well batch adsorption-desorption experiments. The combined use of the batch and column transport experiments provides better constraints on adsorption and desorption kinetics than either method by itself. Batch experiments are useful for evaluating rapid adsorption kinetics because column experiments often cannot effectively interrogate fast kinetics. Small-scale column experiments can also be very useful for identifying the presence of additional sorption sites and their kinetic behavior. The concentration rise during the injection portion of a column experiment can provide useful constraints on adsorption rates and surface densities of sites with slower rates than the fastest reaction. Interrogation of the reaction parameters associated with the slower sites can be improved by increasing the duration of the injection pulse to observe a longer approach to the injection concentration. The shape of the breakthrough curve in small-scale column experiments after the transition from injection of radionuclide solution to radionuclide-free solution can yield valuable insights into adsorption-desorption hysteresis behavior. Uranium transport in crushed granodiorite materials at pH 6.9 appears to be governed by adsorption to and desorption from multiple sites that have different kinetics.
- *Interaction of intrinsic Pu colloids with clay:* The stability of three different types of intrinsic Pu colloids and Pu oxides in the presence of montmorillonite at 25 and 80°C under atmospheric conditions were examined. Intrinsic Pu colloids made in dilute basic solution were found to dissolve quickly, particularly when a strong thermodynamic gradient is provided (i.e., Pu sorption to montmorillonite). At 25°C, the dissolution of intrinsic Pu colloids is slower than at 80°C. Nevertheless, formation and dissolution of intrinsic Pu colloids appears to be a reversible process. Pu dissolution rates and the affinity for montmorillonite increase with temperature. The reversible nature and relatively fast dissolution rates of intrinsic Pu colloids precipitated in a basic solution suggests that these types of colloids are not very stable and their presence downstream of a nuclear waste repository setting is unlikely. In contrast, intrinsic Pu colloids produced from acidic solution and Pu oxides calcined at 300 and 800°C are stable over the 3 months investigated. Under these formation conditions, intrinsic Pu colloids and/or Pu oxides may play an important role in the migration of

intrinsic Pu colloids away from nuclear waste repository setting. Therefore, how Pu oxides are formed impacts their ultimate chemical stability. Heat may play an important role in enhancing the stability of intrinsic colloids by increasing its crystallinity.

- *Modeling Pu transport in clay materials:* A thermal-hydrologic-chemical (THC) model was developed using code TOUGHREACT V2 to simulate the transport of Pu in the engineered barrier system (EBS) bentonite and the natural system (NS) clay formation. The simulations were conducted for a hypothetical bentonite-back-filled nuclear waste repository in clay rock. The simulations demonstrate that Pu has very low mobility in the EBS bentonite and the NS clay formation, due to its adsorption via surface complexation. The redox environment in the EBS bentonite is critical for the fate of Pu, because of its impact on the solid-phase Pu and aqueous complexes of Pu. This calls for a reliable characterization of redox conditions in the EBS bentonite and NS clay formation. The simulations demonstrate our ability to simulate the migration of radionuclides in a complex, interactive THC environment. Such modeling effort is useful for differentiating the relative importance of various processes.
- *Preliminary study for thermal limits of clay materials/host rocks:* Establishing the thermal limit for clay minerals in a nuclear waste repository is a potentially important component of repository design, as flexibility of the heat load within the repository can have a major impact on the selection of repository design. The thermal limit plays a critical role in the time that waste packages would need to cool before being transferred to the repository. In FY13, a preliminary study for thermal limits of clay materials was initiated. A variety of clays (illite, mixed layer illite/smectite, montmorillonite, and palygorskite) were heated for a range of temperatures between 100-500 °C and characterized for surface area, pore structure, and cation exchange capacity (CEC). It was found that thermal treatments have significant effects on CEC for all four clays studied. For illite and illite-smectite, an order of magnitude increase in CEC is seen even at 100 °C. Given the ubiquity of illite in sealing/host formations, e.g. shale caprocks, this result could have an important effect on transport and fate in the near field in the case where the repository is in a clay rich host formation. For montmorillonite, the significant increase in CEC at 400 °C is perhaps of only of marginal importance, as this range of temperatures is likely well beyond any future allowance for the thermal limit in a repository environment. This work is complementary to the hydrothermal study of clay alteration for the EBS work package.

Based on the work accomplished in FY13 and the prior years, the future work is recommended to include:

- Continue the existing effort on experimental methodology development to better understand and quantify radionuclide interaction and migration in geologic environments. Emphasis will be given to the direct measurements of radionuclide interactions and material behaviors under high rock/water ratios, high pressure/stress and high temperature conditions. Expand the measurements to a systematic set of radionuclide and materials.
- Integrate multi-scale measurements into coherent conceptual and mathematical models for total system performance assessments.

Given the importance of material thermal limits in repository design, continue the study of thermal effects on clay material performance, with focus on understanding of how chemical and swelling properties of clay materials change with thermal treatment. This work will be closely tied to the study of the disposal of large size dual purpose canisters.

CONTENTS

1.0	Objectives and Outline	1
1.1	References	3
2.0	Iodide Interaction with Clays: An Batch-Sorption Study	5
2.1	Introduction	5
2.2	Materials and Methods	6
2.2.1	CEC and surface area determinations	6
2.2.2	Clay minerals and purification	6
2.2.3	Iodide sorption experiments	7
2.3	Results	7
2.3.1	CEC and surface area	7
2.3.2	Iodide batch uptake experiments	8
2.3.3	Discussion	13
2.4	Conclusions	15
2.5	References	16
3.0	Iodide Interaction with Clays: Constant Confining Pressure Diffusion Experiments	19
3.1	Introduction	19
3.2	Methods	19
3.2.1	Clay pellet formation	20
3.2.2	Diffusion experiment	21
3.3	Results and Discussion	21
3.3.1	Through diffusion	21
3.3.2	Out diffusion	23
3.4	Conclusions and Discussion	26
3.5	References	26
4.0	Characterization of Pore Structures and their Evolution in Clays Using Small-Angle Neutron Scattering	27
4.1	Introduction	27
4.2	Pore structures and Advantages of Neutron Scattering	28
4.3	Small-angle Neutron Scattering (SANS)	31
4.3.1	Principle	31
4.3.2	Analysis of SANS Data	32
4.3.3	Instrumentation	33
4.3.4	Sample Environment	33
4.4	Materials	34
4.5	Results	35
4.5.1	Characterization of Clay Minerals and Field Clay Samples	35
4.5.2	Pore Characterization of Clays	36
4.6	Conclusions	45
4.7	References	45
5.0	An Experimental Methodology for Improving Radionuclide Transport Process Models using Uranium and Grimsel Granodiorite as a Case Study	47
5.1	Introduction	47
5.2	Materials and Methods	48
5.2.1	Ground Water	48
5.2.2	Rocks	49
5.2.3	Uranium and Tritiated Water	51

5.2.4	Analytical Measurements	52
5.2.5	Batch Adsorption and Desorption Experiments	52
5.2.6	Column Transport Experiments	54
5.2.7	Interpretive Modeling	56
5.3	Results	58
5.3.1	Batch Sorption and Desorption Experiments	58
5.3.2	Column Transport Experiments	60
5.4	Discussion	69
5.5	References	74
6.0	Stability of Intrinsic Pu colloids in the Presence of Montmorillonite at 25 and 80 °C: High-fired and freshly prepared PuO₂ oxides	77
6.1	Introduction	77
6.2	Previous Work	78
6.3	Technical Approach	78
6.4	Technical Results and Discussion	84
6.5	Conclusions and Future Work	87
6.6	References	87
7.0	THMC Effects on Radionuclide Transport in a Clay Repository	89
7.1	Introduction	89
7.2	Technical Approach	90
7.2.1	Simulator	90
7.2.2	Model Setup	90
7.2.3	Chemical Model	92
7.3	Modeling Results	7.3
7.3.1	THC Evolution in the First 1000 Years	102
7.3.2	THC Evolutions and Pu Migration until 10000 Years	111
7.4	Conclusions and Future Work	122
7.5	References	123
8.0	Thermal Effect on the Chemical Behavior of Clays	127
8.1	Introduction	127
8.2	State of the Art	127
8.3	Technical Approaches	128
8.4	Results	128
8.5	Conclusions and Future work	132
8.6	References	133
9.0	Summary	135

1.0 Objectives and Outline

This report summarizes work accomplished in FY13 to support the natural system evaluation and tool development within the Used Fuel Disposition Campaign (UFDC). The natural system evaluation and tool development work directly supports the following UFDC objectives:

- Develop a fundamental understanding of disposal system performance in a range of environments for potential wastes that could arise from future nuclear fuel cycle alternatives through theory, simulation, testing, and experimentation.
- Develop a computational modeling capability for the performance of storage and disposal options for a range of fuel cycle alternatives, evolving from generic models to more robust models of performance assessment.

The natural system is an integral part of a geologic nuclear waste repository. Spatially, it extends from the disturbed rock zone (DRZ) around a disposal room, created by mechanical, thermal and chemical perturbations due to underground excavation or waste emplacement, to the surrounding geologic media, and continues all the way to a specified repository boundary. The natural system evaluation and tool development work package supports all four stages of geologic repository development: site screening, site selection, site characterization, and site suitability study. The information collected in this work package will play a pivotal role in site screening and site selection. From the well accepted multiple barrier concept for waste repository safety, each barrier is supposed to be utilized for its safety function independently to the optimal extent. In this sense the natural barrier needs to be evaluated and necessary research conducted to ensure its optimal safety function. From a repository design point of view, an appropriate balance must be maintained between the natural system and the engineered barrier system (EBS) in the contribution to the total system performance. In practice, there is a risk to place too much reliance on the engineered barrier while not fully taking credits for the natural system. Such practice often results in an overly conservative, very expensive EBS design. Thus, as one of its main objectives, the natural system evaluation and tool development work package will ensure that sufficient research will be conducted to fully exploit the credits that can be taken for the natural system barrier.

This reports documents the work that has been conducted in fiscal year 2013 on two topics that were identified based on the UFDC R&D roadmap (Wang, 2013).

- Topic #P10: Better understanding of radionuclide interaction with geomeia
- Topic #P11: New perspective of colloid-facilitated radionuclide transport
- Topic #P14: Technical basis for thermal loading limits.

As radionuclides are released from the engineered barrier they will move through and interact with the natural system. The transport behavior of the radionuclides can and will change due to complex physical and chemical interactions with the surrounding geologic media. Existing models generally assume that radionuclide retention in the natural system can be described with a linear, equilibrium Kd approach. The reality is much more complex. Tasks under topic P10 are designed to carry out experiments to help support model development to improve our ability to predict how radionuclides migrate in the subsurface. Tasks under topic P10 support experiments and model development in the following areas:

- Thermodynamics and kinetics of radionuclide sorption/desorption from representative mineral (e.g., different clay minerals).

- Radionuclide behaviors in high rock/water ratio environments, especially in nanopores and interlayers.
- Coupling of redox reactions with radionuclide sorption.
- Complexation of radionuclides with natural organic matter.
- Radionuclide sorption in the presence of competing species, high ionic strength media, or at elevated temperatures.
- Extrapolation from simple system measurements to complex systems.
- Radionuclide transport in low permeability media (e.g., membrane effect of clay formation).

The second topic (P11) identified based on the UFDC Natural System R&D Plan is designed to determine when colloid-facilitated transport is important under given repository conditions. Colloid facilitated transport (CFT) may have been overestimated in previous performance assessments because many aspects of CFT are not well constrained, thus making pessimistic bounding assumptions necessary. CFT is also an important issue for confidence building of a performance assessment model. Important uncertain processes and parameters associated with CFT include: desorption processes and rates, colloid immobilization processes and associated parameters, the degree to which colloids behave as heterogeneous populations in the subsurface, the role of chemical and flow transients in mobilizing and immobilizing colloids, and colloid generation processes. This task focuses on two key aspects of the CFT: (1) Colloid particle formation and transport in porous geologic media and (2) radionuclide partitioning among pore water, colloid particles, and stationary substrates. In recent years, much progress has been made in nanoscience and nanotechnology and as a result, it is important to re-examine CFT mechanisms taking into account new advances in nanoscience and nanotechnology. For example, we do not currently know if geochemical processes that are relevant at high concentrations in near-field environments are the same as at low concentrations expected in the far field. In addition, new technology allows us to investigate colloid processes occurring at low, environmentally relevant concentrations. The work under task P11 will involve laboratory measurements, model development, and field testing. Novel in-situ colloid characterization techniques will be explored. Specific activities include the following:

- Better understanding of colloid-radionuclide-stationary mineral phase interactions
- Development of novel in-situ techniques for characterizing CFT
- Development of modeling capabilities for simulating CFT.

The repository thermal loading limits are of concern for repository design and waste emplacement. Thermal expansion, tensile and compressive stresses, and altered properties of fractures, faults, and the rock matrix are possible. There can also be thermal-chemical alteration of the host rocks and the other geologic units, including, mineral precipitation, dissolution, alteration of minerals with attendant volume changes, and altered properties of fractures, faults, the rock matrix, and the formation of near-field chemically altered zones (rind). Topic #14 is focused on systematic examination of the technical basis for the thermal limits of various disposal media/materials with an objective to relax or even eliminate the existing restrictive thermal limits.

The work reported here was performed in the collaboration among four national laboratories (SNL, LLNL, LBNL, and LANL) and is presented as eight self-contained but interrelated sections:

- Section 2 reports a new discovered mechanism for iodide interaction with clays, which has important implications to the migration of iodine-129 in repository environments (SNL).
- Section 3 describes a new high pressure/high stress experimental setup for measuring radionuclide interaction with compacted clay samples and reports a preliminary testing result for iodide diffusion and sorption (SNL).

- Section 4 reports our first attempt to use Small-Angle Neutron Scattering to characterize pore structures of clay/shale samples to provide important material structure information for understanding radionuclide interaction in clay formations (LANL).
- Section 5 describes how to use small column flow-through experiments to constrain radionuclide sorption and transport parameters in geologic materials and the result of applying the methodology to uranium transport in crushed granodiorite materials (LANL).
- Section 6 summarizes the results for experimental determination of intrinsic Pu colloids in the presence of clay minerals (LLNL).
- Section 7 describes a thermal-hydrologic-chemical model for simulating Pu transport in the EBS bentonite and clay-based host rock (LBNL).
- Section 8 provides a preliminary result of the experimental study of the potential effect of thermal treatment on clay physical and chemical properties (SNL).
- Section 9 provides the summary of the FY13 work on radionuclide interaction with representative geomedial and recommends the future work (SNL).

1.1 References

- (1) Wang, Y., 2013. *Research & Development (R&D) Plan for Used Fuel Disposition Campaign (UFDC) Natural System Evaluation and Tool Development (Rev 1)*.

2.0 Iodide Interaction with Clays: An Batch-Sorption Study

2.1 Introduction

Subsurface clay formations are one of the major rock types being considered by several countries for geologic disposal of nuclear waste. Even when clays will not be used as a host rock, engineered barrier materials often include a compacted bentonite buffer surrounding the waste package both for chemical and structural stabilization. Clays are an ideal material as they possess low permeabilities where ion transport is dominated by diffusion. Clays also possess high sorption capacities for many cations present in nuclear waste. The high cationic sorption capacities are caused by the simultaneous presence of negatively charged cation exchange sites on the planar surfaces of clay layers, and amphoteric surface complexation sites on the edge of the layer. The negative structural charge minimizes anion interaction with clays. Iodine is expected to be present as iodide under the reducing conditions of waste disposal in clay [1]. The assumed lack of interaction between iodide and clays causes iodine-129 to have the earliest breakthrough and the largest contribution to the predicted dose from a deep geological repository [2, 3]. Performance assessment calculations show that even a small retention capability of clay materials for iodide can make a huge difference in total dose predictions [2].

A growing body of work points to the potential presence of a weak interaction between iodide and clays [4-6] [7, 8]. The weakness of the interaction has made experimental measurements somewhat contradictory. Several major hypotheses exist to explain observed interactions, including: isotopic dilution with native iodine [9, 10], co-precipitation or uptake into carbonates [11], the presence of organic matter [12-14], uptake to ancillary minerals [15, 16], impure radiotracers and unconsidered alterations to iodide redox state [9, 17, 18]. All of these explanations rely on the premise that iodide does not interact with clays in any meaningful way, and the observed iodide uptake and retardation are caused by other components or processes occurring in natural clay samples.

Attempts to gain a mechanistic understanding of iodide interaction with clays and clay bearing soils are rare. In two separate studies iodide uptake tends to increase with decreasing pH both for pure illite and a natural soil sample [14, 19]. This is consistent with an outer sphere interaction with highly protonated, positively charged metal oxides and clay edge sites. However, most diffusion studies and porewater analysis from clay mineral systems have pH values >7 [20] limiting this mechanism in natural systems. As pointed out by others [9], if this mechanism was controlling iodide behaviors similar responses would be expected between clays with similar edge charge behavior such as illite and montmorillonite. But illite has been shown to have much higher uptake than montmorillonite [19].

The goal of this study is to consider interactions between iodide and clays beyond those described in classical interpretations of clay surface chemistry [21, 22]. This new view requires a different experimental approach. Most studies examining iodide interactions with clay minerals use clay samples from a specific formation of interest to a national nuclear waste disposal program, or on purified clay minerals generically relevant to waste disposal, most commonly montmorillonite and illite. The focus on these clays and clay minerals is pragmatic and directly useful; however, it limits data interpretation within the confines of classical clay surface chemistry models and/or with K_D values. Single clay studies remove the ability to compare uptake as a function of other key clay characteristics, including: structural charge variability, different layer structures, and variable nanopore scale chemistry caused by constrained space within the clay mineral [23]. In this study, we focus on a series of clay minerals, and measure iodide uptake under several swamping electrolyte strengths and compositions. The use of a multi-clay study allows for the clarification of mineral structure controls on iodide uptake in addition to the traditional consideration of pH and electrolyte composition and concentration. Specifically, iodide uptake is reported as a function of lattice substitution (represented by the cation exchange capacity value, CEC) and as a

function of clay structure. Two classes of clay structure are used in these experiments, layered and fibrous clays. Layered clays (e.g., illite, montmorillonite, kaolinite) are far more heavily studied due to their relevance to waste disposal and environmental abundance. Fibrous clays are largely irrelevant to nuclear waste disposal, but are well studied for other industrial applications. The results imply a mechanism including ion-pair formation and the concentration of iodide within the interlayers and other confined pore spaces.

2.2 Materials and Methods

2.2.1 CEC and surface area determinations

The surface areas and CEC of the clay minerals were measured using N_2 BET, methylene blue exchange, and $BaCl_2$ exchange. Nitrogen is generally considered unable to enter the interlayer porosity and only represents the external surface area of clays. Methylene blue adsorption takes place in aqueous solution where the clays can de-laminate giving both a total surface area determination as well as a measurement of CEC. The methylene blue (MB) procedure requires sodium exchanged clays [24]. The clays were converted to the sodium form using a method similar to the gentle purification method in [25]. The clays were mixed with a 1.0M NaCl solution overnight. For all of the clays except montmorillonite, a single centrifugation for 60 minutes at 4400 g was sufficient to separate the clay from the solution. The montmorillonite often required several centrifuge cycles (6-7 hours). Once a pellet was formed, the solution was decanted and discarded, and fresh NaCl solution was added. The mixing and centrifugation processes were repeated three times. The entire process was repeated three times with DI water instead of 1.0M NaCl. Once the clays were washed they were dried in a 100°C oven for several days. Barium exchange also takes place in aqueous solution. Barium is added in excess to a clay slurry thereby displacing all of the native cations. Major cations (Na, Ca, K, Mg, Fe) can then be measured and the exchange capacity determined [26]. The major cations were measured by inductively coupled plasma-optical emission spectroscopy (ICP-OES).

2.2.2 Clay minerals and purification

The clays used all originate from the Clay Mineral Society source clays project at Purdue University. Seven total clays were used including: kaolinite, ripidolite, illite, montmorillonite, palygorskite, sepiolite, and a 70/30 illite/smectite mixed layer (ID numbers: KGa-1b, CCa-2, IMt-1, SWy-2, PFI-1, SepNev-1, and ISCz-1, respectively). The layered clays are kaolinite, ripidolite, illite, montmorillonite and the illite/smectite mixed layer. The fibrous clays are palygorskite and sepiolite. All of the clay minerals were subjected to dry sieving at 75 microns. The <75 micron fraction was used in all the experiments presented here. Each clay was examined by X-ray diffraction (XRD) analysis for impurities. The kaolinite, sepiolite, and ripidolite did not have any measurable impurity minerals. All of the other clays had measurable amounts of quartz. There were no other clearly identifiable oxides or carbonates. The best match to the illite spectrum was muscovite, although due to the small degree of crystallinity, the spectra peaks were small. The XRD spectra for the illite/smectite mixed layer clay most closely resembled pure illite, although the match was not exact. Initially surface titrations were considered as a part of the study. While not reported here, significant pH buffering around pH 8.3 did suggest a calcite impurity in the illite and montmorillonite samples that was not detectable using XRD. The buffering capacity was non-existent in samples subjected to the Na-exchange procedure described below. For the iodide uptake experiments, the <75 micron fraction was used without further purification.

2.2.3 Iodide sorption experiments

Batch iodide sorption experiments were completed in at least triplicate for all of the clay minerals. For each set of experiments, the ionic composition and concentration of the swamping electrolyte was held constant. The electrolytes and concentrations used are shown in Table 2-1. A constant solid:solution ratio of 100 g/L was used in all of the experiments.

Table 2-1. Summary of electrolytes and concentrations for batch uptake experiments. An × denotes which were used in these experiments.

Concentration (M)	NaCl	NaBr	KCl
1.0	×		
0.1	×	×	×
0.01	×		

The batch reactors were 50mL centrifuge tubes. Blanks (electrolyte and iodide spike without clay) confirmed the absence of wall sorption or iodide loss to volatilization. Clay blanks (electrolyte and clay without iodide) confirmed the lack of leachable iodide from the clays. To each tube the clay and electrolyte solution was added, and the suspensions were equilibrated overnight. An iodide spike was added after equilibration. A constant iodide concentration of 3.94E-4 M (50 mg/L) was used for all of the batch reactors. The spike was an ion chromatography (IC) iodide standard with no detectable iodate. The batch reactors were mixed in the dark at room temperature for 7 days in a horizontal position on a shaker table. After 7 days, the samples were centrifuged for 1 hour at 4400g. The supernatant was removed with a pipette and refrigerated for analysis. The pH was measured immediately before the iodide spike was added, and again at the end of the 7 day mixing period both before and after centrifuging. No attempt was made to keep the pH constant or at a specific level. As mentioned above, the pH in the illite and montmorillonite reactors was controlled both by the clay and through some amount of calcite dissolution. For all of the other clays, the pH was controlled only through clay buffering. The pH reported is the equilibrium pH for the given clay minerals in the specified electrolyte. After the uptake sample had been removed, an equal amount of DI water was added to the vial. The slurry was mixed for four days. At the end of four days the sample was centrifuged as above, and a sample was removed for analysis. This sample represents a reversal of the uptake process, and gives information regarding the oxidation state of the iodine species after uptake.

The samples were analyzed using a Dionex 1100 ion chromatograph (IC) with an AS23 guard and analytical column, and a bicarbonate/carbonate eluent. Methods were developed to simultaneously measure iodide and iodate.

2.3 Results

2.3.1 CEC and surface area

Table 2-2 shows the results of the CEC and surface area determinations. CEC values between the MB and BaCl₂ methods are generally in good agreement, approximately within a factor of 2 of each other

and to published values for the source clays [27]. Besides direct determination of CEC, methylene blue also allows for the calculation of surface area assuming monolayer sorption and a molecular area of 130 Å². Generally methylene blue surface areas are higher than BET surface area determinations. The BET surface area is interpreted as representing only the external surface area of the clay particles; the methylene blue surface area is more representative of the total surface area. The difference between them is the interlayer area. Sepiolite is the one exception to the general behavior. The BET surface area was larger than the methylene blue surface area, probably due to N₂ condensation within the nanochannels of the material [28]. This leads to the physically meaningless negative internal surface area shown in Table 2-2.

Table 2-2. CEC and surface area values for the clays used. Surface area determination methods are explained in the text.

	MB CEC (meq/100 g)	BaCl ₂ CEC (meq/100 g)	BET S.A. (m ² /g)	MB S.A. (m ² /g)	Internal S.A. (m ² /g)
Kaolinite	1.50	4.61	11.31	11.76	0.45
Ripidolite	3.00	6.03	8.02	23.49	15.47
Illite	14.98	27.61	31.46	117.21	85.76
Illite/Smectite	24.69	30.39	29.82	193.23	163.41
Montmorillonite	109.53	151.92	28.29	857.17	828.88
Sepiolite	17.41	8.98	201.43	136.27	-65.16
Palygorskite	39.96	29.22	141.52	625.45	483.93

2.3.2 Iodide batch uptake experiments

Tables 2-3 and 2-4 show the pH values at different points in the experiments. Table 2-3 shows the pH values for equimolar electrolyte concentrations but varying electrolyte identities. Table 2-4 shows the pH values for varying concentrations of NaCl electrolytes. In general the values are somewhat bimodal being centered around pH 4 or pH 8. During the course of mixing, the pH changed only slightly, typically decreasing within ~0.2 pH units. Centrifuging caused larger shifts in pH, the largest being 0.98 pH units for the KCl electrolyte experiments with ripidolite. Differences between equimolar electrolytes are fairly small suggesting similar Na⁺/H⁺ and K⁺/H⁺ exchange constants. With increasing sodium concentration, the pH decreases consistent with Na⁺ exchange for H⁺ on the basal surfaces of the clays.

Solid:liquid partitioning coefficients (K_D values, mL/g) were calculated using equation (2.1),

$$K_D = \frac{(C_I - C_F) * S * 1000}{C_F} \quad (2.1)$$

where C_I is the initial aqueous iodide concentration (mg/L), C_F is the final aqueous iodide concentration (mg/L), and S is the solid:solution ratio (g/mL). Table 2-5 shows iodide K_D values as a function of

electrolyte identity, and Table 6 shows iodide K_D values as a function of NaCl concentration. Negative values are most generally interpreted to be anion exclusion due to the fixed negative charge of the clay interface. The correction of iodide uptake for this anion exclusion effect is difficult due to the inability to quantify the liquid volume affected by anion exclusion. The K_D values presented here can thus be viewed as a lower bound for iodide uptake. As with other studies, the error (standard deviation of at least three replicates) is often the same magnitude or larger than the K_D value. Instead of considering the values themselves, trends between the clays under the different electrolyte conditions are of interest. For the layered clays, K_D values are strongly correlated with the total surface area of the clay minerals for both NaCl and KCl electrolytes (Figure 2-1). Since the total surface area is dominated by the internal surface area, similar correlations are found with internal surface area or CEC. No obvious trends are found when uptake is plotted as a function of external surface area (see Supporting Information). The nature of the correlations is influenced by swamping electrolyte compositions, but they are essentially independent of pH (Tables 2-3 and 2-4). For example, the iodide uptake trend with NaCl declines with increasing total surface area, while the uptake trend with NaBr is quite flat. In both the NaCl and NaBr experiments the pH values are similar. For experiments with variable concentrations of NaCl, the uptake trends are similar in nature for both the 0.01M and 0.1M NaCl; uptake decreases with increasing total surface area (Figure 2-2). Also, the uptake is larger with 0.1M NaCl concentrations than with 0.01M. At the 1.0M NaCl concentration, the trend is dramatically different with positive K_D values for all of the layered clays, and a very slight increase with increasing surface area. The fibrous clays (palygorskite and sepiolite) act substantially different than the layered clays. For four out of the five electrolyte identities and concentrations, the K_D value increases with CEC; the one exception is at 0.01M NaCl.

While iodide was quantified using the IC technique, iodate quantitation was hampered by an impurity present in many of the clays which could not be resolved from iodate. However, the unresolved peak areas in the iodide uptake samples were no larger than peak areas from the clay blanks suggesting no conversion of iodide to iodate. Further, in the water rinses performed after the iodide uptake experiments, iodide was present and quantifiable. The impurity peak areas were again no larger than those from clay banks treated in an identical manner. The amount of iodide associated with the clays was an insignificant fraction of the total mass added, invalidating attempts to use mass balance calculations to determine iodide to iodate conversions. These results suggest that all of the uptake behaviors presented are iodide interactions with clay minerals, and there was little to no conversion to iodate.

Table 2-3. pH values at different points in the experiment for equimolar electrolytes

	0.1M Electrolyte								
	NaCl			NaBr			KCl		
	Before spike	Before Centrifuging	After Centrifuging	Before spike	Before Centrifuging	After Centrifuging	Before spike	Before Centrifuging	After Centrifuging
Kaolinite	4.23	4.21	4.39	4.43	4.47	4.28	4.18	4.12	4.07
Ripidolite	8.73	8.51	8.10	8.76	8.63	8.20	8.79	8.59	7.81
Illite	8.45	8.27	8.16	8.48	8.31	7.95	8.28	8.08	8.01
Illite/Smectite	4.00	4.06	4.24	4.22	4.26	4.03	3.91	3.85	3.82
Montmorillonite	8.15	8.05	8.05	8.19	8.14	8.05	8.09	8.03	7.90
Sepiolite	7.89	7.66	7.83	7.98	7.63	7.75	7.92	7.64	7.80
Palygorskite	7.98	7.76	7.90	8.05	7.84	7.82	7.84	7.63	7.87

Table 2-4. pH values at different points in the experiment for changing concentrations of NaCl electrolyte

	NaCl Electrolyte								
	0.01M			0.1M			1.0M		
	Before spike	Before Centrifuging	After Centrifuging	Before spike	Before Centrifuging	After Centrifuging	Before spike	Before Centrifuging	After Centrifuging
Kaolinite	4.70	4.83	4.73	4.23	4.21	4.39	4.04	4.27	4.19
Ripidolite	8.79	8.57	8.15	8.73	8.51	8.10	8.74	8.59	8.37
Illite	8.68	8.46	8.30	8.45	8.27	8.16	8.37	8.22	7.87
Illite/Smectite	4.38	4.57	4.40	4.00	4.06	4.24	3.57	3.65	3.74
Montmorillonite	8.65	8.55	8.50	8.15	8.05	8.05	7.78	7.77	7.73
Sepiolite	7.92	7.64	7.83	7.89	7.66	7.83	7.78	7.50	7.71
Palygorskite	8.17	7.93	7.99	7.98	7.76	7.90	7.83	7.75	7.75

Table 2-5. K_D values for iodide in the different swamping electrolytes used. Standard deviation is presented in parentheses.

0.1M Electrolyte				
	BaCl ₂ CEC	K_D [mL/g] (Std. Dev.)		
	meq/100g	NaCl	NaBr	KCl
Kaolinite	4.61	1.61 (0.28)	0.02 (0.63)	-0.01 (0.22)
Ripidolite	6.03	1.13 (0.38)	-0.16 (0.72)	-0.31 (0.17)
Illite	27.61	0.54 (0.12)	0.13 (0.002)	-0.50 (0.24)
Illite.Smectite	30.39	0.38 (0.08)	-0.01 (0.11)	-0.49 (0.11)
Montmorillonite	151.92	-0.32 (0.35)	-0.58 (0.07)	-1.69 (0.90)
Sepiolite	8.98	0.01 (0.28)	0.79 (0.14)	0.11 (0.30)
Palygorskite	29.22	0.24 (0.30)	1.26 (0.05)	0.99 (0.17)

Table 2-6. K_D values for iodide in variable concentrations of NaCl electrolyte. Standard deviation is presented in parentheses.

NaCl Electrolyte				
	BaCl ₂ CEC	K_D [mL/g] (Std. Dev)		
	meq/100g	0.01M	0.1M	1.0M
Kaolinite	4.61	0.48 (0.26)	1.61 (0.28)	0.11 (0.29)
Ripidolite	6.03	0.14 (0.21)	1.13 (0.38)	0.44 (0.17)
Illite	27.61	-0.46 (0.41)	0.54 (0.12)	0.27 (0.21)
Illite.Smectite	30.39	-0.16 (0.25)	0.38 (0.08)	0.30 (0.08)
Montmorillonite	151.92	-1.35 (0.54)	-0.32 (0.35)	0.60 (0.09)
Sepiolite	8.98	1.38 (4.03)	0.01 (0.28)	-0.01 (0.30)
Palygorskite	29.22	-0.23 (0.54)	0.24 (0.30)	0.70 (0.26)

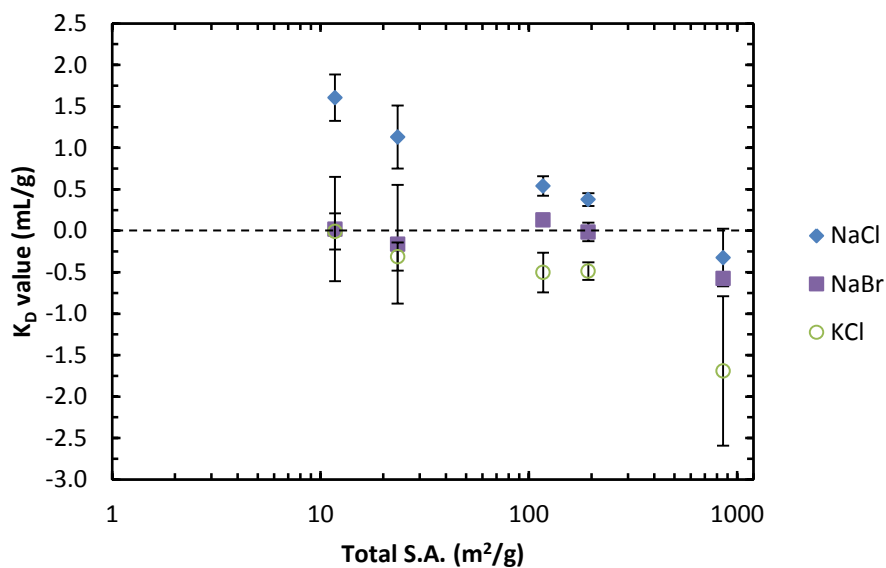


Figure 2-1. K_D values for the layered clays as a function of the total surface area for the three electrolytes considered.

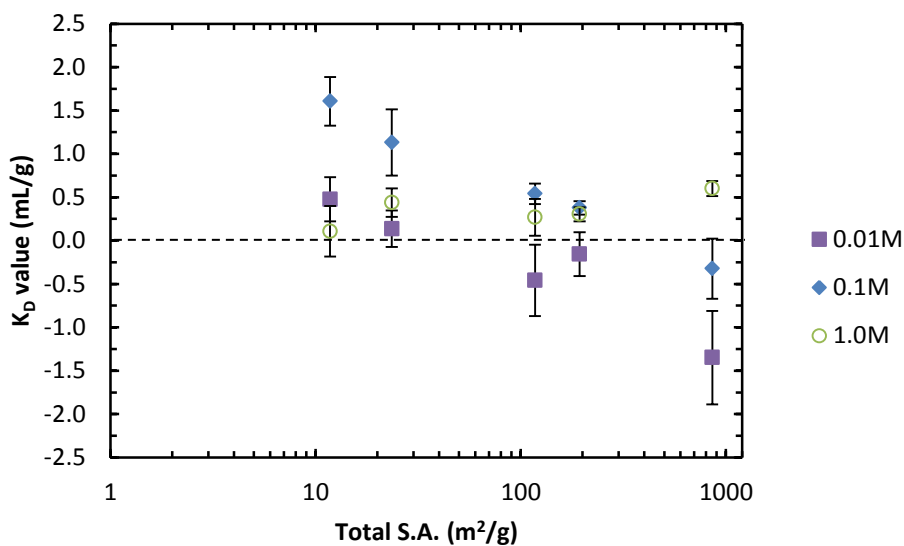


Figure 2-2. K_D values for the layered clays as a function of total surface area for each of the NaCl concentrations used.

2.3.3 Discussion

In developing a conceptual model for iodide uptake in these experiments two major factors need to be considered. The first is the K_D relationship as a function of electrolyte composition. If an anion exchange type of mechanism were controlling iodide behavior, similar results would be expected for equimolar Cl^- concentrations. Since the NaCl and KCl experiment showed very different results anion exchange can be ruled out, corroborating the mathematical analysis rejecting non-specific anion exchange in [9]. If the interaction were based solely on surface charge properties and the nature of the electrical double layer, similar results would be expected between the NaCl and NaBr experiments. With the Na^+ ion being present in equimolar concentrations, the interlayer spacing for a given clay should be identical as should the surface charge distribution into solution. However, the iodide did not behave similarly in these two systems either. The underlying mechanism is dependent both on the cation and anion present in the swamping electrolyte. The second major consideration is the physical location of iodide. The strong correlation between K_D and CEC with total surface area (Figures 2-1 and 2-2) and lack of trend with BET surface area (Supporting Information) suggest iodide interactions with negatively charged sites on the clay surfaces. This is supported by the facts that the observed correlation is essentially independent of solution pH (Tables 2-3 and 2-4) and that there is no obvious correlation between K_D and external surface area (Supporting Information), both indicating that external surface sites, especially the edge sites of clays, do not play a significant role in iodide uptake by clay materials for the conditions considered here. Using classical clay models, iodide cannot approach areas of negative charge due to electrical repulsion. This suggests the iodide is not present as free iodide, but instead as a neutral species. In the 1.0M NaCl experiments, the K_D relationship with CEC nearly reverses including the only positive K_D value for montmorillonite. Charge neutralization arguments are inadequate to describe the positive uptake as common monovalent salts up to 2M in concentration are insufficient to reverse the surface charge of montmorillonite as determined by zeta potential [29]. A more likely explanation of the positive K_D value is that the local concentration of sodium is higher near the negatively charged surface, which would favor more NaI ion pair formation and subsequent uptake. Ion-pairing and subsequent interaction with the clays is a potential mechanism consistent with the data. It has also been suggested as a possible mechanism in clay diffusion studies [30] [31] and has been studied as a process for a significant period of time [32-34] [35]. Previous work predominantly focuses on a monovalent anion association with a polyvalent cation yielding an aqueous species with an overall positive charge (e.g., CaCl^+ and $\text{CaB}(\text{OH})_4^+$). However, in this case the expected ion-pairs are neutral (e.g., $\text{NaI}_{(\text{aq})}$), which removes the thermodynamic driving force of positively charged ion-pair association with the negatively charged clay surface.

To gain a driving force for the neutral ion-pair to concentrate in the zone of negative charge on the clay surfaces, relative hydration energies and polarizability of the anions may need to be invoked. Within 1-2 water layers surrounding a mineral phase, water properties are heavily affected by the mineral surface and are distinctly different from those in bulk solution [36]. For most minerals in dilute systems this effect is generally negligible. However for clays, the large specific surface area and interlayer environments may create a significant amount of confined volume where water properties are different from bulk solution. Most notably, the confined structure decreases the dielectric constant in both charged and uncharged pores [37, 38]. Ion pair formation is increasingly favored as the dielectric constant decreases [39, 40]. Thus within the confined spaces of the clay interlayer, free iodide is less likely than in bulk solution. Furthermore, at air-water and hydrophobic surface-water interfaces, a similar change to water structure and dielectric is expected. Within about 2nm of the interface, halogen concentrations follow the Hofmeister series, $\text{F} < \text{Cl} < \text{Br} < \text{I}$. Bromide and iodide concentrations are larger at the interface than in bulk, chloride is approximately equally distributed, and fluoride concentrations are smaller at the interface than in bulk solution (Figure 2-3a) [41-43]. This trend is explained by comparing the relative polarizability of the anions. It is more thermodynamically favored for the highly polarizable iodide to be

present in areas where water is more structured. In equimolar halogen solutions, the relative concentrations are also a function of surface charge [42]. The data presented here is generally consistent with the work completed for other types of surfaces. Bromide and iodide have more similar polarizabilities than chloride and iodide. When shifting from a NaCl to a NaBr electrolyte, the Br competes more directly with iodide uptake mechanisms, and the relatively higher concentration of Br can displace iodide leading to smaller iodide K_D values. Chloride is less likely to displace iodide as it is significantly less polarizable than iodide, and the iodide K_D values are higher. This conceptual model is also consistent with [19] who found increased iodide desorption efficiency when mixed with equimolar salt solutions in the order $F < Cl < Br < I$. Also, the larger iodide uptake in Na dominated systems compared to the K systems for the layered clays is consistent with the trend in ion pair formation constants [39]. Considering the role of structured water in a confined space favorably compares with the data as the electrolyte identity changes, and it may also explain the difference in iodide behavior between the clay structures.

The channel structure of the fibrous clays is considerably different from the platy structure of the layered clays and so is iodide uptake. Palygorskite and illite have similar CEC values, and yet the iodide uptake as a function of electrolyte concentration and identity is significantly different. When moving from the NaCl to either the NaBr or KCl electrolyte uptake decreases in illite while increasing with palygorskite. Furthermore, comparing uptake between palygorskite and sepiolite, the expectation based on charge exclusion is less iodide uptake for the more highly negatively charged palygorskite. And yet uptake is almost always higher with palygorskite than it is with sepiolite. This conformational difference between the fibrous and layered clays and the different sizes of the pore channels between the fibrous clays may lead to variable water properties leading to increased uptake despite the higher structural charge [44, 45].

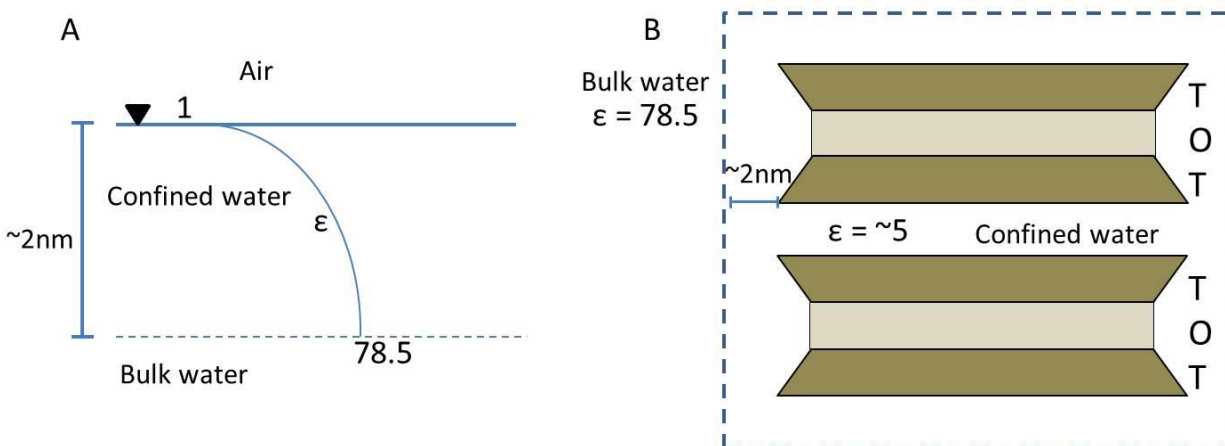


Figure 2-3. A- Conceptual model of the dielectric constant change near the air-water interface, B- 2-box model proposed here for clay minerals

Current mathematical interpretations of the changing dielectric constant describe the dielectric as a function of distance away from the interface [43] [42]. These models use interconnected partial differential equations, which may or may not be informed/simplified by molecular dynamics calculations. Clays are simpler in that a 2-box model may be sufficient; one box represents the bulk water and the other box represents the confined water (Figure 3B). However, calculating the dielectric constant in the interlayer is not trivial. The exact interlayer spacing depends on the structural charge of the clay as well as

the exchanging ion [46]. The dielectric constant will depend on both the spacing and the geometry of the interlayer (layered vs. fibrous). The 2-box model would be similar in concept to previously developed Na/Cs exchange models [47, 48]. In those cases, hydration energy alone was sufficient to suggest why Cs uptake is favored over Na uptake as a function of increasing compaction. In this case, a similar conceptual model may still hold, but the variables of interest need to include: the polarizability of the anion, the formation constant of the ion pair, changes to the dielectric constant based on geometry and clay charge, as well as the hydration energies of the ions involved. Molecular simulations would be required to understand the ultimate driving force for iodide concentration near the clay surfaces.

It is difficult to extrapolate such results to more disposal relevant systems. Generally the ionic strength of clay pore waters is on the order of 0.1M, and tend to be dominated by NaCl, although Ca^{2+} , Mg^{2+} , K^+ , SO_4^{2-} , and HCO_3^- are also generally present. Given the variability between the iodide uptake in the different swamping electrolytes it is unclear if the behaviors observed would still occur in mixtures of those electrolytes. Finally, if the proposed interpretation is correct, iodide uptake should be exacerbated in compacted systems where a larger proportion of the pore water is affected by the clay surfaces. The proposed interpretation may also help to explain the diffusion of anions at large dry densities ($>\sim 1600\text{kg/m}^3$). At these very high densities there is a theoretical point where the clay double layers overlap, filling the pore space and excluding anions from diffusing. One hypothesis to explain anion diffusion above that critical dry density is non-uniform pore structure [49]. An alternative version is that some anions are diffusing as neutral ion-pairs, and thus would not be affected by the charge domain in solution.

Iodide interactions with clay minerals are so weak experimental attempts at understanding them are hampered by the fact that the error is generally larger than the K_D value. The same was true here. However, in this case, using a broad study of several clay minerals allowed for the observation of trends as a function of lattice substitution and clay structure. This in turn gave insight into a possible, generally unconsidered mechanism for direct iodide interaction with clays that does not violate current surface complexation/ion exchange models for clays. This relationship appears valid despite the variability in pH values for the different electrolyte systems, the chemical variability between the clays used and the general lack of clay purification. The iodide uptake mechanism appeared as an emergent property heavily related to structural charge and clay texture alone. However, the thermodynamic driver of iodide accumulation near clay surfaces is still vague. And, although the experimental data indicates that iodide can directly interact with clay minerals despite the negative charge, it also remains unclear what ultimately controls the slope of iodide uptake as a function of CEC.

2.4 Conclusions

Understanding iodide interactions with clay minerals is critical to quantifying risk associated with nuclear waste disposal. Current thought assumes that iodide does not interact directly with clay minerals due to electrical repulsion between the iodide and the negatively charged clay layers. However, a growing body of work indicates a weak interaction between iodide and clays may exist under certain conditions. A reasonable explanation for such an interaction is still lacking. This section is to report a conceptual model for iodide interaction with clays by considering clay mineral structures and emergent behaviors of chemical species in confined spaces. To approach the problem, a suite of clay minerals was used with varying degrees of isomorphic substitution, chemical composition, and mineral structure. Iodide uptake experiments were completed with each of these minerals in a range of swamping electrolyte identities (NaCl, NaBr, KCl) and concentrations. Iodide uptake behaviors form distinct trends with cation exchange capacity and mineral structure. These trends change substantially with electrolyte composition and concentration, but do not appear to be affected by solution pH. The experimental results suggest that iodide may directly interact with clays by forming ion-pairs (e.g., $\text{NaI}_{(\text{aq})}$) which may concentrate within

the interlayer space as well as the thin areas surrounding the clay particle where water behavior is more structured relative to bulk water. Ion pairing and iodide concentration in these zones is probably driven by the reduced dielectric constant of water in confined space and by the relatively high polarizability of the iodide species. This new conceptual model has far-reaching implications to the capability of clay materials as a geo-membrane for anion exclusion and isolation.

2.5 References

- (1) Whitehead, D. C., The distribution and transformations of iodine in the environment. *Environment International*, 1984, 10: 321-339.
- (2) Altmann, S., 'Geo'chemical research: A key building block for nuclear waste disposal safety cases. *J. Contam. Hydrol.*, 2008, 102: 174-179.
- (3) Mallants, D.; Marivoet, J.; Sillen, X., Performance assessment of the disposal of vitrified high-level waste in a clay layer. *Journal of Nuclear Materials*, 2001, 298: 125-135.
- (4) Bazer-Bachi, A. R.; Tevissou, E.; Descostes, M.; Grenut, B.; Meier, P.; Simonnot, M.-O.; Sardin, M., Characterization of iodide retention on Callovo-Oxfordian argillites and its influence on iodide migration. *Physics and Chemistry of the Earth*, 2006, 31: 517-522.
- (5) Jansson, M.; Eriksen, T. E., In situ anion diffusion experiments using radiotracers. *J. Contam. Hydrol.*, 2004, 68: 183-192.
- (6) Van Loon, L. R.; Soler, J. M.; Bradbury, M. H., Diffusion of HTO, $^{36}\text{Cl}^-$, and $^{125}\text{I}^-$ in Oplains clay samples from Mont Terri effect of confining pressure. *J. Contam. Hydrol.*, 2003, 61: 73-83.
- (7) Descostes, M.; Blin, V.; Bazer-Bachi, F.; Meier, P.; Grenut, B.; Radwan, J.; Schlegel, M. L.; Buschaert, S.; Coelho, D.; Tevissen, E., Diffusion of anionic species in Callovo-Oxfordian argillites and Oxfordian limestones (Meuse/Haute-Marne, France). *Appl Geochem*, 2008, 23: 655-677.
- (8) Wittebroodt, C.; Savoye, S.; Gouze, P., Influence of initial iodide concentration on the iodide uptake by the argillite of Tournemire. *Physics and Chemistry of the Earth, Parts A/B/C*, 2008, 33: 943-948.
- (9) Tournassat, C.; Gaucher, E. C.; Fattahi, M.; Grambow, B., On the mobility and potential retention of iodine in the Callovian-Oxfordian formation. *Physics and Chemistry of the Earth*, 2007, 32: 539-551.
- (10) Gaucher, E.; Robelin, C.; Matray, J. M.; Négrel, G.; Gros, Y.; Heitz, J. F.; Vinsot, A.; Rebours, H.; Cassagnabère, A.; Bouchet, A., ANDRA underground research laboratory: Interpretation of the mineralogical and geochemical data acquired in the Callovian-Oxfordian formation by investigative drilling. *Physics and Chemistry of the Earth, Parts A/B/C*, 2004, 29: 55-77.
- (11) Claret, F.; Lerouge, C.; Laurieux, T.; Bizi, M.; Conte, T.; Ghestem, J. P.; Wille, G.; Sato, T.; Gaucher, E. C.; Giffaut, E.; Tournassat, C., Natural iodine in a clay formation: Implications for iodine fate in geological disposals. *Geochim. Cosmochim. Acta*, 2010, 74: 16-29.
- (12) Fuge, R.; Johnson, C. C., The geochemistry of iodine - a review. *Environ. Geochem. Health*, 1986, 8: 31-54.
- (13) Hu, Q.; Moran, J. E., Simultaneous analyses and applications of multiple fluorobenzoate and halide tracers in hydrologic studies. *Hydrological Processes*, 2005, 19: 2671-2687.
- (14) Kaplan, D. I., Influence of surface charge of an Fe-oxide and an organic matter dominated soil on iodide and pertechnetate sorption. *Radiochim. Acta*, 2003, 91: 173-178.
- (15) Couture, R. A.; Seitz, M. G., Sorption of anions of iodine by iron oxides and kaolinite. *Nuclear and Chemical Waste Management*, 1983, 4: 301-306.
- (16) Fuhrmann, M.; Bajt, S.; Schoonen, M. A. A., Sorption of iodine on minerals investigated by X-ray absorption near edge structure (XANES) and I-125 tracer sorption experiments. *Appl Geochem*, 1998, 13: 127-141.

- (17) Glaus, M. A.; Muller, W.; Van Loon, L. R., Diffusion of iodide and iodate through Opalinus clay: Monitoring of the redox state using an anion chromatographic technique. *Appl Geochem*, 2008, 23: 3612-3619.
- (18) Hu, Q.; Zhao, P.; Moran, J. E.; Seaman, J. C., Sorption and transport of iodine species in sediments from the Savannah River and Hanford sites. *J. Contam. Hydrol.*, 2005, 78: 185-205.
- (19) Kaplan, D. I.; Serne, R. J.; Parker, K. E.; Kutnyakov, I. V., Iodide sorption to subsurface sediments and illitic materials. *Environ Sci Technol*, 2000, 34: 399-405.
- (20) Gaucher, E. C.; Blanc, P.; Bardot, F.; Braibant, G.; Buschaert, S.; Crouzet, C.; Gautier, A.; Girard, J. P.; Jacquot, E.; Lassin, A.; Negrel, G.; Tournassat, C.; Vinsot, A.; Altmann, S., Modelling the porewater chemistry of the Callovian-Oxfordian formation at a regional scale. *C. R. Geosci.*, 2006, 338: 917-930.
- (21) Bradbury, M. H.; Baeyens, B., A mechanistic description of Ni and Zn sorption on Namontmorillonite Part II: Modeling. *J. Contam. Hydrol.*, 1997, 27: 223-248.
- (22) Baeyens, B.; Bradbury, M., A mechanistic description of Ni and Zn sorption on Namontmorillonite Part I: Titration and sorption measurements. *J. Contam. Hydrol.*, 1997, 27: 199-222.
- (23) Miller, A. W.; Wang, Y., Radionuclide interaction with clays in dilute and heavily compacted systems: A critical review. *Environ Sci Technol*, 2012, 46: 1981-1994.
- (24) Kahr, G.; Madsen, F. T., Determination of the cation exchange capacity and the surface area of bentonite, illite and kaolinite by methylene blue adsorption. *Applied Clay Science*, 1995, 9: 327-336.
- (25) Bergaya, F.; Theng, B. K. G.; Lagaly, G., *Handbook of clay science*. 2006, Amsterdam: Elsevier. 1248.
- (26) Gillman, G., A proposed method for the measurement of exchange properties of highly weathered soils. *Soil Research*, 1979, 17: 129-139.
- (27) Borden, D.; Giese, R. F., Baseline studies of the clay minerals society source clays: Cation exchange capacity measurements by the ammonia-electrode method. *Clays and Clay Minerals*, 2001, 49: 444-445.
- (28) Cases, J. M.; Grillet, Y.; Francois, M.; Michot, L.; Villieras, F.; Yvon, J., Evolution of the porous structure and surface area of palygorskite under vacuum thermal treatment. *Clays and Clay Minerals*, 1991, 39: 191-201.
- (29) Kosmulski, M.; Dahlsten, P., High ionic strength electrokinetics of clay minerals. *Colloid Surface A*, 2006, 291: 212-218.
- (30) Appelo, C. A. J.; Van Loon, L. R.; Wersin, P., Multicomponent diffusion of a suite of tracers (HTO, Cl, Br, I, Na, Sr, Cs) in a single sample of Opalinus clay. *Geochim. Cosmochim. Acta*, 2010, 74: 1201-1219.
- (31) Kozaki, T.; Inada, K.; Sato, S.; Ohashi, H., Diffusion mechanism of chloride ions in sodium montmorillonite. *J. Contam. Hydrol.*, 2001, 47: 159-170.
- (32) Sposito, G., Effect of chloride ions on sodium-calcium and sodium-magnesium exchange on montmorillonite. *Soil Sci. Soc. Am. J.*, 1991, 55: 965-967.
- (33) Mattigod, S. V.; Frampton, J. A.; Lim, C. H., Effect of ion-pair formation on boron adsorption by kaolinite. *Clays and Clay Minerals*, 1985, 33: 433-437.
- (34) Sposito, G.; Holtzclaw, K. M.; Charlet, L.; Jouany, C.; Page, A. L., Sodium-calcium and sodium-magnesium exchange on Wyoming bentonite in perchlorate and chloride background ionic media. *Soil Sci. Soc. Am. J.*, 1983, 47: 51-56.
- (35) Charlet, L.; Tournassat, C., Fe(II)-Na(I)-Ca(II) cation exchange on montmorillonite in chloride medium: Evidence for preferential clay adsorption of chloride – metal ion pairs in seawater. *Aquat Geochem*, 2005, 11: 115-137.
- (36) Hiemstra, T.; Van Riemsdijk, W. H., Physical chemical interpretation of primary charging behaviour of metal (hydr) oxides. *Colloids and Surfaces*, 1991, 59: 7-25.

- (37) Senapati, S.; Chandra, A., Dielectric constant of water confined in a nanocavity. *The Journal of Physical Chemistry B*, 2001, 105: 5106-5109.
- (38) Yeh, I. C.; Berkowitz, M. L., Dielectric constant of water at high electric fields: Molecular dynamics study. *J Chem Phys*, 1999, 110: 7935-7942.
- (39) Fuoss, R. M., Conductimetric determination of thermodynamic pairing constants for symmetrical electrolytes. *Proceedings of the National Academy of Sciences*, 1980, 77: 34-38.
- (40) Shock, E. L.; Helgeson, H. C., Calculation of the thermodynamic and transport properties of aqueous species at high pressures and temperatures: Correlation algorithms for ionic species and equation of state predictions to 5 kb and 1000°C. *Geochim. Cosmochim. Acta*, 1988, 52: 2009-2036.
- (41) Jungwirth, P.; Tobias, D. J., Molecular structure of salt solutions: A new view of the interface with implications for heterogeneous atmospheric chemistry. *The Journal of Physical Chemistry B*, 2001, 105: 10468-10472.
- (42) Lima, E. R. A.; Bostrom, M.; Horinek, D.; Biscaia, E. C.; Kunz, W.; Tavares, F. W., Co-ion and ion competition effects: Ion distributions close to a hydrophobic solid surface in mixed electrolyte solutions. *Langmuir*, 2008, 24: 3944-3948.
- (43) Manciu, M.; Ruckenstein, E., On the interactions of ions with the air/water interface. *Langmuir*, 2005, 21: 11312-11319.
- (44) Ockwig, N. W.; Greathouse, J. A.; Durkin, J. S.; Cygan, R. T.; Daemen, L. L.; Nenoff, T. M., Nanoconfined water in magnesium-rich 2:1 phyllosilicates. *Journal of the American Chemical Society*, 2009, 131: 8155-8162.
- (45) Galan, E., Properties and applications of palygorskite-sepiolite clays. *Clay Minerals*, 1996, 31: 443-453.
- (46) Laird, D. A., Influence of layer charge on swelling of smectites. *Applied Clay Science*, 2006, 34: 74-87.
- (47) Teppen, B. J.; Miller, D. M., Hydration energy determines isoivalent cation exchange selectivity by clay minerals. *Soil Science Society of America Journal*, 2006, 70: 31-40.
- (48) Van Loon, L. R.; Glaus, M. A., Mechanical compaction of smectite clays increases ion exchange selectivity for cesium. *Environ Sci Technol*, 2008, 42: 1600-1604.
- (49) Tournassat, C.; Appelo, C. A. J., Modelling approaches for anion-exclusion in compacted Na-bentonite. *Geochim. Cosmochim. Acta*, 2011, 75: 3698-3710.

3.0 Iodide Interaction with Clays: Constant Confining Pressure Diffusion Experiments

3.1 Introduction

As discussed in Section 2.0, pore confinement may play an important role in radionuclide interaction with clay materials. Following the same thought line, in this section, we present our preliminary study of radionuclide interaction with compacted clay materials under a confining pressure. Such a study is also important for the development of constitutive relationships for modeling coupled thermal-hydrologic-mechanical-chemical (THMC) processes in clay buffers or clay host rocks in a deep geologic repository. In order to link chemical reactions with mechanical stress states, chemical behaviors need to be measured as a function of stress state. All of the diffusion experiments carried out so far use a similar experimental apparatus (see [1] for a schematic), characterized by a sample chamber of fixed volume. While different confining pressures are possible with such a system, the pore pressure remains uncharacterized. For non-swelling clays (e.g., illite), the change in pore pressure upon hydration with different salt solutions may be negligible, but for swelling clays (e.g., montmorillonite) the pore pressure may increase considerably upon hydration and will vary with the identity of the salts present. In the constant volume system, the expanding clay and larger pore pressure may lead to a different nanopore distribution than if the clay were housed under conditions of constant confining pressure. The changing nanopore distribution may affect how chemical reactions proceed as discussed in the previous section. Diffusion experiments of reactive components with a constant confining pressure boundary are exceedingly rare.

The goal of this section is to describe the design and operation of a constant confining pressure diffusion system. Initial experiments have been completed for iodide diffusion through a montmorillonite pellet at 1MPa in a swamping electrolyte of 0.1M NaCl. The system will be used to complete experiments with different clays, increasing confining pressures and variable ionic compositions.

3.2 Methods

Figure 3-1 shows a schematic of the ideal diffusion apparatus we have developed. As shown in the figure, the system would allow for independent control of pore pressure and confining pressure in any given diffusion experiment. The sample is jacketed in Viton rubber within a pressure containment vessel. The containment vessel is connected to a Teledyne ISCO pump capable of maintaining high pressures (2000psi maximum) for extended periods of time. Two independent loops circulate the solutions of interest to the jacketed sample, through a polyethylene frit used as an endfilter, and out to either be re-circulated or to waste. Pore pressure is controlled through the pressure generated by the HPLC pumps, and through a separate ISCO pump. The Rheodyne sample valve allows for sample withdrawal at high pressure.

In the experiments described below pore pressure is not controlled, so the system is not as complex as shown in Figure 3-1. The sample is jacketed and subjected to a confining pressure, but the HPLC pumps are not used to re-circulate fluids. The closed loops are controlled with a piston pump and a peristaltic pump at atmospheric pressure.

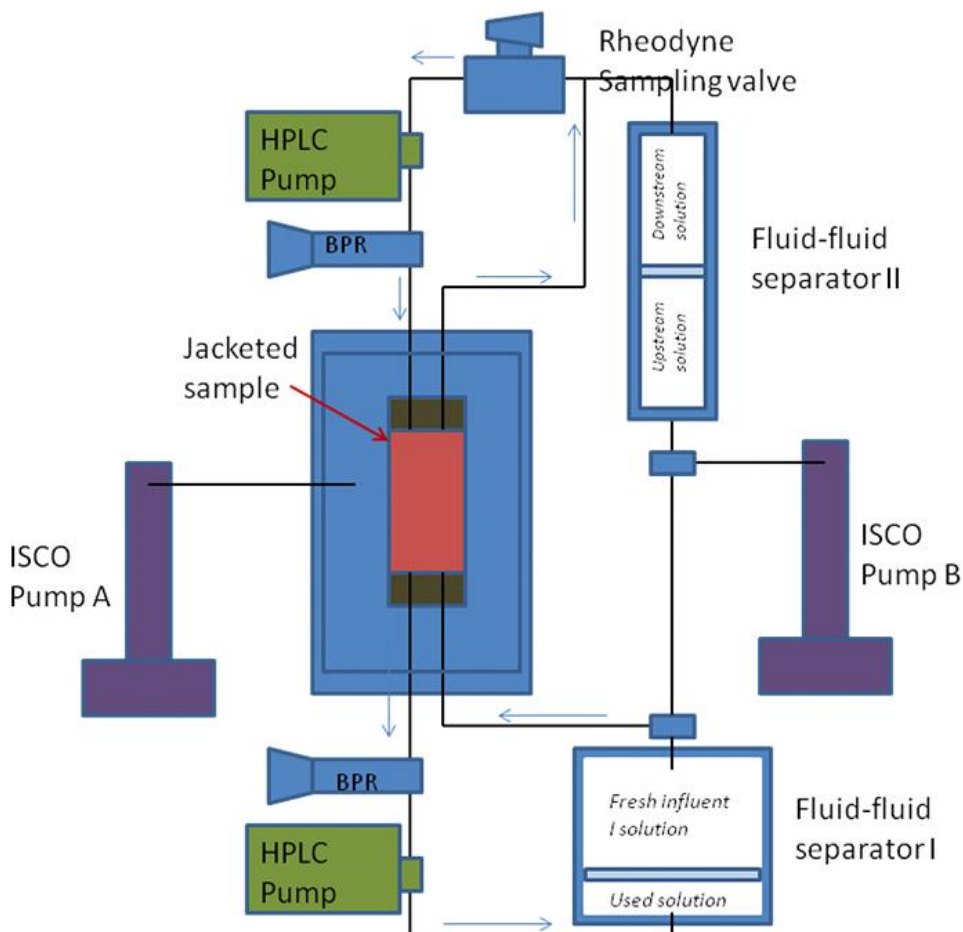


Figure 3-1. Diffusional system schematic. ISCO pump A controls the confining pressure, ISCO pump B controls the pore pressure. The HPLC pumps control the recirculation rate of diffusion solutions. Back pressure reducing regulators (BPR) are necessary to control the pressure gradient across the piston pump head in the HPLC pumps. The Rheodyne sampling valve allows for sample withdrawal at high pressures. Figure originally designed by Tom Dewers.

3.2.1 Clay pellet formation

The montmorillonite used were originated from the Clay Bank Repository. It was dry-sieved at 75 microns, and the <75 micron fraction was used in the diffusion system. No other purification was completed. The target pellet size was 2.54 cm in diameter and 1.27 cm in height. To pack the pellet a metal plug was placed inside the Viton tubing. A known clay mass was poured directly into the Viton tubing. The Viton tubing was surrounded by a hose clamp to minimize horizontal deformation during the compaction process. A second metal plug was placed on top of the clay, and the clay was compacted to an initial dry density of 1.6 g/cm^3 using a bench scale lab press. The pellet remained under pressure for approximately 10 minutes, after which the pressure was released, and the metal plugs were removed. Endfilters were cut to fit the inner diameter of the Viton (50-90 micron pore size, 0.157cm thick,

polyethylene), and two filters were placed in either end of the pellet. The endfilters were held in place by metal plugs; these metal plugs had been welded to the fluid recirculation lines. The hose clamp that had been controlling lateral deformation was removed, and the metal plugs were held in place with hose clamps.

3.2.2 Diffusion experiment

Once packed, the pellet and associated equipment was loaded into the pressure chamber which was filled with water. The chamber was sealed and connected to the ISCO pump which applied 145 psi (1MPa) of pressure. A second ISCO pump was filled with DI water, and connected to the lower recirculation lines while the upper lines were left open. The pump pressure was increased to 100psi, and the pellet was allowed to fully hydrate. It was assumed that the pellet was fully hydrated when water started eluting from the upper recirculation lines. This process took approximately two weeks. When water was seen eluting, the ISCO pump was disconnected and two large reservoirs of 0.1M NaCl were connected to the recirculation lines. Flow was controlled in the upper recirculation loop with a peristaltic pump. The lower recirculation loop required a small amount of pressure (~5 psi) to maintain flow; a piston pump was used as the peristaltic pump could not supply that much pressure. The NaCl solution was recirculated on both ends of the clay pellet for 6 weeks to allow for clay equilibration with the NaCl solution. The NaCl solutions were replaced several times during that period.

After the equilibration period the solution reservoirs were changed to initiate the diffusion experiment. The up-gradient solution was replaced with a 0.1M NaCl solution spiked with I at 50mg/L (3.93×10^{-4} M), and fresh 0.1M NaCl solution was placed in the down-gradient reservoir. The up-gradient reservoir was 500 mL while the down gradient reservoir was 7.5 mL. The down gradient side was sampled on a regular basis by replacing the 7.5 mL with fresh NaCl solution. Iodide was quantified with ion chromatography. This ‘through diffusion’ experiment was allowed to run until the diffusive flux appeared to be at steady state. At that point, the up and down gradient solutions were replaced with 7.5 mL of clean NaCl solution. Both sides were sampled at regular intervals to examine ‘out diffusion.’

3.3 Results and discussion

3.3.1 Through diffusion

Figure 3-2 shows the iodide flux through the pellet normalized to the total cross sectional area. Figure 3-3 shows the total moles of eluted iodide as a function of elapsed time. The iodide flux appears to peak quite early, and consistently drop off with experimental time. The expectation was for the iodide flux to increase to a value and remain constant over the experimental timeframe (i.e., reach steady state). It is currently unclear as to why the flux is declining. The amount of iodide eluted is an insignificant amount of that present in the up-gradient reservoir. Further, samples of the influent reservoir had constant iodide concentrations. When at steady state, the total eluted moles of iodide as a function of time should be linear, and again this is not the case. While generally linear for a certain timeframe, the slope of the line changes with time. The change in slope corresponds to changes made in sampling frequency. Days 4-7 were sampled twice daily, while days 8-12 were sampled only once daily. Beyond day 12, one, two or three days elapsed between samples. It is clear that the sampling rate affects the iodide concentration, which also affects the flux values in Figure 3-2. The estimated analytical error for the iodide analysis is quite high (~15%) as the concentrations are quite low. While this may explain some of the data, it does not explain the clear connection to sampling time intervals.

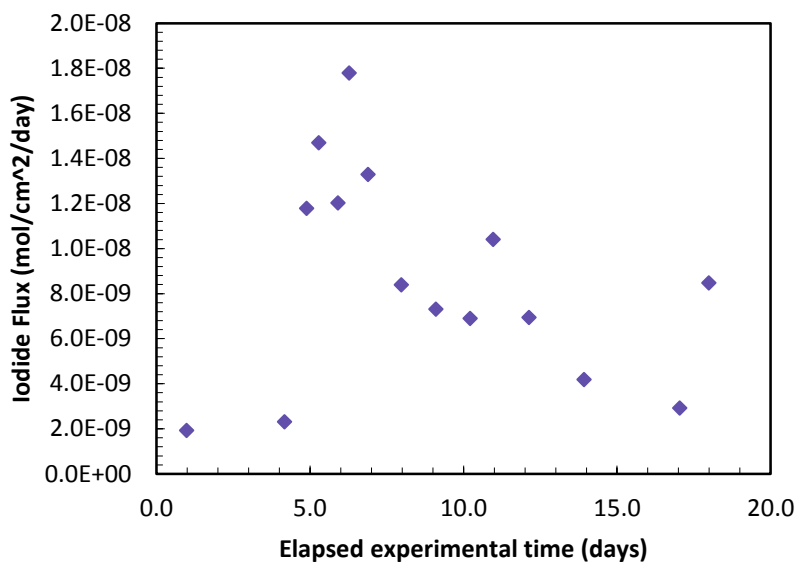


Figure 3-2. Iodide flux as a function of elapsed experimental time

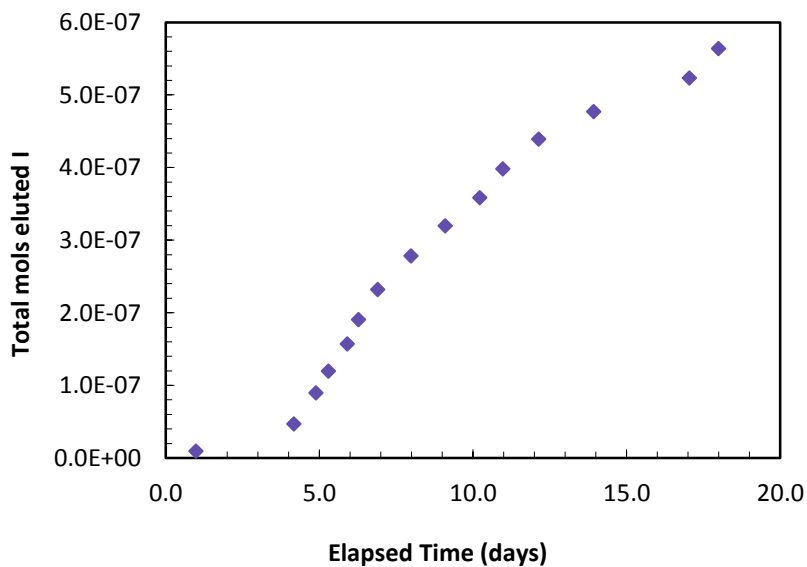


Figure 3-3. Total eluted iodide as a function of experimental time.

3.3.2 Out diffusion

The out diffusion experiments include sampling on both the up-gradient (high concentration side during through diffusion) and the down-gradient (clean electrolyte side during the through diffusion experiments) sides of the pellet. Figures 3-4 and 3-5 respectively show the iodide flux and the total moles eluted iodide on the up-gradient side of the pellet. Figures 3-6 and 3-7 show the same measurements for the down-gradient side of the pellet. On both sides of the clay pellet there is an initial period of higher flux followed by a longer period of lower fluxes. Within the experimental timeframe, iodide was still diffusing out of the clay pellet.

The early period of high flux and extended period with lower flux values corresponds to a large initial increase in the number of total moles eluted iodide and a longer period with smaller increases. When the initial time period of large increase is excluded, the eluted iodide on the effluent side of the pellet appears linear with time ($r^2 = 0.996$) and it becomes less linear when plotted as a function of the square root of time ($r^2 = 0.970$). On the influent side however, the total eluted moles as a function of time is less linear ($r^2 = 0.975$) and it becomes more linear when plotted as a function of the square root of time ($r^2 = 0.999$). These changes in correlation coefficient are slight and may not be significant, but they imply the up-gradient side is more diffusion dominated than the down-gradient side.

Further testing using this system will include experiments to solve the problem of unexpected iodide flux values. This will include changing the concentration gradient across the clay pellet, as well as taking more samples earlier in the experimental timeframe to better characterize breakthrough. The overarching goal is to complete an experimental matrix of diffusion experiments where clay mineralogy, swamping electrolyte, and confining pressure are all varied. Clay minerals will include illite, montmorillonite, and palygorskite. The swamping electrolytes may include NaCl, NaBr, or KCl to compare results to those in Section 2.0. And the confining pressure will vary between 1MPa and the upper limit of the confining pressure system.

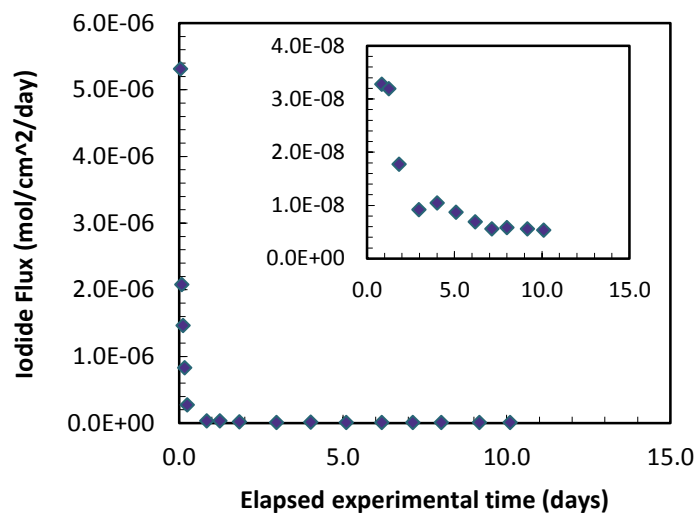


Figure 3-4. Iodide flux as a function of time for the out diffusion experiment on the up-gradient side of the pellet. The inset is the same data plotted on an exaggerated y-axis.

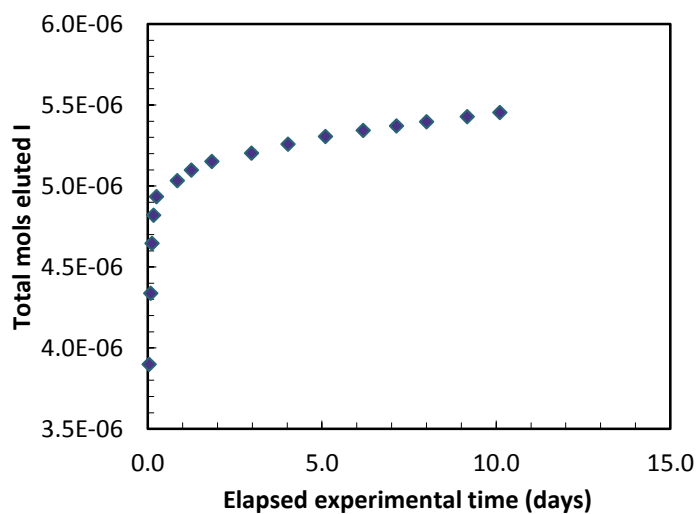


Figure 3-5. Cumulative moles of eluted iodide as a function of experimental time for the out diffusion experiment on the up-gradient side of the pellet.

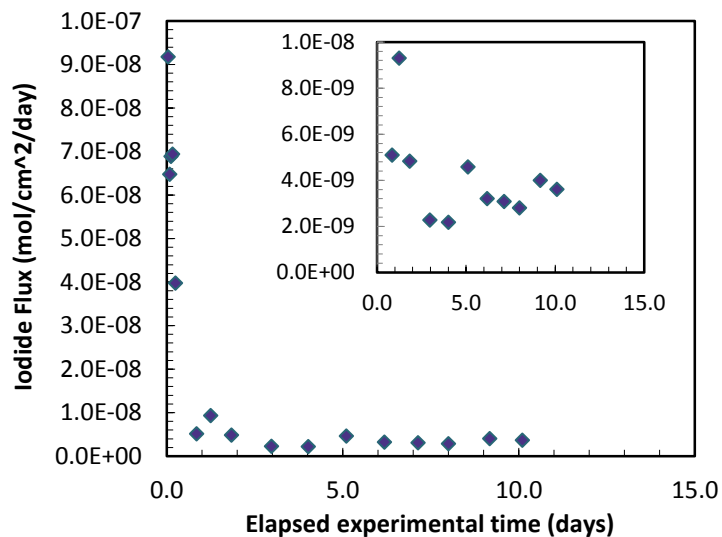


Figure 3-6. Iodide flux as a function of time for the out diffusion experiment on the down-gradient side of the pellet. The inset is the same data plotted on an exaggerated y-axis.

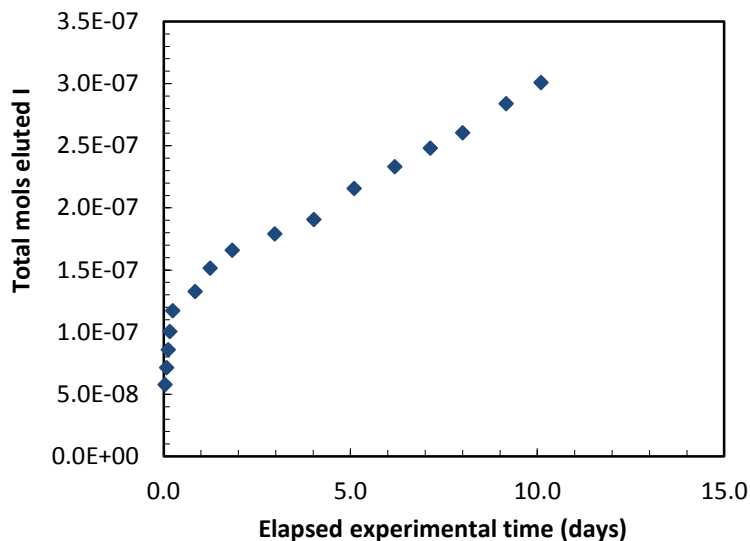


Figure 3-7. Cumulative moles of eluted iodide as a function of experimental time for the out diffusion experiment on the up-gradient side of the pellet

3.4 Conclusions and discussion

Setting up the described system was more challenging than anticipated. The diffusion results shown are from the third pellet. In the initial two pellets, tubing within the confining pressure vessel clogged due to either clay delamination or rusting of the initial endfilter materials. Furthermore, the method for clay hydration and equilibration was developed through trial and error. These problems were eventually overcome but the nature of the experiment is one of long set up and equilibration time. Each time the system clogged, work had to be restarted at the expense of months. While the initially planned experiments could not be completed, the system is currently operational and represents a hard won, unique experimental apparatus which can be used in future experiments and proposals. In combining THMC models, connections between the sub-models may require experiments with different boundary conditions. Connecting the hydrological to the chemical may be best suited by the constant volume experiments described above. Connecting the mechanical to the chemical may be best suited by constant confining pressure experiments. Integrating the different frames of reference within the different disciplines represented by the THMC framework requires a critical examination of both the discipline specific defining equations as well as the methods for solving such equations to decide which experiments are most useful to forge model connections.

A new set of iodide diffusion experiments were started. More measurements will become available. The immediate steps for future research will include (1) developing a mathematical model to extract iodide diffusion coefficients and retardation factors from the experimental data and (2) then compared the constrained retardation factors with those obtained from batch experiments to further clarify the effect of pore confinement on radionuclide interaction and transport in clay materials.

3.5 References

- (1) Van Loon, L. R.; Soler, J. M.; Jakob, A.; Bradbury, M. H., Effect of confining pressure on the diffusion of HTO, $^{36}\text{Cl}^-$ and $^{125}\text{I}^-$ in a layered argillaceous rock (opalinus clay): Diffusion perpendicular to the fabric. *Appl Geochem*, **2003**, 18: 1653-1662.

4.0 Characterization of Pore Structures and their Evolution in Clays Using Small-Angle Neutron Scattering (SANS)

4.1 Introduction

Pore structures of clay materials and their evolution are important parameters for understanding radionuclide interaction and transport in those materials, as shown in the previous sections. The Small-Angle Neutron Scattering (SANS) technique is a useful tool for characterizing low-permeability clay materials. As one of the on-going R&D evaluating and tool development activities for the natural system work package [1], the SANS study presented in this section is focused on the investigation of pore characteristics and the associated fluid transport properties of clay or shale samples under relevant repository conditions.

In nuclear waste management, clays are canonical materials in the construction of engineered barriers because of their good swelling/sealing properties [2]. They are also naturally occurring reactive minerals which play an important role in radionuclide retention and colloidal facilitated transport in the far field [3]. The microstructure and evolution of pore space in clays is a crucial factor controlling fluid flow properties such as retention of water and sequestration of radionuclides. It has been known that absorption of water will impact on pore geometry in layered clays. As a consequence, it will impact the performance of clays as a barrier material and their role in regulating radionuclide transport in subsurface environments [4]. Though the importance of macro-scale porosity in fluid transport in porous media has long been recognized, the role of nanometer-scale to micro-scale porosity and pore networks has only recently started to be investigated [5]. Due to the sensitivity of the pore geometry of clay materials to moisture content, temperature, and confining pressure, the fundamental insight of water flow regimes and their transport behaviors as function of microstructure of clays, which is of particularly importance for the performance assessment of a repository system, is not yet fully established.

To remedy this knowledge gap, we have carried out neutron scattering studies and in particular Small-Angle Neutron Scattering (SANS) to assess the microstructure and evolution of various clay samples. Recent developments in small-angle neutron scattering (SANS) techniques allow quantitative measurement of pore morphology and size distribution of various materials in their pristine state under various sample environments (exposure to solution, high temperature, etc.) [6,7]. Furthermore, due to the dramatic different neutron scattering properties of hydrogen and deuterium, one can readily use contrast variation, which consists of isotopic labeling with various ratios of H and D (e.g. mixture of H₂O/D₂O) to highlight or suppress features in the sample. This is particularly useful in the study of complex pore system such as clays. It has been used successfully to characterize pore morphology in explosives [7].

In this study, we have characterized the pore features of clay minerals including illite, palygorskite, smectite, and montmorillonite, as well as field clay samples including WY bentonite and two shale clays from South Dakota Belle Fourche (designated S.D. Clay #1) and Skull Creek (designated S.D. Clay #2), and Callovo-Oxfordian mud stone from the French underground testing laboratory using small-angle neutron scattering (SANS). We have measured their evolution over the relevant ranges of humidity, temperature, pressure, composition, and length scale. Our results demonstrate that each clay sample shows unique pore features. The effects that impact on pore features include sample form and sample environment (the ambient humidity, temperature, and pressure). Our results also indicate that each clay sample shows a significant difference in water retention. The results of our study provide new experimental capabilities and a fundamental insight into microstructure and evolution of pore features of clays at repository field conditions.

The purpose of this work is to investigate the utility of small-angle neutron scattering as a viable technique for probing and quantifying information on size and shape of pores and their evolutions in the field conditions for clay samples. These characteristics are the pertinent variables required for modeling efforts in performance assessment of clays as engineered barrier materials and as essential natural system media for nuclear waste repository systems. It will be exploited here for the first time to investigate pore features and their evolution at the atomic to micrometer scale, providing a novel experimental approach in exploring the parameters prerequisite for field transport model development and in uncovering the nature of factors and their evolution crucial in determining transport in low permeable media at conditions relevant to the field. These results hold the promise of achieving new fundamental breakthroughs significantly improving applications in field prediction models.

4.2 Pore structures and advantages of neutron scattering

Behavior of multiphase fluid-solid systems on a variety of scales has been perceived as a critical basic research need for energy-related geosciences in several DOE missions (e.g., CO₂ sequestration, hydrocarbon recovery, enhanced geothermal systems, legacy waste stewardship, high-level radioactive waste disposal) [8]. The common characteristic of these systems is their complexity and heterogeneity at multiple scales. Over the past two decades, researches have primarily pursued reactive transport problems in complex systems from two distinct processes and scales. One is from the atomic scale (Fig. 4-1a.) to obtain details on structure and reactivity of idealized mineral-water interfaces and suspended phases of particles [9-11]. Another is from the macro-scale (Fig.4-1c.) to develop quantitative transport models for field prediction [12-14]. Phenomena at the pore-scale (Fig.4-1b.), an enigmatic realm that bridges cooperative molecular processes with field application models, have not been considered either experimentally or theoretically until recently [15-17]. These results and our preliminary studies have suggested that pore processes and characterization from *nanometer-to micrometers* have a significant effect on fluid flow and reactive transport in porous media, particularly for transport processes in low permeable media such as clays [18].

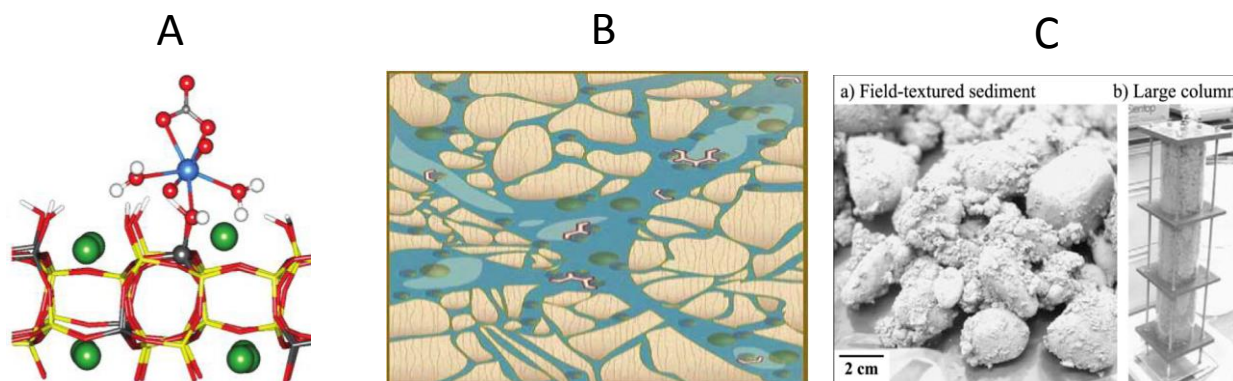


Figure 4-1. Schematic view of scales in subsurface studies. A) Atomic scale (0.1-10 Å), B) Pore scale (1 nm -100 μm) [16], C) Macroscale (> 100 μm) [12].

Following are three distinct advantages in using neutron spectroscopy techniques and tomography for the investigation of water movement and transport in nuclear waste disposal systems:

- *Neutrons can penetrate deep within a sample.* Neutrons have no charge, thus penetrating matter far better than charged particles. Furthermore, neutrons interact with atoms via nuclear rather than electrical forces. Nuclear interactions are very short range. As a consequence, neutrons can travel large distances through most solid materials without being scattered or captured. Thus, samples can be examined in their pristine state, kept in solution or a container under external constraints such as high T and P. It is well suited for *in situ* and non-destructive testing.
- *Neutrons can be used to probe microstructures.* Neutron scattering techniques can be used to probe the structures of materials from nanometer to (sub)micrometer (porous media) scale. One of its unique advantages is that neutrons can be used to probe the structure of molecules containing light atoms (e.g., H in H₂O). This distinct advantage makes it the technique of choice for the investigation of water movement and transport in porous media. Recent developments in small-angle neutron scattering (SANS) techniques allow quantitative measurement of pore morphology and size distribution of various materials in their pristine state under external conditions (exposure to solution, high temperature, and so on).
- *Neutron scattering is sensitive to light elements (e.g., H in H₂O).* X-ray scattering is proportional to the square of the total number of electrons in an atom. It therefore obscures scattering contributions from light elements in the presence of heavier ones. Neutron scattering has not such a systematic proportionality. Figure 4-2 shows the total neutron scattering cross section for hydrogen is negative and the one for deuterium larger than that for silicon. In addition, due to the dramatic different neutron scattering cross section of hydrogen and deuterium (Table 4-1), one can readily use contrast variation, i.e. isotopic labeling using various ratios of H and D (e.g. mixture of H₂O/D₂O) to highlight or suppress features in a sample. This is particularly useful in the study of complex systems to separate scattering arising from external effects from that of internal ones.

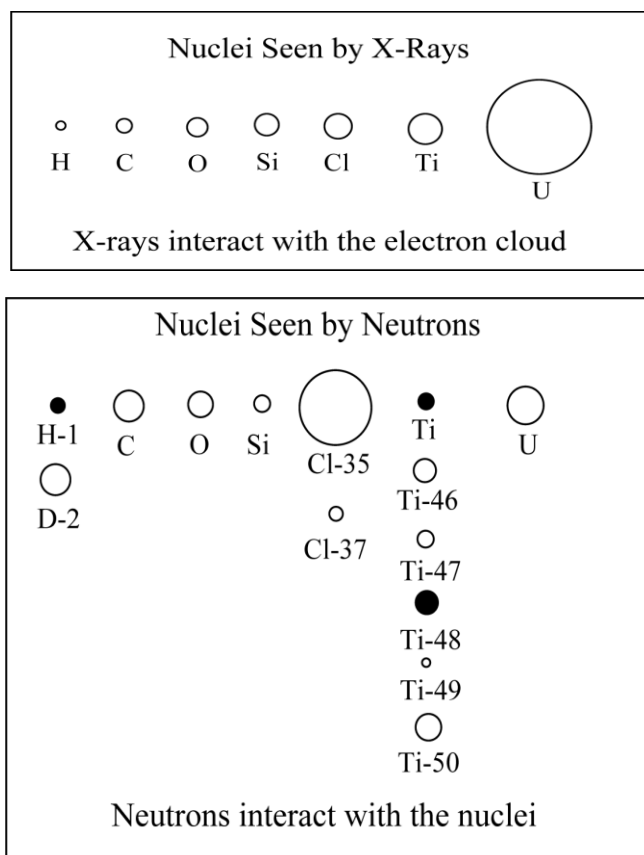


Figure 2. Comparative scattering cross-sections of X-rays and neutrons for several common elements.

Table 4-1. Neutron scattering lengths between hydrogen and deuterium

Element	Scattering Length b[fm]	
	Coherent	Incoherent
^1H	-3.742	25.274
^2H ("D")	6.674	4.04

Recent developments in small-angle neutron scattering (SANS) techniques allow quantitative measurement of pore morphology and size distribution of various materials in their pristine state under various sample environments (exposure to solution, high temperature, etc.). LANL's unique SANS capabilities at Lujan Center, LANSCE is well suited for investigation pore characteristics in 1 nm 100 nm scale. These capabilities (SANS) are well adapted for *in situ* investigation of pore features, water characterization and their evolution of clays in nuclear waste repository systems.

4.3 Small-angle neutron scattering (SANS)

4.3.1 Principle

The microstructure and evolution of pore space in the geologic subsurface is crucial in determining fluids transport behavior in many geological formations. SANS is well suited to a statistical characterization of pores from the nano- to micro-scale. Details concerning the theory and practice of small angle scattering are outside the scope of this report. However, some basic background is essential.

The scattering intensity observed in a SANS measurement is directly related to the structure of the sample, characterized by a scattering length density $\rho(r)$. At any position, r , within the sample, the scattering length density is equal to the sum of the atomic and isotopic neutron scattering amplitudes in a small volume around that position [19]:

$$\rho = \frac{\sum n_i b_i}{V_m} \quad (4.1)$$

Here, b_i is the atomic neutron scattering length, n_i the number of atomic nuclei of a given type in a molecule, and V_m the molecular volume. A fraction of the incident neutrons is scattered into a scattering vector, Q , of magnitude $Q=(4\pi/\lambda)\sin\theta$, where λ is the wavelength of the incident neutron and θ is half of the scattering angle, from fluctuations in the scattering length density. $\rho(r)$ reflects the microscale structure in the sample in density, chemical, and isotopic composition.

The scattering intensity, $I(Q)$, is measured as the absolute, differential cross section per unit scattering mass (cm^2g^{-1}) as a function of the magnitude of Q . For elastic scattering events, $I(Q)$ is proportional to the squared Fourier transform of $\rho(r)$. It can be expressed as:

$$I(Q) = K \left| \int \rho(r) \exp(-ir \cdot Q) dr \right|^2 = KP(Q)S(Q) \quad (4.2)$$

Here, $P(Q)$ is the normalized particle form factor, which contains the particle shape information. K is a constant. $S(Q)$ is the structure factor, which takes into account distance correlations between particles.

The interpretation of $I(Q)$ in terms of the sample structure, $\rho(r)$ involves careful comparison with calculations of the scattering expected from model structures. Various transformations are also commonly used to interpret the data. The first tool used to analyze SANS data consists of a set of standard transformation plots that yield direct results after data reduction.

In this report, we will present only the raw SANS scattering plots. Various transformation plots which we used to analysis the data will not be included. For example, based on the Porod-law, which is expressed as:

$$I(Q) = 2\pi S \Delta\rho^2 Q^{-4} \quad (4-3)$$

where S is the interfacial area per gram of material. We can use the Porod transform (plotting $I(Q)$ as function of Q^{-4}) to calculate the surface area of a material.

4.3.2 Analysis of SANS Data

Much information can be obtained about the pore structure of materials from SANS. Most relevant to transport modeling are;

- Surface area of pores
- Pore size distribution (from nm to 100 nm, USANS can reach to micrometer): pore fraction vs. r ,
- Pore number: pores/per volume vs. r .

Detailed data analysis is beyond the scope of this report. Some basic background on how to read the raw SANS scattering curves is warranted. Figure 4-1a shows a schematic example of a scattering curve plotting [16]. The Y-axis is the log of scattering intensity (I) in units of cm^{-1} as a function of the log of the scattering vector (Q), X-axis, in units of inverse Angstroms.

In many samples the scattering intensity is constant as a function of Q at high Q . In this range, coherent (structural) scattering is overwhelmed by the flat incoherent background, which is primarily a function of the hydrogen content of the sample.

The slopes of the remaining parts of the curve are determined by the scattering of the surface, determining surface form and shape of objects. Slopes between -2 and -3 are characteristic of mass fractal systems. A slope between -3 and -4 is surface fractal systems. A slope of -4, a characteristic for all our salt samples, indicates a smooth interface according to Porod's law behavior. We observed slopes of -2 to -3 are for all clay samples.

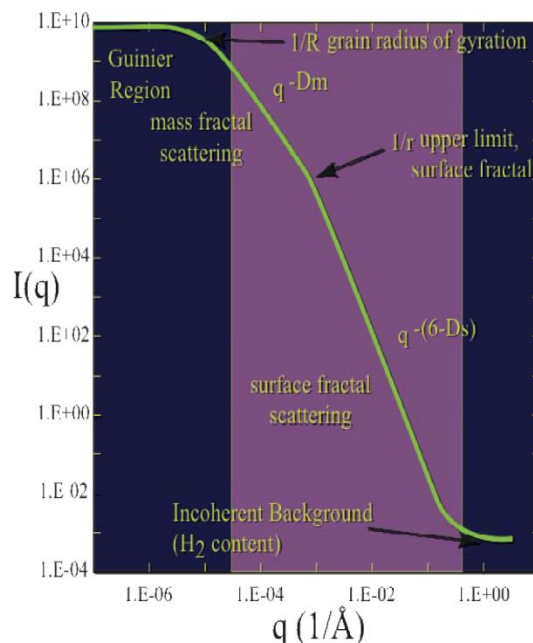


Figure 4-3. Schematic of typical scattering curve [16]

4.3.3 Instrumentation

All SANS measurements reported in this section were carried out at the low-Q Diffractometer , LQD Flightpath 10 in the Manuel Lujan, Jr. Neutron scattering center, which is designed to study structures with dimensions from 10 Å to 1000 Å (1 nm – 100 nm). Figure 4-4 is the schematic view of the Flightpath 10 (LQD).

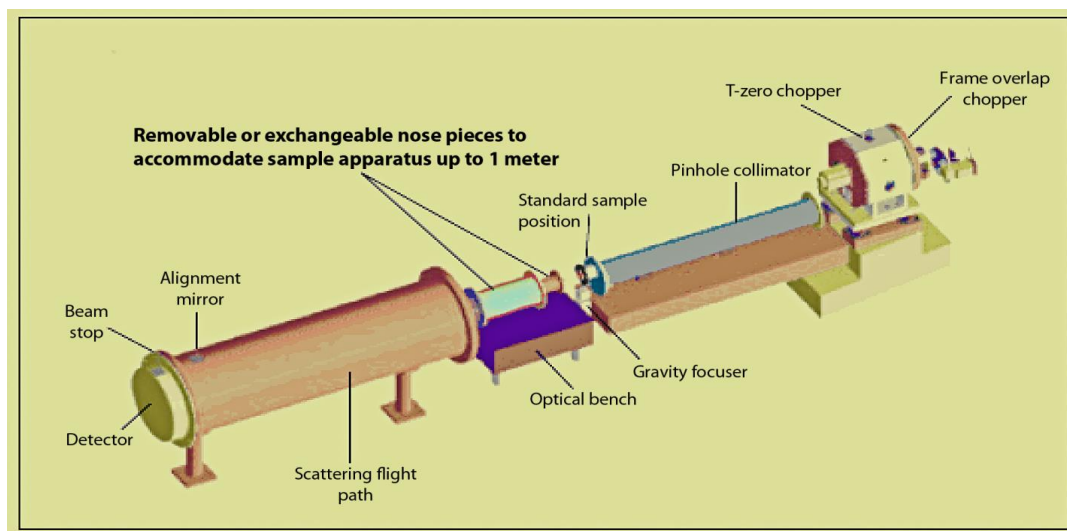


Figure 4-4. Schematic view of Flightpath 10 (LQD) at the Manuel Lujan, Jr. Neutron Scattering Center, LANSCE, LAN.

4.3.4 Sample Environment

We have used a several different sample holders for various sample forms and different sample environments. These are discussed below.



Figure 4-5. Cuvette cell sample holder

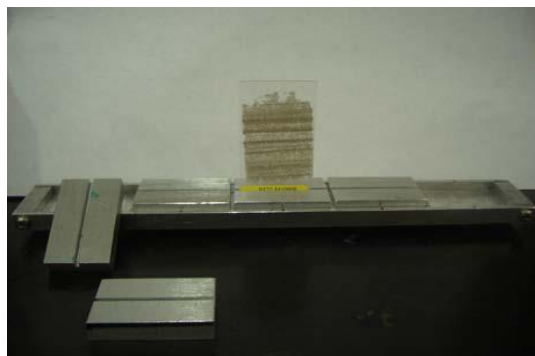


Figure 4-6. Basic sample holder

Cuvette Cell Holder: Figure 4-5 shows the sample holder for cuvettes. Cuvettes are easy to fill with solid and liquids. The thickness of the cell is 1 or 2 mm. We used this cell for all powdered samples measurements.

Basic Sample Holder: Figure 4-6 shows the basic sample holder. This sample holder offers various possibilities to mount samples. We used this holder for intact samples, thin sections as well as pelletized samples.



Figure 4-7. Humidity cell



Figure 4-8. Commercial vacuum desiccator

Humidity Cell: Figure 4-7 shows the humidity cell. This cell was used for *in situ* SANS measurements under controlled relative humidity using super saturated salt solutions at various temperatures (up to 100 °C).

Moisture Control Using Commercial Vacuum Desiccator: Figure 4-8 shows the commercial vacuum desiccator which was used for relative humidity control at room temperature using super saturated salt solutions under vacuum condition.

4.4 Materials

Four clay minerals were used in this study: illite, palygorskite, smectite, and montmorillonite, four field samples (Wyoming bentonite), and shale samples from South Dakota Belle Fourche (designated S.D. Clay #1), Skull Creek (designated S.D. Clay #2), and Callovo-Oxfordian mud stone from the French underground testing laboratory. All clay samples were powders. Three of the four field clays were chips. Smectite used in the experiments was separated from fracture fills in the tuff from Los Alamos, New Mexico.

Four sample forms were tested in this study: powdered, pelletized, intact, and thin section. All powdered sample were sieved (particulate size range < 75 μm), and vacuum dried over night at 120 °C. Pelletized sample were prepared by pressing ~ 0.2 gram powdered sample (particulate size < 75 μm) to 150 bar for ~1 minute. The pellet is about 1.2 cm diameter and ~1 mm thick. A minimally disturbed (intact) WY bentonite sample was dry-sliced from a large field sample. The thickness of the intact bentonite sample is ~ 1 mm. A 30 micron thin section was ground without using fluids. The thin section

was mounted on quartz glass to prevent high background adsorption due to boron, which is a common constituent in conventional glass. Figure 4-9 shows representative sample forms of clays.

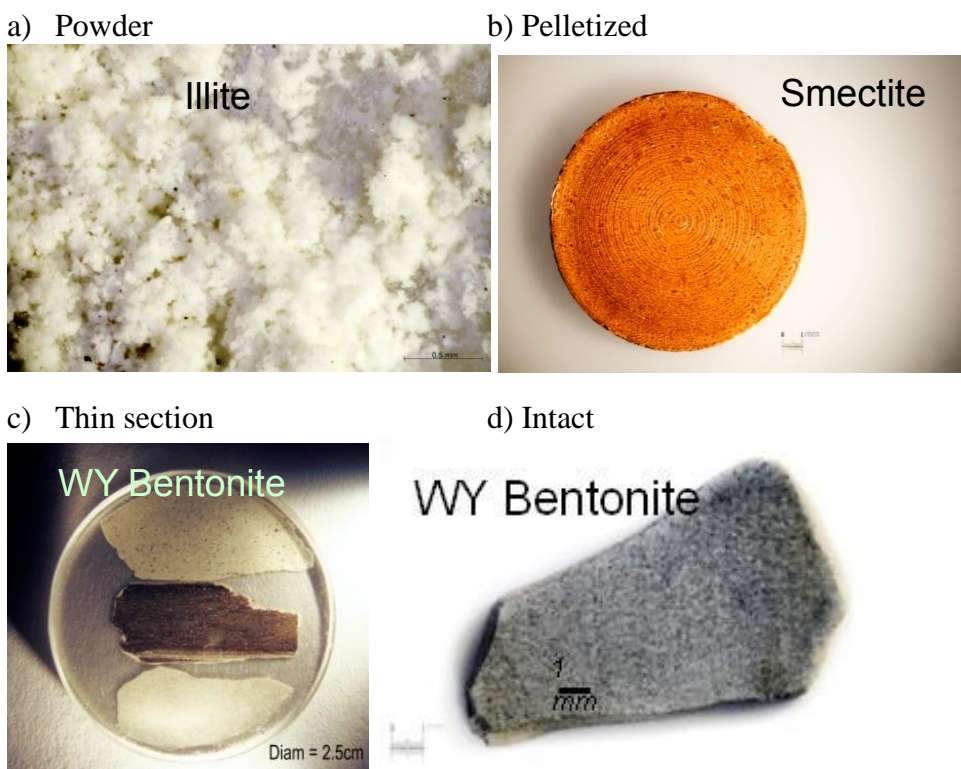


Figure 4-9. Representative sample forms used in SANS measurements.

4.5 Results

4.5.1 Characterization of Clay Minerals and Field Clay Samples

Clay Minerals: The smectite used in this experiment is a naturally occurring clay separated from fracture fills of tuffs from Los Alamos, New Mexico. Quantitative X-Ray Diffraction (QXRD) and X-Ray Fluorescence (XRF) results indicates that it is ~ 99 wt.% pure [20].

Field samples: The field bentonite used in this study is a Na-montmorillonite (~72 wt. %) with minor amounts of clinoptilolite (13%), feldspars (9%), biotite (3%), cristobalite (2%), quartz (1%), and trace amounts of opal-CT and pyrite [21]. Quantitative x-ray diffraction (QXRD) analyses was performed on two shale clays from South Dakota: Belle Fourche (S.D. #1), Skull Creek (S.D. #2), and the Callovo-Oxfordian mud stone. All samples and standards were spiked with 20% Al_2O_3 (from MDI, metallurgical-grade Al_2O_3) and ground under acetone with a Retsch mortar and pestle to a particle size $< 5 \mu\text{m}$. X-ray analyses were ran from 2.0 to $70.0^\circ 2\theta$ scan rate of 12 seconds/step and a step size of $0.02^\circ 2\theta$. Mineral identification was through Jade 7.0 and phase quantification

was determined via Fullpat. The mineralogical composition of two shale samples is listed in Table 4-2.

Table 4-2. Mineralogical composition of three field shale samples

	Callovo-Oxfordian	Skull Creek, S.D. # 2	Belle Fourche, S.D. # 1
quartz	17	36	24
illite/smectite (I/S)	66	44	
smectite			67
illite or mica	2	4	4
kaolinite	2	16	5
pyrite	1		
chlorite	1		
calcite	10		
dolomite	2		
crandallite		+	
I/S Characteristics		~R3 illite(0.9)/smectite	

“+” indicate mineral is present, but is < 0.5 wt.%.

4.5.2 Pore Characterization of Clays

Pore Feature of Powdered Clays: Figure 4-10 shows SANS scattering results of the four clay minerals. Inspection of Figure 10 suggests that each clay sample shows unique pore features over the entire scattering vector Q (0.3 nm-30 nm). Further data analysis of these scattering curves using a Porod plot (log(I) vs log (Q)) and curve fitting indicates that at high Q (\AA^{-1}) domain (Q from 0.05 to 0.1, i.e., corresponding to smaller particles), the Porod slope, n, of clay minerals varies between 2.7 and 3.4. A slope of 1 is obtained for scattering from rigid rods; n = 4 represents a smooth surface for the scattering particle; whereas an n between 3 and 4 characterizes rough interfaces of fractal dimension D with n = 6-D. At low Q (Q from 0.003 to 0.05, i.e., corresponding to structure factor of the interactions in the system), the slopes of clay minerals n vary between 2.3 to 3.2, which are indicative of “mass fractals” such as branched systems (gels) or networks, as illustrated in Figure 4-11. SWy-2 in Figure 4-10 is also montmorillonite from different sources.

Figure 4-12 shows SANS scattering results of the three field clay samples. Figure 4-12 suggests that two shale clays S.D.#1 and S.D.# 2 show similar pore features. In comparison to the clay minerals SANS curves in Figure 4-10, at high Q domain, Porod plot slopes of field samples are about the same as

clay minerals, n varying between 2.7 and 3.4. However, at low Q , the slopes of clay minerals are between 3.1 to 3.5, suggesting a much less “mass fractal” feature of the field samples. This is attributed to the fact that field samples contained phases besides clay minerals such as quartz which has a smooth surface and thus less “mass fractal” feature.

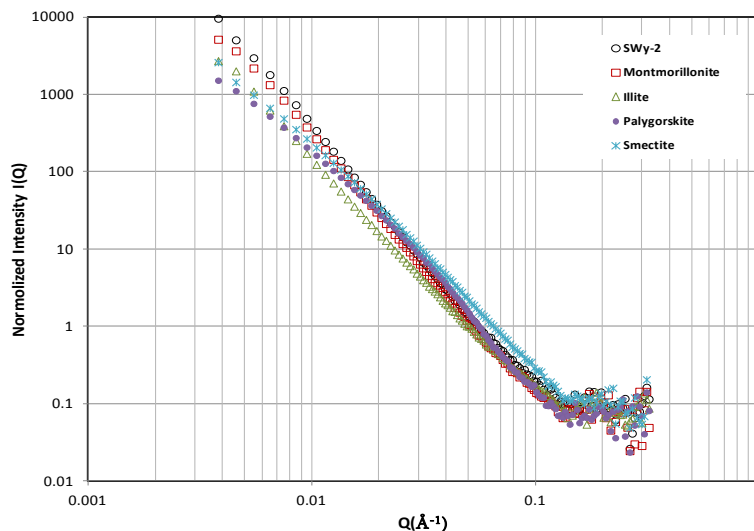


Figure 4-10. SANS scattering curves of clay minerals. Note: the length unit used here is $1/\text{Å}$. The conversion from Å to nm is $10\text{Å}=1\text{ nm}$.

The Porod Plot

The Porod region corresponds to a probed range smaller than the scattering objects so that the scattering radiation is probing the local structure

$$I(Q) = A/Q^n + B \quad \text{or} \\ \text{Log}[I(Q) - B] = \text{Log}(A) - n\text{Log}(Q)$$

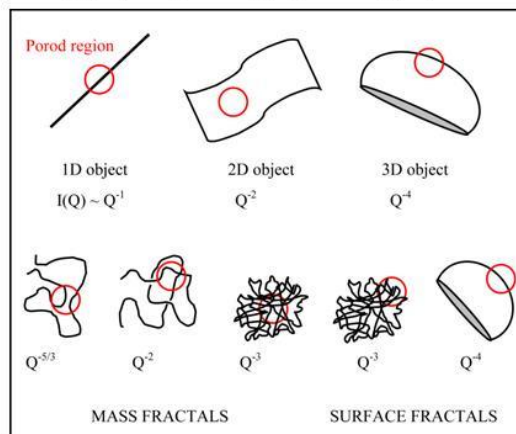


Figure 4-11. Assortment of Porod law behavior for different shape objects

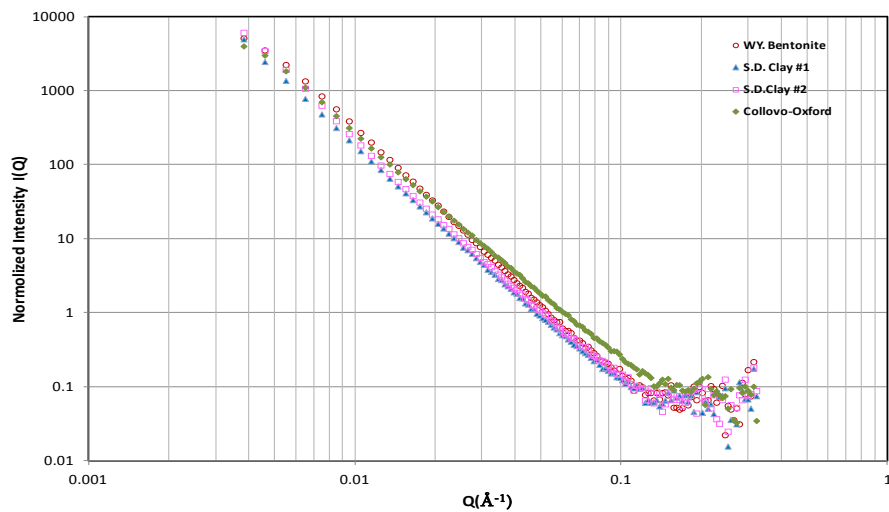


Figure 4-12. SANS scattering curves of field samples.

As an example, Figure 4-13 represents detailed data fitting and analysis for the illite pore structure obtained from its SANS scattering curve. Data fitting was performed on all contrast matching samples using a bimodal Guinier-Porod law (Figure 4-14). The results show the presence of two pore sizes in illite: the intracrystalline small one and a large one due to stacked bricks of illite sheets, as shown in Figure 4-15.

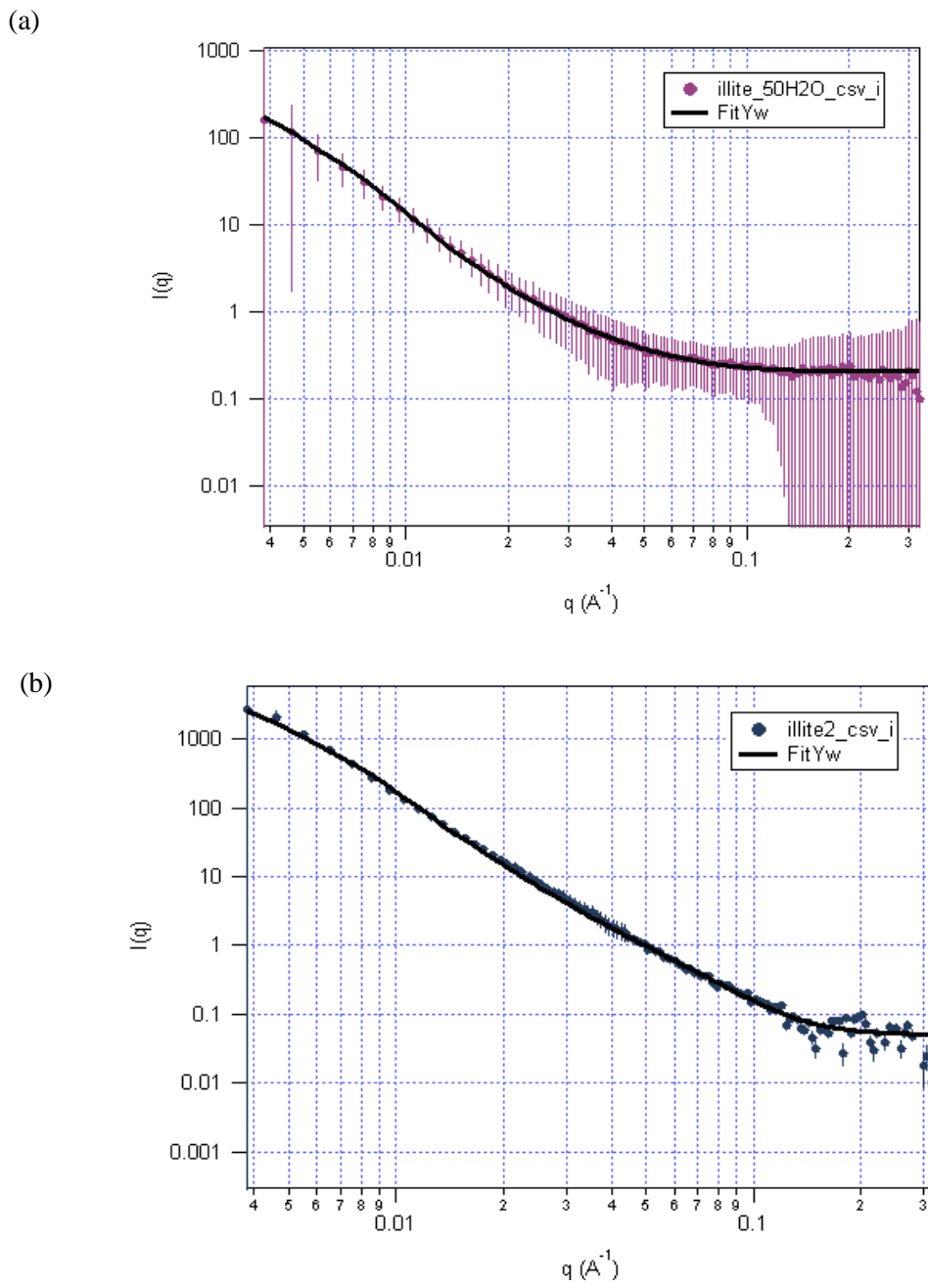


Figure 4-13. SANS scattering curves and data fitting results for dry illite dry (a) and with 50% H₂O (b)

Guinier –Porod Model

The low-Q Guinier

$$I(Q) = I(0) \exp\left(-\frac{Q^2 R_g^2}{3}\right) \text{ where } R_g^2 = \frac{L^2}{12} + \frac{R^2}{2}$$

The intermediate-Q Guinier Model

$$I(Q) = \frac{I(0)}{Q} \exp\left(-\frac{Q^2 R_g^2}{2}\right) \text{ where } R_g^2 = \frac{R^2}{2}$$

Figure 4-14. Form factor showing the low-Q Guinier region, the intermediate-Q Guinier region and the high-Q Porod region.

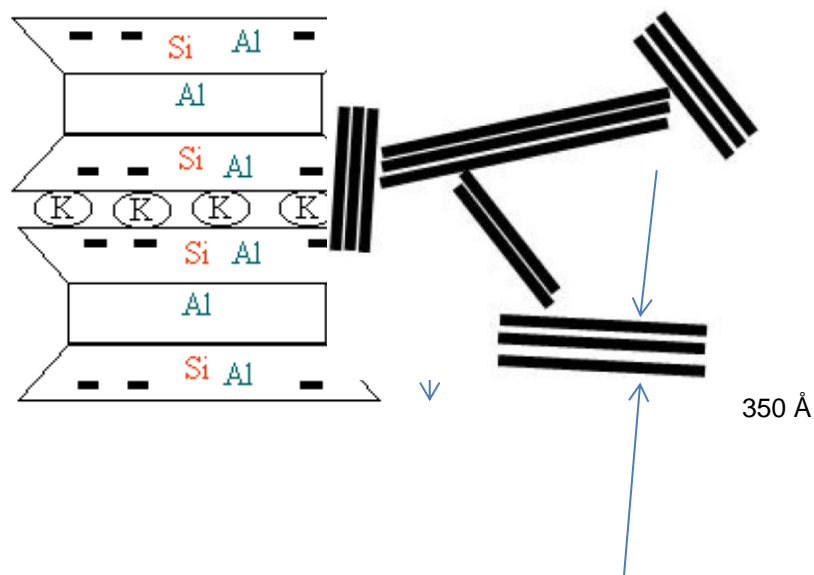
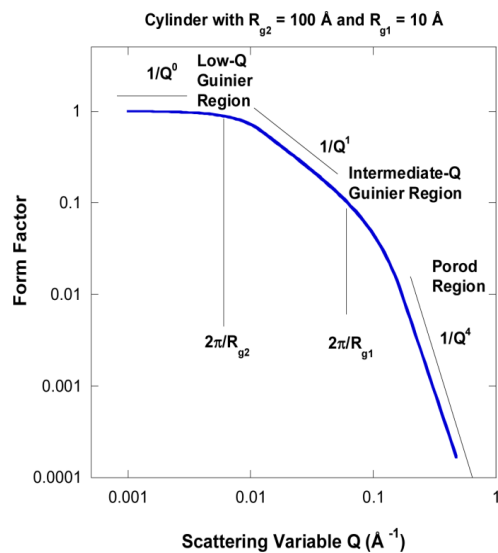


Figure 4-15. The layered structure and stacked bricks of illite

Effects of Sample Forms on Pore Features: Commonly samples used in the laboratory tests are ground and sieved from a field sample. One of the advantages using neutron scattering technology is that neutrons can penetrate deep within a sample. Thus, samples can be examined in their pristine state, kept in solution or a container under external constraints such as high T and P. It is well suited for *in situ* and non-destructive testing. Figure 4-16 shows that with increasing sample density, the intensity of the SANS spectrum increases together with its slope particularly at the low-Q Porod region. These results indicate that a sample with large density has a more surface fractal and less mass fractal nature.

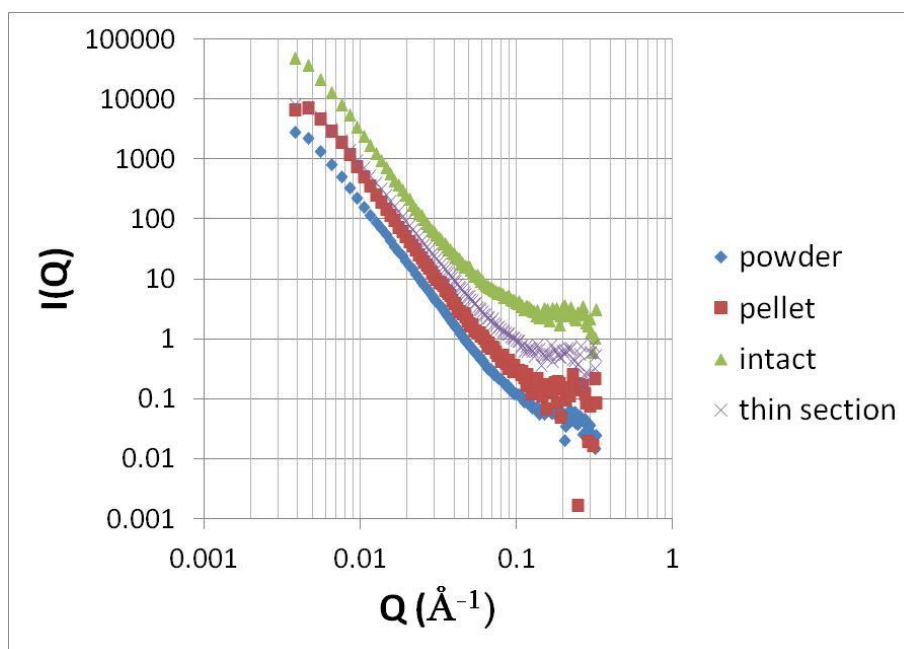


Figure 4-16. SANS scattering curves of WY bentonite in various forms.

Effects of Sample Environments on Pore Features: For the application in nuclear repository systems, elevated temperature and pressure are also considered as important environmental factors that may affect the pore structure, hence transport processes in repository formations. However, almost all conventional laboratory bench tests are conducted at room temperature. As discussed above, neutron scattering is well suited for *in situ* and non-destructive testing. Figure 4-17 is a SANS spectrum of pelletized smectite at controlled relative humidity (RH=100) as function of temperature. The results presented in Figure 4-17 suggest that, at controlled humidity and temperature in the testing range from 25°C to 75 °C pore features are affected particularly in the low Q Guinier region, i.e. the larger pores. Comparing the Porod plot ($\log(I)$ vs $\log(Q)$), we found that the slope of these scattering curves changed from 2.5 at 25°C to 2.8 at 75 °C, suggesting a smoother sample surface at higher temperature due to water adsorption.

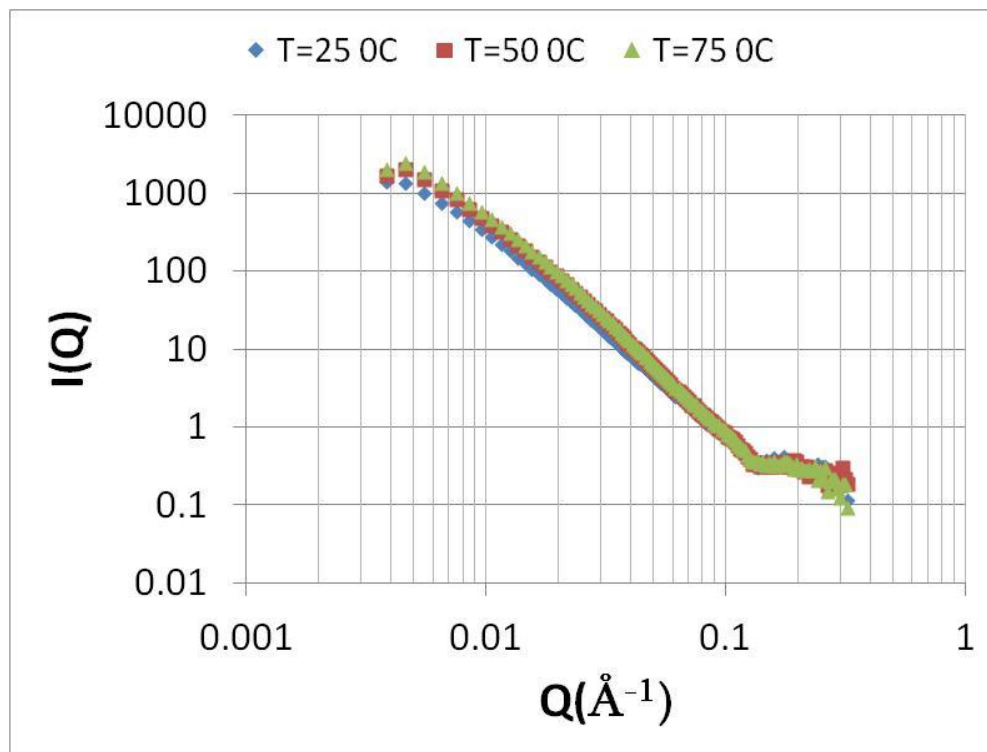


Figure 4-17. SANS scattering curves of smectite at controlled relative humidity RH=100% as function of temperature

Pore Characteristics and Water Absorption in Clays: Conventional laboratory transport studies involve a saturated scenario, though in reality flow and transport ubiquitously occur at low water content. Hence, water movement and moisture transport in clays in relation to pore structure are particularly crucial to provide fundamental insights into their performance efficiency as barrier material and their role in regulating radionuclide transport in nuclear waste repositories. Figure 4-18 presents SANS scattering curves of clays exposed to water vapor. The absorption of water was controlled by varying the relative humidity (RH=100%, RH=75%). In this experiment, dried, powdered sample was exposed to atmospheres with variable humidity in a commercial vacuum desiccator at room temperature for specific times. RH=75% was controlled by using saturated NaCl solutions.

The results indicate that swelling (WY bentonite, smectite) and non-swelling clays (illite, palygorskite) vary significantly in water absorption and moisture diffusivity. A precise water profile can be obtained as demonstrated for in illite in Figure 4-19 by subtracting “dry illite” from water-bearing illite.

The detailed illite water profile indicates that pore water is cylindrical in shape with a diameter of 19 Å after 1 day under controlled RH=100%. In 6 days, the water forms layers with a thickness of 24Å, as ascertained by the increase in slope in Figure 4-20.

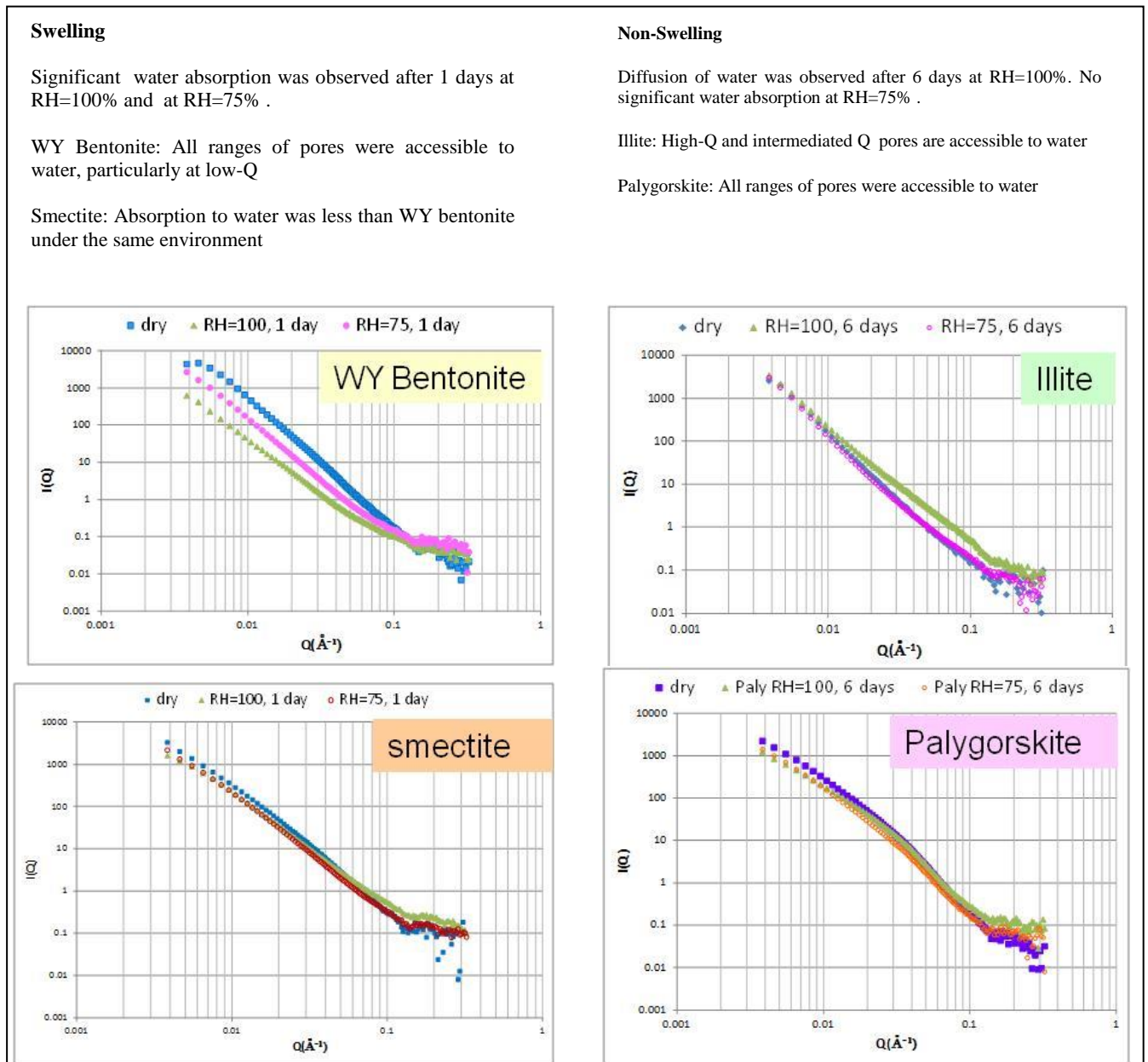


Figure 4-18. SANS scattering curves of clays exposure to water vapor as functions of relative humidity at room temperature.

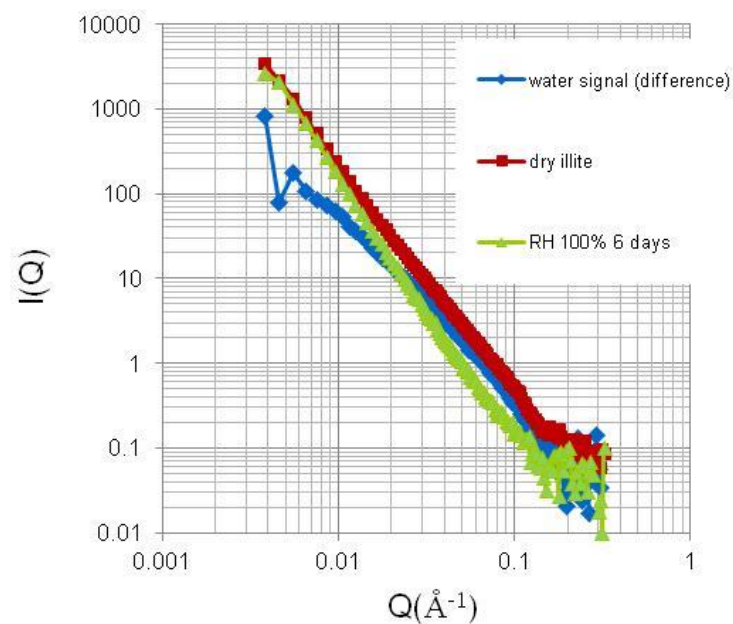


Figure 4-19. SANS scattering curve of illite before and after exposure to RH=100% water vapor.

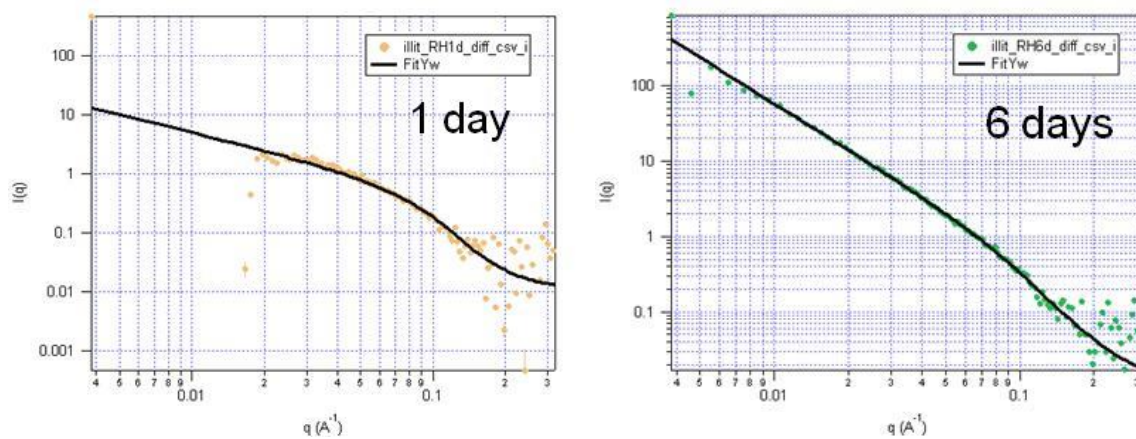


Figure 4-20. Water in illite profiles fitting results.

4.6 Conclusions

- Nano- to micro-scale structural characterization is crucial in providing insights into pore-scale transport processes, which are pertinent to upscale continuum model development.
- Clays show unique pore features, water adsorption and moisture diffusivity under various sample environments.
- This study suggests that SANS is the technique of choice in providing explicit details for characterization of pore processes and their evolution in the relevant ranges of humidity, temperature, pressure, composition, and length scale in high-level waste geological repositories. It is a useful technique enabling to experimentally investigate for nuclear repository systems flow and transport at low water content, in low permeability and heterogeneous media and in fractured systems under field conditions. Thus, further investigations in multi-staged phases should be conducted.

4.7 References

- (1) Wang Y., 2013, Research & Development (R&D) Plan for Used Fuel Disposition Campaign (UFDC) Natural System Evaluation and Tool Development (Rev.1), Sandia National Laboratories.
- (2) MEUNIER, A., VELDE, B., and GRIFFAULT, L., 1998, The reactivity of bentonites: a review. An application to clay barrier stability for nuclear waste storage. *Clay Minerals*, 33, 187-196.
- (3) PARKER A. and J.E. RAE, (eds.), 1998, Environmental Interactions of Clays, Springer-Verlag
- (4) Knudsen K.D., J.O. Fossum, G. Helgesen, V. Bergaplass, 2003, Pore characteristics and water absorption in a synthetic smectite clay, *J. Appl. Cryst.*, 36, 587-591.
- (5) Radalinski A.P., 2006, Small-angle neutron scattering and microstructure of rocks, *Review in Mineralogy and Geochemistry*, 63, 13-37.
- (6) Knudsen K.D., J.O. Fossum, G. Helgesen, V. Bergaplass, 2003, Pore characteristics and water absorption in a synthetic smectite clay, *J. Appl. Cryst.*, 36, 587-591.
- (7) Many J.T., R.P. Hjelm, E.G. Francois, 2010, Measurement of porosity in a composite high explosive as a function of pressing conditions by ultra-small-angle neutron scattering with contrast variation, *Propellants Explos. Pyrotech*, 35, 7-14.
- (8) Department of Energy, 2007, *Basic Research Needs for Geosciences: Facilitating 21st Century Energy Systems*, 287pp.
- (9) Rajaram, H., 1997, Time and scale dependent effective retardation factors in heterogeneous aquifers, *Adv. Water Resour.*, 20(4), 317-230.
- (10) Hochella M., White A.F.(editors), 1990, Mineral-Water Interface Geochemistry, *Reviews in Mineralogy*, 23, 603pp.
- (11) Ding, M., B.H.W.S. de Jong, S.J., Roosendaal, A. Vredenberg, 2000, XPS studies on the electronic structure of bonding between solid and solutes: Adsorption of arsenate, chromate, phosphate, Pb^{2+} , and Zn^{2+} ions on amorphous black ferric oxyhydroxide, *Geochim. Cosmochim. Acta*, 64(7), 1209-1219.

- (12) Lui, C., J.M. Zachara, N.P. Qafoku, Z. Wang, 2008, Scale-dependent desorption of uranium from contaminated subsurface sediments, *Water Resour. Res.*, 44, W08413, doi:10.1029/2007WR006478.
- (13) Ding, M., 2005, Radiotracer method in study of reactive transport across chemical gradients in porous media, *J. Radioanalytical and Nuclear Chem.*, 264, 489-494.
- (14) Gramling, C. M., C. F. Harvey, and L. C. Meigs, 2002, Reactive transport in porous media: A comparison of model prediction with laboratory visualization, *Environ. Sci. Technol.*, 36, 2508–2514, doi:10.1021/es0157144
- (15) Holmboe, M., S. Wold, M. Jonsson, 2012, Porosity investigation of compacted bentonite using XRD profile modeling, *J. of Contaminant Hydrology*, 128, 19-32.
- (16) Anovitz, L.M., G. Rother, D.R. Cole, 2011, Characterization of rock pore features in geothermal systems using small angle neutron scattering (SANS), *Proceedings, Thirty-Sixth Workshop on Geothermal Reservoir Engineering*, Stanford University, CA, Jan. 31-Feb. 2, 2011, SGP-TR-191.
- (17) Cole, D.R., E. Mamontov, G. Rother, 2009, Structure and dynamics of fluids in microporous and mesoporous earth and engineering materials. In: *Neutron Applications in Earth, Energy, and Environmental Sciences*, L. Liang, R.Rinaldi and H. Schober, editors, Springer Verlag, 547-570.
- (18) Ding, M., H.Xu, M. Hartl, R. Hjelm, Y. Wang, 2013, Pore characteristics and their evolution in clays using small angle neutron scattering, *Proceedings 2013 IHLRWM*, Albuquerque, NM, April 28-May 2, 2013.
- (19) Zaccai G. and Jacrot B., 1983, Small angle neutron scattering, *Ann. Rev. Biophys. Bioeng.*, 12, 139-157.
- (20) Vaniman D.T., S.J. Chipera, D.L. Bish, M.C. Duff, and D.B. Hunter, 2002, Crystal chemistry of clay-Mn oxide associations in soils, fractures, and matrix of the Bandelier Tuff, Pajarito mesa, New Mexico, *Geochimica et Cosmochimica Acta*, Vol. 66, No.8, 1349-1374.
- (21) Cheshire, M.C., F.A. Caporuscio, C. Jove-Colon, M.K. McCamey, 2013, Alteration of clinoptilolite into high-silica analcime within a bentonite barrier system under nuclear repository conditions, *Proceedings of International High-Level Radioactive waste management Conference*, 2013.

5.0 An Experimental Methodology for Improving Radionuclide Transport Process Models using Uranium and Grimsel Granodiorite as a Case Study

5.1 Introduction

The interaction of weakly adsorbed radionuclides such as iodine-129 with clays was addressed in Sections 2 and 3. This section will focus on the interaction of moderately adsorbed radionuclides such as uranium with granitic materials. In FY 2013, Los Alamos National Laboratory (LANL) has attempted to develop and demonstrate an experimental methodology for refining and parameterizing more robust radionuclide transport process models that can be readily incorporated into systems models used for nuclear waste repository risk assessments. The experimental program has focused on uranium transport in the saturated, fractured granodiorite system at the Grimsel Test Site (GTS) in Switzerland. Uranium is likely to be an important radionuclide in risk or dose calculations for most geologic repository systems (if it is not recovered by nuclear fuel reprocessing) because of its large inventory in used fuel and its relatively weak adsorption in many geochemical environments. The Grimsel granodiorite system was chosen because it is representative of a generic crystalline rock repository, and it also avoids any perceived ties to potential future U.S. repository locations. Also, the Used Fuel Disposition Campaign has entered into a formal collaboration with the international Colloids Formation and Migration (CFM) project that is being conducted at the GTS, so materials from this site are readily available, and field transport experiments involving uranium and other radionuclides are being conducted at the site. These experiments offer a unique opportunity to observe field-scale radionuclide transport behavior that can be compared and contrasted to laboratory experimental results.

We note that while this study is focused on a specific geochemical system, the intent is that the methods developed be widely applicable to any media or system relevant to nuclear waste geologic disposal, including engineered barrier systems. We also note that in last year's Used Fuel Campaign natural systems report we mentioned the possibility of transitioning our experimental efforts from uranium to ^{237}Np because uranium adsorption to the Grimsel granodiorite was very weak (not measurable) at the ambient GTS pH of ~ 9 . However, we continued to focus on uranium transport in FY 2013 for the following reasons:

- We observe significant adsorption of uranium to GTS materials at pH less than ~ 9 , and lower pHs are more relevant to many crystalline rock systems around the world.
- Np adsorption to GTS materials at pH ~ 9 was not definitively greater than uranium in FY 2012 batch sorption experiments, and field data from GTS tracer experiments conducted in 2002, both with and without bentonite colloids, indicated that uranium and neptunium had essentially indistinguishable transport behavior, with ^{237}Np actually having a slightly higher reported recovery in a colloid-free tracer experiment [1].
- It is easier and more cost effective for us to work with uranium than Np. We can adjust uranium concentrations somewhat independently of radioactivity levels by combining ^{233}U with natural uranium that is readily available as ICP-MS standards. Also, the higher specific activity of ^{233}U compared to ^{237}Np offers greater analytical sensitivity to uranium by inexpensive liquid scintillation counting, allowing us to interrogate a wider range of concentrations than for Np.
- The literature on Uranium aqueous geochemistry and transport processes is much more abundant than for Np, so experimental results can be more readily benchmarked and compared against results of other studies.

5.2 Materials and Methods

The experimental approach to date is described in this section. Briefly, the approach has included a combination of batch and small-scale column experiments using mostly crushed Grimsel granodiorite as the geologic material. However, once it became available, the emphasis shifted from the crushed granodiorite to GTS fracture fill material because the latter material is much more representative of the mineralogy in fracture flow pathways that transmit groundwater through the granodiorite (and in which the GTS field tracer experiments are being conducted).

5.2.1 Ground Water

The ground water used in all experiments is a synthetic Grimsel ground water (SGGW) with the recipe given in Table 5-1. The synthetic water was prepared with deionized water and analytical-grade reagents. The as-prepared pH of the SGGW is 8.8-9.1, which agrees well with the field-measured pH of 8.8-8.9 at the GTS. However, because uranium adsorption was negligible at this pH, N-morpholino-ethanesulfonic acid (MES) was used to buffer the SGGW to lower values to induce adsorption (necessary for method development in this project). MES was selected as the buffer because it offers effective buffering in the pH 6-8 range while having a low tendency to complex with metal ions [2], including uranyl ion ($U_{(VI)}^{2+}$). Buffering with inorganic acid/base pairs such as a carbonate or phosphate could affect the aqueous speciation and transport behavior of uranium by forming uranyl complexes (carbonate) and possibly uranyl precipitates (phosphate). The use of MES as a buffer for uranium and actinide studies also follows examples set by others [3].

Table 5-1. Synthetic Grimsel Groundwater Recipe.

Compound	g/L
Na ₂ SO ₄	0.1440
KCl	0.0048
MgCO ₃	0.0427
NaHCO ₃	0.2733
CaCl ₂	0.0130
H ₄ SiO ₄	0.0341
pH	8.8-9.1

The two primary target pHs of the MES-buffered SGGW were 6.9 and 7.9, approximately 2 and 1 pH units, respectively, lower than the natural pH of the water. After some trial and error, SGGW at these pHs could be readily prepared and would remain stable with respect to pH changes for extended periods of time. Uranium adsorption partition coefficients (K_d values) onto many different minerals have been reported to vary over several orders of magnitude between pH 7 and 9 [4-7], with essentially zero K_d at pH of 9 or higher, consistent with our FY 2012 results. For a given pCO_2 , uranium exhibits much stronger adsorption at the low end of this pH range because of the greater abundance of positively-charged uranyl species ($U_{(VI)}^{2+}$ and $U(OH)^+$) and the lesser abundance of nonsorbing neutral and negatively-charged uranyl carbonate or uranyl-Ca/Mg-carbonate complexes at neutral pH. Table 5-2 shows relative abundances of uranium-bearing species in SGGW as predicted by PHREEQC [8] using the llnl.dat database [9] with the addition of uranyl-calcium-carbonate and uranyl-magnesium-carbonate complexation constants from reference [10].

Table 5-2. Fractional Abundance of Uranium-Bearing Species in SGGW as a function of pH (from PHREEQC).

Constituent	pH 6.9	pH 7.9	pH 8.8
$\text{UO}_2\text{Ca}(\text{CO}_3)_3^{2-}$	0.478	0.562	0.563
$\text{UO}_2\text{Mg}(\text{CO}_3)_3^{2-}$	0.181	0.217	0.230
$\text{UO}_2(\text{CO}_3)_2^{2-}$	0.141	0.0171	0.00261
$\text{UO}_2\text{Ca}_2(\text{CO}_3)_3^0$	0.0868	0.0998	0.0900
$\text{UO}_2(\text{CO}_3)_3^{4-}$	0.0785	0.0943	0.105
$\text{UO}_2(\text{CO}_3)^0$	0.0180	0.00022	---
$\text{UO}_2\text{Mg}_2(\text{CO}_3)_3^0$	0.00790	0.00935	0.00943
$\text{UO}_2(\text{OH})^+$	8.5e-5	1.1e-6	2.4e-8
UO_2^{2+}	2.5e-6	1.9e-9	8.8e-12
SUM	0.9910	0.9993	0.9999

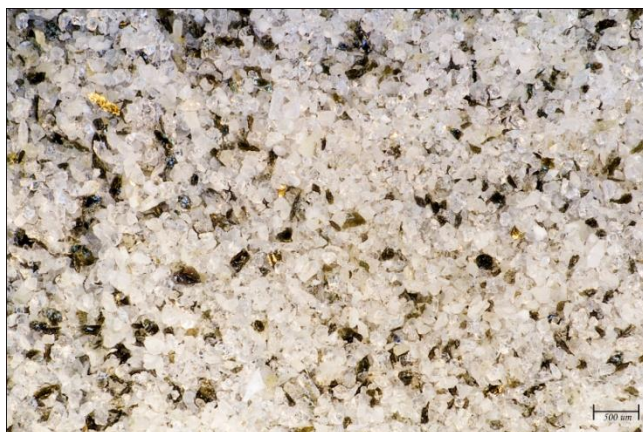
5.2.2 Rocks

The solids used for the experiments were provided by our Grimsel collaborators. These included:

- Crushed granodiorite core from borehole CFM 11.002 at the GTS (avoiding an open fracture with altered shear zone surfaces, since there was not enough of this material to include representatively in the experiments) sieved to size ranges of 75-150 μm , 150-355 μm , and 355-500 μm .
- Gently crushed fracture fill material (FFM) from a coring of the MI shear zone at the GTS, which is the shear zone in which all CFM field experiments are conducted. The core was collected in a tunnel adjacent to the CFM tunnel because the shear zone is not currently exposed in the CFM tunnel. The FFM material used in the experiments was sieved to within the 150-355 μm size range.

The granodiorite material was crushed and sieved at LANL. Microphotographs of this material are provided in Figure 5-1, and its mineralogy, as determined from quantitative x-ray diffraction (QXRD) analysis, is listed in Table 5-3. Figure 5-2 shows a microphotograph of the FFM, and Table 5-4 lists the major mineralogy from QXRD for this material. Table 5-4 also lists the QXRD-determined mineralogy of a granodiorite sample and a sample scraped from the surface of the open fracture in the core from borehole CFM 11.002. The mineralogy of the FFM and the granodiorite matrix are clearly different, although it is also apparent that there are differences in the analyses of the granodiorite matrix from two different analysts (Table 5-3 vs. 5-4). Table 5-5 lists the bulk chemical analyses by x-ray fluorescence of the granodiorite and FFM samples (splints of the samples reported in Table 5-4). The bulk chemical

differences are minor, with significant enrichment of Mg, minor enrichments of K and Fe, and minor depletions of Si, Na and Ca in the FFM compared to the unaltered granodiorite.



75-150 µm



150-355 µm



355-500 µm

Figure 5-1. Microphotographs of the three different grain sizes of crushed and sieved Grimsel granodiorite

Table 5-3. Quantitative X-ray diffraction interpretation (wt%) of Grimsel granodiorite materials of Fig. 5-1.

Sample	Quartz	Plagioclase	K-Feldspar	Mica	Chlorite	Kaolinite	Epidote*	Total
75-150 μm	42.9	27.5	4.2	24.9	0.2	0.4	---	101.1
150-355 μm	24.3	43.8	7.8	23.6	0.2	0.2	---	99.9
355-500 μm	15.3	46.4	6.7	30.9	0.2	0.5	---	100.0

*There are tiny amounts (probably a few tenths of percent) of epidote.

5.2.3 Uranium and Tritiated Water

The uranium used in all experiments was a combination of ^{233}U (Eckert and Ziegler) and natural uranium from a 1000 mg/L ICP-MS standard (SpexCertiPrep). For all uranium solutions, approximately 98% of the uranium was taken from the ICP-MS standard, and about 2% ^{233}U was added to ensure accurate quantification of concentrations by inexpensive and rapid liquid scintillation counting. Several thousand samples were analyzed over the course of the experiments, so a rapid and cheap method of analysis was very important. It was assumed that the ^{233}U radiotracer and the ^{238}U comprising the vast majority of the uranium in the ICP-MS standard would behave identically with respect to adsorption and speciation in all experiments. A groundwater concentration of $6.5\mu\text{M}$ uranium was targeted for most experiments, which is approaching the solubility limit for uranium at neutral pH in the SGGW. However, this concentration was verified

Table 5-4. Quantitative X-ray diffraction interpretation (wt%) of Grimsel granodiorite and FFM materials.

Mineral	Granodiorite	Shear Zone Surface	FFM
Quartz	32	18	13
Microcline	10	8	5
Albite	42	44	34
Biotite	5	11	31
Chlorite	1	--	
Muscovite	10	19	16
Epidote	<1	--	--
Smectite	--	--	1
Calcite	--	<1	<1

experimentally to be under the solubility limit at all test pHs, and it was also predicted to be under the limit in PHREEQC calculations (with the exception of a slight supersaturation with respect to soddyite, $(\text{UO}_2)_2\text{SiO}_4 \cdot 2\text{H}_2\text{O}$, at pH 6.9). A high uranium concentration was desirable because we wanted to maximize sorption site occupancy at a given pH in the small-scale column experiments, with the intent

being to later conduct experiments at significantly lower concentrations for comparative purposes. The uranium stock solutions were acidic, but very little was needed for each experimental solution, so the acidity was easily buffered by the MES buffer.

Tritium in the form of tritiated water was co-injected with uranium in all column experiments as an ideal conservative tracer to provide mean groundwater residence times and dispersivities in the columns.

5.2.4 Analytical Measurements

Tritium and uranium concentrations were measured by liquid scintillation counting, or LSC (Perkin Elmer Tri-Carb 2550 or Perkin-Elmer Quantulus), with energy ranges of 0-20 keV for tritium and 100-260 keV for uranium. An aliquot of a groundwater sample was weighed and diluted to 6 mL with deionized water to ensure uniform sample volume. The diluted sample was then poured into a 20 mL polypropylene scintillation vial and 14 mL of liquid scintillation cocktail (Packard, Ultima Gold AB) was added, followed by vigorous shaking of the samples for at least 15 seconds. Samples were typically counted for 30 minutes. The transformed index of an external standard (tSIE) was used to adjust for variable quenching of the samples.

pH measurements were made using a pH meter (Orion Model 290) and a glass pH electrode (Fisher AccupHast). The electrode was calibrated with commercially-available pH 4.01, 7.00 and 9.01 buffers (Fisher).

5.2.5 Batch Adsorption and Desorption Experiments

Batch adsorption experiments were conducted with the 150-355 μm fraction of crushed granodiorite material at pHs of 6.8 and 8.8. Batch adsorption and desorption experiments were also conducted with the 150-355 μm fraction of FFM material at pHs of 6.9, 7.9 and 8.8. The granodiorite batch experiments were conducted in 50-ml polypropylene centrifuge tubes with 12 ml of uranium-spiked SGGW (6.5 μM U) being placed in contact with either 0.2, 0.5, or 1.0 g of granodiorite. The FFM experiments were conducted in Teflon centrifuge tubes with 10 ml

Table 5-5. X-ray fluorescence analysis (wt%) of Grimsel materials.

Constituent	Granodiorite bulk	FFM bulk	Detection Limits
fuse ratio	7:1	7:1	7:1
Na ₂ O	4.01	3.15	0.0451
MgO	0.725	4.28	0.0300
Al ₂ O ₃	14.0	14.3	0.0313
SiO ₂	70.9	63.4	0.1507
P ₂ O ₅	0.115	0.124	0.0049
K ₂ O	4.22	4.90	0.0112
CaO	1.90	1.03	0.0084
TiO ₂	0.436	0.491	0.0092
MnO	0.081	0.086	0.0252
Fe ₂ O ₃	3.10	3.83	0.0041
V	29	41	13
Cr	bdl	bdl	10
Co	bdl	bdl	15
Ni	bdl	bdl	5
Cu	bdl	bdl	5
Zn	31	53	5
Ge	bdl	bdl	24
As	bdl	bdl	15
Rb	110	192	4
Sr	135	71	5
Zr	217	236	6
Ba	403	372	19
W	bdl	bdl	43
U	bdl	bdl	4
LOI	0.35	4.28	
total	99.931	99.970	

bdl = below detection limit
LOI = loss on ignition

of uranium-spiked SGGW being placed in contact with 0.2, 0.5, or 1.0 g of FFM. Control experiments were conducted at each pH in the same centrifuge tubes (either polypropylene or Teflon) without the geologic materials present to evaluate adsorption to container walls and correct for this if necessary. The experimental matrix is summarized in Table 5-6. All experiments were conducted in duplicate. The centrifuge tubes were vertically positioned on an orbital shaker (VWR Scientific, DS-500) and horizontally oscillated at 180 RPM (Fig 5-3). The tubes were also manually inverted several times at least once a day to ensure adequate mixing of the media and solution.

Table 5-6. Batch adsorption-desorption experimental matrix.

Material	SGGW pH = 6.9	SGGW pH = 7.9	SGGW pH = 8.8
0.2 g Granodiorite	4 adsorption times	---	4 adsorption times
0.5 g Granodiorite	4 adsorption times	---	4 adsorption times
1.0 g Granodiorite	4 adsorption times	---	4 adsorption times
Control (no rock)	4 adsorption times	---	4 adsorption times
0.2 g FFM	6 ads. and 5 des. times	6 ads. and 5 des. times	6 ads. and 5 des. times
0.5 g FFM	6 ads. and 5 des. times	6 ads. and 5 des. times	6 ads. and 5 des. times
1.0 g FFM	6 ads. and 5 des. times	6 ads. and 5 des. times	6 ads. and 5 des. times
Control (no rock)	6 ads. and 5 des. times	6 ads. and 5 des. times	6 ads. and 5 des. times

Note: Granodiorite experiments started with 12 ml solution; FFM experiments with 10 ml solution.

In the granodiorite experiments, 1 mL samples were collected after 1, 10, 100, and 1000 minutes and were measured for total uranium concentration. The supernatant and solids were separated by centrifugation, which was abbreviated for the early-time samples. The solution removed for analysis was not replaced. In the FFM experiments, 0.75-ml samples were collected after 10, 100, 1000, 5900, 17200, and 18600 minutes. After 18600 minutes, all SGGW except for ~0.5 ml was removed from each centrifuge tube, and then 9.5 ml of pH-adjusted uranium-free SGGW was added to each tube to bring the solution volume back to 10 ml. 0.75-ml samples were then removed after 10, 100, 1000, 8300, and 17100 minutes to observe the desorption behavior of the uranium from the FFM material.

In addition to the experiments of Table 5-6 involving granodiorite and FFM materials, a small number of experiments were conducted to evaluate adsorption to experimental system components. These components included Tygon tubing, polyethylene tubing used for columns, glass wool used as a fill material at the ends of some columns, and polyfiber material that was also considered for use as a fill material.



Figure 5-3. Granodiorite batch adsorption-desorption experiment setup.

5.2.6 Column Transport Experiments

Several column transport experiments were conducted during FY 13. These experiments involved an evolution of methods and experimental components as lessons were learned. Our FY 12 column experiments conducted at pH 8.8 indicated no measurable adsorption or retardation of uranium to either the granodiorite or to the low-cost materials used in these experiments (i.e., polyethylene columns and Tygon® tubing, R-3606). A typical result from these experiments is shown in Figure 5-4. Also, our previous experience with polyethylene and Tygon® tubing at pHs of 8 and above had indicated minimal, if any, uranium interaction with these materials. Consequently, we initially conducted a series of granodiorite column experiments at pH 6.9 using the same experimental materials that were used at a pH of 8.8.

For the column experiments, small columns were constructed from 6 cm lengths of 1 cm diameter polyethylene tubing or Teflon tubing (in later experiments). These small columns were devised to allow rapid and economical evaluation of sorption/desorption behavior under flowing conditions (and in duplicate or triplicate). The inside of the ends of the polyethylene columns were tapped to accept threaded polyethylene fittings with hose barbs on one end, and the Teflon columns were tapped to accept threaded Teflon fittings with tubing connectors on one end. Tygon® tubing (R-3606) (polyethylene columns) or Teflon tubing (Teflon columns) and 3-way polycarbonate stopcocks were used to connect the columns to 60 mL polypropylene syringes (BD Falcon) at the influent side of the column and to a fraction collector (Gilson, FC-200) on the effluent side of the column. The fraction collector was enclosed and had an evaporation pan to increase

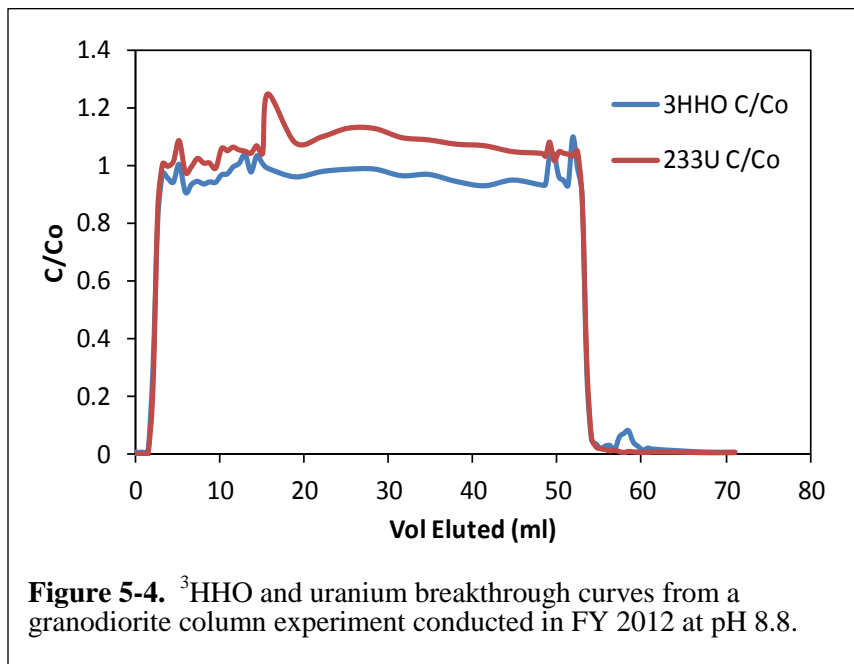


Figure 5-5. Small column experimental setup.



Figure 5-6. Close up of experimental columns.

the humidity in the enclosure and to limit evaporation of samples before analysis. The polypropylene syringes containing either uranium-bearing or uranium-free solution were loaded into syringe pumps (KD Scientific, Model 100) that were set to a flow rate of $\sim 0.3 \text{ mL h}^{-1}$. Column flow was in the upward direction to help maintain saturation. Columns were packed with $\sim 5 \text{ g}$ of dry material, and a small amount of glass wool ($\sim 0.04 \text{ g}$) was used at the top and bottom of the granodiorite columns to prevent grains from entering the tubing.

Figure 5-5 shows a typical setup that includes a fraction collector capable of collecting effluent from five small columns run in parallel. The columns were typically taped to the outside of the fraction collector, as shown close up in Figure 5-6. The columns were initially flushed with uranium-free SGGW until the effluent pH stabilized. The influent solution was then switched to solution containing uranium and tritium. Syringes were refilled or changed several times during the course of the experiments, and at some predetermined time the influent solution was switched back to a uranium- and tritium-free solution to allow observation of desorption behavior in the column. Samples were collected in tared 13 cm x 100 cm polypropylene test tubes at increments ranging from 90 minutes for early samples to 900 minutes for later samples. Sample mass was weighed with a digital balance (Mettler, PL1200) prior to withdrawing sample for liquid scintillation counting. The weights were used to determine actual column flow rates. pH measurements were recorded for all samples from one of the columns run in parallel.

Table 5-7. Summary of Granodiorite Column Experiments (3 Polyethylene columns with 75-150 μm material, 3 with 150-355 μm , and 3 with 355-500 μm). Flow rate in all columns $\sim 0.27 \text{ ml/hr}$.

Conditions	Approximate Start Time, hr	Approximate Start Volume, ml
Inject 6.5 mM U at pH 7.2	0	0
Inject U-free SGGW, pH 6.9	340	90
30-day Flow Interruption	575 (1290 end)	160
7-hr Flow Interruption	1380	185
4-day Flow Interruption	1425 (1520 end)	200
Double Flow Rate (approx.)	1650	240
Halve Flow Rate and pH to 7.2	1770	295
pH to 8.8	1900	330

Note: Volumes and times varied from column to column.

The granodiorite column experimental summary is provided in Table 5-7. Note that flow interruptions or flow rate changes and the changes in influent pH were introduced as flow or geochemical transients to help elucidate uranium adsorption and desorption mechanisms. The results of the granodiorite experiments (see Section 5.3) suggested that we should follow up with some additional experiments to evaluate uranium interactions with the experimental components. These follow-up experiments included both the batch experiments mentioned at the end of the previous section and a series of column experiments that effectively served as controls because they included all the experimental components except for either the granodiorite or FFM. The matrix of control column experiments is listed in Table 5-7. These experiments revealed significant interaction of uranium with system components at pH 6.9, prompting a transition to Teflon columns and tubing in subsequent FFM experiments.

Table 5-8. Matrix of Blank/Control Polyethylene Column Experiments (all with Polypropylene Syringes and ~ 50 ml injections of 6.5 μ M Uranium at ~0.27 ml/hr)

Tubing	Other Components	pH
Tygon [®]	Glass Wool (full)	6.9, 7.2, 8.8
Tygon [®] (2 Columns)	Glass Wool (0.04 g)	6.9, 8.8
Tygon [®]	None	6.9, 8.8
Tygon [®] (3 columns)	None	7.9, 8.8
Teflon (2 columns)	None	7.9, 8.8

Two FFM column experiments were conducted at pH 6.9 in the Teflon system, with two parallel columns being run as controls (no FFM) to evaluate uranium interactions with system components. Polypropylene syringes and polycarbonate stopcocks were the only non-Teflon components in the flow systems. These experiments were conducted in a similar manner as the granodiorite column experiments except that the flow rate was kept constant throughout the experiments and a pH decrease to 0 (1M HCl) was introduced at the end of the experiments to desorb all uranium and check for mass balance closure. The experimental conditions are summarized in Table 5-9.

Table 5-9. Summary of FFM column experiments (2 columns with 150-355 μ m material in Teflon columns) and control columns. Flow rate in all columns ~0.27 ml/hr.

FFM Column Conditions	Approximate Start Time, hr	Approximate Start Volume, ml
Inject 6.5 μ M U at pH 6.9	0	0
Inject U-free SGGW, pH 6.9	601	164
pH to 7.9	947	258
pH to 8.8	1345	365
Inject 1 M HCl	1670	450
Control Column Conditions		
Inject 6.5 μ M U at pH 6.9	0	0
Inject U-free SGGW, pH 6.9	210	60
Inject U-free SGGW, pH 7.9	530	149
Inject U-free SGGW, pH 7.9	672	192

Note: Volumes and times varied from column to column. No flow interruptions.

5.2.7 Interpretive Modeling

The batch and column experiments were interpreted using a multisite/multirate reaction modeling approach where each different type of site could be assigned different adsorption and desorption rate constants as well as different surface site densities. Two separate Fortran programs were used for modeling the two different types of experiments, although the equations used to model the adsorption and desorption reactions in each program were identical. The governing equations in the batch experiment model were:

$$\frac{\partial S_i}{\partial t} = k_{fi}c \left(1 - \frac{S_i}{s_{mi}}\right) - k_{ri}S_i \quad (5.1)$$

$$\frac{\partial c}{\partial t} = \frac{M}{V} \left[-\sum_i k_{fi}c \left(1 - \frac{S_i}{s_{mi}}\right) + \sum_i k_{ri}S_i \right] \quad (5.2)$$

where, c = concentration in aqueous phase, mol/ml

s_i = concentration on surface sorption site i , mol/g

t = time, hr

k_{fi} = adsorption rate constant for sorption site i , ml/g-hr

k_{ri} = desorption rate constant for site i , hr⁻¹

s_{mi} = surface site density (maximum adsorption capacity) for sorption site i , mol/g

M = mass of solids, g

V = volume of solution, ml

The governing equations for the column transport model were equation (5.1) plus the following equation for the mobile aqueous phase:

$$\frac{\partial c}{\partial t} - v \frac{\partial c}{\partial x} + D \frac{\partial^2 c}{\partial x^2} + \frac{\rho_B}{\phi} \left[-\sum_i k_{fi}c \left(1 - \frac{S_i}{s_{mi}}\right) + \sum_i k_{ri}S_i \right] \quad (5.3)$$

where, v = flow velocity, cm/hr

D = dispersion coefficient, cm²/hr

ρ_B = bulk density of solids, g/cm³

ϕ = porosity

In addition to solving equations (5.1) and (5.2), the batch model allowed the volume of solution in the reactor to be changed at specified times to simulate sampling, and it also allowed for a specified volume of uranium-free water to be added to the reactor to simulate the start of the desorption phase of the experiments. Equations (5.1) and (5.2) were solved using a 4th-order Runge-Kutta algorithm.

The column model solved equations (5.1) and (5.3) simultaneously using an implicit finite difference algorithm. The model allowed for arbitrary injection functions to be specified at the column entrance ($x = 0$), and it also allowed for flow rate changes and changes to the reaction parameters k_{fi} , k_{ri} , and s_{mi} to be specified multiple times during an experiment simulation. Changes to the reaction parameters could be specified when the pH of the injection solution was changed or when a transition was made from injecting uranium-spiked water to uranium-free water (to simulate adsorption-desorption hysteresis). The changes to reaction parameters were propagated through the columns in the same manner as a conservative tracer.

The approach to interpreting the experiments was to try to simultaneously match the combined data from both the batch and column experiments for a given rock type using a single set of reaction

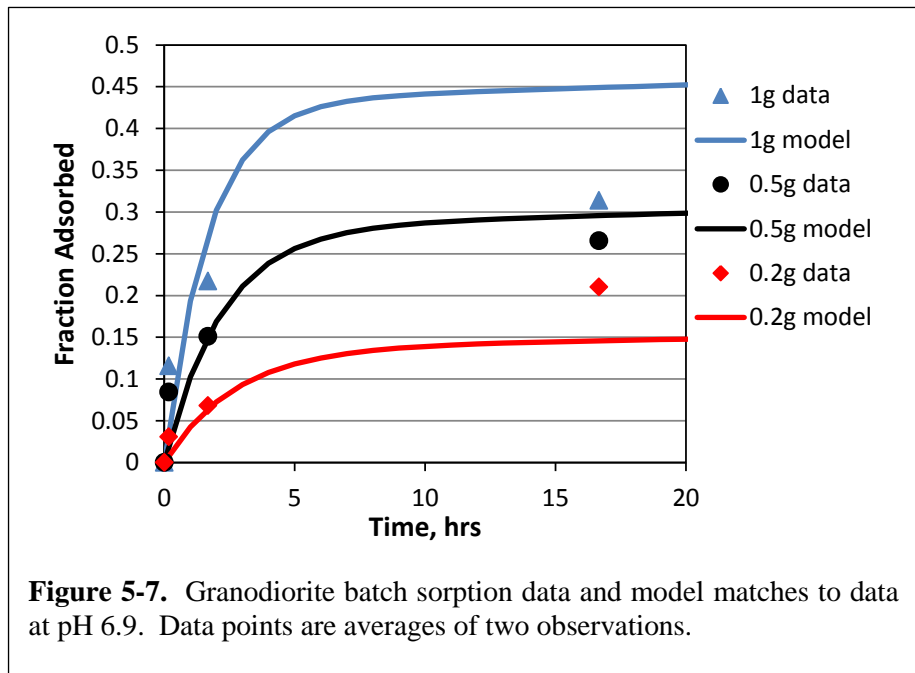
parameters and a minimal number of sorption site types. The set of chemical reactions used for modeling can be found in reference [10a]. By matching both the batch and column data the reaction parameters were more highly constrained than if the data from only one type of experiment were matched. It was recognized that more types of sites with different reaction rates could always provide a better simultaneous match to the data sets, so the goal was to use only as many sites as necessary to achieve a reasonable qualitative match to the data.

An automated parameter estimation algorithm, such as PEST [11-12], was not employed to obtain the matches to the data. Such tools are certainly desirable for future endeavors, but the complexity and subtleties of the data-matching exercise coupled with the limited time between data collection and reporting made it impractical to employ these tools at this stage. Often it was considered important to match subtle data features containing only a few observations even if it meant a poorer match to features containing many data points that would have dominated a least-squares or other minimization exercise. Also, we were not able to rigorously assess uncertainty and nonuniqueness of the modeling matches to the data in time for this report. These activities are reserved for future efforts.

5.3 Results

5.3.1 Batch Sorption and Desorption Experiments

Figure 5-7 shows the results of the batch adsorption experiments onto the granodiorite, with model matches to the data. Because these were short-term experiments that involved only adsorption with no desorption, they were useful primarily for placing an upper limit on the uranium adsorption rate constant onto the granodiorite. The model curves in Figure 5-7 were generated using the same reaction parameters, k_{fi} , k_{ri} , and s_{mi} , to simultaneously match the data sets. These model curves demonstrate a recurring theme with the batch experiments; i.e., adsorption in the experiments with the largest solid-mass-to-solution-volume ratio tended to be overpredicted by the model while adsorption in the experiments with the smallest solid-mass-to-solution-volume ratio tended to be underpredicted. We do not have an explanation for this behavior. If adsorption sites tended to be filled in the experiments, the effect should have been most pronounced in the experiments with smaller solid-mass-to-solution-volume ratios, leading to less adsorption per unit mass of solids than in the experiments with larger ratios (the model curves of Figure 5-7 all have approximately the same sorption per unit mass of solid, with a minor amount of suppression of sorption occurring for the smaller solid masses). Thus, reducing the number of sorption sites on the solids only exacerbates the



overprediction of sorption at larger solid-mass-to-solution-volume ratios and the underprediction at smaller ratios. The model also accounts for the tendency for solution concentrations to remain higher in the experiments with smaller ratios, which results in greater apparent adsorption to smaller masses, but the magnitude of this effect is not large enough to account for the observed trends. In effect, the results of Figure 5-7 suggest that the smaller solid masses were more reactive than the larger solid masses.

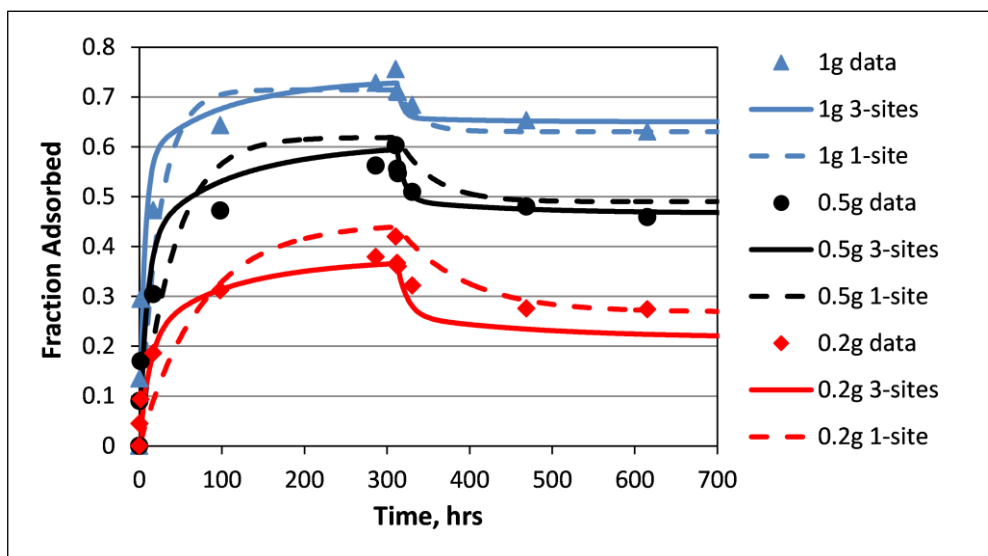


Figure 5-8. FFM batch sorption and desorption data at pH 6.9, with 3-site and 1-site model matches to the data. Data points are averages of two observations.

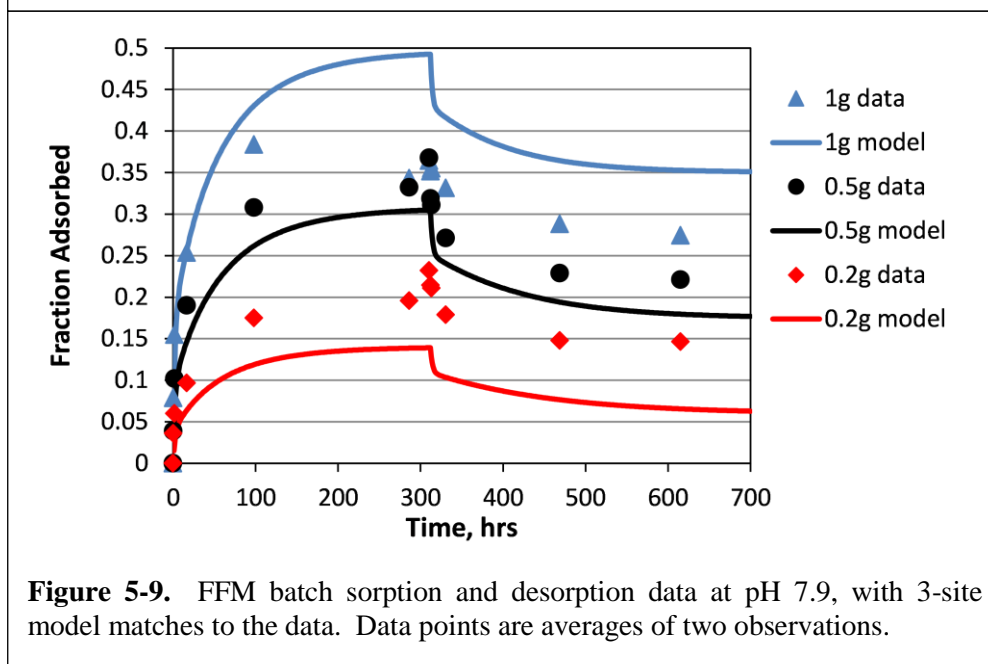


Figure 5-9. FFM batch sorption and desorption data at pH 7.9, with 3-site model matches to the data. Data points are averages of two observations.

Figures 5-8 and 5-9 show the results of the batch experiments onto the FFM at pH 6.9 and 7.9, respectively, with model matches to the data. The results of the pH 8.8 experiments are not shown because they indicated no apparent adsorption of uranium to the FFM. For the pH 6.9 and 7.9 experiments, both adsorption and desorption observations were made, so the model results have more constraints than in the case of the granodiorite experiments (Figure 5-7). However, the two different model curves in the plots of Figure 5-8 illustrate the nonuniqueness associated with matching the batch data. One set of curves in Figure 5-8 assumes a single-site model with a large (effectively unlimited) number of sorption sites and the other set of curves assumes three sites that have significantly different reaction parameters. The values of the parameters from both sets of curves, as well as for the curves of Figure 5-9, are listed in Table 5-10. One would normally consider the single-site model to be the best model because it involves the fewest number of adjustable parameters, but the three-site model is also included here because it provides a much better simultaneous match to the FFM column transport data, discussed in the next section. It is noteworthy that the data of Figure 5-8 at pH 6.9 are matched reasonably well by the models for all the different solid-mass-to-solution-volume ratios (with the lowest ratio being slightly underpredicted), whereas the model curves of Figure 5-9 at pH 7.9 exhibit the same overprediction at high ratios and underprediction at low ratios that was observed in the granodiorite experiments (Figure 5-7).

The pH 6.9 control samples showed slight decreases in uranium concentration (about 10% relative to starting concentrations) at the latest times during the adsorption phase of the experiments, but negligible decreases were observed in the pH 7.9 experiments. The decreases in concentrations at pH 6.9 could reflect a slight tendency for adsorption to the Teflon containers or more likely a small amount of adsorption to colloidal silica phases that were centrifuged out of the samples. The solutions were predicted by PHREEQC to be slightly oversaturated with respect to SiO₂ phases at pH 6.9. The solutions were also predicted by PHREEQC to be slightly oversaturated with respect to soddyite ((UO₂)₂SiO₄·2H₂O), so a small amount of uranium precipitation cannot be ruled out. However, the 6.5-μM uranium stock solution buffered to pH 6.9 (the solution used as the starting solution in all the batch experiments) remained stable with respect to uranium concentrations throughout the period of the batch experiments, which suggests that the apparent loss of uranium in the experiments was either an artifact or perhaps some sorption or precipitation induced by handling of the Teflon centrifuge tubes or by introduction of foreign material (e.g., dust) into the tubes when they were open. The stock solution was stored in a Teflon bottle.

Table 5-10. Reaction model parameters yielding matches to FFM batch adsorption-desorption data shown in Figures 5-8 and 5-9.

pH 6.9	k_f , ml/g-hr	k_r , hr ⁻¹	S_m , μmol/g
1-site model	0.3	0.005	1.3
3-site model, site 1	0.8	0.06	1.3
3-site model, site 2	0.1	0.003	0.104
3-site model, site 3	0.07	0.001	0.026
pH 7.9			
3-site model, site 1	0.8	0.4	1.3
3-site model, site 2	0.05	0.005	0.039
3-site model, site 3	0.05	0.001	0.013

5.3.2 Column Transport Experiments

Granodiorite Column Experiments: The pH 6.9 granodiorite column experiments were a challenge to interpret because it quickly became apparent that there were significant interactions between uranium and

some of the column materials. Before presenting the results of these experiments, it is helpful to present the results of experiments that were conducted to quantify these unwanted interactions and to discuss measures taken to account for these interactions when interpreting the column results.

Some simple batch experiments were initially conducted to screen for the uranium interactions with system components. The results of these experiments are presented graphically in Figure 5-10, which shows that uranium interacted significantly with virtually all of the granodiorite column system components. Based on these results, two column experiments were conducted in which all the experimental components of the granodiorite columns were used but no geologic materials were packed into the columns.

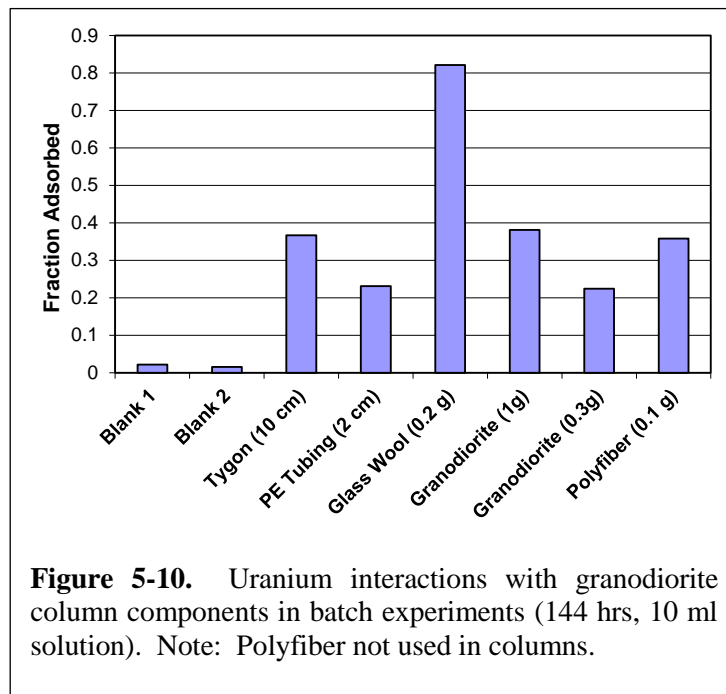


Figure 5-10. Uranium interactions with granodiorite column components in batch experiments (144 hrs, 10 ml solution). Note: Polyfiber not used in columns.

Figure 5-11 shows the results of these experiments, and model matches to the data to capture the effects of the system components on the transport of uranium (note that the decrease in concentration following the pulse injection was recorded in only one of the two experiments). The results of the modeling were used to simulate the injection pulse in the granodiorite experiments after accounting for the effects of the other system components. This simulation of the injection pulse was not as simple as assuming that the breakthrough curves of Figure 5-11 applied to the granodiorite experiments

because (1) the injection pulses were longer in the granodiorite experiments, and (2) the dispersion in the granodiorite columns was much less than in the empty columns used as blanks. To approximate the injection pulses in the granodiorite columns, the attenuation parameters from the interpretive modeling of Figure 5-11 were used to predict the injection pulses using the pulse durations and dispersion parameters deduced from the tritium data in the granodiorite experiments.

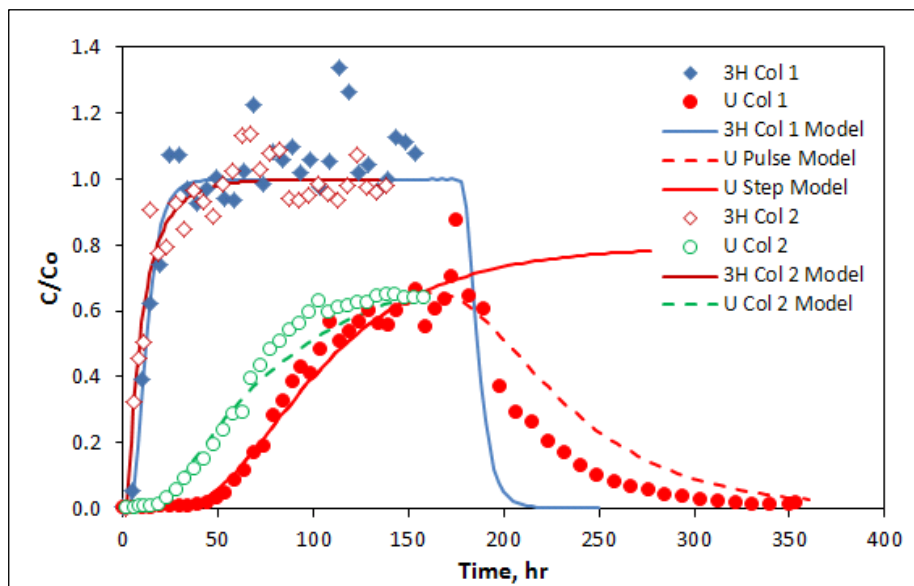


Figure 5-11. Tritium and uranium breakthrough curves in control columns at pH 6.9. Model parameters from red model curves were used to construct injection functions in granodiorite column experiments.

Additional experiments were conducted to evaluate the influence of column components at pH 7.9 and also to better quantify the effects of the glass wool on uranium transport at pH 6.9 (see Table 5-8), but these results are not presented here because they do not directly pertain to the FY 2013 experiments. The pH 7.9 experiments included separate systems with either Tygon® or Teflon tubing with polyethylene columns, and it was apparent that (1) there was less attenuation of uranium in the Tygon®/PE system than at pH 6.9, although attenuation was still significant enough to have to account for it (no delay in uranium arrival relative to tritium as in Figure 5-11, but normalized uranium concentrations did not rise above about 0.8), and (2) there was no attenuation of uranium relative to tritium in the Teflon/PE columns, suggesting that interactions with the PE columns at pH 7.9 are minimal and the observed uranium attenuation in the Tygon®/PE system are probably resulting from interactions with the Tygon® tubing.

Table 5-11. Reaction model parameters yielding matches to granodiorite column transport data shown in Figures 5-12 through 5-14.

75-150 μm material	k_f, ml/g-hr	k_r, hr⁻¹	S_m, μmol/g
pH 7.2 adsorption	2.5, 0.02, 0.02	0.3*, 0.0025, 0.001	1.3, 0.042, 0.042
pH 6.9 desorption	2.5, 0.02, 0.02	0.0055, 0.0001, 0.0001	1.3, 0.042, 0.042
pH 7.2 desorption	2.5, 0.02, 0.02	0.3*, 0.0025, 0.001	1.3, 0.042, 0.042
pH 8.8 desorption	1., 0.2, 0.2	3., 0.2, 0.01	1.3, 0.042, 0.042
150-355 μm material	k_f, ml/g-hr	k_r, hr⁻¹	S_m, μmol/g
pH 7.2 adsorption	1.8, 0.014, 0.014	0.3, 0.0025, 0.001	1.3, 0.042, 0.042
pH 6.9 desorption	1.8, 0.014, 0.014	0.0055, 0.0001, 0.0001	1.3, 0.042, 0.042
pH 7.2 desorption	1.8, 0.014, 0.014	0.3, 0.0025, 0.001	1.3, 0.042, 0.042
pH 8.8 desorption	1., 0.2, 0.2	3., 0.2, 0.01	1.3, 0.042, 0.042
355-500 μm material	k_f, ml/g-hr	k_r, hr⁻¹	S_m, μmol/g
pH 7.2 adsorption	1.3, 0.012, 0.012	0.3, 0.0025, 0.001	1.3, 0.042, 0.042
pH 6.9 desorption	1.3, 0.012, 0.012	0.0055, 0.0001, 0.0001	1.3, 0.042, 0.042
pH 7.2 desorption	1.3, 0.012, 0.012	0.3, 0.0025, 0.001	1.3, 0.042, 0.042
pH 8.8 desorption	1., 0.2, 0.2	3., 0.2, 0.01	1.3, 0.042, 0.042

Notes: In all cases, first number is for Site 1, second number is Site 2, and third number is Site 3.
Red text indicates values that were varied for different size fractions.
*The desorption rate constant for one of the three 75-150-μm columns was 0.35 hr⁻¹.

The results of the granodiorite column experiments using the 75-150-μm-sieved granodiorite are shown in Figure 5-12 along with model matches to the data. Figures 5-13 and 5-14 show the results and model matches for the experiments using the 150-355-μm-sieved and 355-500-μm-sieved granodiorite, respectively. Also shown in these figures are the simulated uranium injection functions that take into account uranium attenuation in the tubing and other column system components. The reaction parameters resulting in the model curves are listed in Table 5-11. Figure 5-15 shows the pH as a function of volume eluted in one of the 75-150-μm-sieved granodiorite columns.

The reaction parameters of Table 5-11 are in good agreement for a given sieve size fraction of the granodiorite, reflecting the good reproducibility of the experiments. They are also in relatively good agreement with each other for any of the size fractions, although there is some allowance for increasing the adsorption rates for the smallest sieve size fraction and decreasing the adsorption rates for the largest

size fraction because the rates should scale with specific surface area, which should be largest for the smallest size fraction. Slight differences in reaction parameters for the different replicate columns were also allowed in recognition that there were probably minor differences in both the porosities and the material heterogeneity in the columns. The only constraint provided by the short-duration batch adsorption experiments (Figure 5-7) was that the adsorption rate constant of the fastest adsorption reaction should be about 2 ml/g-hr (much faster or slower rate constants would result in a poor match to the batch data). The three-site model curves in Figure 5-7 were obtained using the same rates and site densities as in Table 5-11, so, in effect, these parameters match both the batch and column data.

Several points are worth discussing with respect to the reaction parameters of Table 5-11 and the uranium breakthrough curves of Figures 5-12 through 5-14. First, although these parameters provide good matches to the column data sets, they should not be considered unique. There are some known correlations between the parameters for a given site; for instance, very similar results can be obtained by increasing the surface site density and decreasing the adsorption rate constant for a site (particularly for sites that have relatively small surface densities to begin with) while keeping the desorption rate constant approximately the same for that site. Other combinations of parameters may also offer relatively good matches to the data.

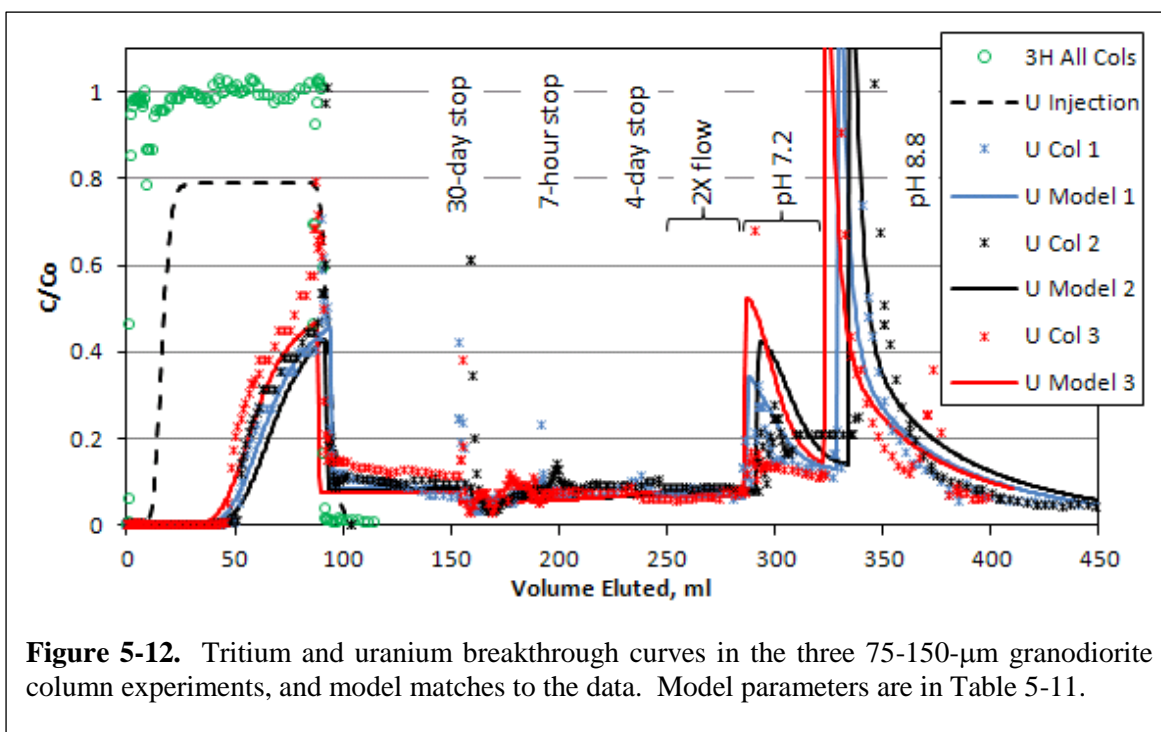
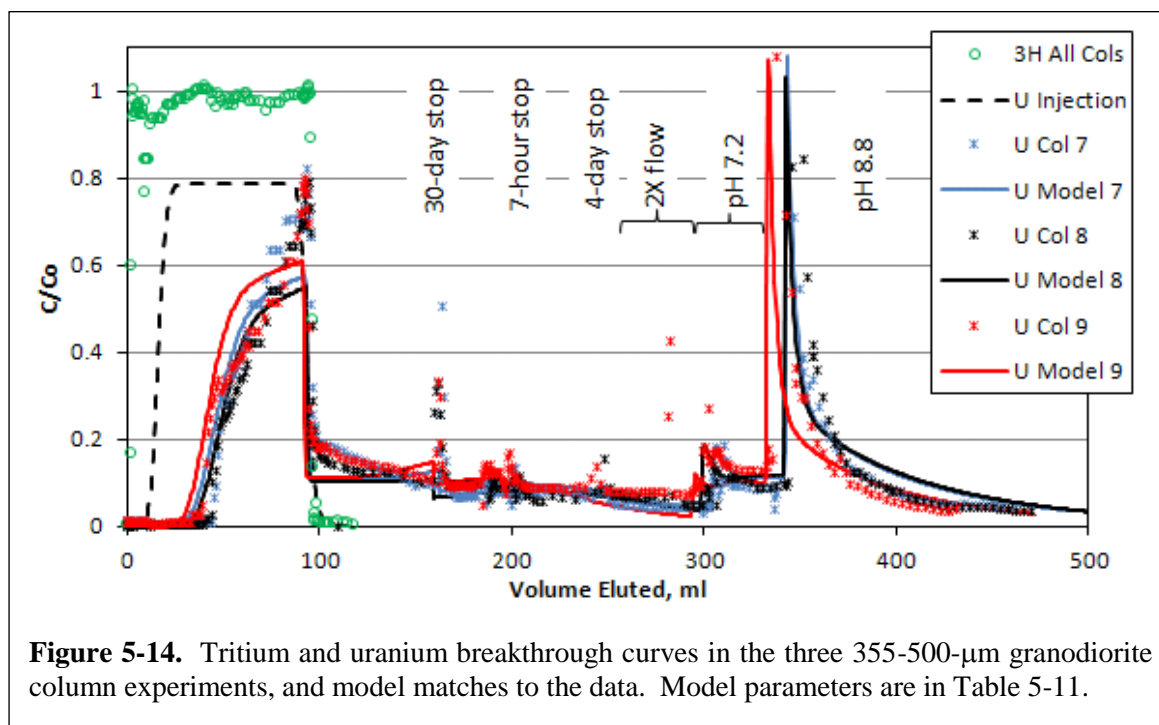
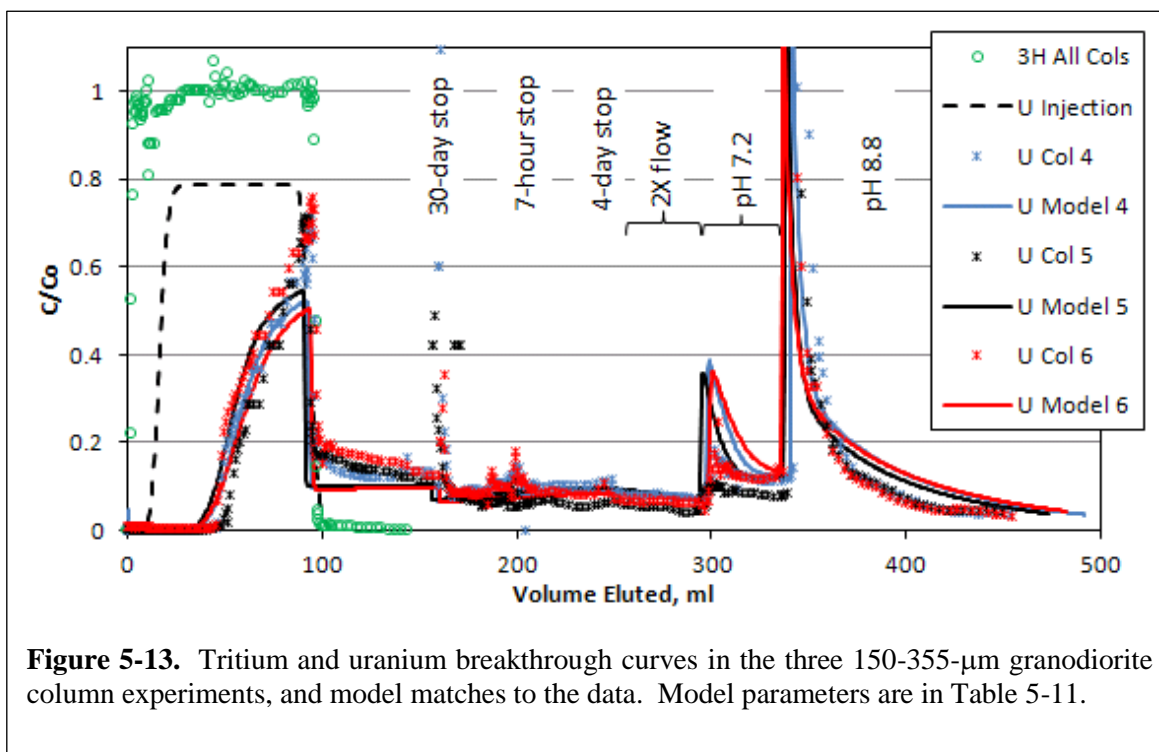


Figure 5-12. Tritium and uranium breakthrough curves in the three 75-150- μm granodiorite column experiments, and model matches to the data. Model parameters are in Table 5-11.



Second, it was found that for the model to capture the abrupt drop in uranium concentrations immediately after the transition from injection of uranium-bearing water to uranium-free water, the desorption rate constant for the fastest sorption site had to be decreased significantly at the time of the transition. It was simply not possible to model both the slow rise in uranium concentrations before the transition and the abrupt drop after the transition without a step decrease in the desorption rate constant. Imposing such a condition is essentially invoking adsorption-desorption hysteresis, with the desorption kinetics being significantly slower when solution concentrations are decreasing than when they are increasing. We note that the pH of the

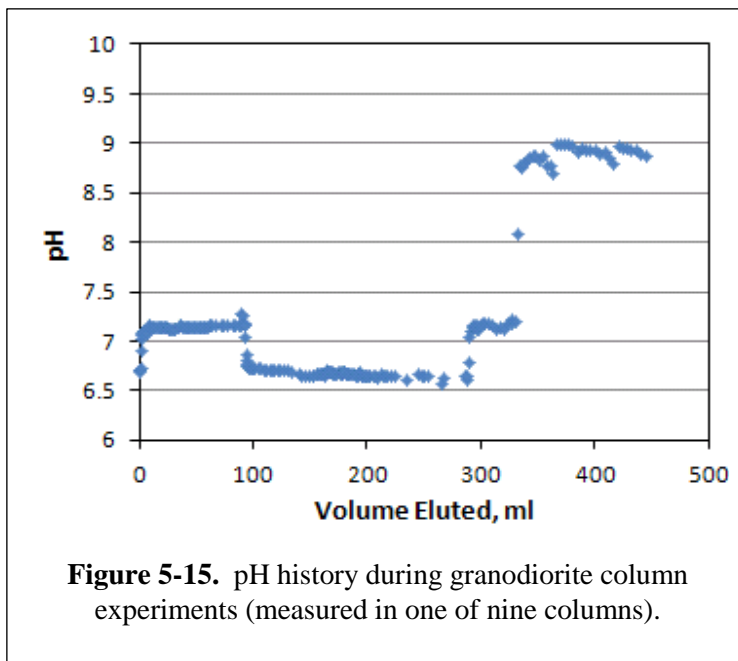


Figure 5-15. pH history during granodiorite column experiments (measured in one of nine columns).

uranium injection solution was slightly higher than the uranium-free water injected before and after the injection pulse (Figure 5-15), with the difference being about 0.4 pH units (7.2 vs. 6.8). This difference in pH may have contributed to the observed hysteretic behavior, as greater adsorption and slower desorption would be expected at the lower pH. We also note that the transition from high to low uranium injection concentrations frequently resulted in a short spike in uranium concentrations at the time of the transition, which we attribute to a pressure transient during the syringe change-out that likely resulted in some uranium mobilization, possibly from the tubing surfaces rather than the geologic media. These short spikes were consistently observed during this transition, and they occasionally occurred during other transitions as well.

Third, the flow interruptions and flow rate changes had relatively minor effects on the uranium concentrations, with the exception of the 30-day flow interruption, which resulted in a significant rebound in concentrations that the model did not capture. However, the 30-day interruption was unplanned (due to an unrelated contamination incident that prevented entry into the laboratory for 30 days), and much of the column outlet tubing dried out during this time, so when flow was re-established, it is very possible that the first water collected had artificially high uranium concentrations because of re-dissolution or possibly even colloidal transport of precipitated uranium in the tubing. Interestingly, the model predicted that the long flow interruption would actually result in an increase in uranium adsorption rather than desorption, and the slight dip in uranium concentrations observed after the initial spike after the flow interruption is consistent with this prediction. The two subsequent flow interruptions and the increase in the flow rate did not result in significant shifts in uranium concentrations, consistent with model predictions.

Fourth, increases in pH clearly promoted uranium desorption, although it was interesting that the increase to pH 8.8 did not result in extremely rapid or complete desorption of the uranium, which might be expected based on the fact that no uranium adsorption was observed in either the batch or column experiments conducted at pH 8.8. This result is consistent with the hysteretic adsorption-desorption behavior deduced during the transition from high to low injection concentrations of uranium at pH 6.9, as it suggests that uranium that had adsorbed to surfaces earlier was somewhat resistant to desorption. Even after an extended period of flow at pH 8.8, mass recovery calculations indicated the following fractions of

injected uranium still remained in the columns at the end of the experiments: 75-150 μm – 0.24, 0.23 and 0.19; 150-355 μm – 0.18, 0.28, 0.19; and 355-500 μm – 0.14, 0.17, 0.18. However, these fractions cannot be unequivocally attributed to the geologic materials because of the observed interactions of uranium with the system components (about 20% of the uranium injected into the columns was assumed to be held up by the column system components based on the results of the blank/control column experiments (Figure 5-11)).

FFM Column Experiments: The results of the two FFM column transport experiments conducted at pH 6.9 are shown in Figure 5-16, and the results of the control column experiments at this pH are shown in Figure 5-17. Model curves for the FFM experiments are also shown in Figure 5-16. The reaction parameters associated with the model curves are listed in Table 5-12. Figure 5-18 shows the pH exiting one of the two FFM columns as a function of volume eluted through the column. The parameters of Table 5-12, particularly for the uranium injection time period, are consistent with those for the three-site model in Table 5-10 from the FFM batch sorption experiments. This is not a coincidence, as the batch and column data sets were interpreted in parallel to obtain a set of parameters that matched both data sets. Figure 5-19 shows a comparison of the model curves during the pH 6.9 portion of the column tests using both the three-site model and a one-site model with reaction parameters that match the batch adsorption-desorption data. It is apparent that the three-site model offers a significantly better match to the rise in concentrations in the column experiments than the one-site model.

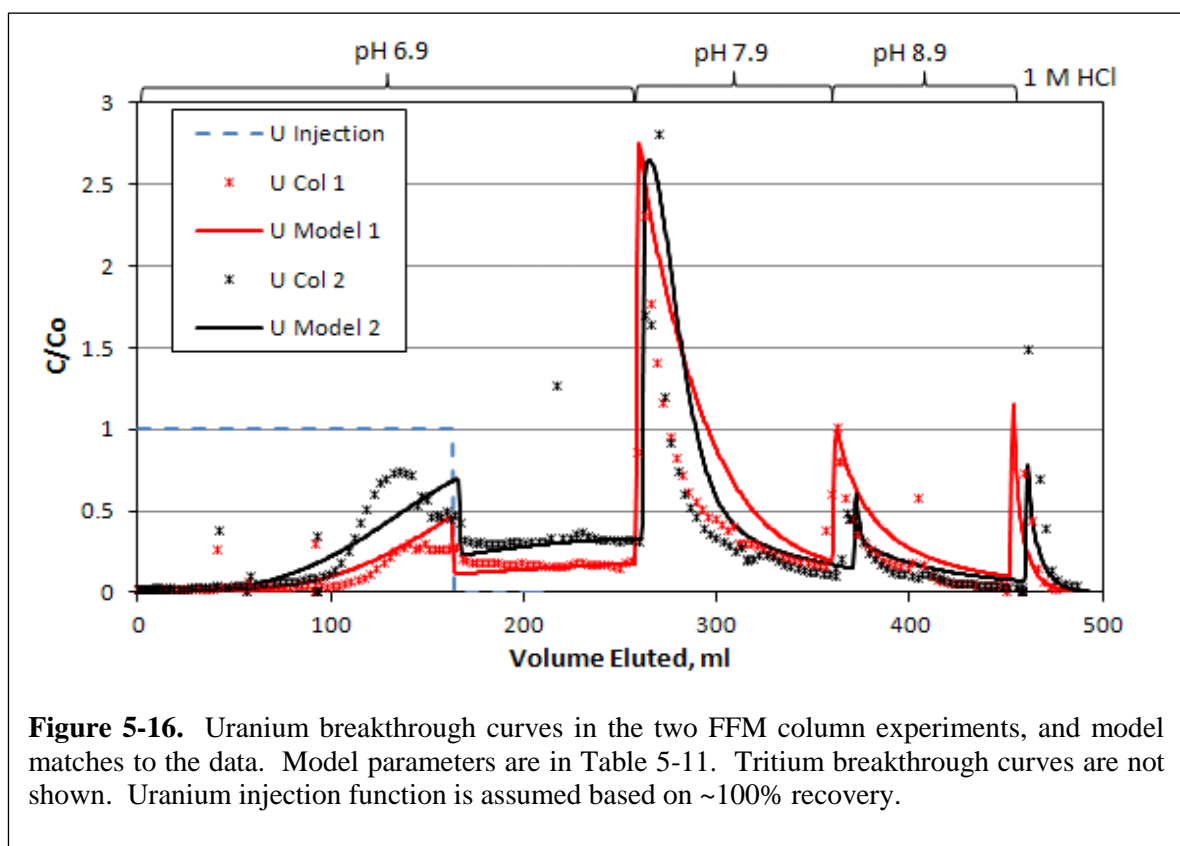


Table 5-12. Reaction model parameters yielding matches to both the batch and column FFM data (shown in Figures 5-8 and 5-16).

Column 1	k_f , ml/g-hr	k_r , hr ⁻¹	S_m , μmol/g
pH 6.9 adsorption	0.8, 0.1, 0.07	0.045, 0.003, 0.001	1.3, 0.104, 0.026
pH 6.9 desorption	0.8, 0.05, 0.05	0.009, 0.002, 0.001	1.3, 0.104, 0.026
pH 7.9 desorption	0.12, 0.05, 0.05	0.02, 0.0015, 0.0005	1.3, 0.039, 0.013
pH 8.8 desorption	0.2, 0.2, 0.2	0.16, 0.02, 0.01	1.3, 0.039, 0.013
1M HCl desorption	0.1, 0.2, 0.2	1., 0.5, 0.1	1.3, 0.039, 0.013
Column 2	k_f , ml/g-hr	k_r , hr ⁻¹	S_m , μmol/g
pH 6.9 adsorption	0.8, 0.1, 0.07	0.07, 0.003, 0.001	1.3, 0.104, 0.026
pH 6.9 desorption	0.8, 0.05, 0.05	0.02, 0.002, 0.001	1.3, 0.104, 0.026
pH 7.9 desorption	0.8, 0.05, 0.05	0.15, 0.005, 0.001	1.3, 0.039, 0.013
pH 8.8 desorption	0.2, 0.2, 0.2	0.4, 0.02, 0.01	1.3, 0.039, 0.013
1M HCl desorption	0.1, 0.2, 0.2	1., 0.5, 0.1	1.3, 0.039, 0.013
Batch Experiments	k_f , ml/g-hr	k_r , hr ⁻¹	S_m , μmol/g
pH 6.9	0.8, 0.1, 0.07	0.06, 0.003, 0.001	1.3, 0.104, 0.026
pH 7.9	0.8, 0.05, 0.05	0.4, 0.005, 0.001	1.3, 0.039, 0.013

Notes: In all cases, first number is for Site 1, second number is Site 2, and third number is Site 3. Red text indicates values that were varied for the two different columns.

Figure 5-16 shows that the two FFM columns had poorer reproducibility than the granodiorite columns, which we tentatively attribute to a greater degree of mineralogic heterogeneity of the FFM than the granodiorite. Also, the model matches to the rise in uranium concentrations during the FFM column experiments are qualitatively poor. The model was not capable of duplicating the peak in uranium concentrations followed by a drop before the transition to injection of uranium-free water. It is apparent that the three-site model offers a significantly better match to the rise in concentrations in the column experiments than the one-site model.

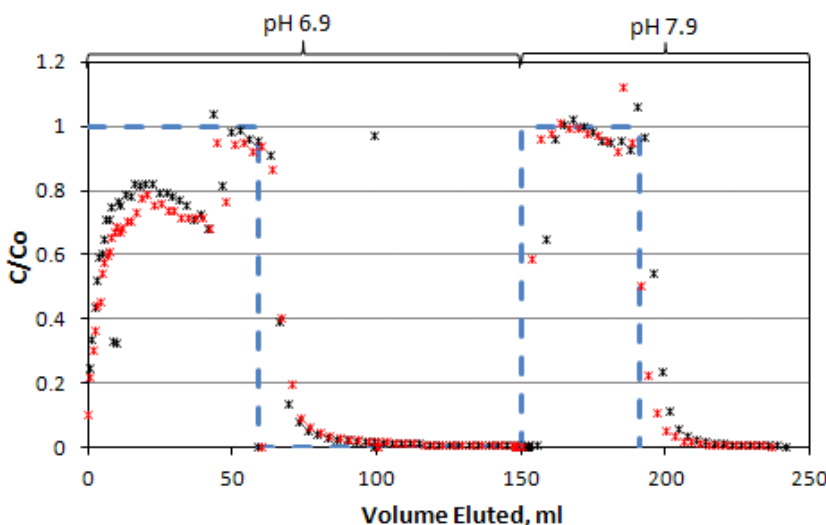


Figure 5-17. Uranium breakthrough curves in FFM control column experiments. Uranium injection pulses shown as blue dashed lines.

We believe that this peak must be the result of some unknown, but reproducible, peak in the uranium injection function during the tests that the model does not account for. The uranium breakthrough curves from the blank/control experiments (Figure 5-17) indicate that uranium concentrations were not steady during these tests, which we believe reflects either adsorption or precipitation occurring in the polypropylene syringes because the rest of the system was Teflon and no such reactions were apparent in the stock solution stored in a Teflon bottle. We suspect adsorption to the polypropylene rather than precipitation because of the Teflon bottle results. The sudden increase in uranium concentration as the syringes became nearly empty (Figure 5-

17) suggests that the movement of the plunger through the syringe may have caused uranium desorption from the syringe walls or perhaps resuspension of precipitates, which then moved out of the syringe as the plunger approached the end. Such behavior could have resulted in an early peak concentration in the FFM columns, especially considering that each FFM experiment involved the injection of nearly 3 full syringes of uranium-bearing water (so there would have been at least 2, and maybe 3, such pulses). However, we modeled the uranium injection function as an ideal pulse with a normalized injection concentration of 1.0 because essentially all the uranium that was injected (based on the starting concentrations in the syringes and the volume injected from the syringes) was recovered during the experiments after the 1 M HCl flush (see discussion below).

As with the granodiorite column experiments, hysteretic adsorption-desorption behavior was also observed in the FFM column experiments at the time of the transition from injection of uranium-bearing water to uranium-free water. However, the

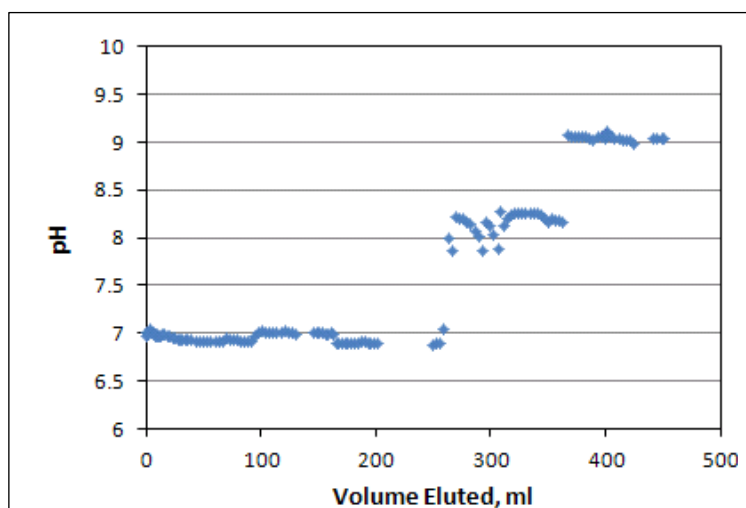


Figure 5-18. pH history during FFM column experiments (measured in one of two columns).

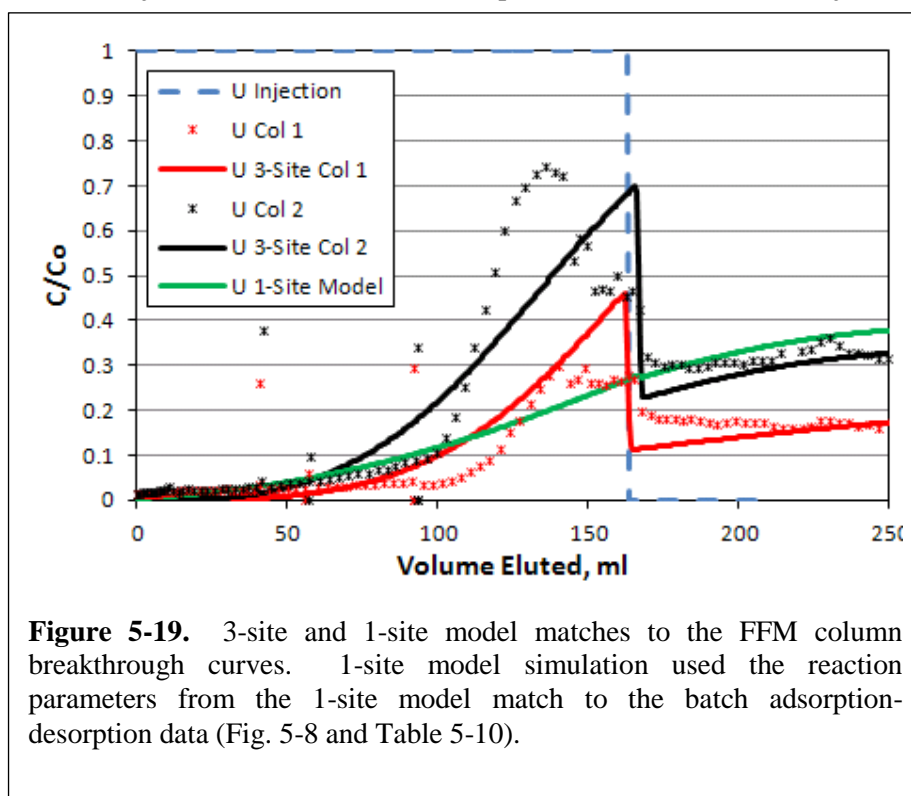


Figure 5-19. 3-site and 1-site model matches to the FFM column breakthrough curves. 1-site model simulation used the reaction parameters from the 1-site model match to the batch adsorption-desorption data (Fig. 5-8 and Table 5-10).

hysteresis was less pronounced than in the granodiorite experiments, with the decrease in uranium desorption rate constant (of the fastest reaction) being much smaller than in the granodiorite columns. The decreased hysteresis may be a result of better pH control of the injection solution in the FFM experiments, as shown in Figure 5-18 (compare to Figure 5-15). At first we thought that the pH increase during the granodiorite injections might be a result of surface complexation reactions consuming H^+ as UO_2^{2+} adsorbed to surfaces and left CO_3^{2-} behind to react with water to form HCO_3^- and OH^- . However, the lack of a pH increase during the injection into the FFM columns, where greater uranium attenuation was observed, suggests that the pH of the uranium-bearing solution injected into the granodiorite columns was probably high.

The pH increases to 7.9 and 8.8 in the FFM columns yielded qualitatively similar results to the granodiorite experiments, with both increases resulting in short spikes of desorbing uranium but with significant amounts of uranium remaining adsorbed. The 1 M HCl flush at the end of each experiment resulted in mass balance closures to within 3.5% of the injected uranium, which was considered to be full mass balance closure within the accuracy of the experimental measurements (both columns actually indicated slightly greater than 100% recovery). These results suggest that little, if any, uranium was left behind in the syringes despite the apparent attenuation in the blank/control column experiments, which indicated only 92-93% uranium recovery. The fraction of injected uranium remaining in the FFM columns prior to the acid flush was ~11% in the column with higher peak concentrations (during uranium injection) and ~27% in the column with the lower peak concentrations.

5.4 Discussion

We believe that we have made steady progress toward our goal of developing an experimental methodology to improve process models of radionuclide transport in nuclear waste repository environments. The FFM batch and column experiments are the most definitive set of experiments we've conducted so far, but we believe that we can make many additional improvements to the methods. While the granodiorite column experiments yielded valuable insights into the transport behavior of uranium in the Grimsel flow system, they were also very useful for identifying some of the potential artifacts and pitfalls that can creep into radionuclide transport experiments.

The general experimental insights from the work we've conducted to date include:

- If there are any doubts about potential unwanted interactions between radionuclides and experimental components, the components or their materials of construction should be screened in simple batch adsorption experiments.
- Blank/control column transport experiments involving the column components without any geologic materials should always be conducted in parallel with experiments containing geologic materials to identify any potential radionuclide interactions that could lead to erroneous and non-conservative experiment interpretations. However, even if radionuclide interactions with experimental components are identified after the fact or cannot be avoided, we have demonstrated a method of using the results of blank/control column experiments to construct injection functions that effectively account for these interactions, thus allowing quantitative interpretations of the experiments. Of course, the uncertainty in these interpretations is undoubtedly greater than in cases where radionuclide interactions with column materials can be ruled out.
- The small-scale columns that were used in our studies appear to be useful for conducting relatively rapid and inexpensive dynamic transport experiments that complement batch adsorption-desorption experiments very well. The combined use of the batch and column

transport experiments provides better constraints on adsorption and desorption kinetics than either method by itself. Batch experiments are useful for evaluating rapid adsorption kinetics because column experiments often cannot effectively interrogate fast kinetics (at least for the fastest adsorption reactions/sites). Once the adsorption kinetics are known from batch experiments, an important upper limit on desorption rates can be determined from either the leveling-off concentration in batch experiments or the arrival time (relative to a conservative tracer) in a column experiment. The leveling-off concentration or the column arrival time is proportional to the ratio of the adsorption rate constant to desorption rate constant (at least for the fastest reaction).

- Small-scale column experiments can be very useful for identifying the presence of additional sorption sites and their kinetic behavior. The concentration rise during the injection portion of a column experiment can provide useful constraints on adsorption rates and surface densities of sites with slower rates than the fastest reaction. However, adsorption rates and surface densities can be positively correlated, so the investigator needs to be aware of this. Interrogation of the reaction parameters associated with the slower sites can be improved by increasing the duration of the injection pulse to observe a longer approach to the injection concentration.
- The shape of the breakthrough curve in small-scale column experiments after the transition from injection of radionuclide solution to radionuclide-free solution can yield valuable insights into adsorption-desorption hysteresis behavior. A sharp drop in concentration at the time of this transition suggests hysteresis with slower desorption rates after the transition. Additionally, the tail of the breakthrough curve after the transition can provide useful constraints on desorption rates associated with different desorption sites (this was not clearly demonstrated in the experiments reported here because changes in solution pH were introduced before the tailing behavior was fully developed).
- Changes in flow rates or flow interruptions of various durations, particularly after the transition from injection of radionuclide-bearing water to radionuclide-free water, can be useful for interrogating adsorption-desorption kinetics in small-scale column experiments. The magnitude of an increase in concentration after a flow interruption or after a decrease in flow rate can provide information on desorption kinetics, although it can also indicate an influence of diffusion and/or adsorption-desorption behavior in secondary porosity in the column [13-14]. The magnitude of a decrease after a flow rate increase can provide the same information. The lack of any significant increase or decrease in concentration after a flow interruption or flow rate change suggests that adsorption and desorption rates are approximately equal at the time of the flow transient (and there are no dual-porosity effects). A decrease in concentration after a flow interruption indicates that adsorption rates are greater than desorption rates at the time of the interruption, which can occur even after the injection of radionuclide-free water if desorption rates are slow and there are still plenty of unoccupied sorption sites. This situation is believed to have occurred after the 30-day flow interruption in the granodiorite column experiments of this study.
- The small-scale column experiments are also useful for evaluating the influence of geochemical transients (e.g., pH in this study) on adsorption-desorption behavior. Responses to geochemical transients can yield valuable insights into adsorption-desorption mechanisms and hysteretic behavior.
- We note here that the same information could be obtained from larger-scale column experiments as from the “small-scale” column experiments we employed in this study, but we pursued the small-scale experiments because (1) they can be conducted more quickly and inexpensively than larger experiments, allowing more replication and/or variation of experimental parameters, and (2) they use much less geologic material than larger columns, which can be important when representative material is scarce (for example with the FFM).

The specific insights into uranium transport in the Grimsel system obtained during this study include:

- Uranium transport at pH 6.9 appears to be governed by adsorption to and desorption from multiple sites that have different kinetics. Although multiple sites were not necessary to match the batch adsorption-desorption data, the column transport experimental data could not be matched well without invoking multiple sites having different rates. While this is not a surprising result (it has been observed by others in different systems; Liu et al., 2008, 2013), our goals are to demonstrate the ability to better interrogate the kinetics of these different sites.
- Uranium appears to have hysteretic adsorption-desorption behavior in the Grimsel system at pH 6.9, with smaller desorption rates when uranium concentrations in solution are decreasing than when they are increasing. This result was revealed by the small-scale column transport experiments; it was not possible to deduce this from the batch experiments. Hysteretic uranium adsorption-desorption behavior has been observed by others [15-16].
- Hysteretic adsorption-desorption behavior was also apparent from the responses to pH changes in the column experiments. The desorption of uranium at pH 7.9 and 8.8 was slower than would have been predicted from batch or column experiments at these pHs. Indeed, no measurable adsorption was observed at pH 8.8 in either batch or column experiments, but when the pH was increased to 8.8 in the pH 6.9 column experiments, only a fraction of the uranium desorbed quickly, and a substantial fraction did not desorb at all during the time of the experiments. These results suggest that uranium that is adsorbed under geochemical conditions favorable for sorption may not necessarily desorb when geochemical conditions become unfavorable for sorption.
- The responses to the flow interruptions and flow rate changes in the granodiorite experiments (none were imposed in the FFM experiments) suggest that there was little difference in the overall rates of adsorption and desorption at the time of the transients (although the dip in concentration after the 30-day flow interruption suggests that there was a small amount of net adsorption occurring at this time). This result suggests that the conditions in the column were not far from a quasi-equilibrium or quasi-steady-state at the time of the transients, which further supports the inference of hysteretic adsorption-desorption behavior.
- The difficulty in simultaneously matching the data from batch adsorption-desorption experiments with different solid-mass-to-solution-volume ratios suggests that there were processes occurring that were not well captured by the model employed or that there were experimental biases resulting from the different ratios. These issues will be explored in future work.

The next steps we are considering to further develop and improve the methods we have developed so far are:

- Evaluate the advantages of doing multiple desorption steps (i.e., multiple replacements of solution) during batch adsorption-desorption experiments instead of just one desorption step (one solution replacement). Our experience has been that multiple desorption steps or even continuous flow desorption experiments involving material that was subjected to batch adsorption [17-18] can place better constraints on multiple desorption rates than a single desorption step. We believe hysteresis could also be better observed and quantified with multiple desorption steps or continuous flow during desorption.
- Conduct batch adsorption-desorption experiments with desorption starting after different periods of adsorption so that the influence of adsorption time on desorption kinetics can be investigated. These types of experiments would be ideal for evaluating so-called “bond-aging” effects [15].

- Allow longer times for desorption under a given set of geochemical conditions in the column experiments before changing the geochemistry so that the tails of the breakthrough curves can be more fully developed to place better constraints on desorption kinetics under these conditions.
- Conduct uranium column experiments with the FFM at pH 7.9 (instead of 6.9) where weaker adsorption will allow experiments to be conducted more rapidly and where there will be less uranium interaction with column components than at pH 6.9. We have already started experiments at pH 7.9 where we know there are negligible interactions between the uranium and the polypropylene syringes (Figure 5-17). These experiments are also more relevant to radionuclide-geologic material systems exhibiting weak adsorption, for which the experimental methodology being developed here will have greater applicability and benefits. Radionuclides exhibiting strong adsorption are much less likely to contribute to geologic repository risk than weaker-sorbing radionuclides, and repository risk assessments are much less sensitive to small differences in reaction parameters of strongly-sorbing radionuclides than they are for weaker-sorbing radionuclides.
- Conduct both batch sorption-desorption experiments and column transport experiments using uranium at lower starting/injection concentrations to evaluate the dependence of adsorption-desorption behavior on concentration. We believe that the concentration dependence of the experimental results (or lack thereof) will yield insights into the surface site densities of slower sorption sites, thus helping to constrain both this reaction parameter and adsorption rate constants (which are correlated with surface densities) for these sites. This is one of the reasons that we have been using uranium at relatively high concentrations in experiments so far and also why we have been using natural uranium spiked with approximately 2% ^{233}U , which allows us to easily decrease overall uranium concentrations without sacrificing analytical sensitivity. As an example, Figure 5-20 shows a predicted result from a uranium FFM column experiment conducted with a one order of magnitude lower injection concentration than the experiments of Figure 5-16 using the reaction parameters that yielded a good match to the higher-concentration data. If this predicted result is not approximated in the experiments at lower injection concentration, then the reaction parameters should be modified to try to simultaneously match the data sets at both injection concentrations.
- Conduct column experiments in which a second injection pulse of uranium is introduced at some time after a first pulse has been desorbing. This type of experiment would further evaluate the

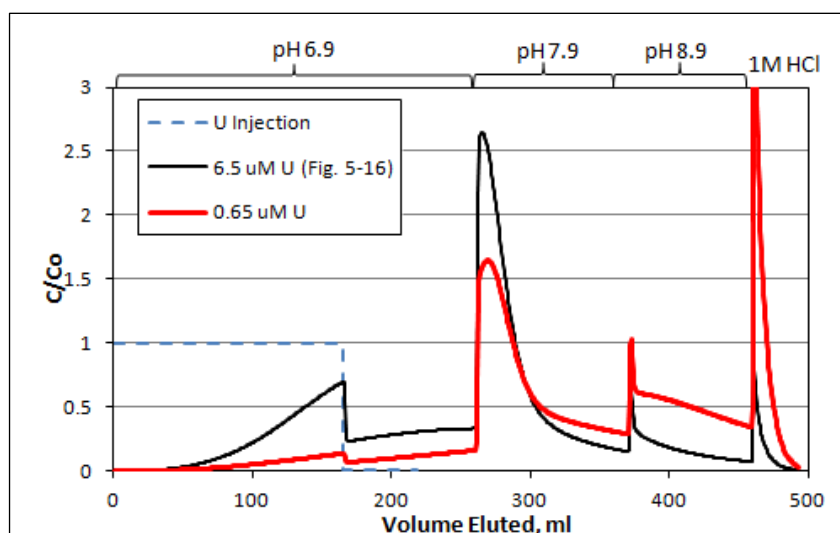


Figure 5-20. Model prediction for FFM column experiment (in column 2) with a one-order of magnitude lower uranium injection concentration (red curve) compared to the model result shown in Fig. 5-16 (black curve).

hysteretic adsorption-desorption behavior of uranium, and it would also place additional constraints on the surface densities of different sites. Higher-concentration pulses could also be injected after low concentration pulses without any intervening desorption period to evaluate how significant site occupancy affects subsequent adsorption and desorption kinetics.

- Conduct column experiments at different flow rates to better elucidate adsorption-desorption reaction kinetics.
- Measure Brunauer-Emmet-Teller (BET) gas-adsorption surface areas of the experimental materials so that the different observed rates of adsorption can be correlated to surface area per unit volume in different experiments. Also, surface area measurements will be useful for conducting reality checks on our assumed surface site densities. Davis and Curtis [6] used a maximum uranium sorption site density of $1.92 \mu\text{moles/m}^2$ on silicate surfaces based on the recommendations of Davis and Kent [19]. In our modeling we assumed $\sim 1.3 \mu\text{moles/g}$ as a maximum surface site density, which implies a specific surface area of $\sim 0.68 \text{ m}^2/\text{g}$ (i.e., $1.3/1.92$) to be in agreement with the value used by Davis and Curtis [6].
- Modify the reaction expressions in the model(s) to simulate the surface transition of adsorbed radionuclides from one type of site to another type of site that has different desorption kinetics. With the current reaction expressions, site transitions occur only when desorption occurs from one site followed by adsorption onto another site. We believe that direct surface transitions, which can simulate bond-aging reactions on surfaces, may help capture the hysteretic behavior observed in the column experiments as well as the dependence of batch adsorption-desorption experiments on solid-mass-to-solution-volume ratios.
- Implement automated parameter estimation algorithms to streamline and quantify the model matches to the experimental data sets, including quantitative assessments of reaction parameter sensitivity and uncertainty.

This report would not be complete without a brief discussion of the implications of the results to date as well as the motivation for future work. Figure 5-21 shows uranium transport predictions for a step-function input over much longer time and distance scales than in our experimental studies (a water residence time of 2000 hours instead of just 7-8 hours); i.e., over scales more relevant for repository performance or risk assessments. These predictions make use of the uranium-FFM reaction parameters obtained in this study at pH 6.9 (Tables 5-10 and 5-12), including both the single-site model parameters that yielded a reasonable match to the batch adsorption-desorption data, and the three-site model parameters that yielded a reasonable match to both the batch and column data. For each

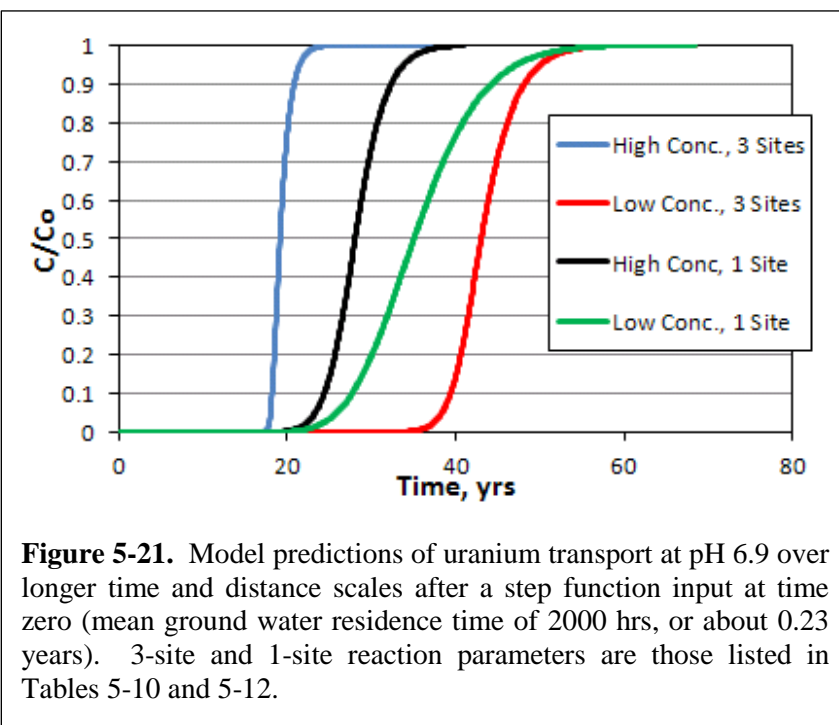


Figure 5-21. Model predictions of uranium transport at pH 6.9 over longer time and distance scales after a step function input at time zero (mean ground water residence time of 2000 hrs, or about 0.23 years). 3-site and 1-site reaction parameters are those listed in Tables 5-10 and 5-12.

model (1-site and 3-site), two inlet step concentrations are simulated; a high concentration equivalent to $6.5 \mu\text{M}$, and a low concentration equivalent to $0.65 \mu\text{M}$. It is apparent that the three-site model has much greater dependence on the inlet concentration than the single-site model, with significantly more attenuation at lower concentrations than the single-site model but less attenuation than the single-site model at higher concentrations. We note that the desorption rate constants and surface densities of the slower sites in the 3-site model are not well constrained by the data collected to date, so refinement of these parameters

could have a profound influence on the 3-site model predictions. The implications of obtaining better estimates of these reaction rate parameters are one of the motivations for our work.

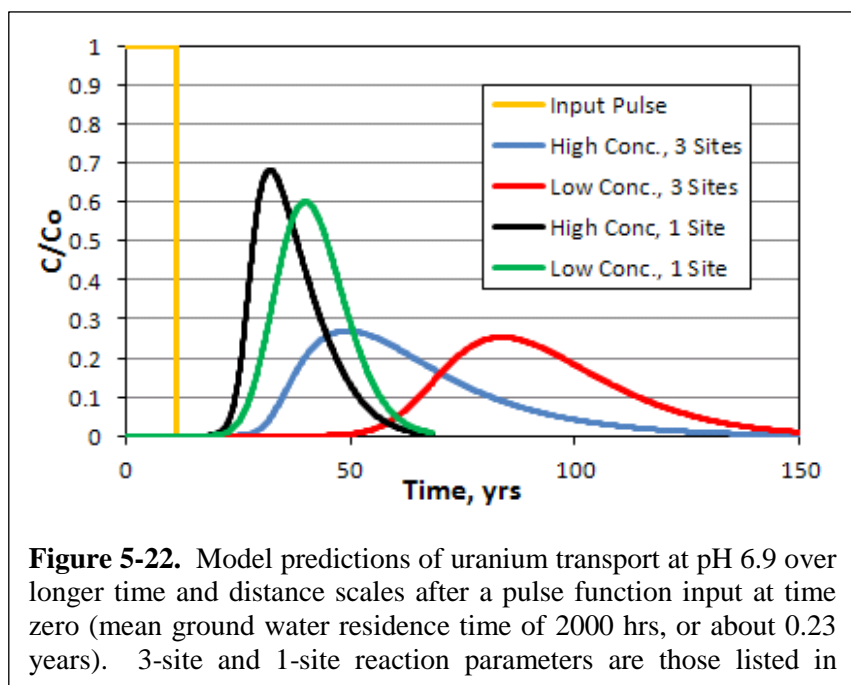


Figure 5-22. Model predictions of uranium transport at pH 6.9 over longer time and distance scales after a pulse function input at time zero (mean ground water residence time of 2000 hrs, or about 0.23 years). 3-site and 1-site reaction parameters are those listed in

Figure 5-22 shows uranium transport predictions for a finite injection pulse input instead of a step-function input using the same reaction parameters, inlet concentrations and flow system parameters as in Figure 5-21 (i.e., mean residence time of 2000 hours). A finite pulse might be more representative of a single waste package failure that releases a short burst of radionuclide mass into the natural system in a repository environment. In Figure 5-22, the 3-site model includes the experimentally-observed effects of adsorption-desorption hysteresis while the single-site model does not. It is clear that the hysteretic behavior has a beneficial impact on the concentration history observed at the downgradient location. In this case, both the high and low concentration injection pulses are more attenuated in the 3-site model than in the single-site model. These results provide additional motivation for our attempts to better parameterize slow desorption kinetics and also to accurately describe hysteretic adsorption-desorption behavior in process models.

5.5 References

- (1) Mōri, A. (Ed.), 2004. The CRR final project report series 1: Description of the Field Phase – Methodologies and Raw Data. *Nagra Technical Report NTB 03-01*. Nagra, Wettingen, Switzerland.
- (2) Good, N. E., Winget, G. D., Winter, W., Connolly, T. N., Izawa, S., Singh, R. M. M. 1966. Hydrogen ion buffers for biological research. *Biochemistry*, **5**(2), pp. 467-477.
- (3) Giammar, D. E. and Hering, J. G., 2001. Time scale for sorption-desorption and surface precipitation of uranyl on Goethite. *Env. Sci. Tech.*, **35**(16), pp. 3332–3337.
- (4) Waite, T. D., Davis, J. A., Payne, T. E., Waychunas, G. A., and Xu, N., 1994. Uranium(VI) adsorption to ferrihydrite – Application of a surface complexation model. *Geochim Cosmochim. Acta*, **58**(4), pp. 5465-5478.

- (5) Echevarria, G., Sheppard, M. I., and Morel, J. L., 2001. Effect of pH on the sorption of uranium in soils. *J. Env. Radioactivity*, **53**(2), pp. 257-264.
- (6) Davis, J. A. and Curtis, G. P., 2003. Application of Surface Complexation Modeling to Describe Uranium(VI) Adsorption and Retardation at the Uranium Mill Tailings Site at Naturita, Colorado, *NUREG/CR-6820*, United States Geological Survey (for Nuclear Regulatory Commission), Menlo Park, CA.
- (7) Joseph, C., Stockmann, M., Schmeide, K., Sachs, S., Brendlet, V., and Bernhard, G., 2013. Sorption of U(VI) onto Opalinus clay: Effects of pH and humic acid. *Applied Geochemistry*, **36**, pp. 104-117.
- (8) Parkhurst, D. L. and Appelo, C. A. J., 2013. PHREEQC (Version 3.0.4) - A computer program for speciation, batch speciation, one-dimensional transport, and inverse geochemical calculations, U.S. Geological Survey Techniques and Methods, Book 6, Chapter A43, 497 p., <http://pubs.usgs.gov/tm/06/a43/>.
- (9) Johnson, J., 2010. Inl.dat 4023 2010-02-09. Data from 'thermo.com.V8.R6.230' prepared by Jim Johnson at Lawrence Livermore National Laboratory, in Geochemist's Workbench format. Converted to PHREEQC format by Greg Anderson with help from David Parkhurst.
- (10) Dong, W. and Brooks, S., 2006. Determination of the formation constants of ternary complexes of uranyl and carbonate with alkaline earth metals (Mg^{2+} , Ca^{2+} , Sr^{2+} , and Ba^{2+}) using anion exchange method. *Env. Sci. Tech.*, **40**(15), pp. 4689-4695.
- (11) Kersting, A., Zavarin, M., Zhao, P., Dai, Z., Carroll, S. A., Wang, Y., Miller, A., James, S., Remus, P., Zheng, L., Li, L., Rutqvist, Liu, H., Birkholzer, J., 2012, Radionuclide Interaction and transport in Representative Geologic Media, FCRD-UFD-2012-000154.
- (12) Doherty, J.E., 2009. *Manual for PEST: Model Independent Parameter Estimation*, in: J.E. Doherty (Ed.). Watermark Numerical Computing, Brisbane, Australia, p. 336.
- (13) Doherty, J.E., 2010. *Addendum to the PEST Manual*, in: J.E. Doherty (Ed.). Watermark Numerical Computing, Brisbane, Australia, p. 131.
- (14) Liu, C., Zachara, J. M., Qafoku, N. P., and Wang, Z., 2008. Scale-dependent desorption of uranium from contaminated subsurface sediments. *Water Resour. Res.*, **44**(8), DOI: 10.1029/2007WR006478
- (15) Liu, C., Shang, J., Kerisit, S., Zachara, J. M., and Zhu, W., 2013. Scale-dependent rates of uranyl surface complexation reaction in sediments. *Geochim Cosmochim. Acta*, **105**, pp 326-341.
- (16) Kaplan, D. I., and Serkiz, S. M., 2004. Quantification of thorium and uranium sorption to contaminated sediments. *J. Radioanal. Nucl. Chem.*, **248**(3), pp. 529-535.
- (17) Missana, T., Garcia-Gutierrez, M., and Alonso, U., 2004. Kinetics and irreversibility of cesium and uranium sorption onto bentonite colloids in a deep granitic environment. *Appl. Clay Sci.*, **26**, pp. 137-150.
- (18) Dean, C.A., 2010. Long-term desorption of uranium and neptunium in heterogeneous volcanic tuff materials, *Ph.D. Dissertation*, Chemical and Nuclear Engineering Department. University of New Mexico, Albuquerque, NM.
- (19) Arnold, B. A., Reimus, P. W., and James, S. C., 2011. Flow and Transport in Saturated Media: FY2011 Status Report. Prepared for U.S. Department of Energy Used Fuel Disposition Campaign, *FCRD-USED-2011-000311*, Sandia National Laboratories and Los Alamos National Laboratory.

- (20) Davis, J.A. and Kent, D. B., 1990. Surface Complexation Modeling in Aqueous Geochemistry, *Mineral-Water Interface Geochemistry*, Reviews in Mineralogy Series, Mineralogical Society of America, Vol. 23, pp. 177-260.

6.0 Stability of Intrinsic Pu colloids in the Presence of Montmorillonite at 25 and 80 °C: High-fired and freshly prepared PuO₂ oxides

6.1 Introduction

Plutonium (Pu) is one of the dominant long-term dose contributors for any high-level nuclear waste repository because of its toxicity, long half-life (²³⁹Pu half-life = 24,100 yrs.) and current inventory (estimated at >2000 metric tons worldwide) [1]. In an effort to design a long-term barrier system for the safe disposal of nuclear waste, it is important to understand how Pu may migrate in the natural system once it breaches the waste package. Determining the fate and transport of Pu depends not only on the initial chemical form at the source but also the geochemistry and hydrology of the source location and along the down-gradient transport paths. Colloid-facilitated transport of low levels of Pu in both groundwater and surface water has been documented at several DOE sites [2-3]. Pu sorbed to iron oxide colloids has also been detected over 4 km from its original source in Mayak, Russia [4]. These field studies indicate that the Pu associated with mobile colloids has moved on the scale of kilometers, yet the mechanisms are not well understood. Without a conceptual understanding of the dominant processes and a quantitative understanding of the relevant reaction chemistry, current transport models cannot effectively predict Pu concentrations and transport rates in the field.

Pu can be associated with the colloidal fraction of groundwater in two different forms. Pu can migrate as either an intrinsic colloid or sorbed to naturally occurring inorganic, organic or microbial species (called pseudocolloids). At “high” concentrations where actinide ions in solution exceed their solubility, Pu can hydrolyze to form intrinsic colloids (sometimes called eigen-colloids) [5-6]. In the case of Pu, the solubility-limiting concentration may be as low as $\sim 10^{-10}$ M under ambient conditions [6]. Intrinsic Pu colloid transport will be controlled by the stability (both physical and chemical) of the colloid. In contrast, if Pu is sorbed to inorganic or organic colloids, resulting in the formation of a pseudocolloid, transport will be determined by Pu sorption/desorption rates on the colloidal material. Efforts to model the transport of Pu from a near-field to a far-field environment are currently limited due to the lack of understanding of how intrinsic Pu colloids will persist along a changing geochemical flow path away from a high-level nuclear waste repository where intrinsic Pu colloids are most likely to form [7].

In addition to a broad range of geochemical processes and conditions that can affect the overall stability of intrinsic Pu colloids once they are formed, the initial formation conditions may also play a critical role in their long-term stability (e.g. temperature, pH, isotopic composition). Previous investigations on Pu(IV) colloids show that the ultimate morphology is strongly dependent on the conditions of formation and age of solution [8]. In particular, the degree of crystallinity, which can be affected by aging, temperature and original formation conditions, will affect the stability of intrinsic Pu colloids [9]. Published thermodynamic data for Pu(IV) oxide and hydroxide show a range of $\log_{10}K_{s,0}$ values for PuO₂(hyd) and PuO₂(cr) from -50.2 to -58.8 and -60.2 to -64.0, respectively. These data illustrate how crystallinity can have a significant impact on the solubility and stability of PuO₂. Radiation effects from ²³⁸Pu have been reported to damage the crystallinity of PuO₂ that can lead to an increased solubility as well [10].

The objective of this work is to 1) better understanding of radionuclide interaction with geomedial (topic P10), and 2) develop new perspectives on colloid-facilitated radionuclide transport (topic P11). In this current study, we investigated the long-term stability of three different forms of intrinsic Pu colloids, all formed under elevated temperature conditions.

- High-fired Pu oxide, 300°C (Wilk#1)
- High-fired Pu oxide, 800°C (Wilk#2)
- 2-yr old aged intrinsic Pu colloids prepared in an acidic solution.

Results from this study are compared to dissolution rates of both fresh and aged colloids prepared in a basic solution and investigated in FY11 and FY12.

6.2 Previous Work

In FY2011 and FY2012, we examined the long-term stability of intrinsic Pu colloids that were prepared in a dilute basic solution. The long-term stability of both freshly prepared and aged (~1 year) intrinsic Pu colloids was examined. The intrinsic Pu colloids were prepared by neutralizing Pu(IV) stocks using NaOH solution and adjusting the pH to between 9 and 10. This is the same method used to prepare amorphous PuO₂ for the solubility studies performed by Neck *et al.* [6]. After aging for approximately a week, the intrinsic Pu colloids were centrifuged and the supernatant was removed. A dilution of the intrinsic Pu colloids (3×10^{-5} M) in pH 8 buffer solution was used for stability experiments investigated in FY2011. In FY2012, we repeated some of the experiments with the same intrinsic Pu colloids. However, at that point, the intrinsic Pu colloids had been aged for ~1 year. We did not see any difference in our colloid stability experiments, indicating that sample aging had no effect on intrinsic Pu colloid stability. Complete details for the intrinsic Pu colloid preparation can be found in Kersting *et al.* [7].

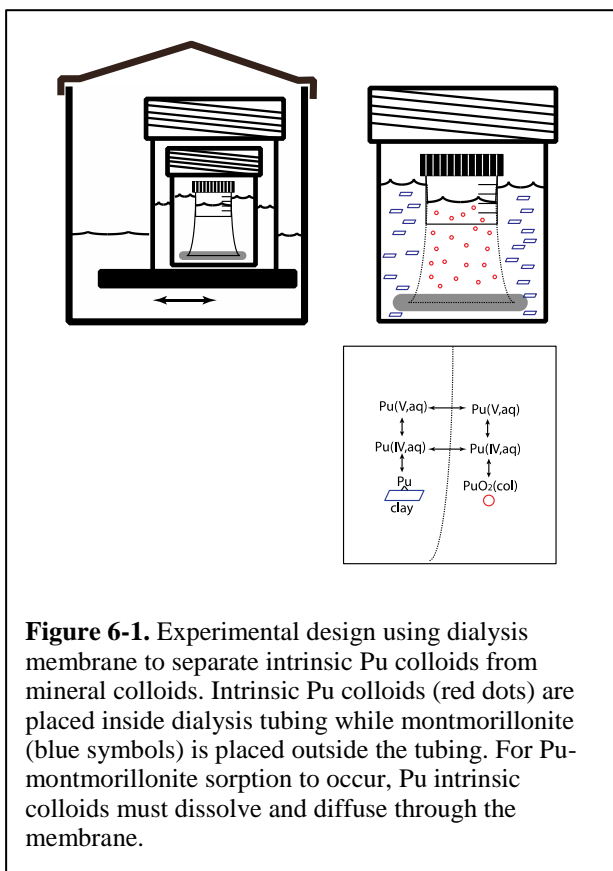


Figure 6-1. Experimental design using dialysis membrane to separate intrinsic Pu colloids from mineral colloids. Intrinsic Pu colloids (red dots) are placed inside dialysis tubing while montmorillonite (blue symbols) is placed outside the tubing. For Pu-montmorillonite sorption to occur, Pu intrinsic colloids must dissolve and diffuse through the membrane.

6.3 Technical Approach

In all of the studies described herein, we used dialysis membranes to test the stability of intrinsic Pu colloids. Dialysis membranes are commonly used to separate suspended solutes or particles of different dimensions in a liquid mixture. Desirable size separation can be achieved by selecting an appropriate membrane pore-size molecular weight cutoff (MWCO). In our experiments, we used membranes with a MWCO of 0.5 to 6 kilo Daltons (kDa), approximately equivalent to a 1 to 2-nm pore size. This MWCO was found to effectively retain intrinsic Pu colloids. Thus, if intrinsic Pu colloids are placed inside the membrane, any Pu found outside of the membrane could be attributed to the “dissolution” of intrinsic Pu colloids. This dissolution, in turn, reflects the stability of the intrinsic Pu colloids. By monitoring solution conditions as a function of time, we are also able to quantify the rates of intrinsic Pu colloid dissolution. Here and in previous experiment, intrinsic Pu colloid stability was examined at two temperatures: 25 and 80°C.

The design of the intrinsic Pu colloid stability experiments is shown in Figure 6-1. Briefly, intrinsic Pu colloids in a pH 8 solution are placed inside a dialysis bag. To avoid solubility limited

dissolution, an “infinite” sink for dissolved Pu is needed. In our case, this is provided by montmorillonite clay that is placed outside the dialysis bag in a pH 8 buffer solution. The montmorillonite clay and the intrinsic Pu colloids are isolated from each other by the dialysis membrane. Over time, Pu detection outside the dialysis membrane represents dissolution of the intrinsic Pu colloids and diffusion of aqueous Pu across the dialysis membrane. The aqueous Pu that diffuses across the membrane can either remain in solution or sorb onto the montmorillonite. However, the large amount of montmorillonite ensures that the majority of Pu will be sorbed. The stability of intrinsic Pu colloids is expected to be a function of solution conditions, temperature, and composition/crystallinity of the colloids. The sorption rate of Pu to montmorillonite will be affected by the aqueous Pu oxidation state, solution conditions, and temperature. In the experiments described below, only the temperature and the composition/crystallinity of the Pu colloids was varied.

High-fired ^{239}Pu oxides: The high-fired Pu oxides were made for this project using reactor fuel grade Pu oxide. The starting material was dissolved in concentrated nitric acid containing a small admixture of HF. After filtering, Pu was converted to the +3 oxidation state using a mixture of hydroxylamine (NH_2OH) and dilute nitric acid. Hydrated Pu(III) oxalate was then precipitated by the addition of oxalic acid or sodium oxalate. The Pu(III) oxalate was precipitated from 3 M nitric acid solution. The precipitate was allowed to digest for 30-60 minutes, filtered, washed with DI water, alcohol, and then dried under vacuum at room temperature. The final step was to calcine the dehydrated precipitates at temperatures of either 300°C (sample Wilk#1) or 800°C (sample Wilk#2) to convert Pu(III) oxalate to PuO_2 . More details regarding the preparation and characterization of these high-fired Pu oxides can be found in Isselhardt and Hutcheon (2012)(Isselhardt and Hutcheon 2012). To prepare the samples for our stability experiments, the Pu oxide powders were suspended in Milli-Q water and allowed to settle for 10 minutes prior to discarding supernatants that contained PuO_2 fines. An average particle size of $4\ \mu\text{m}$ was measured by SEM for samples Wilk#1 and Wilk#2. However, Wilk#1 also contained a significant number of smaller particles that were submicron in size (Figure 2a). The Milli-Q water rinse was repeated three times and the final concentration of the two high-fired Pu oxide suspensions was determined using beta liquid scintillation counting (LSC).

Intrinsic Pu colloids prepared in acidic solution: A ^{242}Pu stock solution that consists of alpha emitters ^{238}Pu , ^{239}Pu , ^{240}Pu , and ^{242}Pu with activity percentages of 15.8%, 0.062%, 5.0%, and 79.1%, respectively, was purified using an AG1x8 100-200 mesh anion exchange resin column. The intrinsic Pu colloids were prepared by heating 1.6×10^{-3} M Pu(IV, aq) solution in 0.1 M HNO_3 on a hotplate at $60\text{-}80^\circ\text{C}$ for 30 min. The dark brown Pu(IV) solution turned to green immediately upon heating. The formation of intrinsic Pu colloids was confirmed by UV/Vis. The fraction of soluble Pu in the intrinsic Pu colloid solution was determined to be $< 0.2\%$ using a 3kDa NMWL (Nominal Molecular Weight Limit) ultracentrifugal filter. After aging for two years, a dilution of the Pu colloids (Pu concentration of 3×10^{-5} M) was made in pH 8 buffer solution and used in our experiments.

Montmorillonite Preparation: SWy-1 Montmorillonite from the Clay Minerals Society was used in our experiments. Detailed summary on the preparation of the homoionic Na-montmorillonite can be found in Kersting et al. (2012). The prepared clay minerals were then suspended in Milli-Q water and centrifuged to obtain the fraction of particle sizes from 50 nm to 2 microns.

Determinations of Pu concentrations: Two different Pu sources (^{242}Pu and reactor fuel grade Pu oxide) were used in this study. For the intrinsic Pu colloids made from ^{242}Pu , alpha liquid scintillation counting (LSC) was used to determine Pu concentrations. The reactor fuel grade Pu oxide contained ^{241}Am , the daughter of ^{241}Pu , as a predominant alpha emitter. ^{241}Am contributed $> 90\%$ of the total alpha activity in the samples. Therefore, it was not possible to use alpha LSC to measure Pu concentrations. To solve this problem, we first quantified the Pu isotopic composition of the samples. The reactor fuel grade Pu oxide

was dissolved and Pu was isolated from ²⁴¹Am using two AG1x8 resin columns. A NuPlasma HR MC-ICP-MS was used to measure the following Pu isotopic ratios: ²⁴⁰Pu/²³⁹Pu, ²⁴¹Pu/²³⁹Pu, and ²⁴²Pu/²³⁹Pu. Alpha spectrometry was used to measure activity ratio of ²³⁸Pu/²³⁹⁺²⁴⁰Pu. The combination of these data provided an exact Pu isotopic composition of the reactor fuel grade Pu oxide. To measure the rate of reactor fuel grade Pu oxide dissolution, we measured the beta LSC activity to determine ²⁴¹Pu concentration in solution. The Pu isotopic ratios obtained from alpha spectrometry and MC-ICP-MS were used to determine the total Pu concentration. For beta LSC quantification, a ²⁴¹Pu quenching curve was generated from a NIST traceable standard.

Dialysis Experiments: A total of 7 dialysis experiments were successfully performed to investigate the stability of intrinsic Pu colloids in the presence of montmorillonite and compared to the experimental results of previous experiments performed in FY11 and FY12. Experiments were performed at 25°C (4 experiments) and 80°C (3 experiments) to evaluate the effect of temperature on colloid stability. At each temperature, intrinsic Pu colloids were added to the inside of the dialysis bag. The initial Pu concentrations in the dialysis bags were above the solubility of PuO₂(am) at pH 8 reported by Neck et al. [6]. For each experiment, the initial Pu concentration inside the dialysis bag along with other experimental parameters is listed in Table 6-1.

Table 6-1. Conditions of intrinsic Pu colloid stability experiments at 25 and 80 °C.

	Expt	Pu Oxide used	Initial Pu conc.	Montmorillonite	medium that forms	Temp. when PuO ₂ formed
			M	g/L	PuO ₂	
25 °C	1	formed in dilute acid	3.9×10 ⁻⁵	1	0.1 M HNO ₃	70 °C
	2	Wilk#1	2.1×10 ⁻⁷	1	3 M HNO ₃	300 °C
	3	Wilk#2	2.1×10 ⁻⁷	1	3 M HNO ₃	800 °C
	4	formed in dilute base	1.3×10 ⁻⁸	1 1	pH9 solution	25 °C
80 °C	5	formed in dilute acid	3.4×10 ⁻⁵	1	0.1 M HNO ₃	70 °C
	6	Wilk#1	2.1×10 ⁻⁷	1	3 M HNO ₃	300 °C
	7	Wilk#2	2.1×10 ⁻⁷	1	3 M HNO ₃	800 °C

Note: In this study, experiment #4 used intrinsic Pu colloids prepared in a basic solution to verify that the experimental set-up and conditions in this study are the same as in FY11 and FY12.

All batch experiments were conducted in 450-mL Teflon jars with air-tight closures. A volume of 235 mL of pH 8 buffer solution (pH 8, 5 mM NaCl/0.7 mM NaHCO₃) was mixed with 15 mL of montmorillonite stock suspension to yield a 250 mL montmorillonite suspension at a solid to liquid ratio of 1g/L and added to the Teflon jars. A sealed dialysis tube containing 15 mL of an intrinsic Pu colloid suspension was then placed in the 250 mL of montmorillonite suspended in pH8 buffer solution. The 450-

mL Teflon jars were submerged in 1-L Teflon containers filled with Milli-Q water to minimize evaporative losses and provide secondary containment to the radioactive samples. Over the course of the experiment, the 25°C samples were placed on a top-loading orbital shaker, and the 80°C samples were submerged in a heated water bath (Innova 3100) and shaken at an orbital speed of 100 rpm.

Each experiment was sampled as a function of time over a three-month period. At each sampling interval, aliquots of the montmorillonite suspension were collected and analyzed for total Pu. The montmorillonite concentration in the suspension was also measured based on light scattering at a wavelength range of 300-500 nm using UV-Vis spectrometry (Cary 500, Varian). At the termination of the experiments, both the total Pu in the clay suspension and the aqueous Pu were measured. Aqueous Pu was determined by conventional centrifugation of the clay suspension and measurement of the supernatant. Alternatively, aqueous Pu was determined by measuring the filtrate Pu concentration after filtering the suspension through 3kDa pore size centrifugal filters. The pH of the clay suspension was monitored and maintained at $\text{pH } 8 \pm 0.5$ at all times.

Characterization of intrinsic Pu colloid: Prior to initiating the intrinsic Pu colloid stability experiments, the starting material was characterized by scanning electron microscopy (SEM) and transmission electron microscopy (TEM). SEM images of the high-fired Pu oxide, Wilk#1 and Wilk#2, are shown in Figure 6-2. Additional images and analysis can be found in Isselhardt and Hutcheon [11]. The predominant morphological structure was a near square platelet with fine porosities observed at higher magnification in both samples (see figures 2b and d). These samples and others investigated in Isselhardt and Hutcheon [11] suggest a slight decrease in porosity and surface area at higher calcination temperature. The range in particle size of the high-fired Pu oxide was generally from 1 to 10 μm with an average of 4 μm . However, the average size of the individual crystallites in Wilk#1 and Wilk#2 were reported to be 4.5 and 100 nm, respectively.

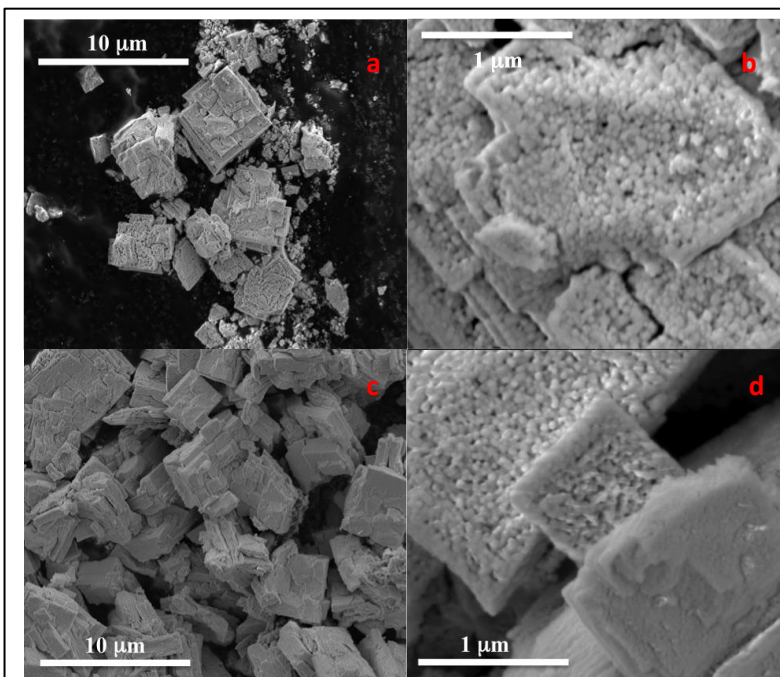
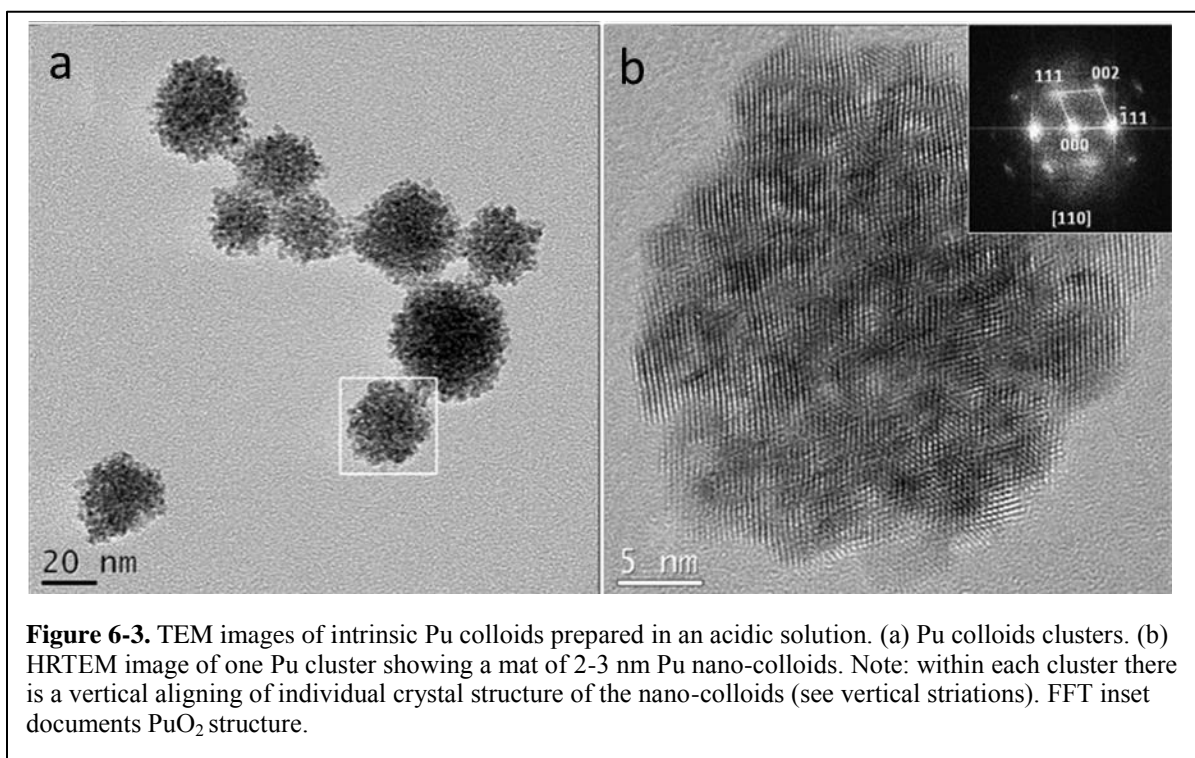


Figure 6-2. SEM Images of high-fired Pu oxide. Wilk#1 (300°C) is shown in figures a and b and Wilk#2 (800°C) is shown in c and d. Both samples show similar appearance and texture. Notice the fine porous nature of the oxides at high resolution (b and d).

TEM images of the intrinsic Pu colloids prepared in acidic solution and used in this study are presented in Figure 6-3. The Pu forms aggregated clusters as seen in Figure 6-3a that range from 10 to 10's of nanometers. However, high-resolution TEM shows that the clusters are composed of individual nano-colloids, or crystallites (Fig. 6-3b). The size range of these nano-crystallites was determined to be 2 to 3 nm with an average size of 2.3 nm. Both X-ray EDS analysis and select-area electron diffraction confirmed the formation of an fcc PuO_2 that has a fluorite structure. Clusters of Pu nano-colloids were also observed in the intrinsic Pu colloids prepared in basic solution and used in the FY11 and FY12 study. But in contrast to the colloids prepared in an acidic solution, the colloids prepared in a basic solution do not show a preferred alignment in their clusters, but appear entirely randomly oriented (Figure 6-4). Neither the freshly prepared nor the aged intrinsic Pu colloids prepared in a basic solution (up to 1 year) showed preferential alignment of the 2-3 nm nano-colloids. We hypothesize that the heating process used to produce the intrinsic Pu colloids in an acidic solution resulted in the incipient alignment of the crystallites within the clusters.



The various intrinsic Pu colloids used in these experiments have different particle sizes and ultimately different surface areas. Due to the health and safety concerns inherent in working with potentially dispersible Pu powders, the high-fired Pu oxides could not be ground to a finer size. The surface area of the various intrinsic Pu colloids was estimated based on the sizes of the crystallites and tabulated in Table 6-2.

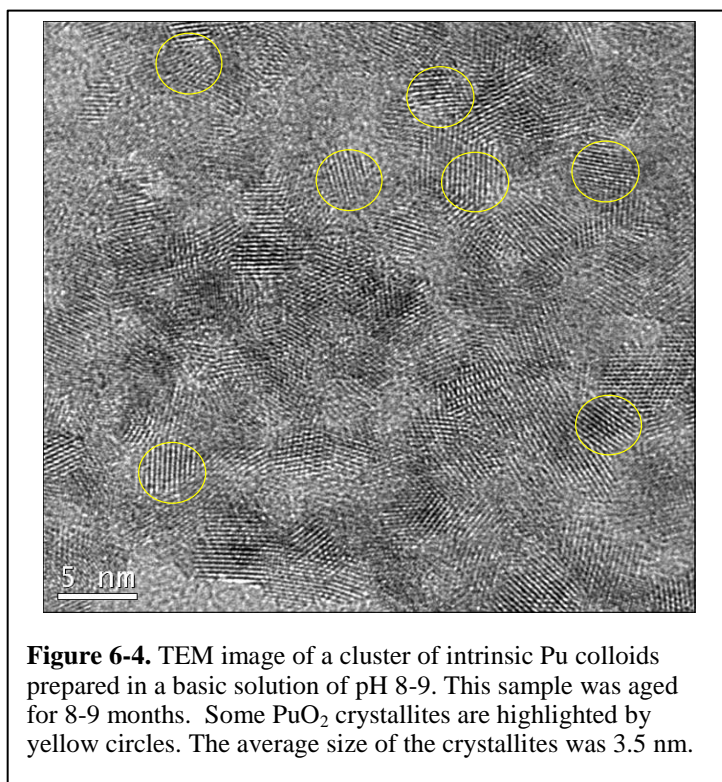


Figure 6-4. TEM image of a cluster of intrinsic Pu colloids prepared in a basic solution of pH 8-9. This sample was aged for 8-9 months. Some PuO_2 crystallites are highlighted by yellow circles. The average size of the crystallites was 3.5 nm.

Table 6-2. Estimated Surface Area of Intrinsic Pu colloids and Montmorillonite

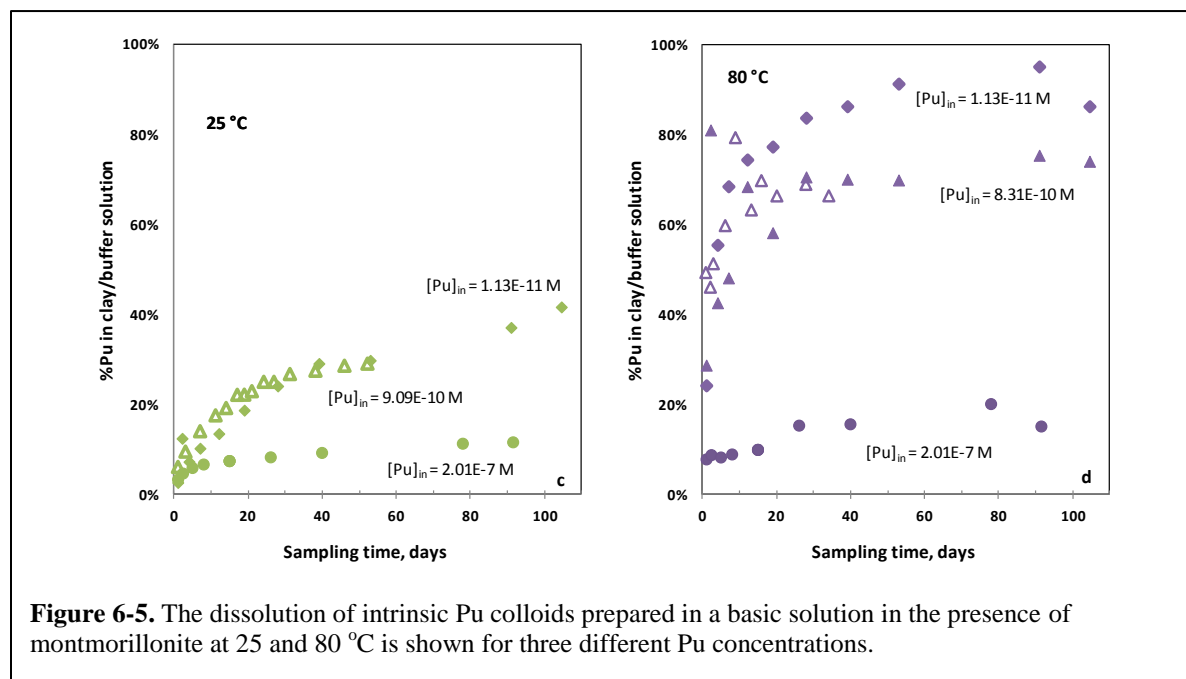
Intrinsic Pu colloid/Clay	Ave. Particle Size, (nm)	Ave. Crystallite Size, (nm)	Density, g/cm^3	Surface Area m^2/g
^{238}Pu colloid prepared in basic solution	30	3.5	11.5	149.1
^{242}Pu colloid prepared in acidic solution	50	2.3	11.5	226.8
High-fired ^{239}Pu oxide, 300 °C	4000	4.5	11.5	115.9
High-fired ^{239}Pu oxide, 800 °C	4000	100	11.5	5.2
Montmorillonite	300	71	2.83	29.9

6.4 Technical Results and Discussion

Intrinsic ^{238}Pu colloids prepared in a basic solution

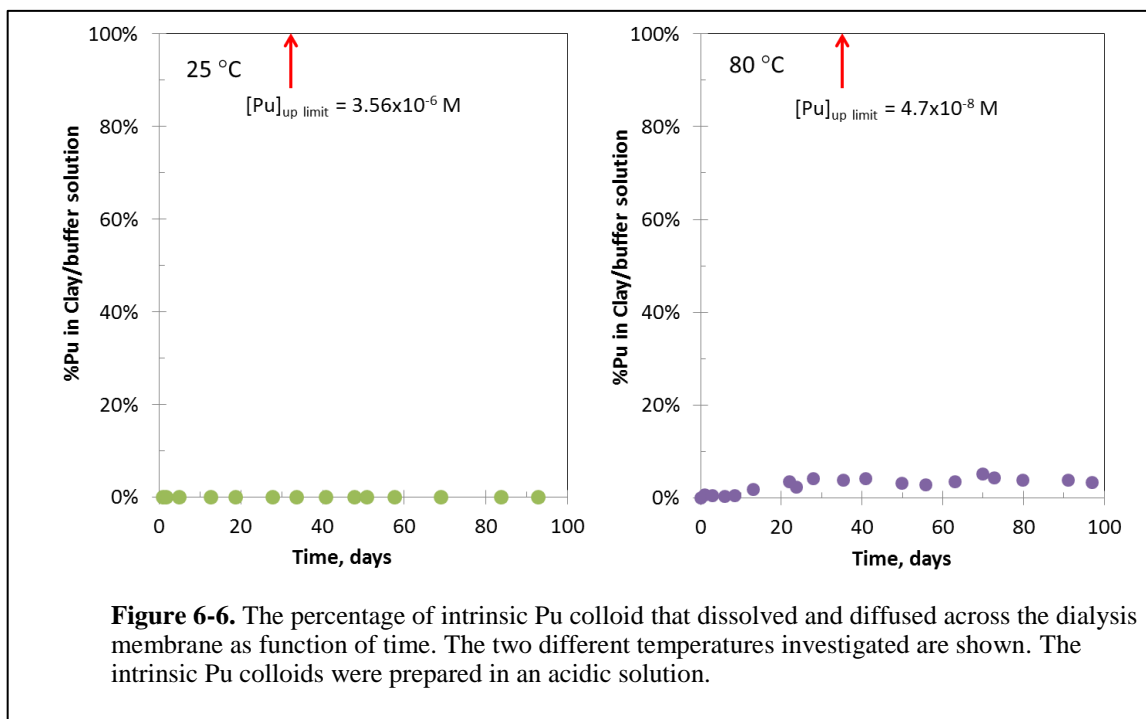
As mentioned previously, the stability of intrinsic Pu colloids prepared in a basic solution (both freshly prepared and aged up to 1 year) was studied in the presence of montmorillonite at 25 and 80°C in FY11 and FY12 [7]. Colloid stability at three different intrinsic Pu colloid concentrations (10^{-11} , 10^{-9} and 10^{-7} M) was examined. These intrinsic ^{239}Pu colloids were aged for 1 month to >1 year prior to use in the stability experiments. No difference in behavior was observed between the fresh and aged samples. The results are briefly summarized here to facilitate comparison with the results from this study. Figure 6-5a and 6-5b shows the percentage of intrinsic Pu colloids that dissolved and diffused across the dialysis membrane over time at 25 and 80°C, respectively. At both temperatures, the intrinsic Pu colloids dissolve, diffuse across the dialysis membrane, and sorb to montmorillonite. However, the reaction kinetics are significantly faster at 80°C than at 25°C. Over the 100 days of these experiments, samples with initial Pu concentrations below the solubility of amorphous PuO_2 as determined in Neck et al. [6] (10^{-11} M and 10^{-9} M) dissolved much more than samples with an initial Pu concentration above the solubility of amorphous PuO_2 (10^{-7} M). Thus, the dissolution of intrinsic Pu colloids prepared in a basic solution is relatively fast and appears to follow the solubility behavior of amorphous PuO_2 . The experimental results suggest that intrinsic Pu colloids prepared in a basic solution are relatively unstable and unaffected by the aging process.

Interestingly, as a consequence of the experimental design, we could also determine the affinity of Pu for the montmorillonite surface at 25 and 80°C. Based on our measurement of total and aqueous Pu in the montmorillonite suspension, the Pu K_d (mL/g) at 80°C was found to be significantly higher than at 25°C. This indicates that Pu has a higher affinity for montmorillonite at elevated temperatures.



Stability of intrinsic ^{242}Pu colloids prepared in an acid solution

These intrinsic Pu colloids were aged for about two years before being used in this study. The initial Pu concentration inside the dialysis bags was 3.9×10^{-5} and 3.4×10^{-5} M in the 25°C and 80°C experiments, respectively. The maximum possible Pu concentration in the montmorillonite suspension, assuming complete dissolution of the intrinsic Pu colloids, would be 3.56×10^{-6} and 4.7×10^{-8} M, respectively. The experiments were run for three months. Figure 6-6 plots the percentage of intrinsic Pu colloids that dissolved and diffused across the membrane as a function of time. For the experiment at 25°C, there was no detectable Pu in the montmorillonite suspension. The method detection limit was 1×10^{-9} M, which is $< 0.03\%$ of the total Pu in the system. For the experiment at 80°C, less than 5% of the intrinsic Pu colloids dissolved and diffused into the montmorillonite suspension. Clearly, intrinsic Pu colloids prepared in an acidic solution are much more stable than intrinsic Pu colloids prepared in a basic solution. It is possible that the alignment of the crystal structure seen in the Pu crystallite clusters result in a more stable structure. It is also possible that the higher dissolution rates observed in the intrinsic ^{238}Pu colloids prepared in a basic solution may have been, in part, the result of greater radiation damage resulting from the short-lived ^{238}Pu isotope contained in this preparation (compared to the intrinsic ^{242}Pu colloids prepared in an acidic solution [12]).



Stability of high-fired Pu oxides

Two high-fired Pu oxides, calcined at 300°C and 800°C, respectively, were used in these stability experiments. The initial high-fired Pu oxide concentrations inside the dialysis bags were 2.1×10^{-7} M for all experiments at 25°C and 80°C. The maximum possible Pu concentration in the montmorillonite suspension, assuming complete dissolution of the high-fired Pu oxides, would be 1.2×10^{-8} M. These experiments have been running for three months and are ongoing. Plotted in Figure 6-7 is the percentage of high-fired Pu oxide that has dissolved and diffused across the membrane as a function of time. For

experiments at both 25 and 80°C, there was no detectable Pu in the montmorillonite suspension. The method detection limit was 5×10^{-11} M, which is $< 0.5\%$ of total Pu in these experiments. These results indicate that both the 300°C and 800°C high-fired Pu oxides are quite stable over the three month period investigated.

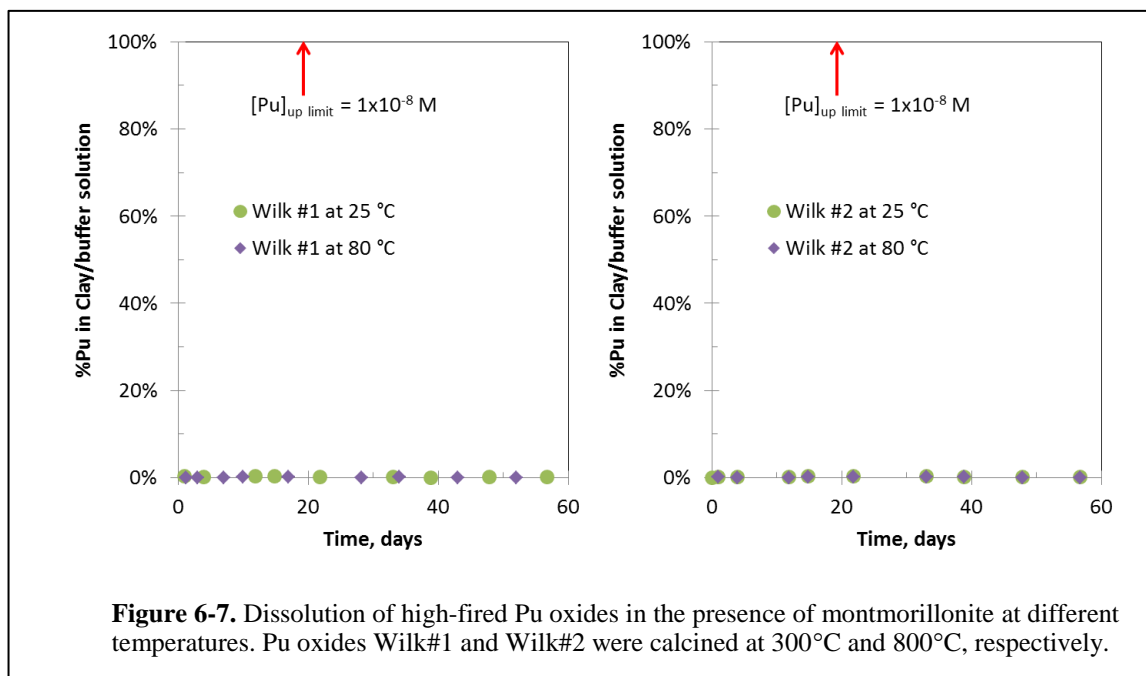


Figure 6-7. Dissolution of high-fired Pu oxides in the presence of montmorillonite at different temperatures. Pu oxides Wilk#1 and Wilk#2 were calcined at 300°C and 800°C, respectively.

In comparing all the experiments to date, it is apparent that Pu oxides produced in a variety of different ways leads to a wide range of intrinsic Pu colloid stability. The intrinsic Pu colloids prepared in a basic solution are the least stable. Their stability is also temperature-dependent, with significantly faster dissolution observed at 80°C compared to 25°C. The high-fired Pu oxides are the most stable; at both temperatures examined to date, both the 300°C and 600°C calcined Pu oxides were stable with no detectable dissolution after 60 days. TEM and SEM analyses indicate that the calcined Pu oxides are morphologically distinct from the intrinsic Pu colloids prepared in acidic and basic solutions. Although it is not possible to directly compare dissolution rates between the different Pu oxides because the surface areas of the intrinsic Pu colloids and high fired Pu oxides are difficult to estimate, general observations can be made. It does not appear that aging makes a difference in the stability of the intrinsic Pu colloids, as no difference in dissolution rates were observed between the freshly precipitated and aged intrinsic Pu colloids prepared in a basic solution. Although intrinsic Pu colloids prepared in basic and acidic solutions both have an fcc crystal structure, those prepared in an acidic solution appear to have a more crystalline structure and some long range order among the aggregated ~ 2.5 nm Pu crystallites. This suggests a more crystalline and stable structure resulting in slower dissolution compared to the more disordered intrinsic Pu colloids prepared in a basic solution. It is also possible that elevated temperatures helped to stabilize the intrinsic Pu colloids prepared in an acidic solution. The intrinsic Pu colloids prepared in a basic solution were kept at 25°C while the intrinsic Pu colloids prepared in an acidic solution were heated during preparation. Thus, the greater stability of intrinsic Pu colloids prepared in an acidic solution may, in part, be the result of sample heating.

6.5 Conclusions and Future Work

In this study, we have examined the stability of three different types of intrinsic Pu colloids and Pu oxides in the presence of montmorillonite at 25 and 80°C under atmospheric conditions. Several conclusions can be drawn:

- Intrinsic Pu colloids made in dilute basic solution were found to dissolve quickly, particularly when a strong thermodynamic gradient is provided (i.e., Pu sorption to montmorillonite). At 25°C, the dissolution of intrinsic Pu colloids is slower than at 80°C. Nevertheless, formation and dissolution of intrinsic Pu colloids appears to be a reversible process. Pu dissolution rates and the affinity for montmorillonite increase with temperature. The reversible nature and relatively fast dissolution rates of intrinsic Pu colloids precipitated in a basic solution suggests that these types of colloids are not very stable and their presence downstream of a nuclear waste repository setting is unlikely.
- In contrast, intrinsic Pu colloids produced from acidic solution and Pu oxides calcined at 300 and 800°C are stable over the 3 months investigated. Under these formation conditions, intrinsic Pu colloids and/or Pu oxides may play an important role in the migration of intrinsic Pu colloids away from nuclear waste repository setting.
- How Pu oxides are formed impacts their ultimate chemical stability. Heat may play an important role in enhancing the stability of intrinsic colloids by increasing its crystallinity. Importantly, the results described here suggest that repository scenarios that include higher heat loading may result in stabilization of Pu oxide phases, which can lead to greater migration of intrinsic Pu colloids. However, the repository temperature history, combined with the predicted timing of canister failure and re-saturation of the repository near field will all play a role in the evolution of any specific repository scenario and the potential for Pu mobilization.

In FY14, we will expand the range of conditions under which intrinsic Pu colloid and high-fired Pu oxide stability is examined. Specifically, the behavior of Pu across a range of ionic strength is essential to extend our studies to Salt Repository scenarios. The role of alpha-recoil effects on destabilization of oxide phases will also be examined. Finally, the effect of iron oxides, which are more relevant for Salt Repository scenarios than clays, in accelerating intrinsic Pu colloid and high-fired Pu oxide dissolution will be examined. The ultimate goal of these experiments is to provide guidance regarding the potential of colloid-facilitated actinide transport to each of the generic repository scenarios under investigation.

6.6 References

- (1) U.S. Office of Civilian Radioactive Waste Management (2002) Yucca Mountain Science and Engineering Report: Technical Information Supporting Site Recommendation Consideration. . In, vol. U.S. Department of Energy, pp 4-466.
- (2) Kersting AB, Efurud DW, Finnegan DL, Rokop DJ, Smith DK, Thompson JL (1999) Migration of Plutonium in ground water at the Nevada Test Site. *Nature* 397(6714):56-59.
- (3) Santschi PH, Roberts KA, Guo LD (2002) Organic Nature of Colloidal Actinides Transported in Surface Water Environments. *Environmental Science & Technology* 36(17):3711-3719 doi:Doi 10.1021/Es0112588.

- (4) Novikov AP, Kalmykov SN, Utsunomiya S, Ewing RC, Horreard F, Merkulov A, Clark SB, Tkachev VV, Myasoedov BF (2006) Colloid transport of plutonium in the far-field of the Mayak Production Association, Russia. *Science* 314(5799):638-641.
- (5) Kim JI (1991) Actinide Colloid Generation in Groundwater. *Radiochim Acta* 52/53:71-81.
- (6) Neck V, Altmaier M, Seibert A, Yun JI, Marquardt CM, and Fanghanel T (2007) Solubility and redox reactions of Pu(IV) hydrous oxide: Evidence for the formation of PuO_{2+x}(s, hyd). *Radiochim Acta* 95(4):193-207.
- (7) Kersting AB (2013) Plutonium Transport in the Environment. *Inorganic Chemistry* 52(7):3533-3546 doi:10.1021/ic3018908.
- (8) Walther C, Denecke MA (2013) Actinide Colloids and Particles of Environmental Concern. *Chemical Reviews* 113:995-1015.
- (9) Haire RG, Lloyd JR (1971) Aging of hydrous plutonium oxide. *Journal Electron Microscopy* 20(1):8-16.
- (10) Park JF, D. L. Catt, D. K. Craig, R. J. Olson, Smith VH (1973b) Solubility Changes of exp 238 Pu Oxide in Water Suspension and Effect on Biological Behavior after Inhalation by Beagle Dogs. In, vol. Dept. of Commerce.
- (11) Isselhardt BH, Hutcheon ID (2012) Pu Oxide-FY11 Year End Report In, vol. Lawrence Livermore National Laboratory., Livermore, CA.
- (12) Park JF, Catt DL, Craig DK, Olson RJ, Smith VH (1973a) Solubility Changes of exp 238 Pu Oxide in Water Suspension and Effect on Biological Behavior after Inhalation by Beagle Dogs. In, vol. National Technical Information Service, US department of Commerce.

7.0 THMC Effects on Radionuclide Transport in a Clay Repository

7.1 Introduction

Geological repositories for disposal of high-level nuclear waste generally rely on a multibarrier system to isolate radioactive waste from the biosphere. The multi-barrier system typically consists of the natural system (NS), which includes the repository host rock and its surrounding subsurface environment, and the engineered barrier system (EBS). Clay/shale has been considered as a host rock for NS throughout the world, because of its low permeability, low diffusion rates, high retention capacity for radionuclides, and capability to self-seal fractures induced by tunnel excavation. For example, Callovo-Oxfordian argillites at the Bure site, France [1], Toarcian argillites at the Tournemire site, France [2], Opalinus Clay at the Mont Terri site, Switzerland [3], and Boom Clay at the Mol site, Belgium [4] have all been under intensive scientific investigation (at both field and laboratory scales) to improve understanding of a variety of rock properties and their relationships to flow and transport processes associated with geological disposal of nuclear waste. Furthermore, an EBS composed of bentonite is routinely considered in the design of nuclear waste repositories in clay formations.

Radionuclide transport through EBS bentonite and NS clay formations is the core of performance assessments for clay repositories. Although radionuclide transport in clay rock has been studied in laboratory tests [5-7], short-term field tests [8-11] and with numerical modeling [12-13], the overall effects of coupled thermal, hydrological, mechanical, and chemical (THMC) processes on radionuclide transport have not been fully investigated.

The objectives of the research activity documented in this report are to improve the modeling capability for coupled THMC processes and apply it to an evaluation of Thermal-Hydrologic-Mechanical-Chemical (THMC) impacts on radionuclide transport. This research activity addresses several key Features, Events and Processes (FEPs), including FEP 2.2.08, Hydrologic Processes, FEP 2.2.07, Mechanical Processes and FEP 2.2.09, Chemical Process—Transport, by studying near-field coupled THMC processes in clay/shale repositories and their impact on radionuclide transport.

Previous studies [14-15] have been conducted to investigate the changes in THMC conditions in the EBS and NS, changes that are of great importance because they determine the environment driving radionuclide transport. Our modeling effort since FY12 has focused on modeling the migration of radionuclides in EBS and NS, including impacts of THMC processes on the fate of radionuclides. The model work of FY12 [16] demonstrated that chemical processes such as aqueous complexation and adsorption are extremely important in controlling the migration of uranium in the host clay formation. In FY13, we focused on the reactive transport of plutonium (Pu) in the EBS bentonite and the NS host clay rock. This report documents the progress made in FY13. Section 2 presents the modeling setup, and Section 3 describes modeling results for Pu transport. Some concluding remarks and plans for future work are provided in Section 4.

7.2 Technical Approach

7.2.1 Simulator

In this study, we used TOUGHREACT V2 [17] to simulate radionuclide transport in clays. TOUGHREACT has been developed by introducing reactive transport into the existing framework of a nonisothermal, multicomponent fluid- and heat-flow simulator TOUGH2 [18]. A number of subsurface thermo-physical-chemical processes are considered under various thermo-hydrological and geochemical conditions with respect to pressure, temperature, water saturation, and ionic strength. TOUGHREACT can be applied to one-, two- or three-dimensional porous and fractured media with physical and chemical heterogeneity. The code can accommodate any number of chemical species present in liquid, gas and solid phases.

The first version of TOUGHREACT code was released in August 2004 and documented in Xu et al. [19]. The code has been widely used for studies in CO₂ geological sequestration, geothermal energy development, nuclear waste isolation, environmental remediation, and (increasingly) for petroleum applications. Over the last several years, many new capabilities have been developed and implemented into Version 2 of TOUGHREACT (V2). Major additions and improvements in Version 2 that are relevant to the current modeling study include:

- Surface complexation reactions
- Multi-site exchange
- Improvement on coupling between chemistry and physics (changes in rock and fluid properties due to reactions).

The geochemical model implemented in TOUGHREACT accounts for a variety of equilibrium and kinetic chemical reactions [19]. Aqueous complexation, acid-base, redox, and cation exchange reactions are assumed to be in thermodynamic equilibrium. The thermodynamic data incorporated within TOUGHREACT are based on the equilibrium constants for aqueous species and minerals given in the EQ3/6 V7.2b Data0.dat database [20].

7.2.2 Model Setup

We use the same model setup as in Zheng et al. [16] to simulate the transport of Pu in the EBS bentonite and the NS clay formation. The simulations were conducted for a hypothetical bentonite-backed nuclear waste repository in clay rock. The repository example involves a horizontal nuclear waste emplacement tunnel at 500 m depth (Figure 7-1) [21]. We constructed a numerical model with a geometry containing one circular tunnel and consisting of 368 gridblocks. The configuration of the model is shown in Figure 7-2. The Z-axis is set as vertical in the model, while the horizontal Y- and X-axes are aligned parallel and perpendicular to the emplacement tunnel, respectively. This is a 2D (Y-Z) model, assuming uniform in the X-direction.

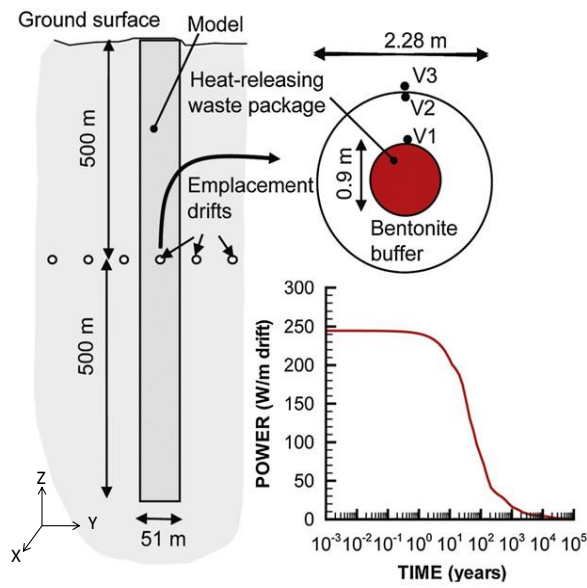


Figure 7.1. Domain for the test example of a bentonite back-filled horizontal emplacement drift at 500 m [21]

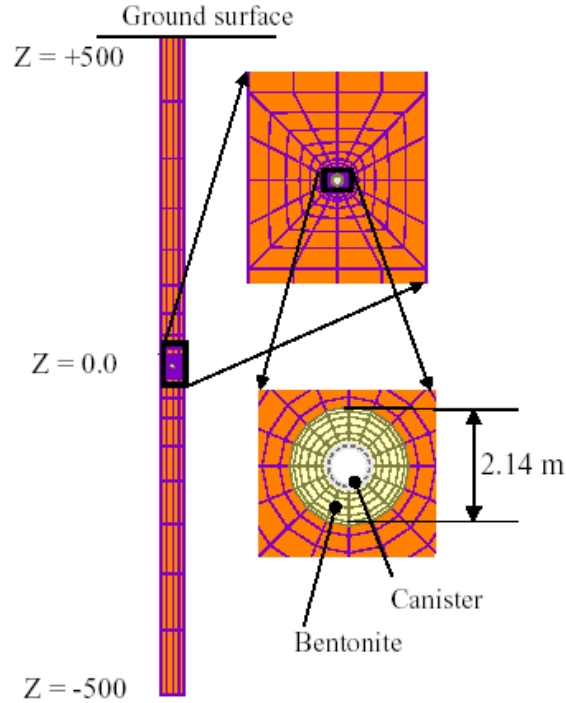


Figure 7.2. Mesh for modeling of horizontal emplacement drift at 500 m depth.

7.2.3 Chemical Model

The general chemical environment

In this hypothetical case, it is assumed that the EBS is composed of Kunigel-V1 bentonite [22] and the host rock is Opalinus Clay [23]. Mineral compositions for the bentonite and clay formation are listed in Table 7-1. The pyrite volume fraction is critical in current simulations because of its impact on redox conditions in the EBS bentonite and NS clay formation. Thury [23] roughly reported on the abundance of pyrite — with the total mass fraction of pyrite and other trace minerals such as siderite and ankerite at 5%, indicating that there is some pyrite present, but its mass fraction varies. Bossart [24] summarized mineralogical composition data determined by various authors [25-28], and reported that pyrite mass fractions range from 0% to 1.1%, whereas Lauber et al. [29] reported pyrite fractions below detection limit. In this report, we first use a pyrite volume fraction of 0.01, and then include a zero volume fraction for pyrite in a sensitivity run.

The initial pore-water compositions in the EBS bentonite and NS clay formation are listed in Table 7-2. The pore-water compositions in the NS clay formation are from Fernandez et al. [30]. The initial water for EBS bentonite was taken from Sonnenthal et al. [31] and used in the benchmark for the DECOVALEX-THMC project (Sonnenthal et al., 2008). For F⁻, Br⁻, and O₂(aq), which were not reported in Sonnenthal et al. [31], we simply assumed that they have the same concentrations as in the NS clay formation. F⁻ and Br⁻, though not of great interest in current simulations, are included to account for their aqueous complexation reactions with Pu. In TOUGHREACT, redox potentials are represented by O₂(aq) concentrations.

Table 7-1. Mineral compositions (volume fraction, dimensionless, volume of mineral/ total volume of solids) for EBS bentonite [22] and NS clay formation [23]

Mineral	Bentonite	Clay formation
Schoepite	0	0
Calcite	0.023	0.13
Illite	0	0.25
Kaolinite	0	0.22
chlorite	0	0.1
Na-montmorillonite	0.475	0.088
Quartz	0.435	0.14
K-Feldspar	0.041	0
Siderite	0	0.03
Dolomite	0.029	0
Ankerite	0	0.03
Pyrite	0.006	0.01

Table 7-2. Pore-water composition of the EBS bentonite (Kunigel-V1) and the NS clay formation (Opalinus Clay)

	Bentonite	Clay formation
pH	8.40	7.40
Eh (mV)	750	230
Cl	1.50E-05	3.32E-01
SO ₄ ⁻²	1.10E-04	1.86E-02
HCO ₃ ⁻	3.49E-03	5.18E-03
Ca ⁺²	1.37E-04	2.26E-02
Mg ⁺²	1.77E-05	2.09E-02
Na ⁺	3.60E-03	2.76E-01
K ⁺	6.14E-05	2.16E-03
Fe ⁺²	2.06E-08	3.46E-06
SiO ₂ (aq)	3.38E-04	1.10E-04
AlO ₂ ⁻	1.91E-09	3.89E-08
F-	1.68E-05	1.68E-05
Br-	3.2E-04	3.2E-04
O ₂ (aq)	1.07E-41	1.07E-41
Pu	1E-30	1E-30

Table 7-3 lists the thermal and hydrodynamic parameters used in the model. Those for bentonite are taken from Sonnenthal [31], while those for clay formations are mostly taken from Thury [23].

Mineral dissolution/precipitation is kinetically controlled, except for Pu minerals that are assumed in equilibrium. The kinetic law for mineral dissolution/precipitation is given in Xu et al. [19]. The kinetic rates for the minerals considered in the current model are given in Table 7-4. Note that the surface areas listed in Table 7-4 have been calculated for tuff [32]. Their applicability to the considered clay formation has to be questioned at this point. Further refinement of the surface-area calculations is needed in the future when the model is applied to a more realistic scenario.

Table 7-3. Thermal and hydrodynamic parameters

Parameter	Clay formation	Bentonite
Grain density [kg/m ³]	2700	2700
Porosity ϕ	0.15	0.41
Saturated permeability [m ²]	5.0×10^{-20}	2.0×10^{-21}
Relative permeability, k_{rl}	$m = 0.6, S_{rl} = 0.01$	$K_{rl} = S^3$
Van Genuchten α [1/Pa]	6.8×10^{-7}	3.3×10^{-8}
Van Genuchten m	0.6	0.3
Compressibility, β [1/Pa]	3.2×10^{-9}	5.0×10^{-8}
Thermal expansion coeff., [1/°C]	0.0	1.0×10^{-4}
Dry specific heat, [J/kg °C]	800	8000
Thermal conductivity [W/m °C] dry/wet	2.2/2.2	0.5/1.3
Tortuosity for vapor phase	$\phi^{1/3} S_g^{10/3}$	$\phi^{1/3} S_g^{10/3}$

Table 7-4. Kinetic properties for minerals considered in the model [19]

Mineral	A (cm ² /g)	Parameters for Kinetic Rate Law							
		Neutral Mechanism		Acid Mechanism			Base Mechanism		
		k ₂₅ (mol/m ² /s)	E _a (KJ/mol)	k ₂₅	E _a	n(H ⁺)	k ₂₅	E _a	n(H ⁺)
Primary:									
Pu(OH) ₄ (am)	Assumed at equilibrium								
Pu(OH) ₃ (s)	Assumed at equilibrium								
Quartz	9.8	1.023×10 ⁻¹⁴	87.7						
K-feldspar	9.8	3.89×10 ⁻¹³	38	8.71×10 ⁻¹¹	51.7	0.5	6.31×10 ⁻¹²	94.1	-0.823
Kaolinite	151.6	6.91×10 ⁻¹⁴	22.2	4.89×10 ⁻¹²	65.9	0.777	8.91×10 ⁻¹⁸	17.9	-0.472
Illite	151.6	1.66×10 ⁻¹³	35	1.05×10 ⁻¹¹	23.6	0.34	3.02×10 ⁻¹⁷	58.9	-0.4
Chlorite	9.8	3.02×10 ⁻¹³	88	7.76×10 ⁻¹²	88	0.5			
Calcite	3.5	1.6×10 ⁻⁷	23.5						
Dolomite	12.9	2.52×10 ⁻¹²	62.76	2.34×10 ⁻⁷	43.54	1			
Ankerite	9.8	1.26×10 ⁻⁹	62.76	6.46×10 ⁻⁴	36.1	0.5			
Smectite-Na	151.6	1.66×10 ⁻¹³	35	1.05×10 ⁻¹¹	23.6	0.34	3.02×10 ⁻¹⁷	58.9	-0.4
Na-montmorillonite	151.6	1.66×10 ⁻¹³	35	1.05×10 ⁻¹¹	23.6	0.34	3.02×10 ⁻¹⁷	58.9	-0.4

Aqueous plutonium reactions

The reactions pertinent to Pu considered in the current model are aqueous complexation, minerals dissolution and adsorption/desorption. But radioactive decay and Pu colloid are not considered. The chemistry of Pu is very complex. Pu can exist in the III, IV, V, and VI oxidation states, and often at multiple oxidation states at the same time. The primary variable that determines the migration of an actinide is its oxidation state. Fernandez et al. [33] measured the redox potential (Eh) in Opalinus Clay, and their measured values ranges from -24.2 mV to 83 mV. Because it is well known [34] that field-measured Eh values are rarely reliable, we use the Eh calculated from the redox couple Fe⁺²/Fe⁺³, which is 230 mV. Despite the mildly oxidizing conditions in Opalinus Clay, the analysis by Wersin et al. [35] indicate that the canister-bentonite in the near field is under permanently reducing conditions after a relatively short oxidic period, with redox potentials of -100 to -300 mV. However, as shown later in this report, due to the presence/absence of reductants and the pH conditions, the redox potential near the canister can vary. We therefore considered aqueous complexes for Pu in its III, IV, V, and VI oxidation states, which are listed in Table 7-5, together with their association constants. These constants are mostly taken from data0.com.V8.R6 of the GEMBOCHS thermodynamic database generated for EQ3/6 [20].

The database data0.com.V8.R6 has also been used by Powell et al. [36] when surface complexation reactions of Pu(IV) and Pu(V) on smectite were derived. According to Runde et al. [13], Pu data in this database are from Lemire and Tremaine [37]. A detailed review of the aqueous chemistry of Pu is beyond the work scope of this report. A recent review on Pu thermodynamic data is given by Altmaier et al. [38].

Table 7-5. The aqueous complexes for Pu

Reactions	LogK (25 °C)
Pu(III)	
$\text{Pu}^{+3} + 2.5\text{H}_2\text{O} + 0.25\text{O}_2(\text{aq}) = 2\text{H}^+ + \text{Pu}(\text{OH})_3^+$	-0.813
$\text{Pu}(\text{SO}_4)_2^- + 2.5 \text{H}_2\text{O} + 0.25\text{O}_2(\text{aq}) = 2\text{H}^+ + 2\text{SO}_4^{-2} + \text{Pu}(\text{OH})_3^+$	-6.356
$\text{Pu}(\text{SO}_4)^+ + 2.5 \text{H}_2\text{O} + 0.25\text{O}_2(\text{aq}) = 2\text{H}^+ + \text{SO}_4^{-2} + \text{Pu}(\text{OH})_3^+$	-4.645
$\text{PuCl}^{+2} + 2.5 \text{H}_2\text{O} + 0.25\text{O}_2(\text{aq}) = 2\text{H}^+ + \text{Cl}^- + \text{Pu}(\text{OH})_3^+$	-2.013
$\text{PuOH}^{+2} + 1.5\text{H}_2\text{O} + 0.25\text{O}_2(\text{aq}) = \text{H}^+ + \text{Pu}(\text{OH})_3^+$	6.087
Pu(IV)	
$\text{Pu}^{+4} + 3\text{H}_2\text{O} = 3\text{H}^+ + \text{Pu}(\text{OH})_3^+$	-4.62
$\text{PuCl}^{+3} + 3\text{H}_2\text{O} = 3\text{H}^+ + \text{Cl}^- + \text{Pu}(\text{OH})_3^+$	-6.42
$\text{PuBr}^{+3} + 3\text{H}_2\text{O} = 3\text{H}^+ + \text{Br}^- + \text{Pu}(\text{OH})_3^+$	-6.22
$\text{PuF}^{+3} + 3\text{H}_2\text{O} = 3\text{H}^+ + \text{F}^- + \text{Pu}(\text{OH})_3^+$	-13.42
$\text{PuF}_2^{+2} + 3\text{H}_2\text{O} = 3\text{H}^+ + 2\text{F}^- + \text{Pu}(\text{OH})_3^+$	-20.24
$\text{Pu}(\text{SO}_4)_2(\text{aq}) + 3\text{H}_2\text{O} = 3\text{H}^+ + 2\text{SO}_4^{-2} + \text{Pu}(\text{OH})_3^+$	-15.604
$\text{PuSO}_4^{+2} + 3\text{H}_2\text{O} = 3\text{H}^+ + \text{SO}_4^{-2} + \text{Pu}(\text{OH})_3^+$	-11.432
$\text{PuOH}^{+3} + 2\text{H}_2\text{O} = 2\text{H}^+ + \text{Pu}(\text{OH})_3^+$	-3.833
$\text{Pu}(\text{OH})_2^{+2} + 2\text{H}_2\text{O} = 2\text{H}^+ + \text{Pu}(\text{OH})_3^+$	-2.96

Table 7-5. Continued

Reactions	logK (25 °C)
$\text{Pu}(\text{OH})_4(\text{aq}) + \text{H}^+ = \text{H}_2\text{O} + \text{Pu}(\text{OH})_3^+$	4.23
$\text{Pu}(\text{OH})_2(\text{CO}_3)_2^{-2} + \text{H}_2\text{O} + \text{H}^+ = 2\text{HCO}_3^- + \text{Pu}(\text{OH})_3^+$	-1.87
$\text{Pu}(\text{OH})_4(\text{CO}_3)_2^{-4} + 3\text{H}^+ = 2\text{HCO}_3^- + \text{Pu}(\text{OH})_3^+ + \text{H}_2\text{O}$	20.91
$\text{Pu}(\text{CO}_3)_4^{-4} + \text{H}^+ + 3\text{H}_2\text{O} = 4\text{HCO}_3^- + \text{Pu}(\text{OH})_3^+$	0.0
$\text{Pu}(\text{CO}_3)_5^{-6} + 2\text{H}^+ + 3\text{H}_2\text{O} = 5\text{HCO}_3^- + \text{Pu}(\text{OH})_3^+$	11.68
Pu(V)	
$\text{PuO}_2^+ + 1.5\text{H}_2\text{O} = 0.25\text{O}_2(\text{aq}) + \text{Pu}(\text{OH})_3^+$	-8.653
$\text{PuO}_2(\text{OH})(\text{aq}) + 0.5\text{H}_2\text{O} + \text{H}^+ = 0.25\text{O}_2(\text{aq}) + \text{Pu}(\text{OH})_3^+$	1.077
$\text{PuO}_2(\text{CO}_3)^- + 1.5\text{H}_2\text{O} + \text{H}^+ = \text{HCO}_3^- + 0.25\text{O}_2(\text{aq}) + \text{Pu}(\text{OH})_3^+$	-3.43
$\text{PuO}_2(\text{CO}_3)_2^{-3} + 1.5\text{H}_2\text{O} + 2\text{H}^+ = 2\text{HCO}_3^- + 0.25\text{O}_2(\text{aq}) + \text{Pu}(\text{OH})_3^+$	6.061
$\text{PuO}_2(\text{CO}_3)_3^{-5} + 1.5\text{H}_2\text{O} + 3\text{H}^+ = 3\text{HCO}_3^- + 0.25\text{O}_2(\text{aq}) + \text{Pu}(\text{OH})_3^+$	17.352
Pu(VI)	
$\text{PuO}_2^{+2} + 2\text{H}_2\text{O} = 0.5\text{O}_2(\text{aq}) + \text{H}^+ + \text{Pu}(\text{OH})_3^+$	-14.35
$(\text{PuO}_2)_2(\text{OH})_2^{+2} + 2\text{H}_2\text{O} = \text{O}_2(\text{aq}) + 2\text{Pu}(\text{OH})_3^+$	-21.171
$\text{PuO}_2(\text{OH})_2(\text{aq}) + \text{H}^+ = 0.5\text{O}_2(\text{aq}) + \text{Pu}(\text{OH})_3^+$	-1.135
$(\text{PuO}_2)_3(\text{CO}_3)_6^{-6} + 6\text{H}_2\text{O} + 3\text{H}^+ = 6\text{HCO}_3^- + 0.5\text{O}_2(\text{aq}) + \text{Pu}(\text{OH})_3^+$	-31.047
$(\text{PuO}_2)(\text{CO}_3)_2^{-2} + 2\text{H}_2\text{O} + \text{H}^+ = 2\text{HCO}_3^- + 0.5\text{O}_2(\text{aq}) + \text{Pu}(\text{OH})_3^+$	-8.149
$(\text{PuO}_2)(\text{CO}_3)_4^{-4} + 2\text{H}_2\text{O} + 2\text{H}^+ = 3\text{HCO}_3^- + 0.5\text{O}_2(\text{aq}) + \text{Pu}(\text{OH})_3^+$	-1.005
$(\text{PuO}_2)(\text{SO}_4)_2^{-2} + 2\text{H}_2\text{O} = 2\text{SO}_4^{-2} + \text{H}^+ + 0.5\text{O}_2(\text{aq}) + \text{Pu}(\text{OH})_3^+$	-18.576
$\text{PuO}_2\text{Cl}^+ + 2\text{H}_2\text{O} = \text{Cl}^- + \text{H}^+ + 0.5\text{O}_2(\text{aq}) + \text{Pu}(\text{OH})_3^+$	-15.036
$\text{PuO}_2\text{Cl}_2(\text{aq}) + 2\text{H}_2\text{O} = 2\text{Cl}^- + \text{H}^+ + 0.5\text{O}_2(\text{aq}) + \text{Pu}(\text{OH})_3^+$	-13.736
$\text{PuO}_2\text{CO}_3(\text{aq}) + 2\text{H}_2\text{O} = \text{HCO}_3^- + 0.5\text{O}_2(\text{aq}) + \text{Pu}(\text{OH})_3^+$	-15.592
$\text{PuO}_2\text{F}^+ + 2\text{H}_2\text{O} = \text{F}^- + \text{H}^+ + 0.5\text{O}_2(\text{aq}) + \text{Pu}(\text{OH})_3^+$	-18.895
$\text{PuO}_2\text{F}_2(\text{aq}) + 2\text{H}_2\text{O} = 2\text{F}^- + \text{H}^+ + 0.5\text{O}_2(\text{aq}) + \text{Pu}(\text{OH})_3^+$	-21.585
$\text{PuO}_2(\text{OH})^+ + \text{H}_2\text{O} = 0.5\text{O}_2(\text{aq}) + \text{Pu}(\text{OH})_3^+$	-8.828
$(\text{PuO}_2)\text{SO}_4(\text{aq}) + 2\text{H}_2\text{O} = \text{SO}_4^{-2} + \text{H}^+ + 0.5\text{O}_2(\text{aq}) + \text{Pu}(\text{OH})_3^+$	-17.636

In reactive transport modeling, it is numerically beneficial to choose the dominant species as the primary component. In this report, we use a Pu(IV) hydrolysis product, $\text{Pu}(\text{OH})_3^+$, as the primary component for Pu, and therefore all reactions are written in terms of $\text{Pu}(\text{OH})_3^+$.

Pu Adsorption/desorption

There are several ways to model adsorption/desorption. A linear sorption isotherm is the simplest approach, in which a distribution coefficient, K_d value, linearly relates the concentration of adsorbent and adsorbate. Surface complexation modeling is another common, but more rigorous method, which uses a series surface species to describe the interactions between aqueous and sorbed phases.

The plutonium K_d value was correlated to parameters specifying the aqueous chemical conditions and solid characteristics using the data of Glover et al. [39]. This data set provides sorption data and a quantitative specification of the mineral phase and solution chemistry associated with each sorption experiment. The correlation indicates that the main controls on sorption are the soluble (or dissolved) carbon content (DC), the clay content (CC), the inorganic carbonate content (i.e., the CaCO_3 content) (IC), the pH , and the solution electrical conductivity (EC). These variables are correlated with the plutonium sorption K_d value based on

$$K_d = A_0 + A_1CC^2 + A_2CC^2DC^2 + A_3IC^2 + A_4IC^2(7 - pH)^2 + EC^2$$

where K_d is in mL/g; DC is in meq/L; CC is in percent; IC is in percent; pH is dimensionless; EC is in mmoh/cm.

These variable combinations were identified purely empirically; however, using $(7 - pH)^2$ was suggested by the typical peak in sorption for plutonium near a pH of 7. A similar correlation approach for determining K_d values based on data by Glover et al. [39] has been reported by the EPA [40]. In this case, a significant correlation between the K_d value and CC , DC , and their products has also been found. According to the EPA report [40], one of the 17 data points in Glover et al. [39] was not used (sample with soil code TN in Glover et al. [39]). Although the reason for excluding this value was not discussed in the EPA report, it is apparent that this data point is strongly inconsistent with the rest of the K_d values. The regression coefficients and P -values are shown in Table 7-6.

Table 7-6. Regression Parameters and P -values

i	A_i	P -value
0	298.1	0.0030
1	0.1283	0.033
2	0.07878	7.9×10^{-6}
3	8.227	0.0034
4	-9.523	0.012
5	-142.8	0.0024

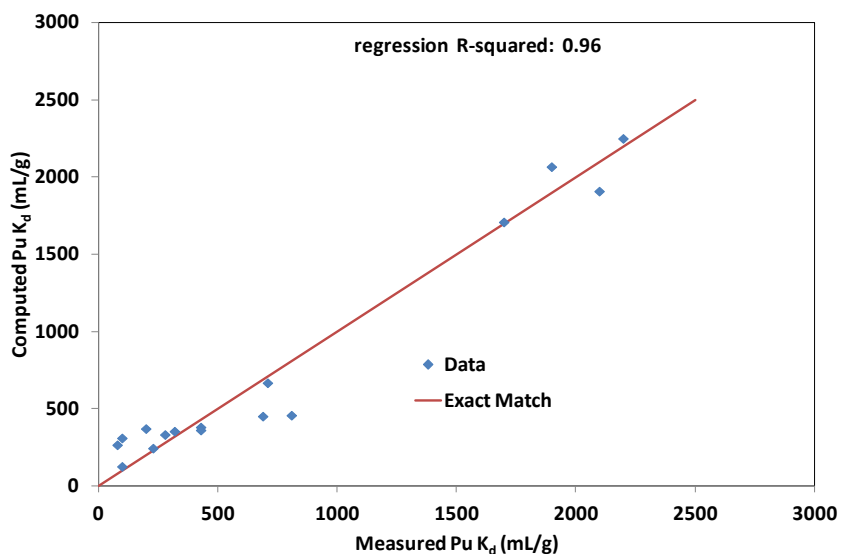


Figure 7-3. Correlation of Pu K_d with aqueous and mineralogical characteristics.

The resulting fit of the Glover et al. [39] data is shown in Figure 7-3. The correlation was performed using the regression routine in Microsoft Excel. This computation provides P -value statistics for the regression coefficients shown in Table 7-6. All of the P -values lie below the standard 5% threshold for significance, and the overall correlation P -value is 2×10^{-6} .

Because of correlation errors, the K_d value can become negative when true sorption is low. Hence, it would make sense to introduce a lower, positive limit for predicted K_d values. The Glover et al. [39] data set is mainly for oxidizing conditions where plutonium is in the V oxidation state (e.g., PuO_2^+). However, aqueous plutonium can also be found in the III, IV, and VI oxidation states. The Glover et al. [39] data also presented Pu sorption K_d values for different aqueous Pu concentrations. The correlation presented here used only the lowest reported Pu aqueous concentration of 10^{-8} M. Experimental results were also available for solution concentrations of 10^{-7} M and 10^{-6} M. The data was limited to the lower concentration results, because of complications that may arise with higher concentrations of aqueous plutonium, in which Pu colloid formation and precipitation could influence results. This highlights the fact that the sorption of dissolved Pu species onto solids may not be the only chemical reaction affecting the transport of plutonium in groundwater.

The correlation was also applied to Pu sorption on 100% montmorillonite using the following values, based on information from Begg et al. [41]: $DC = 0.7$ meq/L, $CC = 100\%$, $IC = 0\%$, $pH = 8$, $EC = 0.35$ mmho/cm. The ionic strength of the solution is based on the solution composition of 0.7 meq/L NaHCO_3 and 5 mM NaCl. The electrical conductivity, EC in mmho/cm, was computed from the ionic strength, 0.0057 M, using a conversion factor of 62 [42]. With these values, the correlation gives $K_d = 14,000$ mL/g, which may be compared with the range of values found for Pu(V) at 30 days: 3,000 to 5,000 mL/g, and at 1 year: 14,000 to 19,000 mL/g [41]. Runde et al. [13] measured a K_d value of 5800 mL/g after 10 days in a comparable batch sorption experiment.

Surface Complexation Modeling Approach

Powell et al. [36] presents one of the few studies that use surface complexation modeling to simulate the sorption of Pu while simultaneously considering the Pu(V)/Pu(IV) redox couple. The modeling exercise conducted in this report is based on their data (See Table 7-7).

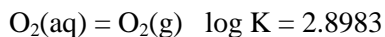
Table 7-7. Revised Pu-aluminol and Pu-silanol surface complexation constants written in terms of the Pu(V)/Pu(IV) redox couple [36]

Species	Reaction	log K
SiOHPuO ₂ ⁺	SiOH + Pu ⁴⁺ + 0.25 O ₂ (g) + 1.5 H ₂ O ↔ SiOHPuO ₂ ⁺ + 3H ⁺	7.55
SiOPuO ₂ ⁰	SiOH + Pu ⁴⁺ + 0.25 O ₂ (g) + 1.5 H ₂ O ↔ SiOPuO ₂ ⁰ + 4H ⁺	2.34
SiOPuO ₂ OH ⁻	SiOH + Pu ⁴⁺ + 0.25 O ₂ (g) + 2.5 H ₂ O ↔ SiOPuO ₂ OH ⁻ + 5H ⁺	-7.86
AlOHPuO ₂ ⁺	AlOH + Pu ⁴⁺ + 0.25 O ₂ (g) + 1.5 H ₂ O ↔ AlOHPuO ₂ ⁺ + 3H ⁺	8.80
AlOPuO ₂ ⁰	AlOH + Pu ⁴⁺ + 0.25 O ₂ (g) + 1.5 H ₂ O ↔ AlOPuO ₂ ⁰ + 4H ⁺	0.35
AlOPuO ₂ OH ⁻	AlOH + Pu ⁴⁺ + 0.25 O ₂ (g) + 2.5 H ₂ O ↔ AlOPuO ₂ OH ⁻ + 5H ⁺	-8.16
AlOPu(OH) ⁺⁺	AlOH + Pu ⁴⁺ + H ₂ O ↔ AlOPu(OH) ⁺⁺ + 2H ⁺	12.82
AlOPu(OH) ₂ ⁺	AlOH + Pu ⁴⁺ + 2H ₂ O ↔ AlOPu(OH) ₂ ⁺ + 4H ⁺	7.34
AlOPu(OH) ₃ ⁰	AlOH + Pu ⁴⁺ + 3H ₂ O ↔ AlOPu(OH) ₃ ⁰ + 4H ⁺	-0.10
SiOPu(OH) ₃ ⁰	SiOH + Pu ⁴⁺ + 3H ₂ O ↔ SiOPu(OH) ₃ ⁰ + 4H ⁺	0.14
SiOPu(OH) ₄ ⁻	SiOH + Pu ⁴⁺ + 4H ₂ O ↔ SiOPu(OH) ₄ ⁻ + 5H ⁺	-7.58

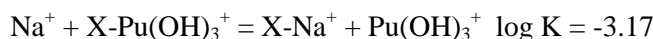
Table 7-8. The surface complexation reactions and their reaction constants for Pu sorption on the surface of smectite.

Species	Reactions	logK (25 °C)
sme_w2OHPuO ₂ ⁺	sme_w2OHPuO ₂ ⁺ + 1.5H ₂ O = Pu(OH) ₃ ⁺ + 0.25O ₂ (aq) + sme_w2OH	-12.89
sme_w2OPuO ₂	sme_w2OPuO ₂ + 1.5H ₂ O + H ⁺ = Pu(OH) ₃ ⁺ + 0.25O ₂ (aq) + sme_w2OH	-7.68
sme_w2OPuO ₂ OH ⁻	sme_w2OPuO ₂ OH ⁻ + 0.5H ₂ O + 2H ⁺ = Pu(OH) ₃ ⁺ + 0.25O ₂ (aq) + sme_w2OH	2.52
sme_w1OHPuO ₂ ⁺	sme_w1OHPuO ₂ ⁺ + 1.5H ₂ O = Pu(OH) ₃ ⁺ + 0.25O ₂ (aq) + sme_w1OH	-14.14
sme_w1OPuO ₂	sme_w1OPuO ₂ + 1.5H ₂ O + H ⁺ = Pu(OH) ₃ ⁺ + 0.25O ₂ (aq) + sme_w1OH	-5.69
sme_w1OPuO ₂ OH ⁻	sme_w1OPuO ₂ OH ⁻ + 0.5H ₂ O + 2H ⁺ = Pu(OH) ₃ ⁺ + 0.25O ₂ (aq) + sme_w1OH	2.82
sme_w1OPu(OH) ⁺²	sme_w1OPu(OH) ⁺² + 2H ₂ O = Pu(OH) ₃ ⁺ + H ⁺ + sme_w1OH	-17.44
sme_w1OPu(OH) ₂ ⁺	sme_w1OPu(OH) ₂ ⁺ + H ₂ O = Pu(OH) ₃ ⁺ + sme_w1OH	-11.96
sme_w1OPu(OH) ₃	sme_w1OPu(OH) ₃ + H ⁺ = Pu(OH) ₃ ⁺ + sme_w1OH	-4.52
sme_w2OPu(OH) ₃	sme_w1OPu(OH) ₃ + H ⁺ = Pu(OH) ₃ ⁺ + sme_w2OH	-4.76
sme_w2OPu(OH) ₄ ⁺	sme_w1OPu(OH) ₄ ⁺ + 2H ⁺ = Pu(OH) ₃ ⁺ + sme_w2OH + H ₂ O	2.96

In Powell et al. [36], the surface complexation of Pu on smectite was modeled with two types of sites: the aluminol and silanol sites, which are conceptually equivalent to the weak sites 1 and 2 in our model. Reactions in Table 7-7 were rewritten in terms of $\text{Pu}(\text{OH})_3^+$ and $\text{O}_2(\text{aq})$ according to the following two reactions:

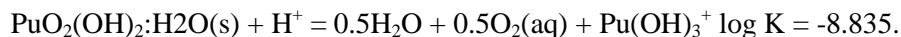
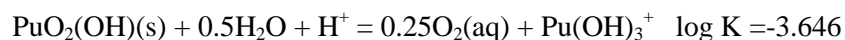
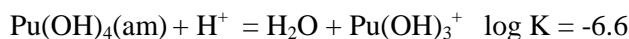
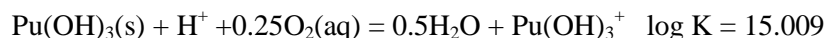


Surface complexation reactions are summarized in Table 7-8. These reactions need to be supplemented with a cation exchange to describe the measured data [36]:



Pu solid phase

Pu solid phases that are relevant for current modeling conditions are Pu oxides/hydroxides, including $\text{Pu}(\text{OH})_3(\text{s})$ for Pu(III), $\text{PuO}_2 \cdot 2\text{H}_2\text{O}$ (or $\text{Pu}(\text{OH})_4(\text{am})$) for Pu(IV), $\text{PuO}_2(\text{OH})(\text{s})$ for (Pu(V)), and $\text{PuO}_2(\text{OH})_2 \cdot \text{H}_2\text{O}(\text{s})$ for Pu(VI). Their reactions and solubility products ($\log K$) are listed below:



As mentioned by Runde et al. [13], the phase diagram of Pu oxides/hydroxides is not well understood. The solid $\text{Pu}(\text{OH})_4(\text{am})$ is the highly investigated one, and is sometimes expressed as $\text{PuO}_2(\text{hyd,aged})$ while still denoting the same Pu(IV) oxides/hydroxides. Experimental studies for Yucca Mountain [43-44] showed that plutonium hydroxides and/or colloids, aging towards $\text{PuO}_2 \cdot x\text{H}_2\text{O}$, are the solubility-controlling solids. In addition to Pu(IV) hydrous precipitates, Pu(IV) hydrolysis forms colloids, and the dissolved Pu could be controlled by both $\text{Pu}(\text{OH})_4(\text{am})$ and Pu colloids. However, as pointed out by Kim and Kanellakopoulos [45], “the experimental differentiation of the two equilibrium reactions is practically impossible.” In this report, we use the $\text{Pu}(\text{OH})_4(\text{am})$ as the solid phase to control the solubility of Pu in most simulations, but other phases were tested as well.

7.3 Modeling Results

It is assumed in the model that waste packages start to release Pu after 1000 years. Note that assuming that canister failure would occur in 1000 years is very conservative in comparison with other THM simulations on radionuclide migration. For example, De Windt et al. [46] assumed that canister failure occurs after 10,000 years. However, after 1000 years, the EBS bentonite becomes fully saturated and water-rock interactions are close to equilibrium conditions, THMC processes evolve very slowly thereafter, unless there were some incidents such as earthquakes. In other words, the THMC environment in which radionuclides migrate would not change substantially from 1000 years to 10,000 years. Therefore, it is expected that the starting time of Pu release, whether it be 1000 years or 10,000 years, would not affect Pu migration significantly. The modeling work consists of two steps. The first step

involves THC simulations for 1000 years, starting with an unsaturated EBS bentonite at 25°C. Using the concentrations, pressure, and temperatures obtained from the first step as initial conditions, the second step includes a series of THC simulations with Pu release.

7.3.1 THC Evolution in the First 1000 Years

TH evolution

The time function for heat release is shown in Figure 1. The temporal evolution of temperature at four monitoring points A, B, C, and D (see Figure 7-4 for their position) are shown in Figure 7-5. The temperature in EBS bentonite peaks at 100°C near the canister (see point A in Figure 7-5), and at 84°C at point B near the NS-EBS interface. After 1000 years, the temperature in EBS bentonite still stays >60°C. In the NS clay formation, the temperature is lower, but still approximately 60°C at a point 10 m from the canister (see point D in Figure 7-5). Figure 7-6 shows the degree of water saturation at these four points. It takes about 20 years to fully saturate EBS bentonite. The NS clay formation near the NS-EBS interface (point C) undergoes desaturation for a short time period.

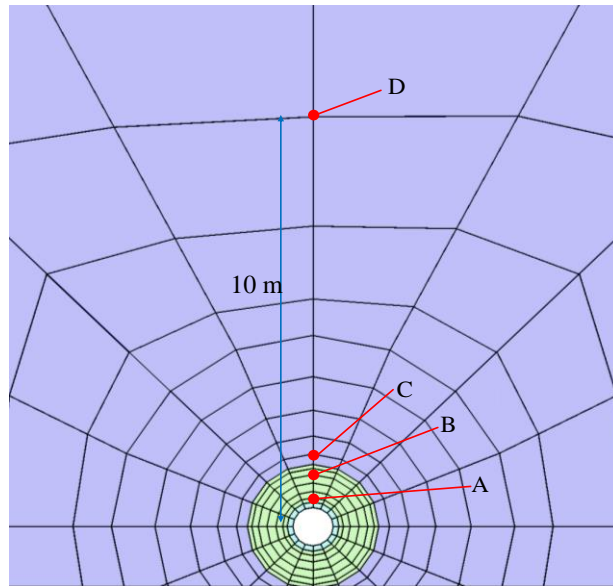


Figure 7-4. Location of key points for monitoring parameter variations in numerical simulations: Point A is near the canister; Point B is inside the bentonite and near the EBS-NS interface; Point C is inside the clay formation and near the EBS-NS interface; and point D is in the far field with a distance of canister of 10 m.

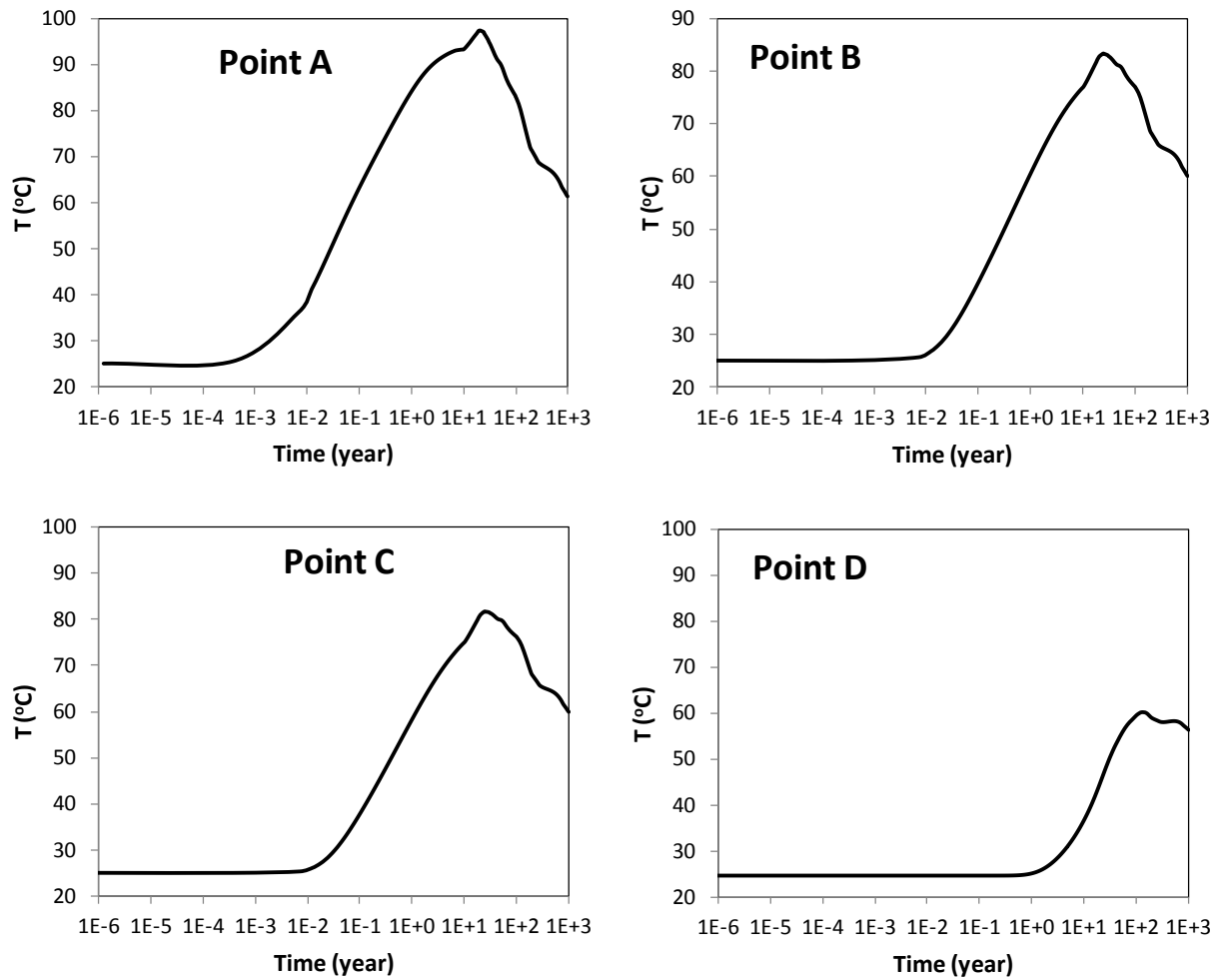


Figure 7-5. The temporal evolution of temperature at point A (near the canister), point B (inside the bentonite and near the EBS-NS interface), point C (inside the clay formation and near the EBS-NS interface), and point D (in the far field with a distance of canister of 10 m).

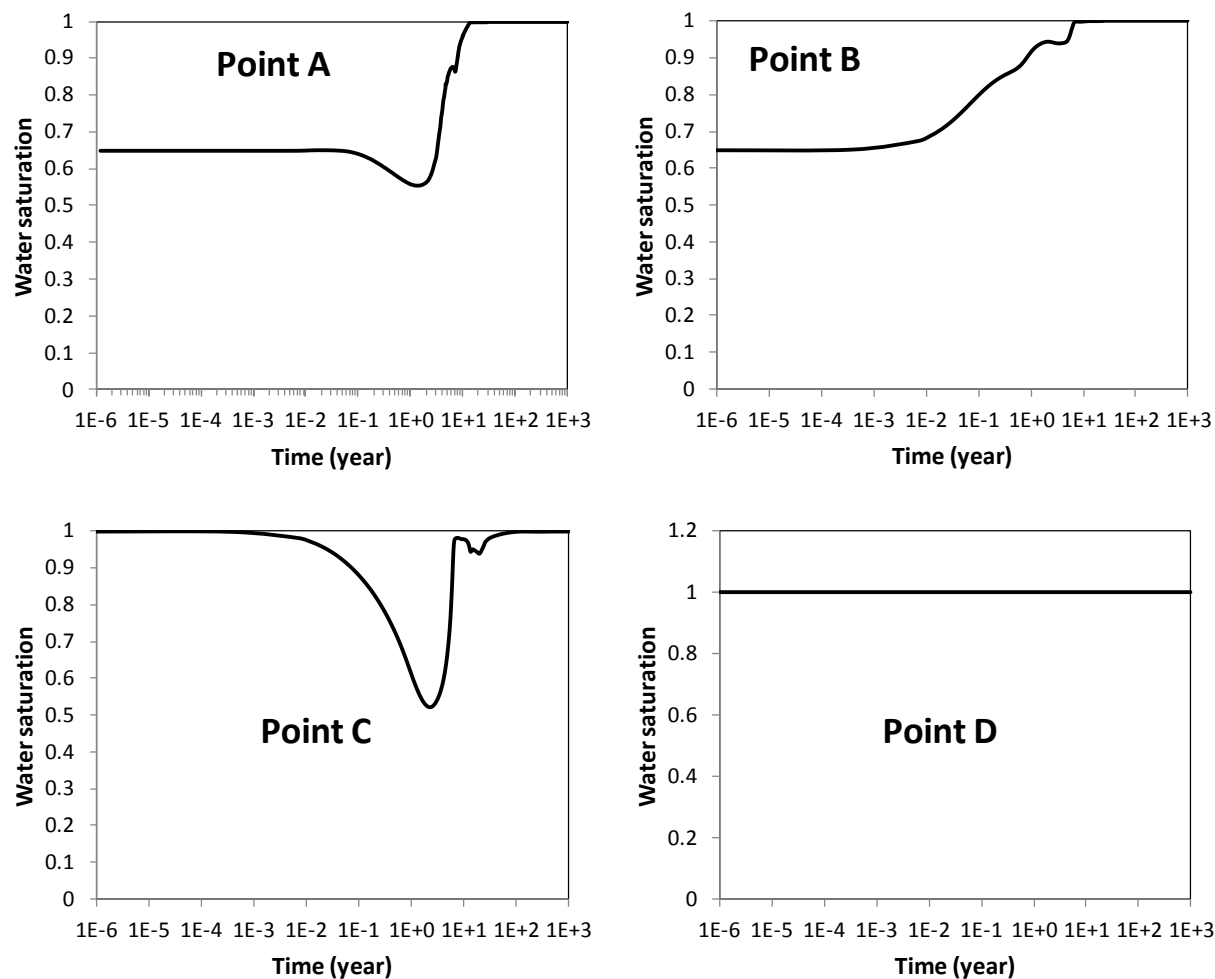


Figure 7-6. The temporal evolution of water saturation at point A (near the canister), point B (inside the bentonite and near the EBS-NS interface), point C (inside the clay formation and near the EBS-NS interface), and point D (in the far field with a distance of canister of 10 m).

Chemical evolution

Temporal changes in aqueous composition and mineral phase abundance in the EBS bentonite and the NS clay formation have been discussed in Zheng et al. [16]. In this report, we focus on the evolution of pH and Eh in the EBS bentonite and the NS clay formation, as they significantly impact the migration of Pu once the canister is corroded and starts releasing Pu. Because the current simulation does not consider any biological and organic reactions, the redox potentials in EBS bentonite and the NS clay formation are mainly controlled by inorganic reactions, among which the dissolution of pyrite is dominant. For a discussion of pH and Eh evolution in the EBS bentonite and the NS clay formation in the first 1000 years, we include two cases. First, in the base case, pyrite is present in both the EBS bentonite and the NS clay formation. Second, we present a case (“V(pyrite)=0”) in which the pyrite volume fraction is set to zero, partially because there is uncertainty in the presence of pyrite in these solids. In addition,

since the current simulation is generic in nature, this second case allows us to explore a system without any oxygen-consuming reactions, which would hence provide rather oxidizing conditions.

The pH changes in the EBS bentonite at the four monitoring points are illustrated in Figure 7-7. The area near the NS-EBS interface is most reactive as the EBS bentonite simultaneously undergoes heating, hydration, and the interactions between the EBS bentonite and NS clay formation. The pH value at point B starts to drop quickly, whereas the pH at point A (near the canister) starts to decrease later (since the water arrives here later). After the bentonite becomes fully saturated, the entire EBS bentonite shows very similar pH conditions; however, eventually the pH drops from 8 to ~ 6.2. The pH in the NS clay formation near the NS-EBS interface (point C) starts to decrease quickly, reaching a value of 6.4 after 1000 years. The pH value also drops at point D, which is at a distance of about 10 m from the canister. This is caused partially by the pH change at the NS-EBS interface, and more importantly, by the reactions occurring locally. Note that as shown in Figure 7-5, even at point D, the temperature triples, which will create geochemical changes. In contrast, an examination of modeling results at points several hundred meters away shows that there are little changes in pH at further distances, where the system experiences only minor disturbances by THC processes.

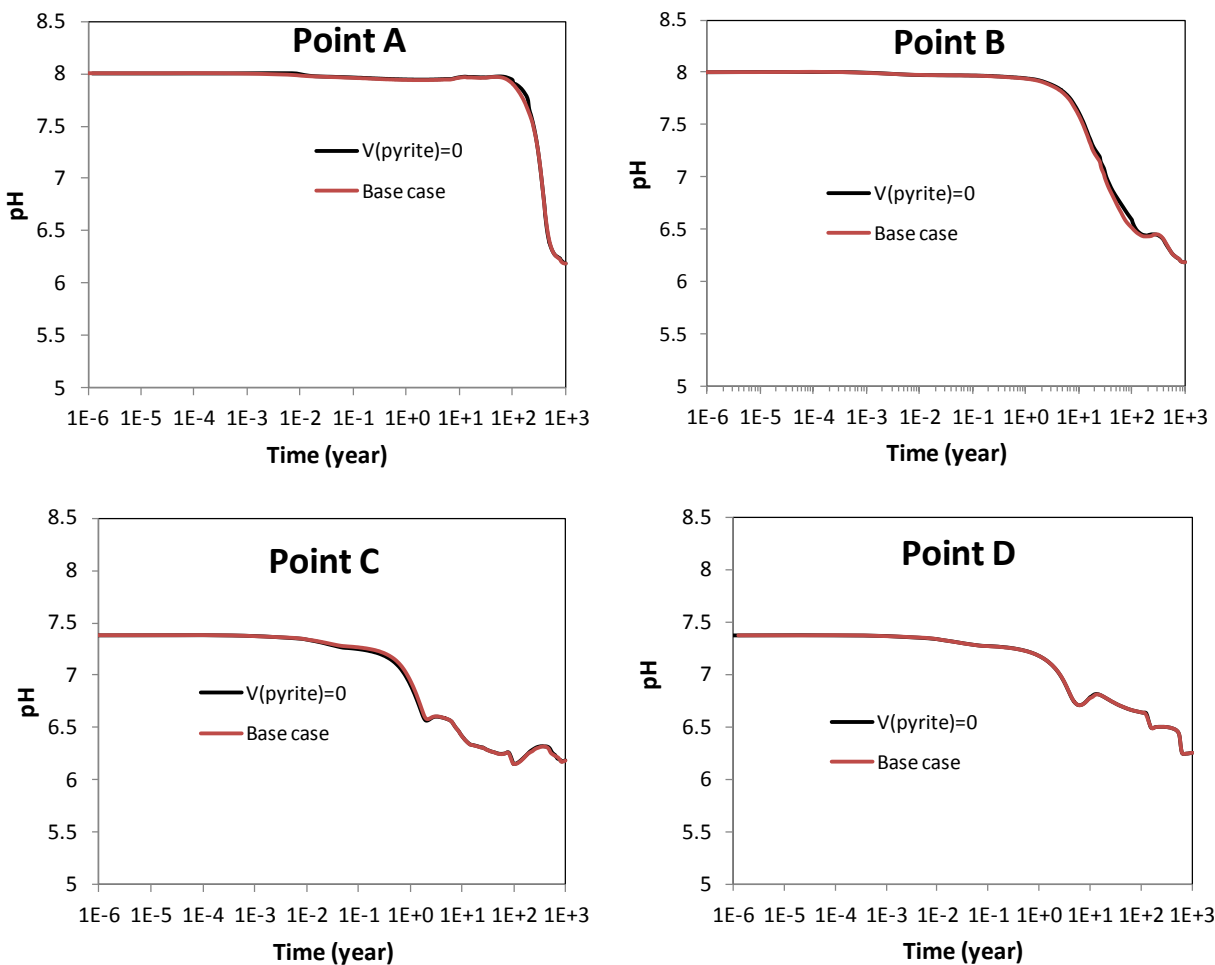
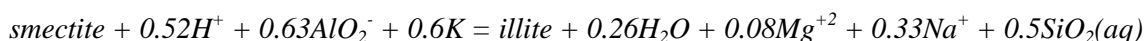


Figure 7-7. The temporal evolution of pH at point A (near the canister), point B (inside the bentonite and near the EBS-NS interface), point C (inside the clay formation and near the EBS-NS interface) and point D (in the far field with a distance of canister of 10 m).

Proton transfer is involved in many reactions. The overall rise or drop of pH is the net effect of all pH related reactions. In the current model, the reactions that lead to a decrease in pH are the precipitation of chlorite and dolomite. The precipitation of chlorite is described by the following reaction:



As shown in this reaction, the precipitation of chlorite generates protons and lowers pH. Figure 7-8 shows the volume fraction changes in chlorite. Chlorite precipitation is most relevant in the area near the NS-EBS interface. Chlorite forms as a byproduct of illitization, a process widely observed in geological systems [47]. Illitization in the EBS bentonite and the NS clay formation is discussed in more detail in another UFD report [48]. In this current report, illitization is modeled as the dissolution of smectite and precipitation of illite. The overall reaction can be written as:



As we can see from this equation, the illitization reaction consumes protons, and hence causes a rise in pH.

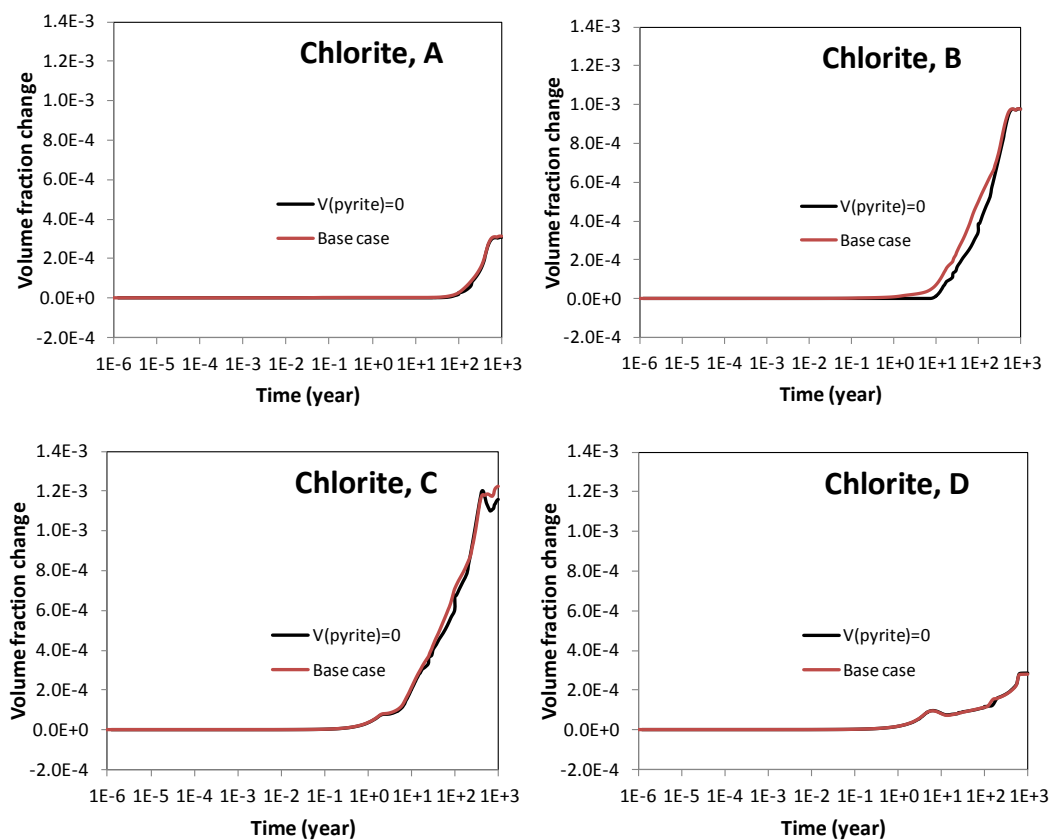


Figure 7-8. The temporal evolution of chlorite volume fraction change at point A (near the canister), point B (inside the bentonite and near the EBS-NS interface), point C (inside the clay formation and near the EBS-NS interface), and point D (in the far field with a distance of canister of 10 m).

Another reaction that acidifies the water is the precipitation of dolomite triggered by the dissolution of calcite. Figures 9 and 10 depict the calculated changes in calcite and dolomite volume fractions at points A, B, C, and D. The overall reactions can be written as:



As the reaction proceeds towards the right-hand side, the concentration of protons (H^+) increases and the pH decreases. When the EBS bentonite is heated, calcite becomes unstable and is transformed into dolomite. Another reason for the dissolution of calcite is the initial disequilibrium between calcite and the aqueous phase in the EBS bentonite.

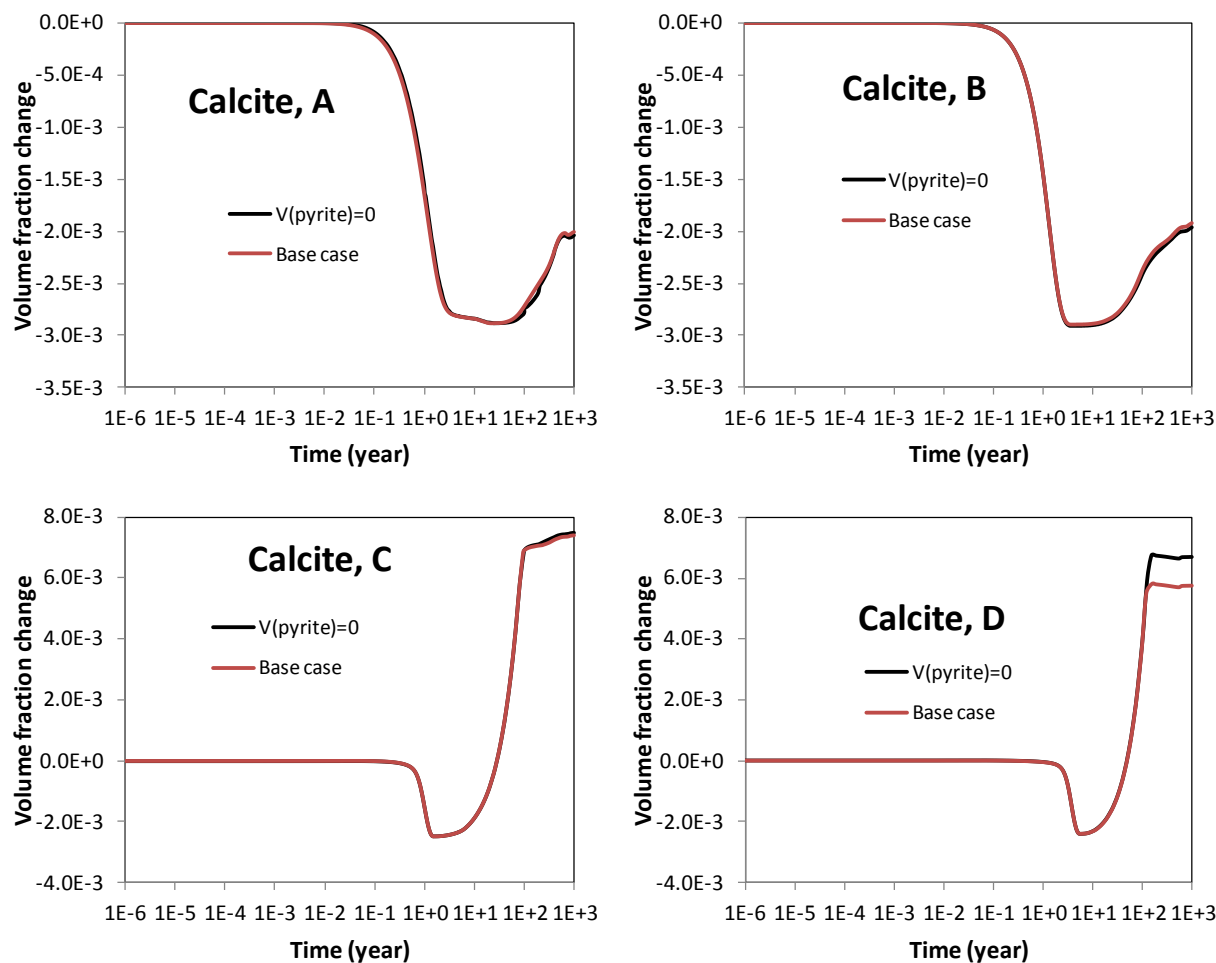


Figure 7-9. The temporal evolution of calcite volume fraction change at point A (near the canister), point B (inside the bentonite and near the EBS-NS interface), point C (inside the clay formation and near the EBS-NS interface), and point D (in the far field with a distance of canister of 10 m).

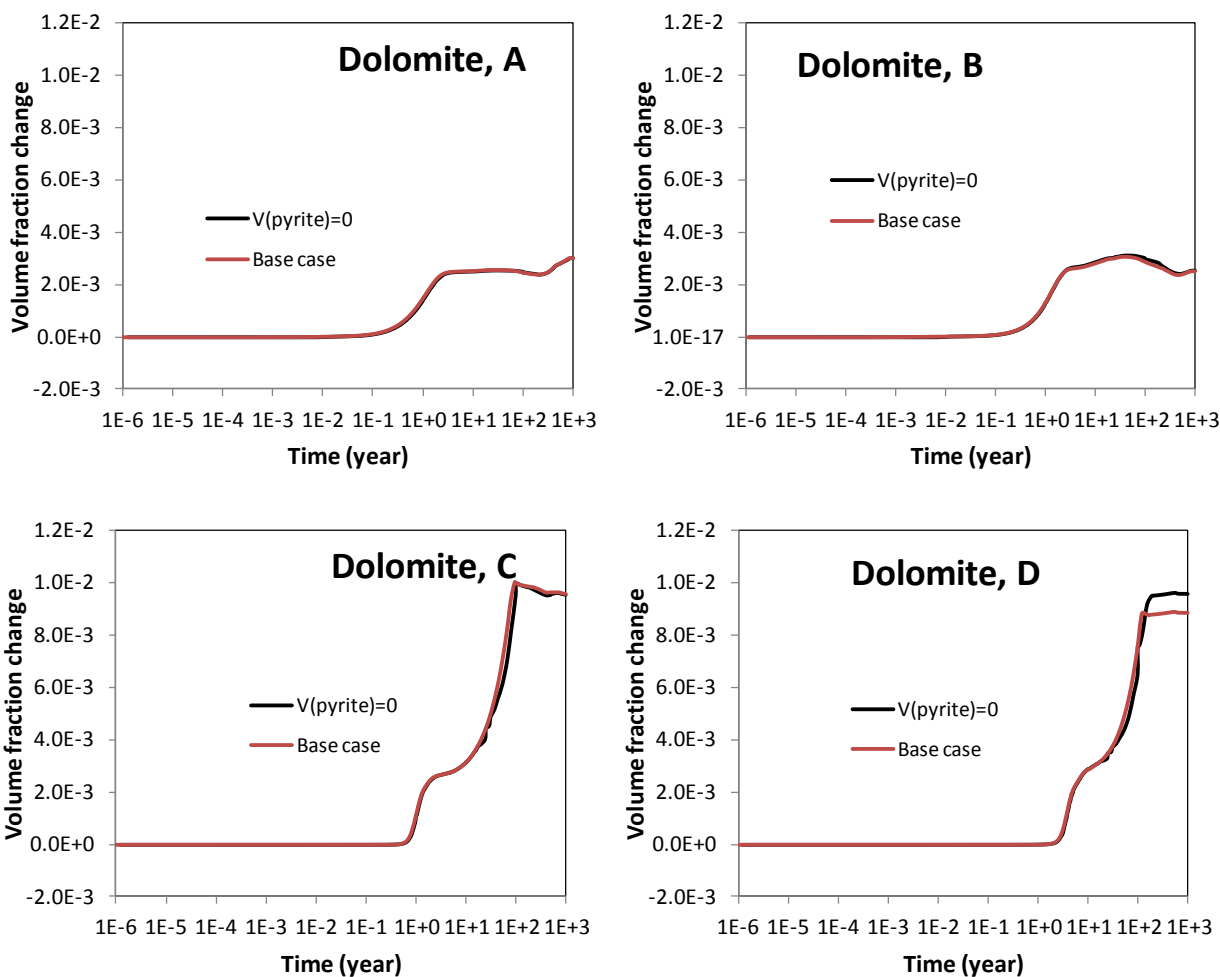
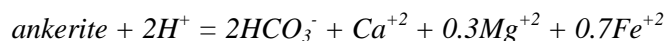


Figure 7-10. The temporal evolution of dolomite volume fraction change at point A (near the canister), point B (inside the bentonite and near the EBS-NS interface), point C (inside the clay formation and near the EBS-NS interface), and point D (in the far field with a distance of canister of 10 m).

In the NS clay formation, although the transformation of calcite into dolomite is observed initially for a short time period, in the long run we can observe both a precipitation of calcite and dolomite (see results at points C and D in Figures 7-9 and 7-10), as a result of the dissolution of ankerite (See Figure 7-11). As shown in the Table 7-1, the NS clay formation contains about 3% of ankerite, while the ankerite content in the EBS bentonite is zero. The dissolution of ankerite is written as the following reaction:



This reaction is really the driving force for calcite and dolomite precipitation, due to increasing Ca^{2+} and carbonate concentrations above their respective solubility limit. The reason for calcite to dissolve and for dolomite to precipitate during a short time period (see Figure 7-9) is that calcite dissolves at a much faster rate than ankerite, and thus ankerite dissolution takes effect only at a later time.

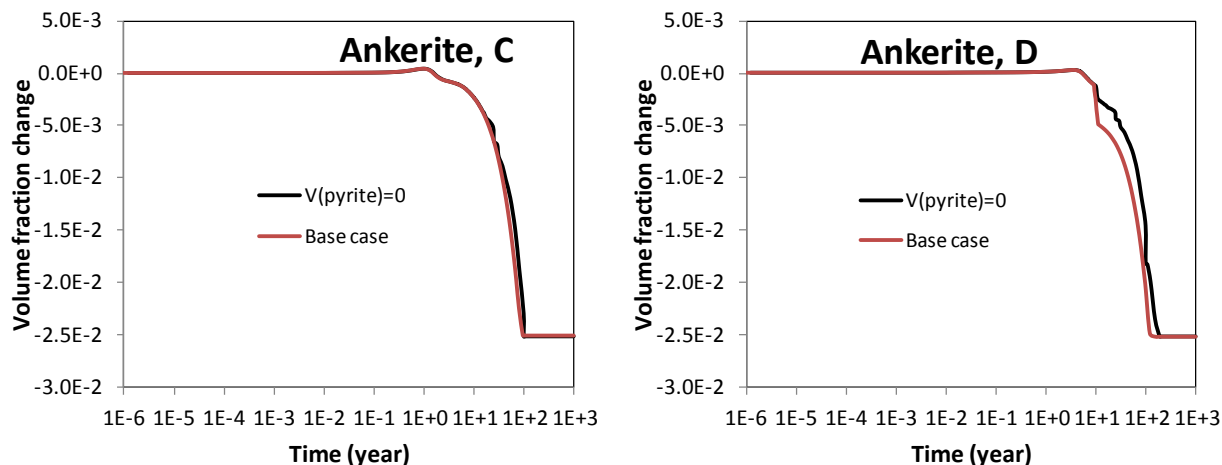


Figure 7-11. The temporal evolution of ankerite volume fraction changes at point C (inside the clay formation and near the EBS-NS interface) and point D (in the far field with a distance of canister of 10 m).

In summary, in EBS bentonite, the precipitation of chlorite and dolomite, which leads to a pH decrease, outpaces the illitization and calcite dissolution, which would lead to a pH increase. This causes a gradual pH decrease from 8 to 6.2. In the NS clay formation, where a small fraction of ankerite is present, the precipitation of chlorite, calcite, and dolomite lead to a decrease in pH, which overcome the pH-rising reactions, including illitization and dissolution of ankerite, and lead to a drop of pH from 7.4 to 6.4.

The Eh evolution in the EBS bentonite and the NS clay formation is illustrated by the time evolution of Eh at points A, B, C, and D in Figure 7-12. As mentioned above, in order to explore the migration of Pu under different redox potentials, we simulate a base case in which pyrite is present in both the EBS bentonite and the NS clay formation, and for a case (“V(pyrite)=0”) in which the pyrite volume fraction is set to zero. The pyrite volume fraction changes are depicted in Figure 7-13.

Initially, the Eh in the EBS bentonite is ~750 mV, which is calculated based on the assumption that the aqueous phase in EBS bentonite is in equilibrium with the atmosphere. After the EBS bentonite is installed, the whole system is closed; hence, there is no longer any external supply of oxygen. In the base case, Eh decreases to -200 mV as a result of the consumption of dissolved oxygen by the dissolution of pyrite in the EBS bentonite. Later on, as the pH decreases and pyrite starts to precipitate, the Eh recovers slightly until it reaches around 10 mV after 1000 years. In the “V(pyrite)=0” case, there is no process that controls the redox conditions in the EBS bentonite. Thus, the Eh remains at its initial value for a short time-period until the Eh in the EBS bentonite is equilibrated with the Eh conditions in the NS clay formation, where Eh is around 230 mV.

The initial Eh in the NS clay formation is calculated from the measured concentrations of the redox couple Fe^{+2}/Fe^{+3} , which is 235 mV. Fernandez et al. (2007) measured the redox potential (Eh) in the Opalinus Clay which ranges from -24.2 mV to 83 mV. However, it is well known [34] that field measurements of Eh values are rarely reliable. In the base case, the dissolution of pyrite quickly shifts the Eh down to -200 mV, but the decrease in pH creates a gradual Eh increase later. After 1000 years, the Eh in the NS clay formation is ~ -6 mV. For the “V(pyrite)=0” case, the Eh in the NS clay formation stays around 200 mV, fluctuating with the changes in pH.

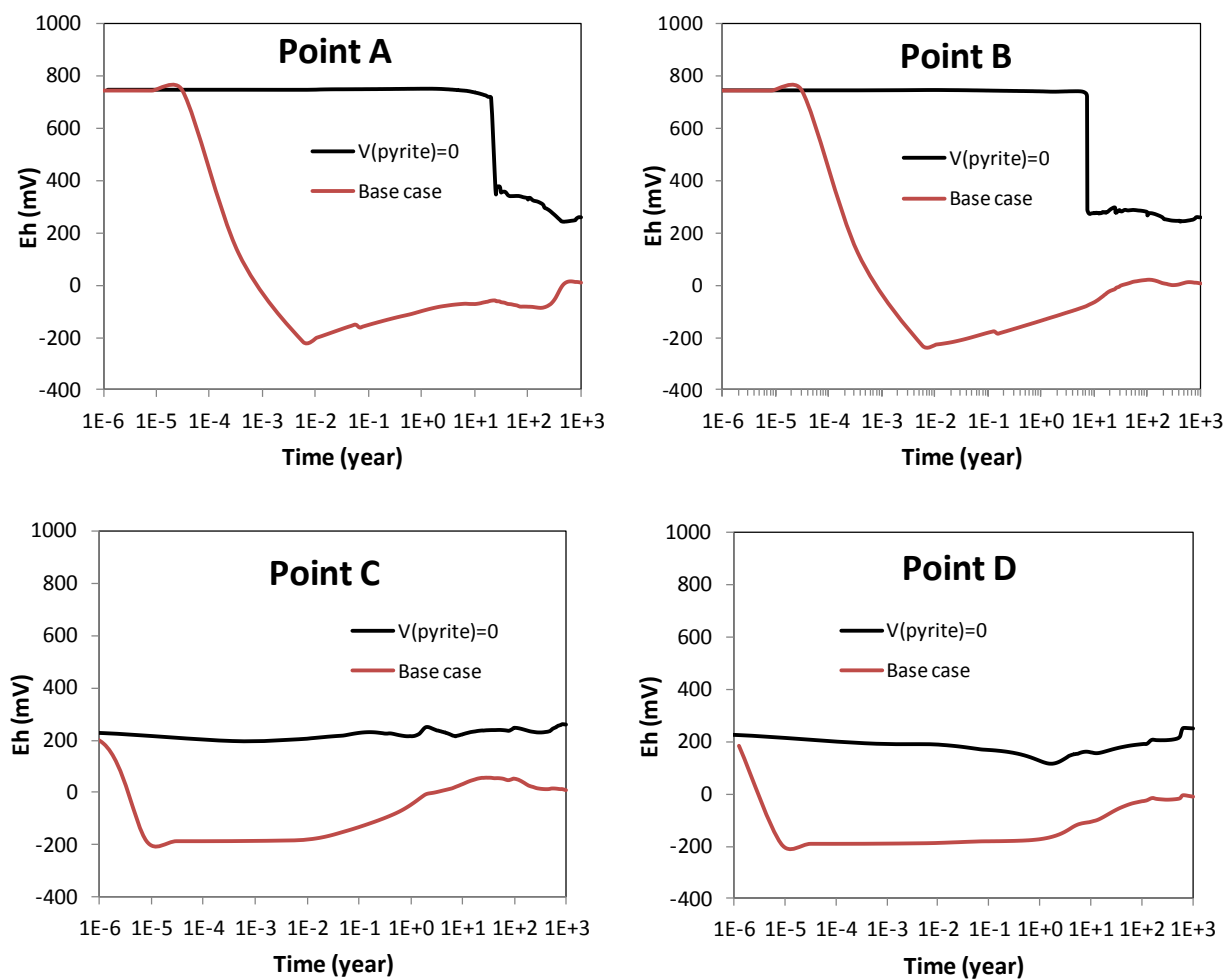


Figure 12. The temporal evolution of Eh at point A (near the canister), point B (inside the bentonite and near the EBS-NS interface), point C (inside the clay formation and near the EBS-NS interface), and point D (in the far field with a distance of canister of 10 m).

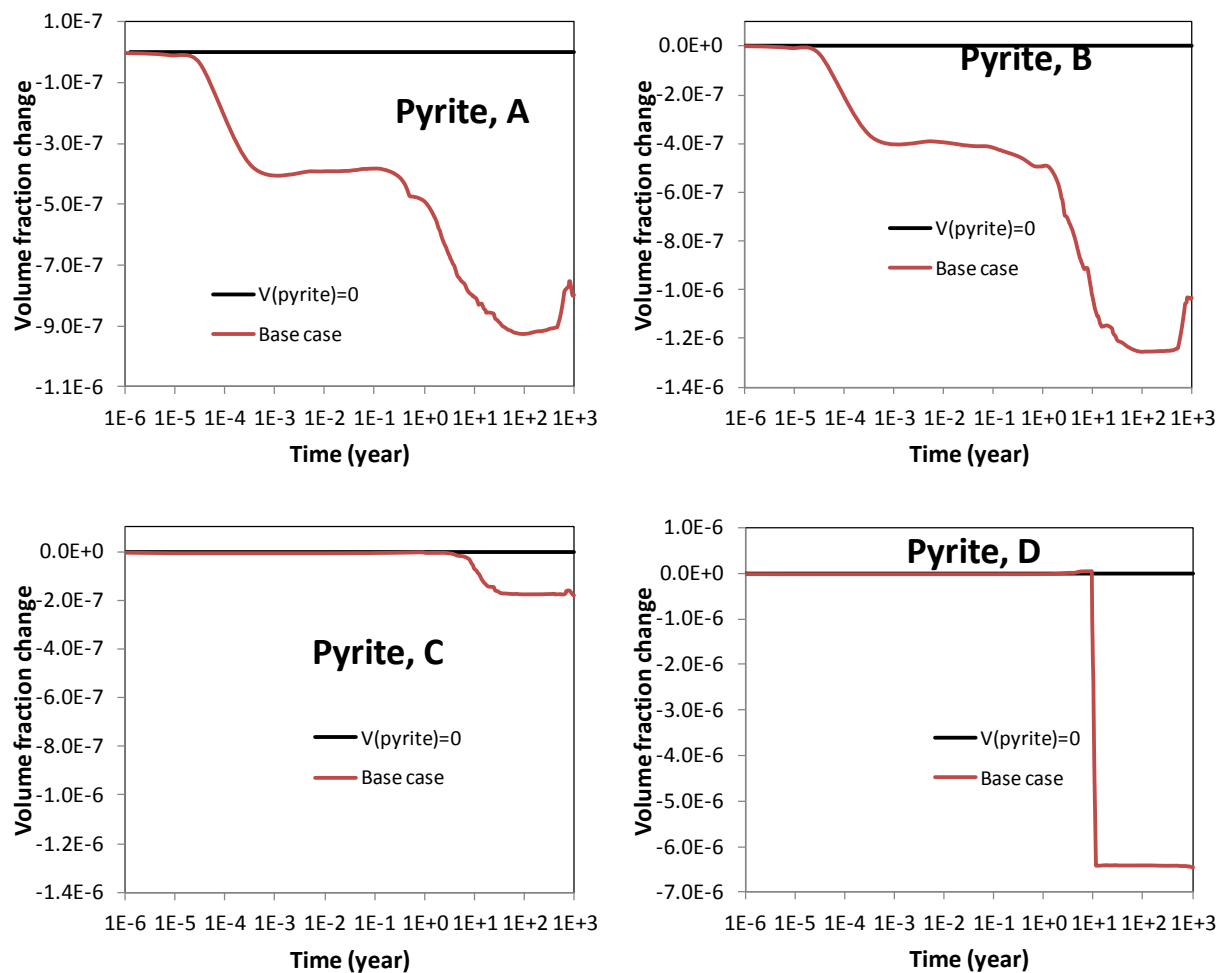


Figure 7-13. The temporal evolution of pyrite volume fraction change at point A (near the canister), point B (inside the bentonite and near the EBS-NS interface), point C (inside the clay formation and near the EBS-NS interface), and point D (in the far field with a distance of canister of 10 m).

7.3.2 THC Evolutions and Pu Migration until 10000 Years

In our current model, it is assumed that canisters have fully degraded after 1000 years. While section 7.2 described the pH/Eh conditions for the first 1000 years, in this section, we focus on the migration of Pu within time frames from 1000 to 10,000 years. We first present a short discussion of the THC changes from 1000 to 10,000 years, to set up the conditions under which Pu is released and transported.

THC evolution

As shown in the previous section, after the temperature profile peaks at ~20 years, the temperature gradually decreases, although the EBS bentonite and NS clay formation remain heated for a long time. From 1000 to 10,000 years, the EBS bentonite and NS clay formation in the near field are at temperature conditions between 45 to ~60°C (Figure 7-14).

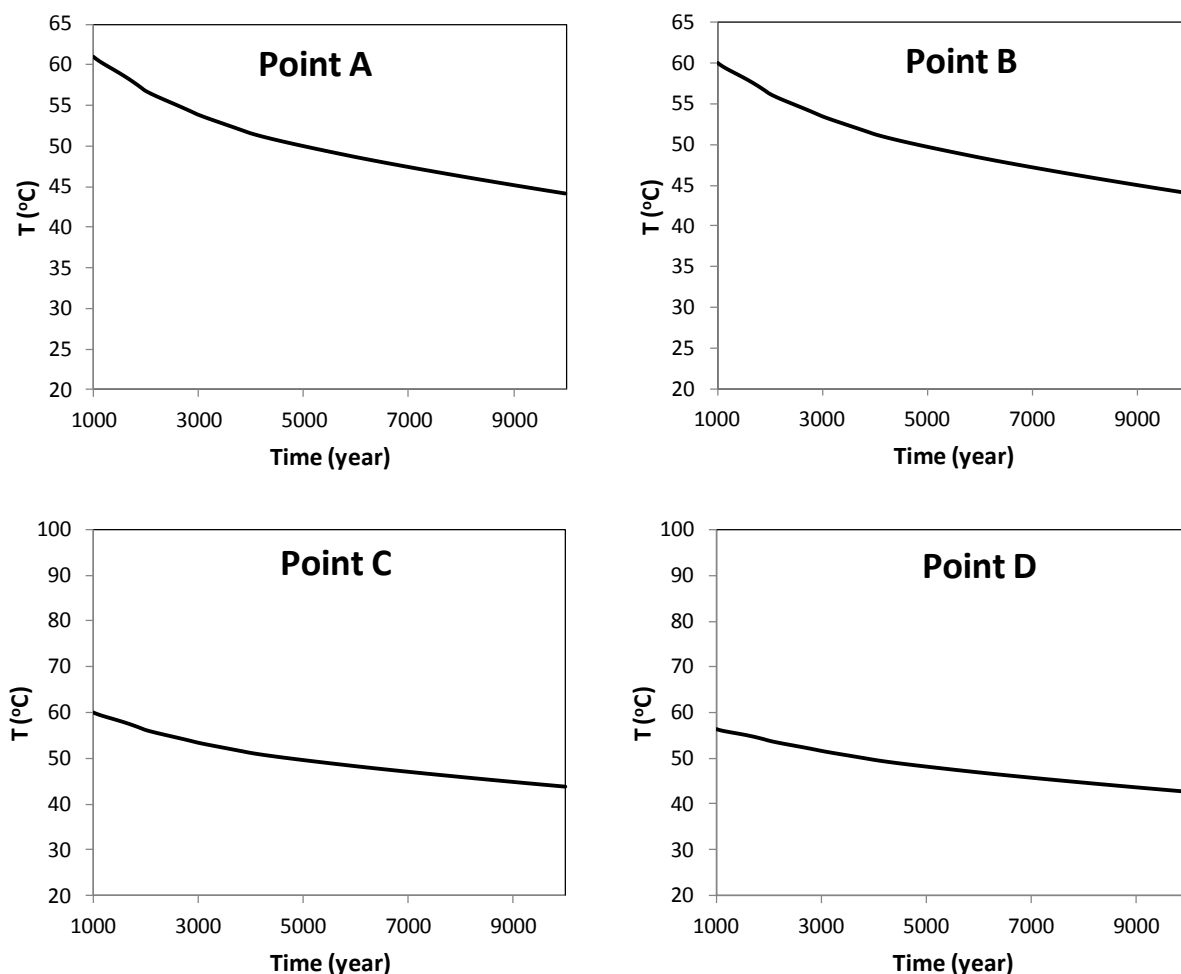


Figure 7-14. The temporal evolution of temperature at point A (near the canister), point B (inside the bentonite and near the EBS-NS interface), point C (inside the clay formation and near the EBS-NS interface), and point D (in the far field with a distance of canister of 10 m) from 1000 years to 10,000 years.

After 1000 years, most reactions are close to equilibrium and temperature decreases. Both of these two phenomena slow down reaction rates. As a result, the pH does not change much—only slightly increasing by 0.15 pH units from 1000 to 10,000 years at points A, B, C, and D (Figure 7-15). The EBS bentonite and the NS clay formation in the near field stay at slightly acidic conditions with a pH of ~ 6.4 . The base case and the “ $V(\text{pyrite})=0$ ” case have the same pH trends, because the fairly small dissolution of pyrite has minimal impact on pH.

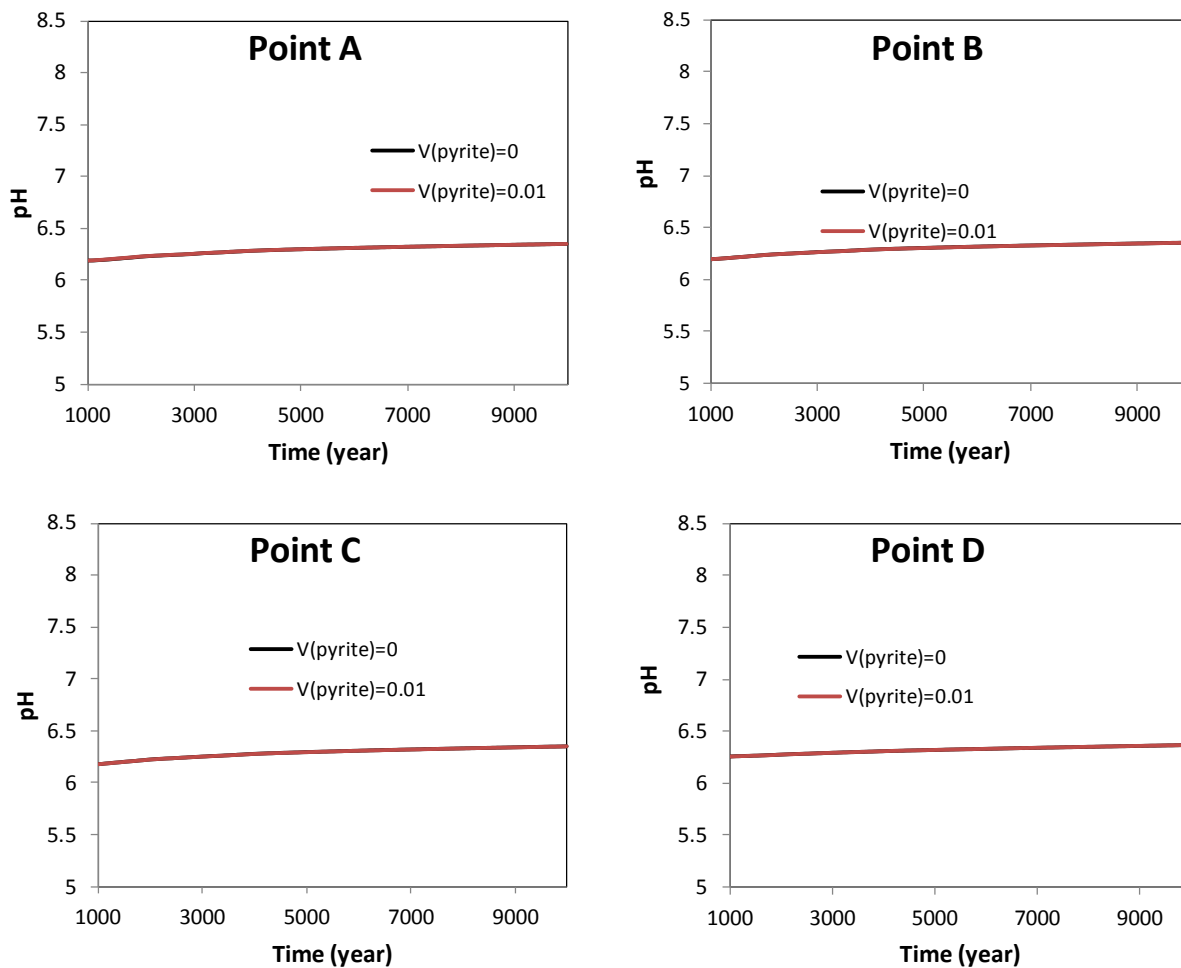


Figure 7-15. The temporal evolution of pH at point A (near the canister), point B (inside the bentonite and near the EBS-NS interface), point C (inside the clay formation and near the EBS-NS interface) and point D (in the far field with a distance of canister of 10 m) from 1000 years to 10,000 years.

Similar to pH, the Eh in the EBS bentonite and the NS clay formation does not change much either (see Figure 7-16). However, the base case and the “ $V(\text{pyrite})=0$ ” case exhibit very different levels of Eh, which provides us with an opportunity to examine the release and migration of Pu under oxidizing (the “ $V(\text{pyrite})=0$ ” case) and mildly reducing conditions (the base case).

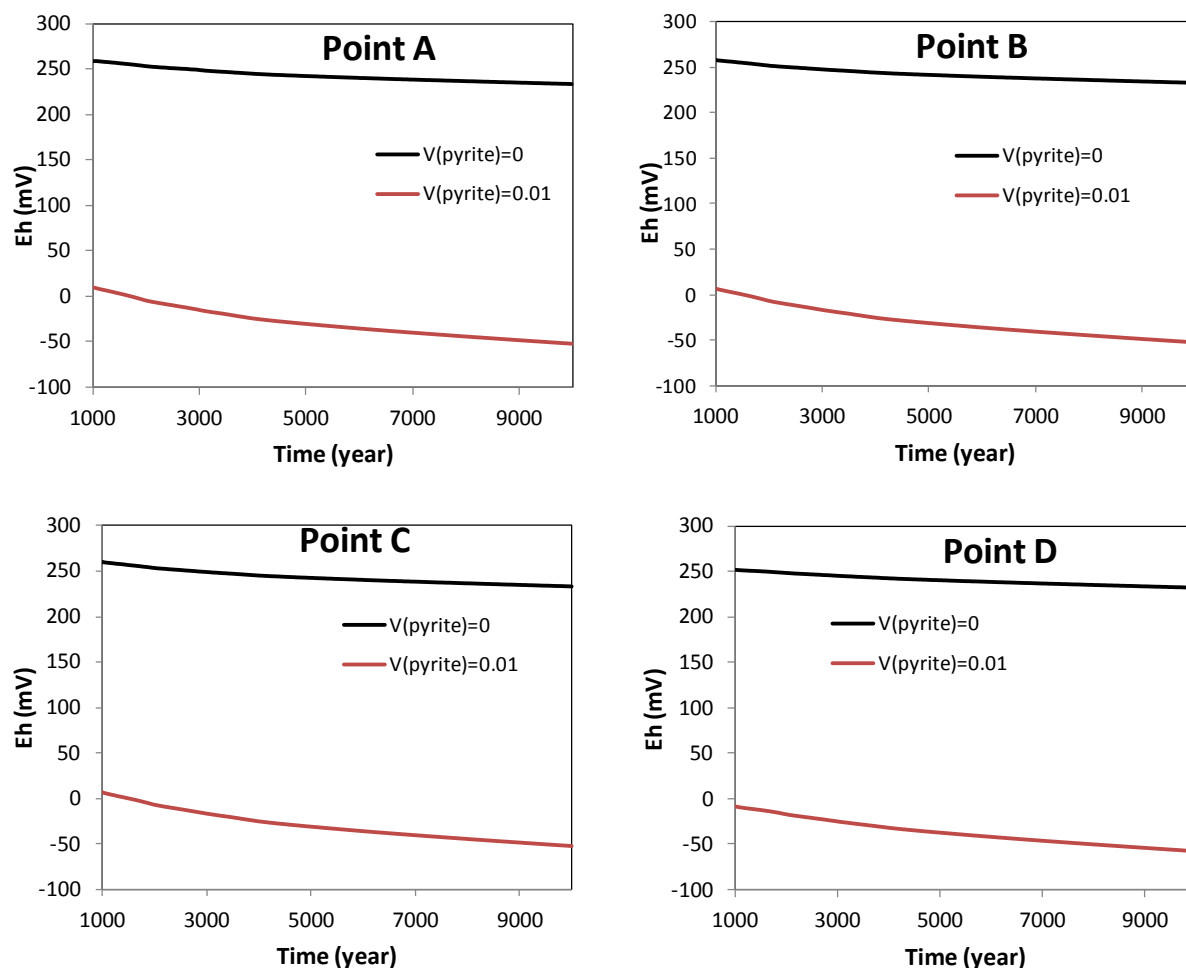


Figure 7-16. The temporal evolution of Eh at point A (near the canister), point B (inside the bentonite and near the EBS-NS interface), point C (inside the clay formation and near the EBS-NS interface) and point D (in the far field with a distance of canister of 10 m) from 1000 to 10,000 years.

Pu migration

Base case — reducing scenario: There are two major assumptions regarding Pu chemical reactions that we should bear in mind while we discuss the model results of Pu. The first one is that the kinetics of Pu minerals dissolution is not considered here, such that the concentration of Pu at the canister is therefore controlled solely by the solubility of these minerals. On the one hand, we are conservative in these modeling exercises. On the other, the kinetics of these minerals is very poorly understood, and actually no kinetics data were found in our current literature review. The second one is that the Pu colloid is not considered here, mainly because thermodynamics between the aqueous phase, solid phase, and colloid are still not very clear; considering the Pu colloid is certainly warranted in future work.

When simulating the release of Pu from the canister to the surrounding environment, the first question is which Pu oxidation state is present in the solid phase in the canister. The Pu oxidation state distribution versus Eh (see Figure 7-17) given by Runde et al. (2002) is a good guideline. Note that Figure 7-17 is based on a pH of 7, while we find a pH of 6.4 in our simulations. However, because the Eh changes just slightly when pH increases from 6.4 to 7, Figure 7-17 remains a good guideline for selecting the oxidation states of Pu in the solid phase. In the base case, when Pu starts to be released from the canister (1000 years), the Eh value at the canister is 10 mV, which indicates that both Pu(III) and Pu(IV) solid phases are possible. We therefore assumed for the base case that the dissolution of Pu(OH)₄(am) controls Pu concentrations in solution. A sensitivity case in which Pu(OH)₃(s) is the solid phase that controls Pu release from the canister will be presented later, in order to illustrate the differences caused by variation in the controlling solid phases.

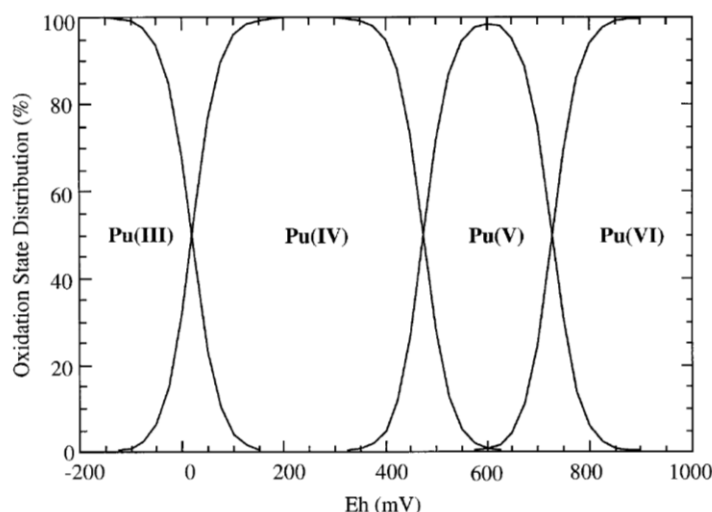


Figure 7-17. The calculated stabilities of Pu(III), (IV), (V), and (VI) as a function of Eh at a pH of 7 and 2.8 mmol total carbonate (Runde et al., 2002).

In the reducing scenario, the dissolution of Pu(OH)₄(am) at the canister leads to a Pu concentration of $\sim 2 \times 10^{-9}$ mol/kg. As Pu migrates through the EBS bentonite, the current modeling results suggest that Pu is significantly retarded. Figure 18 shows the concentrations of total aqueous Pu, a surface complex (sme_w1OPu(OH)₂⁺) and the Pu on the exchangeable sites (X-Pu(OH)₃⁺). As shown in Figure 7-18, Pu is strongly adsorbed to the surface of smectite, with sme_w1OPu(OH)₂⁺ being the dominant surface species. Exchangeable Pu, the X-Pu(OH)₃⁺, seems to play a very minimal role in retarding Pu. Figure 7-19 shows the concentration of total aqueous Pu at points A, B, C, and D. Because of the relatively low Pu solution concentrations at the canister, as well as the strong adsorption of Pu onto smectite surfaces, Pu barely moves out of the EBS bentonite, and the Pu concentration at point D (10 meters away from the canister) is close to zero.

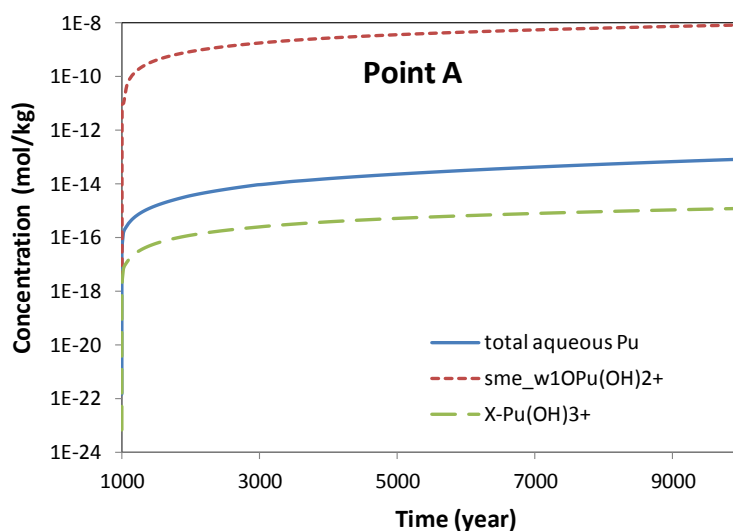


Figure 7-18. The temporal evolution of the concentration of total aqueous Pu, a surface complex (sme_w1OPu(OH)_2^+), and the Pu on the exchangeable sites (X-Pu(OH)_3^+) at point A from 1000 to 10,000 years for the base case with “ $\text{Pu(OH)}_4(\text{am})$ ” as the controlling solid phase.

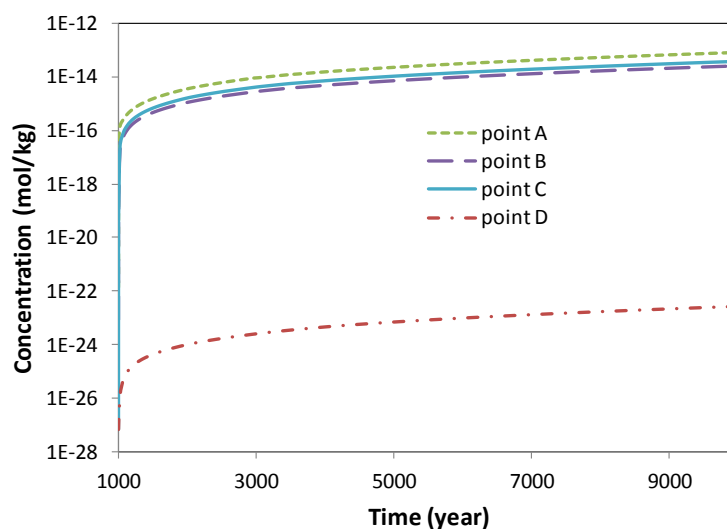


Figure 7-19. The temporal evolution of the concentration of total aqueous Pu at points A, B, C, and D, from 1000 to 10,000 years for the base case with “ $\text{Pu(OH)}_4(\text{am})$ ” as the controlling solid phase.

Typically, in the models for performance assessment, the K_d approach is used due to its simplicity and low computational cost. In this report, we review the published K_d values of Pu for smectite. The maximum is 19,000 mL/g [41], whereas the K_d value of 5800 mL/g measured in Runde et al. [13] is in the lower range. Simulations were also conducted with these two K_d values. The calculated concentrations of Pu in these simulations are compared with that in the base-case model, which used surface complexation reactions derived in Powell et al.[36]. Here, we show the comparison of concentration at point A as an example (see Figure 7-20). Surface complexation reactions derived in Powell et al. [36] lead to an adsorption behavior similar to a K_d of 19,000 mL/g.

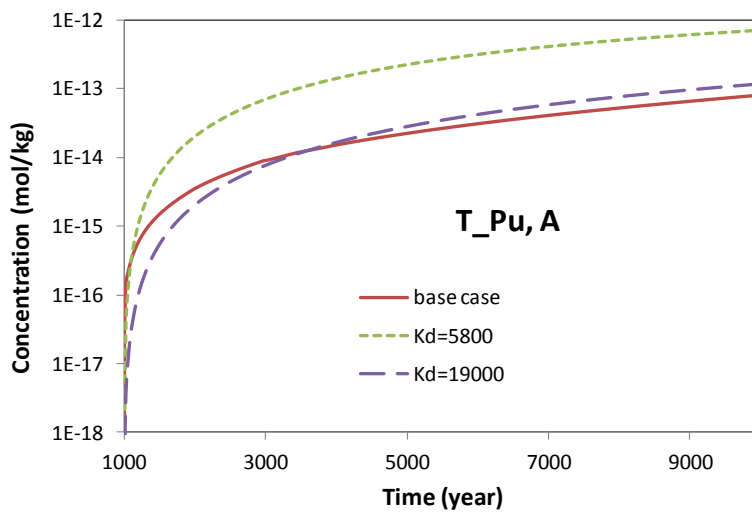


Figure 20. The concentration of total aqueous Pu (T_Pu) at point A calculated with K_d values of 5800 mL/g and 19,000 mL/g and surface complexation reactions (the base case).

The effect of controlling solid phases: In a sensitivity case, referred to as “Pu(OH)₃(s)” below, we used Pu(OH)₃(s) as the solid phase that controls the release of Pu from the canister. The dissolution of Pu(OH)₃(s) produces a Pu concentration of $\sim 3 \times 10^{-4}$. This value is about 5 orders of magnitude higher than the one in the base case with Pu(OH)₄(am) as the controlling solid phase. Subsequently, the concentration of Pu in the EBS bentonite and the NS clay formation is much higher for the “Pu(OH)₃(s)” case than the base case, as shown in Figure 7-21. The dramatic differences in the calculated concentrations of Pu caused by the choice of the dominant solid phase illustrate the importance of thermodynamic data. Among all Pu species, probably Pu(III) solid and aqueous phases are the least studied, owing to the experimental difficulties of maintaining Pu(III) in the aqueous phase. An additional reason could be that the Yucca Mountain project used to drive the study of radionuclide thermodynamic data. At Yucca Mountain, no backfill material was proposed, and the host rock remained under unsaturated conditions; thus, the redox environment under which radionuclides react was expected to be oxidizing. As a result, researchers largely focused on Pu(IV) and Pu(V) phases [13, 36].

Similar to the base case, as shown in Figure 7-22, the strong adsorption keeps the aqueous concentration of Pu in the EBS bentonite at low levels. As Pu moves out of the EBS bentonite, the aqueous concentration of Pu is lowered to values on the order of 10^{-9} M, about 5 orders of magnitude lower than the initial concentration at the canister.

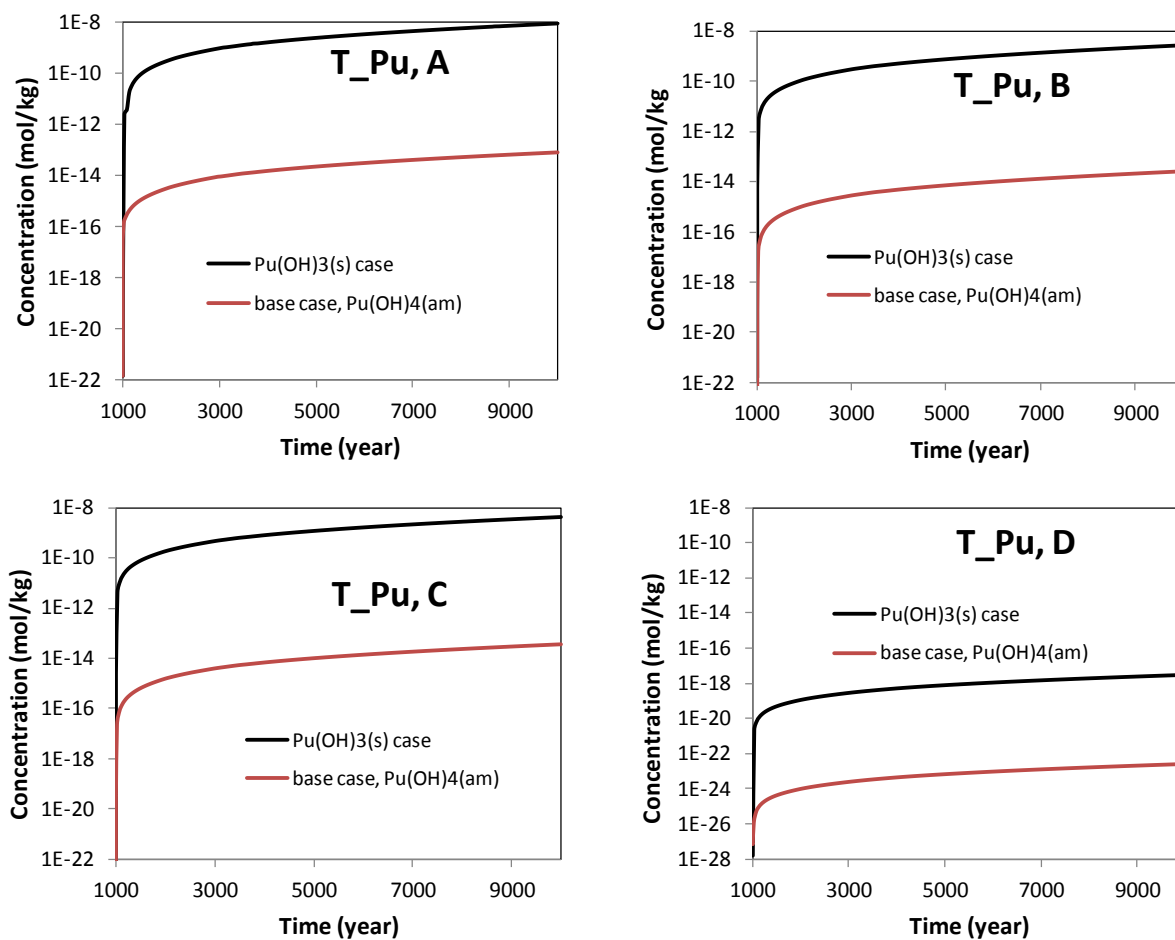


Figure 7-21. The temporal evolution of total aqueous Pu (T_Pu) at points A, B, C, and D for the “Pu(OH)₃(s)” case and the base case which includes “Pu(OH)₄(am)” as the controlling solid phase.

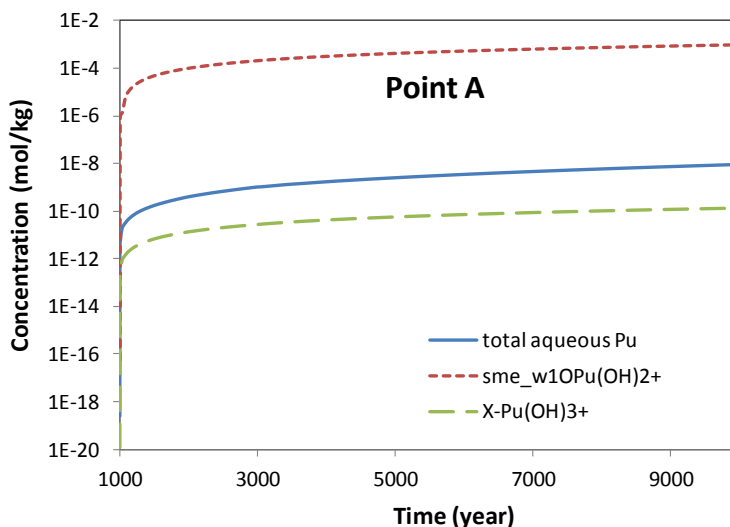


Figure 7-22. The temporal evolution of the concentration of total aqueous Pu, a surface complex (sme_w1OPu(OH)_2^+) and the Pu on the exchangeable sites (X-Pu(OH)_3^+) at point A from 1000 to 10,000 years for the “ $\text{Pu(OH)}_3(\text{s})$ ” case.

The effect of Pu(III) aqueous complexes: The temporal evolution of total aqueous Pu (T_Pu) at points A, B, C, and D for the base case and the sensitivity case where no Pu(III) aqueous complexes shown in Figure 7-23. A close examination of the aqueous speciation of Pu at point A reveals that the Pu(III) species Pu^{+3} , PuSO_4^+ , PuCl^{+2} , PuOH^{+2} , and $\text{Pu(SO}_4)_2^-$ are dominant, with concentrations of about 1 order of magnitude higher than the major Pu(IV) species, $\text{Pu(OH)}_2(\text{CO}_3)_2^-$. This is understandable, since Pu(III) should control Pu solution speciation in the rather reducing conditions of the base case. However, there might be an inconsistency—the surface complexation reactions and their reaction constants describe Pu(IV) sorption [36] under oxidizing conditions, while Pu(III) species dominate the aqueous phase under reducing conditions. Will including Pu(III) aqueous species lead to an overestimation of total aqueous Pu concentrations? To answer this question, we conducted a sensitivity case in which all Pu(III) aqueous complexes were taken out from the simulation. Removing Pu(III) aqueous complexes first leads to a lower solubility of $\text{Pu(OH)}_4(\text{am})$ at the canister: the total aqueous concentration of Pu is now 1.2×10^{-10} mol/kg, which is about 17 times lower than in the base case (2×10^{-9} mol/kg). Consequently, the total aqueous concentrations of Pu in the EBS bentonite and the NS clay formation in the sensitivity case are much lower than those in the base case. The difference is more than three orders of magnitude, which is disproportional to the difference in the concentrations at the canister. The reason is that strong aqueous complexes, which were to be Pu(III) complexes if included, would keep Pu in the aqueous phase and therefore increase its total aqueous concentrations. In the sensitivity case, the deficiency in Pu(III) aqueous complexes drives more Pu to form surface species. Hence, the total aqueous concentrations of Pu are disproportionally lower than expected from the differences in Pu concentrations at the canister alone. The observations from this sensitivity analysis highlight the strong need for thermodynamic data describing Pu(III) sorption, assuming that the EBS bentonite and the NS clay formation are under reducing conditions.

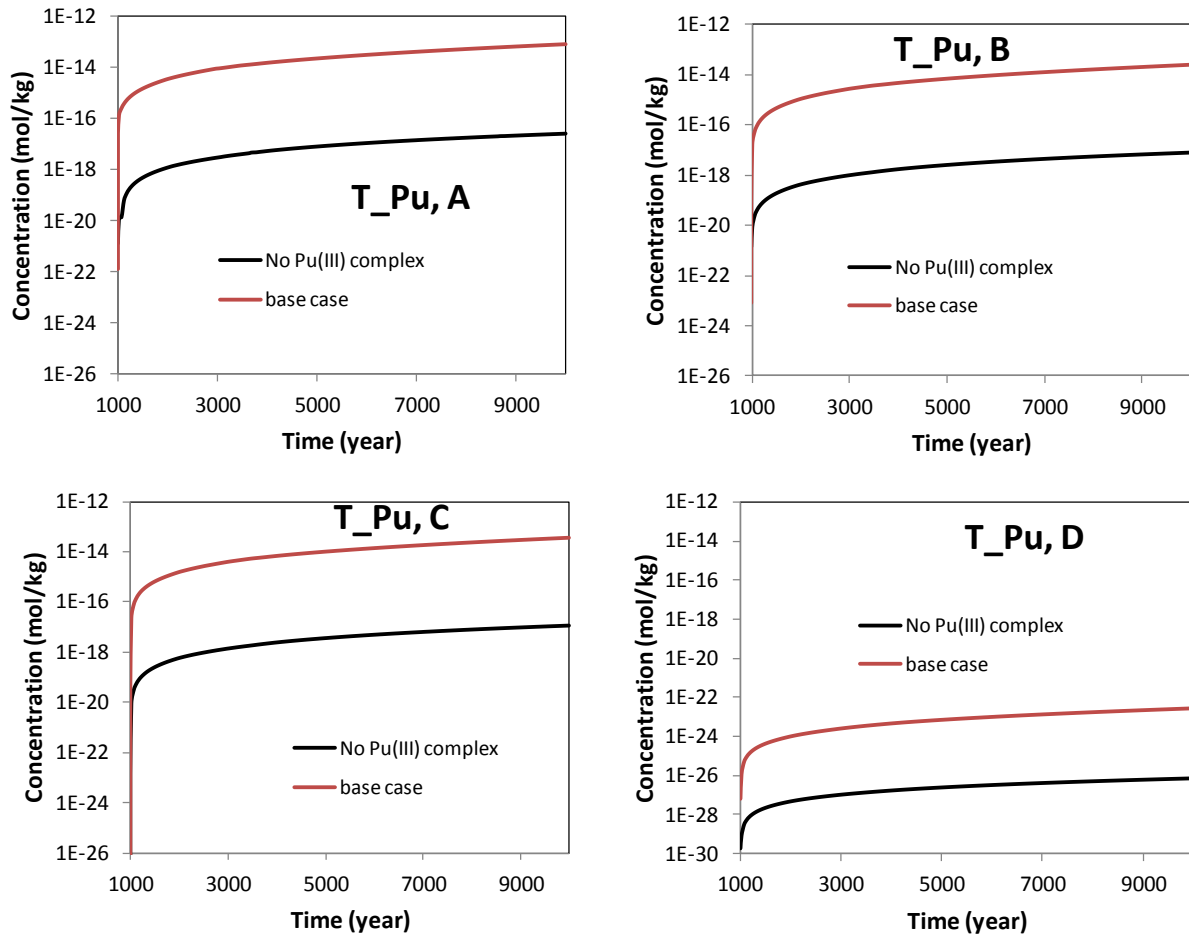


Figure 7-23. The temporal evolution of total aqueous Pu (T_Pu) at points A, B, C, and D for the base case and the sensitivity case where no Pu(III) aqueous complexes were considered.

Sensitivity case – oxidizing scenario: The oxidation state of plutonium can have a significant impact on the mobility of the contaminant. In fact, Choppin and Morgenstern [49] conclude that “the most important property of plutonium with respect to its environmental behavior is its oxidation state because solubility, hydrolysis, complexation, sorption and colloid formation reactions differ significantly from one oxidation state to another.” As presented in the previous section, we have two scenarios in terms of Eh conditions. The first scenario is the base case, in which the Eh is about 10 mV at the 1000 years but decreases to about -50 mV by 10,000 years, representing a scenario under reducing conditions. The second scenario is the “V(pyrite)=0” case, in which Eh is at about 260 mV during the first 1000 years but decreases to about 235 mV by 10,000 years, representing a scenario under oxidizing conditions. In this section, we present the modeling results for the “V(pyrite)=0” case. Note that Pu(OH)₄(am) is still the controlling mineral phase at the canister in the “V(pyrite)=0” case. Similar to what was observed in Runde et al. [13], increasing the redox potential lowers the solubility of Pu(OH)₄(am), which results first in a lower concentration of total aqueous Pu at the canister, and then subsequently in much lower concentrations of total aqueous Pu in the EBS bentonite and the NS clay formation (see Figure 7-24). The concentration differences between the base and sensitivity case again emphasize the importance of a reliable calculation of redox potential in the EBS bentonite. Again we see that surface species dominate the Pu phase distribution (Figure 7-25).

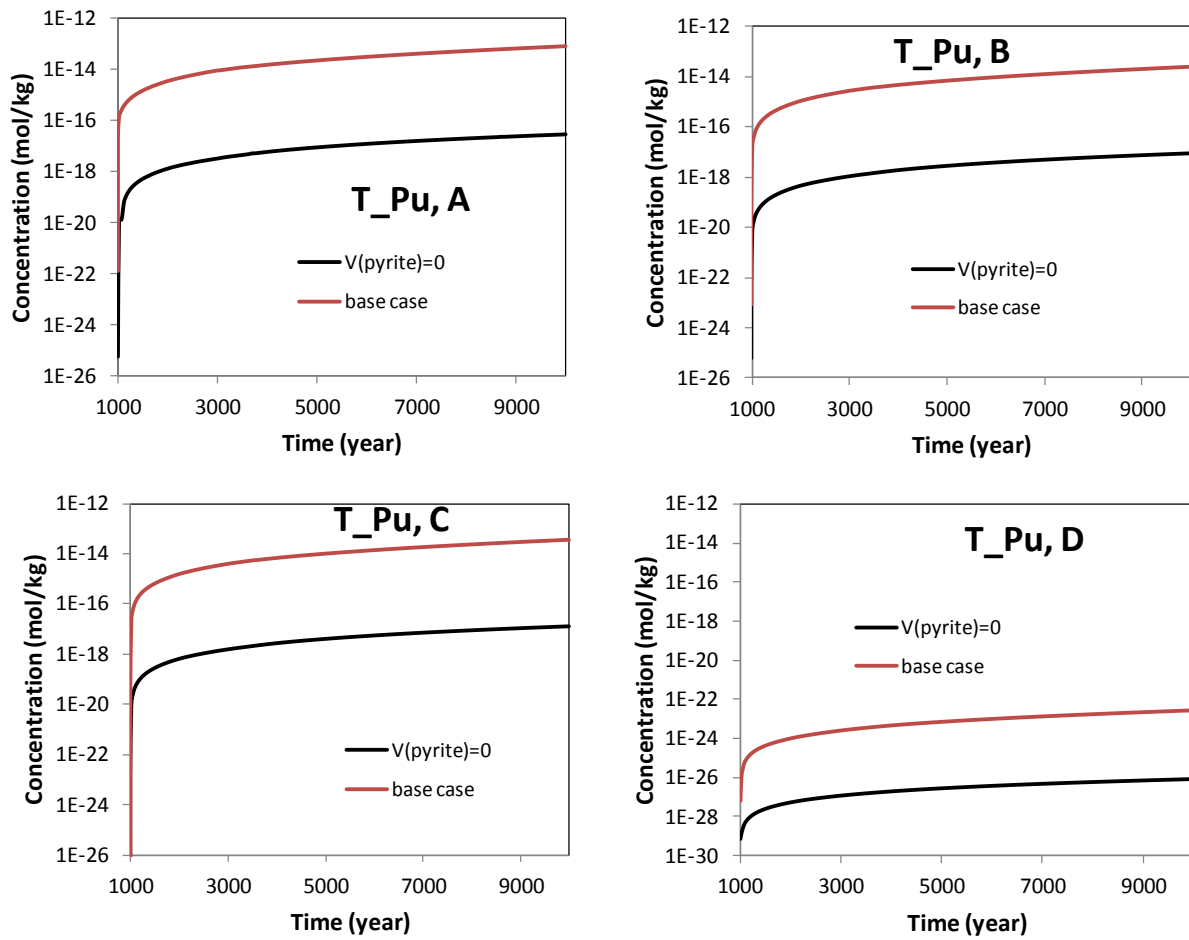


Figure 7-24. The temporal evolution of total aqueous Pu (T_Pu) at points A, B, C, and D for the base case (under reducing condition) and a “V(pyrite)=0” case (under oxidizing condition).

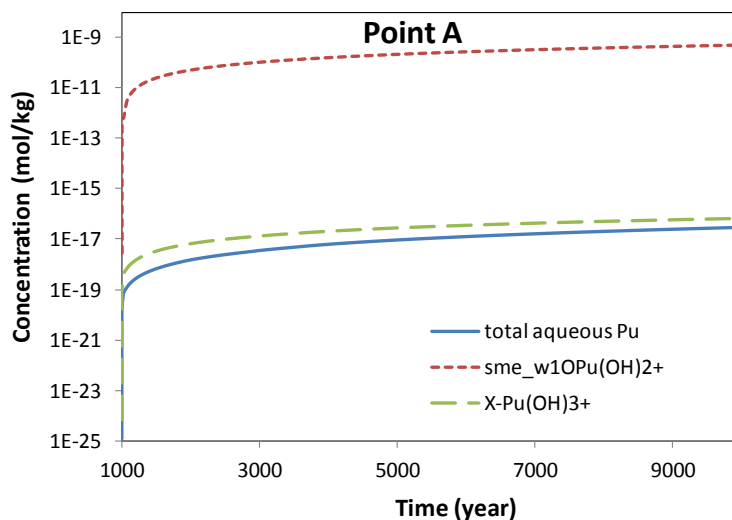


Figure 7-25. The temporal evolution of the concentration of total aqueous Pu, a surface complex (sme_w1OPu(OH)_2^+), and the Pu on the exchangeable sites (X-Pu(OH)_3^+) at point A from 1000 to 10,000 years for the “V(pyrite)=0” case.

7.4 Conclusions and Future Work

Previous studies have been conducted to investigate the changes in THMC conditions in the EBS and NS, which are of great importance since these changes determine the environment for radionuclide transport. Since FY12, our modeling effort has focused on modeling the migration of radionuclides in EBS and NS systems, including impacts of relevant processes, such as adsorption and aqueous complexation on the fate of radionuclides. After simulating the transport of uranium in FY12 [16], in this FY we modeled the reactive transport of plutonium (Pu) in a generic clay repository with bentonite EBS. Current simulations demonstrate that:

- Pu has very low mobility in the EBS bentonite and the NS clay formation, due to its adsorption via surface complexation.
- The redox environment in the EBS bentonite is critical for the fate of Pu, because of its impact on the solid-phase Pu and aqueous complexes of Pu. This calls for a reliable characterization of redox conditions in the EBS bentonite and NS clay formation.

The models presented in this report demonstrate our ability to simulate the migration of radionuclides in a complex, interactive THC/THMC environment. Such modeling effort is useful for differentiating the relative importance of various processes. However, modeling results are better viewed as qualitative rather than quantitative at this point, given that reliable calculations are only possible when site-specific data become available.

Over the course of simulating Pu transport in the EBS bentonite and NS clay formation, some urgent and important research needs became apparent and include:

- Sorption data for Pu(III). The adsorption of Pu, either conceptualized as a linear sorption isotherm (the K_d approach) or surface complexation model, were mostly determined for

- Pu(IV) and Pu(V). Under reducing conditions in which Pu(III) prevails, the applicability of these data is highly questionable.
- Thermodynamic data at elevated temperatures. Most reaction constants, especially solubility constants of the solid phases and surface complexation constants, are only available for a temperature of 25°C. However, current simulations show that after 10,000 years, the EBS bentonite could still remain at a temperature of 50°C. Thermodynamic data at higher temperatures are clearly needed when the impact of elevated temperatures on radionuclide transport is evaluated.
 - An improved understanding of the redox environment at the interface of the canister and EBS bentonite. We currently considered pyrite oxidation exclusively. Other reactions, such as radiolysis and biological reactions, will interact with the mineral phases in the EBS bentonite and the canister, and those reactions need to be conceptualized clearly and modeled in a reliable manner in the future. The experimental work on clay-metal interaction currently conducted for the EBS work package will provide valuable information about the redox environment at the interface of canister-bentonite.

7.5 References

- (1) Fouche O., Wright H., Cleach J. L., and Pellenard P. (2004) Fabric Control on Strain and Rupture of Heterogeneous Shale Samples by Using a Non-Conventional Mechanical Test, *Applied Clay Science* 26, 367-387.
- (2) Patriarche D., Ledoux E., Simon-Coincon R., Michelot J., and Cabrera J, (2004) Characterization and modeling of diffusive process for mass transport through the Tournemire Argillites Aveyron, France, *Applied Clay Science* 26, 109-122.
- (3) Bossart P., Meier P. M., Moeri A., Trick T. and Mayor J.-C. (2002) Geological and hydraulic characterisation of the excavation disturbed zone in the Opalinus Clay of the Mont Terri Rock Laboratory, *Engineering Geology* 66(1-2), 19-38.
- (4) Barnichon J.D. and Volckaert G. (2003) Observations and predictions of hydromechanical coupling effects in the Boom Clay, Mol Underground Research Laboratory, Belgium, *Hydrogeology Journal* 11 (1), 193-202.
- (5) Appelo C. A. J., Van Loon L. R. and Wersin P. (2010) Multicomponent diffusion of a suite of tracers (HTO, Cl, Br, I, Na, Sr, Cs) in a single sample of Opalinus Clay, *Geochimica et Cosmochimica Acta* 74(4), 1201-1219.
- (6) Garcia-Gutierrez, M., J. L. Cormenzana, T. Missana, M. Mingarro, U. Alonso, J. Samper, Q. Yang and S. Yi, Diffusion experiments in Callovo-Oxfordian clay from the Meuse/Haute-Marne URL, France. Experimental setup and data analyses. *Physics and Chemistry of the Earth* 33: S125-S130 (2008).
- (7) Maes N., Salah S., Jacques D., Aertsens M., Van Gompel M., De Cannière P. and Velitchkova, N. (2008) Retention of Cs in Boom Clay: Comparison of data from batch sorption tests and diffusion experiments on intact clay cores. *Physics and Chemistry of the Earth, Parts A/B/C* 33(Supplement 1): S149-S155.
- (8) Garcia-Gutierrez M., Cormenzana J. L., Missana T., Mingarro M. and Martin P. L. (2006) Large-scale laboratory diffusion experiments in clay rocks. *Physics and Chemistry of the Earth* 31(10-14), 523-530.
- (9) Soler J. M., Samper J., Yllera A., Hernández A., Quejido A., Fernández M., Yang C., Naves A., Hernán P. and Wersin P. (2008) The DI-B in situ diffusion experiment at Mont Terri: Results and modeling. *Physics and Chemistry of the Earth, Parts A/B/C* 33(Supplement 1), S196-S207.

- (10) Van Loon, L. R., Wersin P., Soler J. M., Eikenberg J., Gimmi T., Hernan P., Dewonck S. and Savoye S. (2004) In-situ diffusion of HTO, $^{22}\text{Na}^+$, Cs^+ and I^- in Opalinus clay at the Mont Terri underground rock laboratory. *Radiochim. Acta* 92, 757-763.
- (11) Wu T., Amayri S., Drebert J., Van Loon L. R. and Reich T. (2009) Neptunium(V) sorption and diffusion in Opalinus Clay. *Environmental Science & Technology* 43(17), 6567-6571.
- (12) De Windt L., Burnol A., Montarnal P. and van der Lee J. (2003) Intercomparison of reactive transport models applied to UO₂ oxidative dissolution and uranium migration. *Journal of Contaminant Hydrology* 61(1-4), 303-312.
- (13) Runde W., Conradson S.D., Wes Efurud D., Lu N., VanPelt C.E., Tait C.D. (2002) Solubility and sorption of redox-sensitive radionuclides (Np, Pu) in J-13 water from the Yucca Mountain site: comparison between experiment and theory, *Applied Geochemistry*, 17, 837-853.
- (14) Zheng L., Rutqvist J., Houseworth J., Davis J., Tinnacher R., Li L. and Liu H-H. (2011) Investigation of near-field thmc coupled processes, milestone report in UFD, Work Package number 1.02.08.03.
- (15) Rutqvist J., Zheng L., Chen F., Liu H.-H. and Birkholzer J. (2013). *Modeling of Coupled Thermo-Hydro-Mechanical Processes with Links to Geochemistry Associated with Bentonite-Backfilled Repository Tunnels in Clay Formations*. Rock Mechanics and Rock Engineering: 1-20.
- (16) Zheng L., Li L., Rutqvist J., Liu H. and Birkholzer J.T. (2012) *Modeling Radionuclide Transport in Clays*. Lawrence Berkeley National Laboratory. FCRD-UFD-2012-000128.
- (17) Xu T., Spycher N., Sonnenthal E., Zhang G., Zheng L. and Pruess K. (2011) TOUGHREACT Version 2.0: A simulator for subsurface reactive transport under non-isothermal multiphase flow conditions. *Computers & Geosciences* 37(6), 763-774.
- (18) Pruess K., Oldenburg C. and Moridis G., (1999) *TOUGH2 User's Guide, Version 2.0*, Lawrence Berkeley National Laboratory, Berkeley, CA.
- (19) Xu T., Sonnenthal E., Spycher N. and Pruess K. (2006) TOUGHREACT: A simulation program for non-isothermal multiphase reactive geochemical transport in variably saturated geologic media. *Computers and Geosciences* 32, 145-165.
- (20) Wolery T.J. (1993) EQ3/6, *A software package for geochemical modeling of aqueous systems (Version 7.2)*. UCRL-MA 110662, Lawrence Livermore National Laboratory.
- (21) Rutqvist J., Barr D., Birkholzer J.T., Fujisaki K., Kolditz O., Liu Q.-S., Fujita T., Wang W., Zhang C.-Y., A comparative simulation study of coupled THM processes and their effect on fractured rock (2009) Permeability around nuclear waste repositories. *Environmental Geology* 57, 1347-1360.
- (22) Ochs M., Lothenbach B., Shibata M. and Yui M. (2004) Thermodynamic modeling and sensitivity analysis of porewater chemistry in compacted bentonite. *Physics and Chemistry of the Earth, Parts A/B/C* 29(1): 129-136.
- (23) Thury M. (2002) The characteristics of the Opalinus Clay investigated in the Mont Terri underground rock laboratory in Switzerland. *Comptes Rendus Physique* 3(7-8), 923-933.
- (24) Bossart P. (2011), *Characteristics of the Opalinus Clay at Mont Terri*, http://www.mont-terri.ch/internet/mont-terri/en/home/geology/key_characteristics.html
- (25) Waber H.N., Mazurek M. and Pearson F.J. (1998) *Opalinus Clay: reference porewater, mineralogy and porosity*, NAGRA Internal Report.
- (26) De Canniere, P. (1997) *Measurements of Eh on slurries of Opalinus Clay, Mont Terri*. SCK•CEN. Mont Terri Project, Technical Note TN 96-32 (internal unpublished report).
- (27) Thury M. and Bossart P. (1999) *Results of the hydrogeological, geochemical and geotechnical experiments performed in the Opalinus Clay (1996-1997). Chapter 6.4 Organic Matter Characterisation of Rocks and Pore Waters*. Geological report No. 23. Swiss Geological Survey.

- (28) NAGRA (2003): *Geosynthese*. NAGRA Technical Report NTB 02-03. Nagra, Wettingen, Switzerland.
- (29) Lauber M., Baeyens B. and Bradbury M. H. (2000) *Physico-Chemical Characterisation and Sorption Measurements of Cs, Sr, Ni, Eu, Th, Sn and Se on Opalinus Clay from Mont Terri*. PSI Bericht Nr. 00-10 December 2000 ISSN 1019-0643.
- (30) Fernández A. M., Turrero M. J., Sánchez D. M., Yllera A., Melón A. M., Sánchez M., Peña J., Garralón A., Rivas P., Bossart P. and Hernán P. (2007) On site measurements of the redox and carbonate system parameters in the low-permeability Opalinus Clay formation at the Mont Terri Rock Laboratory. *Physics and Chemistry of the Earth, Parts A/B/C* 32(1-7), 181-195.
- (31) Sonnenthal, E. *Chapter 5 in: Birkholzer, J. Rutqvist, E. Sonnenthal, and D. Barr, Long-Term Permeability/Porosity Changes in the EDZ and Near Field due to THM and THC Processes in Volcanic and Crystalline-Bentonite Systems*, DECOVALEX-THMC Project Task D Final Report, 2008.
- (32) Sonnenthal E., Ito A., Spycher N., Yui M., Apps J., Sugita Y., Conrad M. and Kawakami S. (2005) Approaches to modeling coupled thermal, hydrological, and chemical processes in the Drift Scale Heater Test at Yucca Mountain. *Int. J. Rock Mech. Min. Sci.* 42, 6987–6719.
- (33) Fernández A. M., Turrero M. J., Sánchez D. M., Yllera A., Melón A. M., Sánchez M., Peña J., Garralón A., Rivas P., Bossart P. and Hernán P. (2007) On site measurements of the redox and carbonate system parameters in the low-permeability Opalinus Clay formation at the Mont Terri Rock Laboratory. *Physics and Chemistry of the Earth, Parts A/B/C* 32(1-7), 181-195.
- (34) Appelo C. J. A. and Postma D. (1994) *Geochemistry, groundwater and pollution*. Rotterdam, Netherlands, A.A. Balkema.
- (35) Wersin P., Johnson L.H. and Schwyn B. (2004) Assessment of redox conditions in the near field of nuclear waste repositories: Application to the Swiss high-level and intermediate level waste disposal concept, *Mat. Res. Soc. Symp.* Vol 807.
- (36) Powell B.A., Kersting A. Zavarin M., Zhao P. (2011) *Development of a Composite Non-Electrostatic Surface Complexation Model Describing Plutonium Sorption to Aluminosilicates*, Lawrence Livermore National Laboratory, LLNL-TR-408276.
- (37) Lemire R.J. and Tremaine P.R. (1980) Uranium and plutonium equilibria in aqueous solutions to 200 °C. *J. Chem. Eng. Data* 25, 361–370.
- (38) Altmaier M., Gaona X. and Fanghänel T. (2013) Recent advances in aqueous actinide chemistry and thermodynamics. *Chemical Reviews* 113(2), 901-943.
- (39) Glover P. A., Miner F. J. and Polzer W. O. (1976). *Plutonium and Americium behavior in the soil/water environment. I. sorption of Plutonium and Americium by soils*. In Proceedings of Actinide-Sediment Reactions Working Meeting, Seattle, Washington. pp. 225-254, BNWL-2117, Battelle Pacific Northwest Laboratories, Richland, Washington.
- (40) EPA. 1999. Understanding Variation in Partition Coefficient, K_d, Values, Volume II: Review of Geochemistry and Available K_d Values for Cadmium, Cesium, Chromium, Lead, Plutonium, Radon, Strontium, Thorium, Tritium (3H), and Uranium, United States Office of Air and Radiation, Environmental Protection Agency, August 1999, EPA 402-R-99-004B.
- (41) Begg J., Zavarin M., Zhao P., Tumey S., Powell B.A. and Kersting A.B. (2013) Pu(V) and Pu(IV) sorption to montmorillonite, *Environ. Sci. Technol.* 47(10), 5146-5153.
- (42) Aqion. 2013. <http://www.aqion.de/site/130>.
- (43) Efurud D.W., Runde W., Banar J.C., Janecky D.R., Kaszuba J.P., Palmer P.D., Roensch F.R. and Tait, C.D. (1998) Neptunium and Plutonium solubilities in a Yucca Mountain groundwater.” *Environmental Science & Technology*, 32 (24), 3893-3900.
- (44) Nitsche H., Roberts K., Prussin T., Muller A., Becraft K., Keeney D., Carpenter S.A., and Gatti R.C. (1994) *Measured solubilities and speciations from oversaturation experiments of Neptunium, Plutonium, and Americium in UE-25P #1 Well water from the Yucca Mountain*

- Region Milestone Report 3329- WBS1.2.3.4.1.3.1. LA-12563-MS. Los Alamos, New Mexico: Los Alamos National Laboratory.*
- (45) Kim J.I. and Kanellakopoulos B. (1989) Solubility products of Plutonium(IV) oxide and hydroxide.” *Radiochimica Acta*, 48, 145-150.
- (46) De Windt L., Schneider H., Ferry C., Catalette H., Lagneau V., Poinssot C., Poulesquen A. and Jegou C. (2006) Modeling spent nuclear fuel alteration and radionuclide migration in disposal conditions. *Radiochim. Acta* 94, 787-794.
- (47) Wersin P., Johnson L.H. and McKinley I.G. (2007) Performance of the bentonite barrier at temperature beyond 100°C: A critical review, *Physics and Chemistry of the Earth* 32, 780-788.
- (48) Liu H.H., Houseworth J., Rutqvist J., Zheng L., Asahina D., Li L., Vilarrasa V., Chen F., Nakagawa S., Finsterle S., Doughty C., Kneafsey T. and Birkholzer J. (2013) *Report on THMC modeling of the near field evolution of a generic clay repository: Model validation and demonstration*, FCRD-UFD-2013-000244, Lawrence Berkeley National Laboratory, Berkeley, CA.
- (49) Choppin G. R. and Morgenstern A. (2001) Distribution and movement of environmental plutonium, in *Plutonium in the environment*, A. Kudo, ed., 2001. pp. 91-105.

8.0 Thermal effect on the chemical behavior of clays

8.1 Introduction

Clay minerals are likely candidates to aid in nuclear waste isolation due to their low permeability, favorable swelling properties, and high cation sorption capacities. Establishing the thermal limit for clay minerals in a nuclear waste repository is a potentially important component of repository design, as flexibility of the heat load within the repository can have a major impact on the selection of repository design. For example, the thermal limit plays a critical role in the time that waste packages would need to cool before being transferred to the repository.

Understanding the chemical and physical changes that occur in clay minerals at various temperatures above the current thermal limit (of 100 °C) can enable decision-makers with information critical to evaluating the potential trade-offs of increasing the thermal limit within the repository. Most critical is gaining understanding of how varying thermal conditions in the repository will impact radionuclide sorption and transport in clay materials either as engineered barriers or as disposal media. In this study, a variety of clays (illite, mixed layer illite/smectite, montmorillonite, and palygorskite) were heated for a range of temperatures between 100-500 °C. These samples were characterized by nitrogen adsorption for porosimetry and barium chloride exchange for cation exchange capacity (CEC). For illite and illite-smectite, dramatic increases in CEC (20-fold and 10-fold, respectively) have been observed even after heat treatment of 100 °C, and this increase is maintained through heat treatment of 400 °C. Smectite (montmorillonite) and palygorskite CEC appears unchanged until 400 °C heat treatment, at which point they display CEC increases of 10-fold and 2-fold, respectively.

This work is directly relevant to “Topic P14” – *Technical Basis for thermal loading limits* – of the Natural System Work Plan. Experimental measurements for clay mineral response to thermal loads are critical as direct evidence of material response under thermal load, as well as for parameter input for thermal-hydrologic-mechanical-chemical (THMC) models of repository materials under different thermal loadings. Due to the high sorption potential of clays, in depth understanding of transport and uptake of radionuclides in clay mineral is key. By characterizing the changes in pore structure and cation exchange as a function of thermal load, this work has the potential to provide key parameters for THMC modeling for repository performance assessments.

8.2 State of the Art

While the dehydration and dehydroxylation of clay minerals over a range of temperatures from 100 °C to well over 1000 °C have been studied [1-2], focus has been on understanding structural changes during dehydroxylation, which for most clay minerals of interest occurs at temperatures over 500 °C. Other studies involving thermal treatments of clay minerals have mostly focused on clay-type identification [3] and heating in conjunction with chemical treatments to enhance dispersion of clay minerals as pillared nanomaterials [4] or for applications in catalysis and environmental remediation [5]. Onal [6] studied the simultaneous effect of heat and sulfuric acid treatment on bentonite, and measured CEC and swelling capacity as a function of temperature over a range of 100 °C to 1300 °C. Studies aimed at understanding the thermal effects on clay minerals in the natural environment tend to focus on diagenesis and sedimentology, in which case the interplay between physical structure (e.g., pore evolution, d-spacing) and chemical properties (CEC, anion uptake) are not the main focus. Studies in the literature tend to focus on a single clay mineral – we have broadened our study to include clay minerals

relevant to the repository environment (i.e. illite and smectite), as well as a mixed layer clay (illite-smectite), and a morphological and structural “wildcard” (the fibrous palygorskite).

8.3 Technical Approaches

Clay minerals and purification: The clays used all originate from the Clay Mineral Society source clays project at Purdue University. Four clays were used: illite, montmorillonite, palygorskite, sepiolite, and a 70/30 illite/smectite mixed layer (ID numbers: IMt-1, SWy-2, PFl-1, and ISCz-1, respectively). The clays used were relatively pure. The main purification step used for all of the clays was mechanical separation at 75 microns. The <75 microns size fraction was used in all the experiments presented here.

Heat Treatments and nitrogen adsorption porosimetry (BET): For each clay, samples of the <75 micron size fraction were individually heated for 2 hours at 100 °C, 200 °C, 300 °C, 400 °C, and 500 °C. Samples were weighed before and after heat treatments to measure weight loss. Immediately after heat treatment, samples were stored in a desiccator to prevent any re-uptake of ambient moisture. Heat treated samples were analyzed by nitrogen adsorption (NAD), using a Micromeritics Tristar 3000 to obtain data for BET surface area, BJH adsorption-desorption isotherms, and t-plot micro pore surface area.

Cation Exchange Capacity (CEC) measurements: Cation Exchange Capacity was measured using the barium chloride method, as described by Gillman [7]. Heat treated samples were weighed and 0.1M BaCl₂ solution was added at a solid to solution mass ratio of ~1:20. The suspension of clay and BaCl₂ solution was then shaken for 24 hours, centrifuged, and sampled (from the supernatant). After removing all of the supernatant for sampling, fresh BaCl₂ was added to the clay, which was again shaken, centrifuged, and sampled. This was repeated a third time – all 3 supernatant samples were collected cumulatively (i.e. sequentially added to a single sample collection vial) and analyzed on a Perkin Elmer 8000 series ICP-OES. Each clay sample was prepared and analyzed in triplicate.

8.4 Results

Weight loss: Heat treated samples were weighed before and after to measure weight loss during heating, and the results are shown in Figure 8-1. Palygorskite showed the most mass loss during the heat treatments, likely owing to its fibrous morphology which would enable faster transport/evaporation of water during heating. Also, mass loss was greater for smectite (montmorillonite) than for illite/smectite and illite, though all three showed significantly less mass loss than palygorskite. This figure illustrates how clay morphology and structure can have significant impacts on water transport from clay minerals. Palygorskite possesses sub-nanometer channels in its structure. Water adsorbed in these channels may be more labial to loss than those in the interlayer of clay minerals.

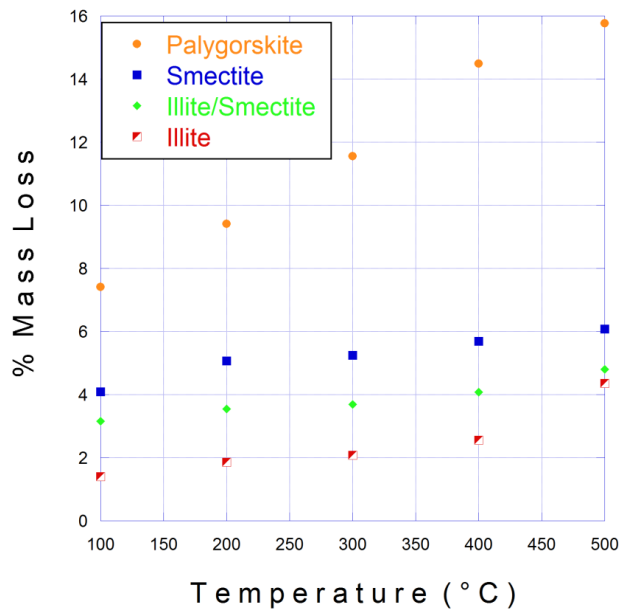


Figure 8-1. Percent mass loss for heat-treated clay samples

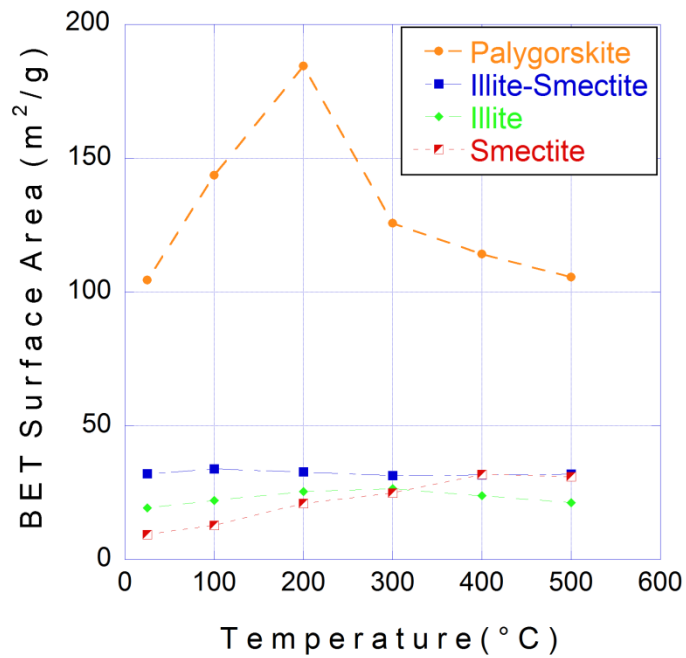


Figure 8-2. Summary of BET surface area vs. heat treatment temperature (note: 25 degree Celsius data point refers to untreated samples)

Nitrogen porosimetry and pore evolution for heat treatments: Nitrogen adsorption was performed on all heat treated clay minerals, as well as on untreated samples of each clay type to form a basis of comparison. Due to the heating involved in standard sample preparation protocols for NAD, none of these samples were heated and pumped under vacuum prior to NAD analysis. While this means that the surface areas reported herein may differ significantly from those reported elsewhere, all samples in this study – including untreated (i.e. no heat treatment) – were all handled and prepared in the same manner such that the results are comparable within the scope of this study. The Brunauer, Emmett, and Teller (BET) isotherm was used to determine surface area (herein referred to as “BET surface area”).

Figure 8-2 shows a plot of BET surface area as a function of heat treatment temperature. As with the mass loss plot shown in Figure 8-1, palygorskite shows a distinct behavior relative to the other clays, both in the magnitude of the BET surface area, but also in the character of its BET versus temperature profile. As mentioned, these differences are almost certainly due to the fibrous morphology and the channel structure of palygorskite. The NAD data can also provide information regarding the composition of the surface, indicating the contribution to overall BET surface area from both micro-pores (less than 1.7 nm) and meso-pores (1.7 nm to 50 nm) / macro-pores (50nm to 300nm). Pores between 1.7 nm and 300 nm (meso- and macro-) from the pore size distribution can be determined via the Barrett-Joyner-Halenda Isotherm (BJH) (specifically the adsorption isotherm), while a t-plot can be used to measure the surface area contribution from micro-pores (sub-1.7 nm). Figure 8-3 shows the surface area partitioned between the micro-pores and meso/macro pore surface area contributions for all four clays as a function of heat treatment temperature.

Illite, smectite, and to some extent palygorskite, show that the micropore surface area and meso/macro pore surface area trend with one another, i.e. as the clay heat treatment temperature rises, the surface area contribution from each either rise or fall together. Illite-smectite shows the exact opposite trend in that micropore surface area increases with temperature, while meso/macro pore surface area decreases as temperature increases. It is worth mentioning that for all clays, the micropore surface area profile with respect to temperature resembles that of the overall BET surface area profile with respect to temperature, notable exception being illite-smectite.

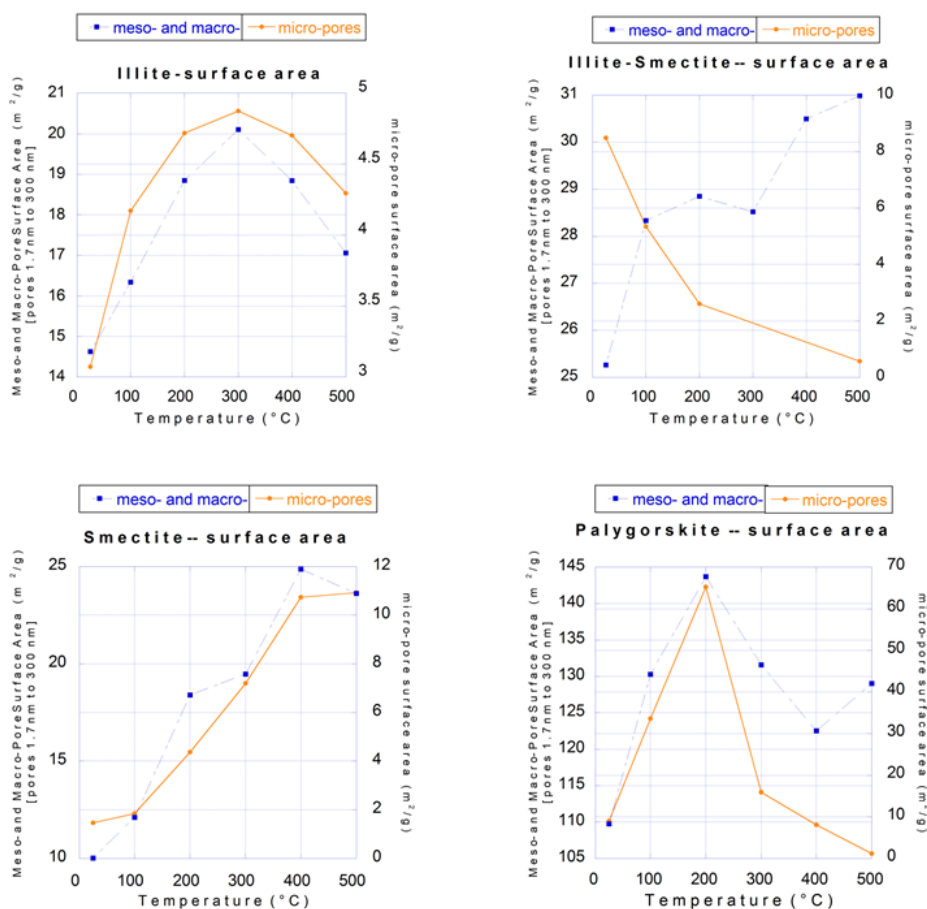


Figure 8-3. Pore size contribution for micro-pores and meso-/macro-pores for each clay type as a function of heat treatment temperature

Cation Exchange Capacity (CEC) Measurements: The cation exchange measurements reveal that there are some dramatic increases in CEC as a function of heat treatment temperature (Figure 8-4). Both the illite and illite-smectite clays shows significant increases in CEC, even at heat treatment of 100 °C, of about 20-fold and 10-fold, respectively. Both level out through 400 °C, and at 500 °C illite drops off slightly, while illite-smectite increases. These results seem contradictory to Onal's observation [6] that the CEC of calcium bentonite decreases with the temperature used in thermal treatment. For smectite and palygorskite, CEC drops slightly (10-20%) through 300 °C, and at 400 °C then experience 10-fold and 2-fold increases, respectively. The initial behavior shows that both smectite and palygorskite CEC are indifferent to BET surface area for heat treatment below 300 °C. Figure 8-4 also summarizes CEC and BET surface area as a function of heat treatment temperature. CEC roughly trends with BET surface area as a function of heat treatment temperature, with a notable exception for Palygorskite. In the case of Palygorskite, CEC increases as BET surface area decreases.

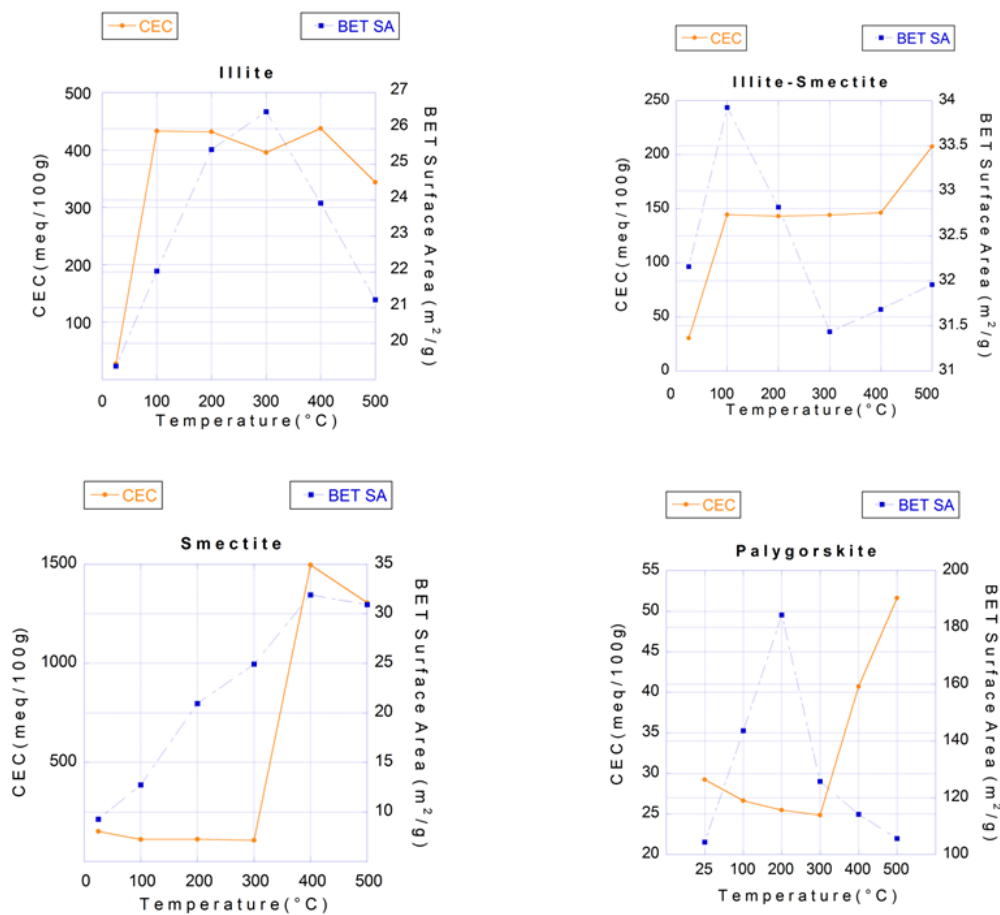


Figure 8-4. Summary of CEC and BET surface area as a function of heat treatment temperature

8.5 Conclusions and Future Work

Thermal treatments show significant effects on CEC for all four clays studied. For illite and illite-smectite, an order of magnitude increase in CEC is seen even at 100 °C. Given the ubiquity of illite in sealing/host formations, e.g. shale caprocks, this result could have an important effect on transport and fate in the near field in the case where the repository is in a clay rich host formation. For montmorillonite, the significant increase in CEC at 400 °C is perhaps of only of marginal importance, as this range of temperatures is likely well beyond any future allowance for the thermal limit in a repository environment. However, taken together, all of these results warrant a case for further study. It remains to be seen what role time duration of thermal treatment may play in alteration of the clay minerals in this study. For example, will longer exposure at a lower temperature, say 200 °C result in a change in CEC equivalent to a shorter duration exposure at 500 °C?

X-ray diffraction (XRD), thermogravimetric (TGA) analysis, and differential scanning calorimetry (DSC) can be used to gain insight into the mechanisms and alterations that have resulted in

changes in the CEC. As a part of future work, heated samples will be analyzed by XRD to ascertain if d_{001} -spacings are changed during heat treatments. TGA will be used to identify mass loss for longer durations of heat treatments, while DSC will be used to identify mineralogical phases that develop during heat treatment. In addition to investigating the effect of duration for temperatures closer to reasonable thermal limits, i.e., 200-300 °C, experimental understanding of how compacted clay responds to thermal treatment is a potential topic for future research.

8.6 References

- (1) Wolters, F., K. Emmerich. (2007) Thermal reactions of smectites – Relation of dehydroxylation temperature to octahedral structure, *Thermochemica Acta*, 462, 80-88.
- (2) Muller, F., V. Drits, A. Plancon, and J. L. Robert. (2000) Structural transformation of 2:1 Dioctohedral layer silicates during dehydroxylation-rehydroxylation reactions, *Clay and Clay Minerals*, 48, 572-585.
- (3) Moore, D. M. and . C. Reynolds. (1997) *X-ray Diffraction and the Identification and Analysis of Clay Minerals*. 2nd Edition, Oxford University Press, NY.
- (4) de Carvalho Costa, T. C., J. D. D. Melo, and C. A. Paskocimas. (2013) Thermal and chemical treatments of montmorillonite clay, *Ceramics International*, 301, 5063-5067.
- (5) Frost, R. L., and Z. Ding. (2003) Controlled rate thermal analysis and differential scanning calorimetry of sepiolites and palygorskites, *Thermochemica Acta*, 397, 119-128.
- (6) Onal, M. (2007) Swelling and cation exchange capacity relationship for the samples obtained by acid activations and heat treatments. *Applied Clay Science*, 37, 74-80.
- (7) Gillman, G., (1979) A proposed method for the measurement of exchange properties of highly weathered soils. *Soil Research*, 17, 129-139.

9.0 Summary

Significant progress has been made in FY13 in both experimental and modeling arenas in understanding and quantifying radionuclide interactions with representative geomaterials that may occur in the nature systems of deep geologic repositories. Three categories of radioelements have been examined: (1) weakly adsorptive radionuclides such as iodide, (2) moderately adsorptive radionuclides such as uranium, and (3) strongly adsorptive radionuclides such as Pu. FY13 work has been focused on two general types of geomaterials: clay/shale and granitic materials. The major accomplishments are summarized below:

- *Iodide interactions with clays:* Understanding iodide interactions with clay minerals is critical to quantifying risk associated with nuclear waste disposal. A suite of clay minerals was used with varying degrees of isomorphous substitution, chemical composition, and mineral structure. Iodide uptake experiments were completed with each of these minerals in a range of swelling electrolytes and concentrations. It has found that iodide uptake behaviors form distinct trends with cation exchange capacity and mineral structure. These trends change substantially with electrolyte composition and concentration, but do not appear to be affected by solution pH. The experimental results suggest that iodide may directly interact with clays by forming ion-pairs (e.g., $\text{NaI}_{(\text{aq})}$) which may concentrate within the interlayer space as well as the thin areas surrounding the clay particle where water behavior is more structured relative to bulk water. Ion pairing and iodide concentration in these zones is probably driven by the reduced dielectric constant of water in confined space and by the relatively high polarizability of the iodide species. This new conceptual model has far-reaching implications to the capability of clay materials as a geo-membrane for anion exclusion and isolation. To understand radionuclide interaction with compacted clay materials under relevant geologic conditions, a high pressure and high stress experimental setup has been developed, and it has been successfully tested for iodide sorption and diffusion.
- *In-situ characterization of pore structures of clay/shale samples:* Nano- to micro-scale structural characterization is crucial in providing insights into pore-scale transport processes, which are pertinent to upscale continuum model development. The Small-Angle Neutron Scattering (SANS) was used to characterize the pore features of various clay and shale samples. The results revealed the multi-scale nature of pore size distribution of clay/shale materials – a critical piece of information for understanding water migration and radionuclide transport in low-permeability clay materials and shale formations. The study suggests that the SANS be a useful technique to experimentally investigate flow and transport in low permeability and heterogeneous geologic media.
- *Column experiments of uranium interaction with granitic materials:* Small-scale columns appear to be useful for conducting relatively rapid and inexpensive dynamic transport experiments, which complement very well batch adsorption-desorption experiments. The combined use of the batch and column transport experiments provides better constraints on adsorption and desorption kinetics than either method by itself. Batch experiments are useful for evaluating rapid adsorption kinetics because column experiments often cannot effectively interrogate fast kinetics. Small-scale column experiments can also be very useful for identifying the presence of additional sorption sites and their kinetic behavior. The concentration rise during the injection portion of a column experiment can provide useful constraints on adsorption rates and surface densities of sites with slower rates than the fastest reaction. Interrogation of the reaction parameters associated with the slower sites can be improved by increasing the duration of the injection pulse to observe a longer approach to the injection concentration. The shape of the breakthrough curve in small-scale column experiments after the transition from injection of radionuclide solution to radionuclide-free solution can yield valuable insights into adsorption-desorption hysteresis behavior. Uranium transport in crushed granodiorite

materials at pH 6.9 appears to be governed by adsorption to and desorption from multiple sites that have different kinetics.

- Interaction of intrinsic Pu colloids with clay: The stability of three different types of intrinsic Pu colloids and Pu oxides in the presence of montmorillonite at 25 and 80°C under atmospheric conditions were examined. Intrinsic Pu colloids made in dilute basic solution were found to dissolve quickly, particularly when a strong thermodynamic gradient is provided (i.e., Pu sorption to montmorillonite). At 25°C, the dissolution of intrinsic Pu colloids is slower than at 80°C. Nevertheless, formation and dissolution of intrinsic Pu colloids appears to be a reversible process. Pu dissolution rates and the affinity for montmorillonite increase with temperature. The reversible nature and relatively fast dissolution rates of intrinsic Pu colloids precipitated in a basic solution suggests that these types of colloids are not very stable and their presence downstream of a nuclear waste repository setting is unlikely. In contrast, intrinsic Pu colloids produced from acidic solution and Pu oxides calcined at 300 and 800°C are stable over the 3 months investigated. Under these formation conditions, intrinsic Pu colloids and/or Pu oxides may play an important role in the migration of intrinsic Pu colloids away from nuclear waste repository setting. Therefore, how Pu oxides are formed impacts their ultimate chemical stability. Heat may play an important role in enhancing the stability of intrinsic colloids by increasing its crystallinity.
- Modeling Pu transport in clay materials: A thermal-hydrologic-chemical (THC) model was developed using code TOUGHREACT V2 to simulate the transport of Pu in the engineered barrier system (EBS) bentonite and the natural system (NS) clay formation. The simulations were conducted for a hypothetical bentonite-back-filled nuclear waste repository in clay rock. The simulations demonstrate that Pu has very low mobility in the EBS bentonite and the NS clay formation, due to its adsorption via surface complexation. The redox environment in the EBS bentonite is critical for the fate of Pu, because of its impact on the solid-phase Pu and aqueous complexes of Pu. This calls for a reliable characterization of redox conditions in the EBS bentonite and NS clay formation. The simulations demonstrate our ability to simulate the migration of radionuclides in a complex, interactive THC environment. Such modeling effort is useful for differentiating the relative importance of various processes.
- Preliminary study for thermal limits of clay materials/host rocks: Establishing the thermal limit for clay minerals in a nuclear waste repository is a potentially important component of repository design, as flexibility of the heat load within the repository can have a major impact on the selection of repository design. The thermal limit plays a critical role in the time that waste packages would need to cool before being transferred to the repository. In FY13, a preliminary study for thermal limits of clay materials was initiated. A variety of clays (illite, mixed layer illite/smectite, montmorillonite, and palygorskite) were heated for a range of temperatures between 100-500 °C and characterized for surface area, pore structure, and cation exchange capacity (CEC). It was found that thermal treatments have significant effects on CEC for all four clays studied. For illite and illite-smectite, an order of magnitude increase in CEC is seen even at 100 °C. Given the ubiquity of illite in sealing/host formations, e.g. shale caprocks, this result could have an important effect on transport and fate in the near field in the case where the repository is in a clay rich host formation. For montmorillonite, the significant increase in CEC at 400 °C is perhaps of only of marginal importance, as this range of temperatures is likely well beyond any future allowance for the thermal limit in a repository environment.

Based on the work accomplished in FY13 and the prior years, the future work is recommended to include:

- Continue the existing effort on experimental methodology development to better understand and quantify radionuclide interaction and migration in geologic environments. Emphasis will be given to the direct measurements of radionuclide interactions and material behaviors under high

rock/water ratios, high pressure/stress and high temperature conditions. Expand the measurements to a systematic set of radionuclide and materials.

- Integrate multi-scale measurements into coherent conceptual and mathematical models for total system performance assessments.
- Given the importance of material thermal limits in repository design, continue the study of thermal effects on clay material performance, with focus on understanding of how chemical and swelling properties of clay materials change with thermal treatment. This work needs to be closely tied to the study of the disposal of large size dual purpose canisters.

FCT Quality Assurance Program Document

**Appendix E
FCT Document Cover Sheet**

Experimental and Modeling Investigation of Radionuclide Interaction and Transport in Representative Geologic Media (M3FT-13SN0807081)

Name/Title of Deliverable/Milestone	UFD Natural Evaluation & Tool Development
Work Package Title and Number	FT-13SN080708
Work Package WBS Number	Yifeng Wang
Responsible Work Package Manager	(Name/Signature)

Date Submitted 9/13/2013

Quality Rigor Level for Deliverable/Milestone	<input checked="" type="checkbox"/> QRL-3	<input type="checkbox"/> QRL-2	<input type="checkbox"/> QRL-1 <input type="checkbox"/> Nuclear Data	<input type="checkbox"/> N/A*
---	---	--------------------------------	---	-------------------------------

This deliverable was prepared in accordance with Sandia National Laboratories
(Participant/National Laboratory Name)

QA program which meets the requirements of
 DOE Order 414.1 NQA-1-2000

This Deliverable was subjected to:

Technical Review

Technical Review (TR)

Review Documentation Provided

- Signed TR Report or,
- Signed TR Concurrence Sheet or,
- Signature of TR Reviewer(s) below

Name and Signature of Reviewers

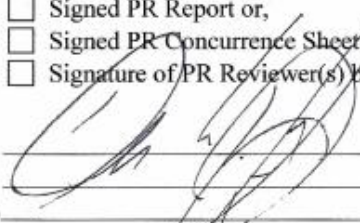
Carlos Jove-Colon

Peer Review

Peer Review (PR)

Review Documentation Provided

- Signed PR Report or,
- Signed PR Concurrence Sheet or,
- Signature of PR Reviewer(s) below



*Note: In some cases there may be a milestone where an item is being fabricated, maintenance is being performed on a facility, or a document is being issued through a formal document control process where it specifically calls out a formal review of the document. In these cases, documentation (e.g., inspection report, maintenance request, work planning package documentation or the documented review of the issued document through the document control process) of the completion of the activity along with the Document Cover Sheet is sufficient to demonstrate achieving the milestone. QRL for such milestones may be also be marked N/A in the work package provided the work package clearly specifies the requirement to use the Document Cover Sheet and provide supporting documentation.

